

1-5-2012

Applications of electronic structure theory to problems in strong-field chemistry, inorganic chemistry, and nanomaterial systems

Jason Anthony Sonk
Wayne State University,

Follow this and additional works at: http://digitalcommons.wayne.edu/oa_dissertations

 Part of the [Physical Chemistry Commons](#)

Recommended Citation

Sonk, Jason Anthony, "Applications of electronic structure theory to problems in strong-field chemistry, inorganic chemistry, and nanomaterial systems" (2012). *Wayne State University Dissertations*. Paper 520.

This Open Access Dissertation is brought to you for free and open access by DigitalCommons@WayneState. It has been accepted for inclusion in Wayne State University Dissertations by an authorized administrator of DigitalCommons@WayneState.

**APPLICATIONS OF ELECTRONIC STRUCTURE THEORY TO PROBLEMS IN
STRONG-FIELD CHEMISTRY, INORGANIC CHEMISTRY, AND NANOMATERIAL
SYSTEMS**

by

JASON ANTHONY SONK

DISSERTATION

Submitted to the Graduate School

of Wayne State University,

Detroit, Michigan

in partial fulfillment of the requirements

for the degree of

DOCTOR OF PHILOSOPHY

2012

MAJOR: CHEMISTRY (Physical)

Approved by:

Advisor

Date

DEDICATION

I dedicate this work to my best friend; my reason for getting up in the morning; my external memory bank; my drive, my hopes and dreams realized; all of these personified

by one person,

Misty.

ACKNOWLEDGMENTS

「虎穴に入らずんば虎子を得ず」

“If you do not enter the tiger’s cave, you will not catch his cub.”

-Japanese Colloquialism

There are a lot of people I would like to take this opportunity to acknowledge. This entire process could not have been completed without their help and support.

First, I would like to thank my advisor, Professor H. Bernhard Schlegel for his guidance, encouragement, and seemingly infinite patience during my entire graduate study.

Thanks are due to the members of my thesis committee: Professor Evelyn M. Goldfield, Professor Claudio N. Verani, and Professor Jeffrey Potoff for their support and guidance during my thesis research. And to Professors Alexander V. Benderskii and Mary T. Rodgers for teaching some of the best physical chemistry courses I have ever taken.

I am very grateful for the support and assistance I have received from the collection of people I have had the privilege of working with over the years, Professor Charles H. Winter, Professor Jeremy J. Kodanko, Dr. Marco M. Allard, Brian "Bribri" T. Psciuk, Dr. Jason. L. Sonnenberg, Dr. Peng Tao, Dr. Barbara. H. Munk, Dr. Jia Zhou, Dr. Michael A. Cato, Adam Birkholz, Dr. Suk Kyoung Lee, Dr. Vincenzo Verderlino, and Dr. Richard Lord.

I cannot thank Melissa Barton, Mary Wood, Erin Scully, Nestor Ocampo, Deborah McCreless, Bernadette Miesik, and Diane Klimas enough for their assistance over the years.

I would like to acknowledge the financial support I received during my graduate studies, provided in part by the National Science Foundation, the National Institutes of Health, the Initiative for Maximizing Student Development, the Department of Chemistry, and Wayne State University.

I would also like to thank my parents Maria and John Sonk. For encouraging me to venture into caves over the years, so that I may catch any cubs I had my sights on.

Lastly and most importantly, I would like to thank my wife, Misty Collette Sonk, who has truly limitless patience, and would accompany me into any tiger cave we may come across.

TABLE OF CONTENTS

Dedication.....	ii
Acknowledgments.....	iii
List of Tables	ix
List of Figures	xi
CHAPTER 1	INTRODUCTION AND DISSERTATION OVERVIEW..... 1
CHAPTER 2	TD-CI SIMULATION OF THE ELECTRONIC OPTICAL RESPONSE OF MOLECULES IN INTENSE FIELDS: COMPARISON OF RPA, CIS, CIS(D) AND EOM-CCSD25
2.1	Introduction.....25
2.2	Methods.....28
2.3	Results and Discussion33
2.4	Summary42
2.5	References.....44

CHAPTER 3	TD—CI SIMULATION OF THE ELECTRONICS OPTICAL RESPONSE OF MOLECULES IN INTENSE FIELDS II: COMPARISON OF DFT FUNCTIONALS AND EOM—CCSD	69
3.1	Introduction.....	69
3.2	Methods.....	70
3.3	Results and Discussion	71
3.4	Conclusions.....	77
3.5	References.....	79
CHAPTER 4	TD—CI SIMULATOIN OF THE STRONG FIELD IONIZATION OF POLYENES	95
4.1	Introduction.....	95
4.2	Methods.....	96
4.3	Results and Discussion	98
4.4	Conclusions.....	105
4.5	References.....	107

CHAPTER 5	THEORETICAL STUDIES OF METAL COMPLEXES DERIVED FROM THE CHIRAL TRIPYRIDALDIAMINE LIGAND BN-CDPY3	121
5.1	Introduction	121
5.2	Computational Methods	123
5.3	Computational Results	124
5.4	Discussion	127
5.5	Conclusions	130
5.6	References	131
CHAPTER 6	A SIMPLE MODEL IN WHICH INTERLIGAND INTERACTION CONTROLS THE CU—CU DISTANCE IN DINUCLEAR CU(II) PADDLEWHEEL COMPLEXES ..	147
6.1	Introduction	147
6.2	Computational Methods	149
6.3	Results and Discussion	150
6.4	Conclusions	153
6.5	References	155

CHAPTER 7	BIOINSPIRED FIVE—COORDINATE IRON(III) COMPLEXES FOR STABILIZATION OF PHENOXYL RADICALS	169
7.1	Introduction.....	169
7.2	Methods.....	171
7.3	Results and Discussion	172
7.4	Conclusions.....	175
7.5	References.....	176
CHAPTER 8	MODELING REACTIONS INSIDE SINGLE WALLED CARBON NANOTUBES	191
8.1	Introduction.....	191
8.2	Methods.....	193
8.3	Results and Discussion	195
8.4	Conclusions.....	201
7.5	References.....	202
CHAPTER 9	CONCLUSIONS	219
	Abstract.....	227
	Autobiographical Statement.....	229

LIST OF TABLES

Table 2-1:	Calculated vertical ionization potentials for butadiene.....	56
Table 3-1:	Lowest excitation energies and vertical ionization potentials for methods used in this study.....	86
Table 3-2:	Comparison of average excitation energies, average transition dipole magnitudes, and the sum of excited state populations.....	87
Table 4-1:	Linear polyenes used in the current study, their experimentally determined ionization potentials, total number of CIS excited states, and maximum number of states used in the current study.....	112
Table 5-1:	Relative energies of the five isomers of [Co(Bn-CdPY3)Cl] ²⁺ , [Zn(Ben-CDPy3)Cl] ⁺ , and [Fe(Bn-CDPy3)Cl] ⁺ in kcal/mol.....	139
Table 5-2:	Comparison of X-ray crystallographic Data and Calculated structures for the [Co(Bn-CdPY3)Cl] ²⁺ , [Zn(Ben-CDPy3)Cl] ⁺ , and [Fe(Bn-CDPy3)Cl] ⁺ cations	140
Table 6-1:	Detailed energetics (in hartree) for all of the species. <i>J</i> values listed in cm ⁻¹	158
Table 6-2:	Isocontour plots (0.05 au) of the corresponding orbitals for the AF coupled singlets. In all cases the alpha and beta orbitals are localized to one side of the molecule, and correspond to a Cu-centered radical consistent with the oxidation assignment Cu ^{II}	159
Table 6-3:	Geometric data for crystal structure and optimized geometries with bond lengths in Å and bond angles in degrees.....	160
Table 7-1:	Mulliken charge and spin density analysis and selected bond lengths (Å) for 1' , 1'⁺ , 1'²⁺ , 2' , 2'⁺ , 2'²⁺	182
Table 7-2:	Orbitals energies for 1' , 1'⁺ , 1'²⁺ , 2' , 2'⁺ , 2'²⁺	183
Table 8-1:	Relaxed scan of the H—Cl bond distance calculated at CCSD/6-311++G(d,p) in the gas phase and using PCM with benzene and water as solvents	208
Table 8-2:	Radius of Nanotubes used.....	208

LIST OF FIGURES

- Figure 1-1:** Electric component of the field of the laser pulse (left) and its effect on the coulombic potential binding an electron to a nucleus (right). The red dot on the electric field represents the magnitude of the electric field at a particular moment in time, the green line in the coulomb potential represents the energy level of a bound electron, and the black arrow is the motion of the electron. (a-b) Magnitude of the electric field is zero and the potential is a typical $1/r$ coulomb potential. (c-d) As the electric field nears a peak of the pulse, the coulomb potential is distorted so that the electron is either no longer bound or has a high probability of tunneling out. (e-f) Half a cycle later the electric field has changed sign and the distortion in the coulomb potential is reversed, accelerating the electron back toward the nucleus.17
- Figure 1-2:** Population of the excited states of butadiene, after the pulse, as a function of field strength calculated using EOM-CC (left). Population of the first four excited states of butadiene during the laser pulse (right, top). Butadiene and the alignment of the laser pulse (right, bottom)18
- Figure 1-3:** Comparison of the sum of the populations after the pulse of the excited states with energies less than 0.5 au for simulations with DFT functionals and wavefunction based methods using the 6-31 3+ G(d,p) basis and 300 excited states. The horizontal lines represent the population of EOM-CC $\pm 25\%$. Population of the excited states of butadiene, after the pulse, as a function of field strength calculated using the long-range corrected BLYP functional (inset, right).....19
- Figure 1-4:** Fraction of the population ionized by the pulse as a function of the intensity (W/cm^2) for ethylene (blue), butadiene (red), hexatriene (green), octatetraene (black) calculated using the 6-31 1+ G(d,p) basis set and Klamroth's heuristic model with $d = 1$ bohr. The 7-cycle cosine pulse used in these simulations (inset, top left) and the four linear polyenes studies (inset, bottom left). The excited states which contribute the most towards ionization of hexatriene as a function of excited state energy and time step in the pulse (inset, bottom right).....20
- Figure 1-5:** Structure of the pentadentate chiral trypridyldiamine ligand synthesized by the Kodanko group21
- Figure 1-6:** Isomers of $\text{M}(\text{Bn-CDPy}_3)\text{Cl}$ determined from calculations: A, B, and C display *mer* orientations of the pyridyl donors; D and E are *fac*.....21

- Figure 1-7:** Left: X-ray crystal structure of the compound isolated by the Winter group Right: Copper acetate compound previously found and characterized.....22
- Figure 1-8:** Left: Total spin density plots showing excess α and β electron spin on each of the atomic centers over the oxidation process.
Right: Full and simplified representations of the Fe(II) system.....23
- Figure 1-9:** Left: Total electron density of a profile of 9,0 single walled carbon nanotube (isovalue 0.01 au) showing the interior cavity.
Right: Cavity used for polarizable continuum model approximating interior nanotube cavity.24
- Figure 2-1:** The highest occupied and lowest unoccupied π molecular orbitals of 1,3-butadiene calculated by HF/6-31G(d,p)57
- Figure 2-2:** Vertical excitation energies of butadiene for the first 30 1B_u states and 1A_g states calculated with the 6-31 3+ G(d,p) basis set (RPA (blue triangles pointing down), CIS (red squares), CIS(D) (green diamonds), EOM-CC (black circles)). IP is the experimentally determined ionization potential58
- Figure 2-3:** Vertical excitation energies for the first 500 states of butadiene (all symmetries) calculated with (a) the 6-31 3+ G(d,p) basis and RPA, CIS, CIS(D) and EOM-CC (blue, red, green and black, respectively), (b) CIS and the 6-31 n+ G(d,p) and 6-31(n+)G(d,p) basis sets (n=1 blue, n=2 red, n=3 green, solid lines (n+), dotted lines n+). Inset: Number of states under the experimental ionization potential59
- Figure 2-4:** Transition dipoles for butadiene calculated with (a) CIS/6-31G(d,p), (b) CIS/6-31 1+ G(d,p), (c) CIS/6-31 2+ G(d,p), (d) CIS/6-31 3+ G(d,p), (e) CIS/6-31(1+)G(d,p), (f) CIS/6-31++G(2df,2pd), (g) RPA/6-31 3+ G(d,p), and (h) EOM-CC/6-31 3+ G(d,p).....60
- Figure 2-5:** Response of model two and three level systems ($\omega_0 = 0.$, $\omega_1 = 0.25$, $\omega_2 = 0.35$; $D_{01} = 2.0$, $D_{12} = 2.0$, $D_{02} = 0.0$ au) to a 3 cycle Gaussian pulse, as a function of the pulse frequency, ω , and the maximum of the pulse envelope, E_{\max} : (a) and (b) ground and excited state populations of the two level system, (d), (e) and (f) ground and excited state populations of the three level system, (c) pulse shape61

- Figure 2-6:** Response of the butadiene π states (1^1A_g ground state and the 1^1B_u , 2^1A_g and 2^1B_u excited states) to a 3 cycle gaussian pulse: (a)-(d) CIS/6-31G(d,p) excited state energies and transition dipoles: $\omega_0 = 0.0$, $\omega_1 = 0.256$, $\omega_2 = 0.344$, $\omega_3 = 0.369$, $\omega_4 = 0.460$; $D_{02} = D_{03} = D_{14} = D_{23} = 0.0$, $D_{01} = -2.575$, $D_{04} = 0.485$, $D_{12} = 0.430$, $D_{13} = 2.620$, $D_{24} = 0.547$, $D_{34} = 3.406$ au. (e)-(h) EOM-CC/6-31G(d,p) excited state energies and transition dipoles: $\omega_0 = 0.0$, $\omega_1 = 0.267$, $\omega_2 = 0.293$, $\omega_3 = 0.358$, $\omega_4 = 0.440$; $D_{02} = D_{03} = D_{14} = D_{23} = 0.0$, $D_{01} = -2.091$, $D_{04} = 0.555$, $D_{12} = -1.581$, $D_{13} = -0.330$, $D_{24} = -1.968$, $D_{34} = -0.114$ au.....62
- Figure 2-7:** Comparison of the response of butadiene calculated with TD-CIS/6-31G(d,p) in a 3 cycle Gaussian pulse ($\omega = 0.06$ au, $E_{\max} = 0.05$ au) in terms of (a) the zero-field states and (b) the instantaneous adiabatic states64
- Figure 2-8:** Excited state populations of butadiene as a function of number of states included in the TD-CIS simulation, at the maximum of the pulse (top row) and after the pulse (bottom row) ($\omega = 0.06$ au, $E_{\max} = 0.05$ au) with the 6-31 n+ G(d,p) basis sets65
- Figure 2-9:** Response of butadiene subject to a 3 cycle Gaussian pulse ($\omega = 0.06$ au, $E_{\max} = 0 - 0.06$ au) calculated by TD-CIS with 500 excited states using the following basis sets (a) 6-31G(d,p), (b) 6-31(2+)G(d,p), (c) 6-31(3+)G(d,p), (d) 6-31 1+ G(d,p), (e) 6-31 2+ G(d,p) and (f) 6-31 3+ G(d,p).....66
- Figure 2-10:** Response of butadiene subject to a 3 cycle Gaussian pulse ($\omega = 0.06$ au, $E_{\max} = 0 - 0.06$ au) calculated with the 6-31 3+ G(d,p) basis set and RPA, CIS,CIS(D) and EOM-CC using 300 states (top row) and 500 states (bottom row).....67
- Figure 2-11:** Dependence of the populations and energies on E_{\max} , the maximum field strength of the pulse: (a) ground state population, (b) sum of the populations of excited states with energies less than 0.5 au, (c) energy deposited in excited states with energies less than 0.5 au (RPA – blue, CIS – red, CIS(D) – green, EOM-CC – black).....68
- Figure 3-1:** Excited state energies for the first 500 states of butadiene (all symmetries) calculated by standard density functionals: B3LYP (red), PBE (blue), HSEPB (green), PW91 (purple) using the 6-31 3+ G(d,p) basis set. For comparison EOM-CC (black, dotted) and RPA (black, dashed) energies are included.....88

- Figure 3-2:** Effect of Hartree-Fock exchange for the first 500 excited states calculated using BLYP (0% HF, red), B3LYP (20% HF, blue), CAM-B3LYP (19-65% HF, purple), BH&HLYP (50% HF, green), EOM-CC (black, dotted), RPA (black, dashed). All methods used the 6-31 3+ G(d,p) basis set.....88
- Figure 3-3:** Excited state energies for the first 500 states of butadiene calculated by long-range corrected density functionals: ω B97XD (blue), CAM-B3LYP (red), LC-BLYP (purple), LC- ω PBE (green), LC-PBE (orange) using the 6-31 3+ G(d,p) basis set. For comparison EOM-CC (black, dotted) and RPA (black, dashed) energies are included.....89
- Figure 3-4:** Excited state energies for the first 500 states of butadiene, calculated with LC- ω PBE/6-31 3+ G(d,p) and varying the ω -parameter: $\omega = 0.2$ (blue), $\omega = 0.4$ (default; red), $\omega = 0.6$ (green), $\omega = 0.8$ (purple), EOM-CC (black, dotted) and RPA (black, dashed) are included for comparison.....89
- Figure 3-5:** Transition dipoles for butadiene calculated with B3LYP/6-31 3+ G(d,p)90
- Figure 3-6:** Response of butadiene subjected to a three-cycle Gaussian pulse ($\omega=0.06$ au, $E_{\max}=0-0.06$ au) calculated with the 6-31 3+ G(d,p) basis set, using 500 states for the standard functionals (a) BLYP, (b) PBE, (c) PW91, and their long range corrected counterparts (e)LC-BLYP, (f)LC-PBE, (g) LC-PW91, (d) RPA, and (h) EOM-CC (300 states)91
- Figure 3-7:** Response of butadiene subjected to a three-cycle Gaussian pulse ($\omega=0.06$ au, $E_{\max}=0-0.06$ au) calculated with the 6-31 3+ G(d,p) basis set, using 500 states for (a) B3LYP, (b) BH&HLYP, (c) CAM-B3LYP, and LC- ω PBE with (d) $\omega = 0.2$, (e) $\omega = 0.4$ (default), (f) $\omega = 0.6$, and (g) $\omega = 0.8$92
- Figure 3-8:** Comparison of the sum of the populations of the excited states with energies less than 0.5 au for simulations with DFT functionals and wavefunction based methods using the 6-31 3+ G(d,p) basis and 300 excited states. The horizontal lines represent the population of EOM-CC $\pm 25\%$93
- Figure 3-9:** Correlation between the average excited state energy and the sum of the population of all excited states after the pulse calculated with the 6-31 3+ G(d,p) basis, $E_{\max} = 0.05$ au and 300 states for the standard DFT functionals (red), long-range corrected functionals (green), wavefunction based methods (blue) and EOM-CC (black). ($R^2=0.89$ for a linear fit and $R^2=0.98$ for a quadratic fit)..... 94

- Figure 4-1:** Ionization rates for the excited states of (a) ethylene, (b) butadiene, (c) hexatriene, and (d) octatetraene, using the 6-31 1+ G(d,p) (blue), 6-31 2+ G(d,p) (red), and 6-31 3+ G(d,p) (green) basis sets and a distance parameter of $d = 1$ bohr in Equation (4-2).113
- Figure 4-2:** Density of states for (a) ethylene, (b) butadiene, (c) hexatriene, (d) octatetraene, found using the 6-31 1+ G(d,p) (blue), 6-31 2+ G(d,p) (red), and 6-31 3+ G(d,p) (green) basis sets, all CIS excited states, and a distance parameter $d = 1$ bohr.114
- Figure 4-3:** Loss of norm as a function of the distance parameter d (in bohr) for (a) ethylene, (b) butadiene, (c) hexatriene, and (d) octatetraene, using the 6-31 1+ G(d,p) (blue), 6-31 2+ G(d,p) (red), and 6-31 3+ G(d,p) (green) basis sets for $E_{\max} = 0.05$ au115
- Figure 4-4:** (a) Electric field for a seven cycle 760 nm cosine pulse with intensity of 0.88×10^{14} W cm⁻² ($E_{\max} = 0.05$ au), (b) time evolution of the wavefunction norm during the pulse and (c) instantaneous ionization rate for ethylene (blue), butadiene (red), hexatriene (green) and octatetraene (black) with a distance parameter $d = 1$ bohr using the 6-31 1+ G(d,p) basis set.....116
- Figure 4-5:** Instantaneous ionization rates as a function of state number and time for (a) ethylene and (b) hexatriene. The simulations used a 7 cycle 760 nm cosine pulse with $E_{\max} = 0.05$ atomic units, and employed a distance parameter $d = 1$ bohr, 288 excited states for ethylene and 999 excited states for hexatriene computed with the 6-31 1+ G(d,p) basis117
- Figure 4-6:** Contributions of individual states to the loss of norm for (a) ethylene with escape distance parameter $d = 1$ bohr, (b) hexatriene with $d = 1$ bohr, (c) ethylene with $d = 10$ bohr and (d) hexatriene with $d = 10$ bohr. The simulations used a 7 cycle 760 nm cosine pulse with $E_{\max} = 0.05$ atomic units, and employed 288 excited states for ethylene and 999 excited states for hexatriene computed with the 6-31 1+ G(d,p) basis118
- Figure 4-7:** Effect of basis set size and number of states on the wavefunction norm after the pulse as a function of field strength for (a) butadiene with the 6-31 1+ G(d,p) basis set and 150 states (blue), 250 states (red), and all 957 CIS excited states (green), (b) butadiene, (c) hexatriene and (d) octatetraene with 6-31 1+ G(d,p), 6-31 2+ G(d,p) and 6-31 3+ G(d,p) basis sets (blue, red and green, respectively) with $d = 1$ bohr.....119
- Figure 4-8:** Fraction of population ionized by the pulse as a function of the intensity (W/cm²) for ethylene (blue), butadiene (red), hexatriene (green), octatetraene (black) calculated using the 6-31 1+ G(d,p) basis set and $d = 1$ bohr.....120

- Figure 5-1:** Known pentadentate ligands containing multiple N-donors and their derivatives.....141
- Figure 5-2:** Structure of (*R,R*)-Bn-CDPy3 (**1**), a chiral pentadentate ligand.....142
- Figure 5-3:** Isomers of M(Bn-CDPy3)Cl determined from calculations: A, B, and C display *mer* orientations of the pyridyl donors; D and E are *fac*.....142
- Figure 5-4:** Comparison of calculated and observed chemical shifts of the three protons in the 2-position on the pyridyl rings in isomer C of [Co(Bn-CDPy3)Cl]²⁺ and [Zn(Bn-CDPy3)Cl]⁺ (R² = 0.992).....143
- Figure 5-5:** Observed vs. calculated (in parentheses) chemical shifts for the 2-pyridyl C-H protons (shown in white, other protons omitted for clarity) of (a) [Co(Bn-CDPy3)Cl]⁺ and (b) [Zn(Bn-CDPy3)Cl]⁺.....144
- Figure 5-6:** Structure of the ligand Bn-TPEN and model of the cation [Fe(Bn-TPEN)Cl]⁺ generated using X-ray crystallographic data from ref. 10. The structure of the cation is similar to [Fe (Bn-CDPy3)Cl]⁺, where the Cl group is in a *trans* configuration relative to N(1), and the three pyridyl N-donors N(3)-N(5) adopt a *mer* configuration, with two pyridine N-donors residing in a coplanar conformation with respect to the Fe-Cl bond, while the third ring is perpendicular to that axis145
- Figure 5-7:** Structure Calculated structures of the dication [Co(Bn-CDPy3)Cl]²⁺ C, ent-A (see Figure 5-3), and an overlap of the two structures that illustrates the subtle differences between the two stereoisomers. All hydrogens except those creating key interactions are omitted for clarity. In the case of C, a methylene hydrogen can occupy a position directly above the cyclohexane ring and between two axial hydrogen atoms, whereas with ent-A, the pyridyl substituent rotates to avoid an unfavorable interaction with a closer axial hydrogen atom.....146
- Figure 6-1:** Left: X-ray crystal structure of the compound isolated by the Winter group. Right: Copper acetate compound previously found and characterized.....161
- Figure 6-2:** Perspective view of **1** with selected bond lengths (Å) and angles (°): Cu1-N1 1.996(2), Cu1-N3 1.987(1), Cu2-N2 1.999(2), Cu2-N4 1.997(2), Cu1-O2 1.955(1), Cu1-O4 1.955(1), Cu2-O1 1.963(1), Cu2-O3 1.958(1), Cu1-Cu2 2.4148(3), N1-Cu1-N3 171.21(6), N1-Cu1-O2 89.37(6), N1-Cu1-O4 90.21(6), N3-Cu1-O2 89.28(6), N3-Cu1-O4 90.66(6), O2-Cu1-O4 176.86(5), N2-Cu2-N4 171.15(6), N2-Cu2-O1 89.75(6), N2-Cu2-O3 89.90(6), N4-Cu2-O1 90.66(6), N4-Cu2-O3 89.18(6), O1-Cu2-O3 176.77(6).162

- Figure 6-3:** Definition of the Twist Angle θ163
- Figure 6-4:** CPK model looking down the Cu–Cu axis of the MeN–C_{Me}–NMe model before and after ligand tilting. The shortest H··H distance between neighboring methyl groups is 2.66 and 2.98 Å, respectively.164
- Figure 6-5:** Walsh diagram for the O–C_{Me}–NMe model. The orbital which is most sensitive to the angular tilt is the antisymmetric combination of the ligand π -orbitals.....165
- Figure 6-6:** Correlation between plane-to-plane and Cu-Cu separation. Linear regression analysis: $y = 2.54 x - 3.23$; $R^2 = 0.97$ 166
- Figure 6-7:** Linear regression plot including the amidate complexes. Because the interligand contact plane is not as clearly defined (top), the simple $r \cdot \cos(\theta)$ argument overestimates the Cu–Cu separation. Linear regression plot: $y = 1.63 x - 1.20$; $R^2 = 0.49$167
- Figure 7-1:** Experimental structures of **1** and **2** (top) and computational models for **1'** and **2'** (bottom).184
- Figure 7-2:** Spin density plots for the oxidation series of **1'** (top, left) and **2'** (bottom, left). The white and blue areas of electron density correspond to excess α and β electron spin density, respectively. Superimposition of the optimized geometries of the sequential oxidation of **1'** (top, right) and **2'** (bottom, right).....185
- Figure 7-3:** Average orbital energy ladder (left) and selected frontier orbitals (right, α -SOMOs and spin coupled Pairs with Hydrogen atoms omitted for clarity) for **1'**, **1'⁺**, and **1'²⁺**. (B3LYP/6-31G(d) IEF-PCM dichloromethane).....186
- Figure 7-4:** Average orbital energy ladder (left) and selected frontier orbitals (right, α -SOMOs and spin coupled Pairs with Hydrogen atoms omitted for clarity) for **2'**, **2'⁺**, and **2'²⁺**. (B3LYP/6-31G(d) IEF-PCM dichloromethane).....188
- Figure 8-1:** The H₃N–H–Cl guest system inside a 9,0 single walled nanotube (a) axial view and (b) side view of the nanotube and guest system, exhibiting C_{3v} symmetry.....209
- Figure 8-2:** Relaxed scan of the H–Cl distance for the NH₃–H–Cl hydrogen bonded system. Calculated using CCSD/6-311++G(d,p) in the gas phase (black), in a benzene solution using PCM (red), and in water solution using PCM (green). The zero of energy has been set to the geometry corresponding to the gas phase minimum energy structure ...210

- Figure 8-3:** Relaxed scan along the transfer of H+ from HCl to NH₃ calculated using (black) ONIOM(B3PW91/6-311++G(d,p):UFF), (red) ONIOM(B3PW91/6-311++G(d,p):MNDO), (green) ONIOM(B3PW91/6-311++G(d,p):PM3), compared against (blue) single point energies of the PCM optimized aqueous solution geometries centered in a 9,0 nanotube with C_{3v} symmetry.....211
- Figure 8-4:** Series of single point calculations based on the geometries taken from a relaxed scan of the H—Cl distance for the NH₃—H—Cl guest system in the gas phase calculated using CCSD/6-311++G(d,p). Single point energies calculated using B3PW91/6-311++G(d,p) in the gas phase (green), benzene PCM (blue), chloroform PCM (black), water (red), in a 9,0 SWCNT (dashed purple).....212
- Figure 8-5:** Effect of PCM solvation on chloride ion as a function of dielectric constant and cavity scaling parameter. Calculated using HF/cc-pVDZ213
- Figure 8-6:** (a) Electron isodensity (Isovalue = 0.01 au) surface of the 9,0 nanotube and guest system. (b) Sausage PCM cavity constructed to approximate the interior surface of the nanotube. 12 PCM cavity spheres are centered along the axis of the nanotube every angstrom starting at the tube opening214
- Figure 8-7:** Effect of PCM sausage cavity radius on energies along the reaction coordinate of the transfer of a proton in the hydrogen bonded NH₃—H—Cl system. Calculations were performed using the dielectric of benzene, and the gas phase CCSD/6-311++G(d,p) optimized geometries; energies are calculated using the B3PW91/6-311++G(d,p) level of theory.....215
- Figure 8-8:** Relative energies along the reaction coordinate of the transfer of a proton in the hydrogen bonded NH₃—H—Cl system in a 9,0 nanotube (blue) and an 8,0 nanotube (red). Comparison between the relaxed scan calculated at B3PW91/6-311++G(d,p) using the sausage PCM model (dashed) and single point calculations of the optimized geometries from sausage PCM calculations (solid).....216
- Figure 8-9:** Energies along the reaction coordinate of the transfer of a proton in the hydrogen bonded NH₃—H—Cl system, using fixed geometries optimized from previous sausage PCM calculations. In the gas phase (black), in a 9,0 nanotube (green), in the sausage PCM for a 9,0 nanotube (blue), and in the 9,0 SWCNT sausage PCM with a molecular mechanics tube around the PCM (red).....217

Chapter 1

Introduction and Dissertation Overview

1.1 Introduction

The development of quantum mechanics is arguably one of the greatest advances in physics in the last century. With the advent of quantum mechanics we gained invaluable insight into the nature of the atom and can now reliably model and predict the interactions of subatomic particles. Computational chemistry applies the concepts of quantum mechanics to the larger scale domain of molecules and reactions between them. The level of control afforded by computational methods allows one to probe questions which may not be possible to answer via experimental methods. Computational chemistry allows us to accomplish several things that are not yet possible experimentally such as following the real time dynamics of an electron as it moves from its ground state energy level up through several excited states and back again to the ground state.

This dissertation covers research involving applications of electronic structure theory to problems in chemistry and is divided into eight chapters. Chapters 2 through 4 describe a series of related works which explore applications of excited state electronic structure methods to problems in strong field chemistry. Chapters 5 through 7 discuss the application of electronic structure theory methods to solving problems in inorganic chemistry. Finally, Chapter 8 looks at an application of electronic structure theory to nanomaterials.

As mentioned above Chapters 2 through 4 present research on modeling electron dynamics in strong-field chemistry. Strong-field chemistry utilizes short, intense laser pulses to study a chemical system of interest. These laser pulses tend to have intensities on the order of 10^{14} W/cm². At these intensities, the electric field of the laser rivals that of the coulombic attraction between an electron and the nucleus of an atom which can lead to a variety of effects.¹⁻¹⁰ During the laser pulse (Figure 1-1) , the coulombic barrier can be suppressed enough that an electron is no longer considered bound and is accelerated away from the atom or molecule (Figure 1-1d). A half-cycle later, the sign of the electric field changes and the electron is returned to the parent system with excess energy, leading to either recombination or electron scattering (Figure 1-1f). Because the strength of the electric field in the laser pulse is so large the interaction cannot be modeled using perturbative methods. The effects of strong-field chemistry have successfully been modeled on the small systems with few electrons, using grid based numerical methods.¹¹⁻²⁹ However, modeling methods have yet to be perfected for larger, more chemically complex, many electron systems. Attempts have been made using various approximate methods for a variety of larger molecules.^{24,30-59}

Chapters 2 – 4 discuss exploratory studies on modeling the electron dynamics of butadiene after interaction with a strong field utilizing a time-dependent configuration-interaction (TD-CI) approach. We choose butadiene not only because it is highly polarizable, but also because we can take advantage of its symmetry to preferentially excite a subset of the electrons in the system. We can utilize the dipole approximation for the laser field, which assumes a static dipole model to represent the field at any particular step in time. The TD-CI method can be recast into a set of coupled, linear

differential equations which depend on the field free excited state energies and transition dipole matrix elements projected in the direction of the field. We then explore which theoretical methods provide the best set of excited state energies and transition dipole moments to reliably model the strong-field electron dynamics. Of course these intense fields can lead to ionization, but modeling ionization can be a computationally demanding feat.

To determine which methods perform the best we first look at the change in population of the ground and excited states predicted by wavefunction based methods (Chapter 2) and DFT functionals (Chapter 3), and then consider ionization (Chapter 4). One advantage we have as computational chemists is we can explicitly track the population in the ground state and in each of the excited states at every time step in our simulations. Unfortunately, we lack an experimental reference to directly test the simulations. Instead we utilize the equation-of-motion coupled cluster method (EOM-CC)⁶⁰⁻⁶³ as our gold-standard to check our simulations. In Chapter 2⁶⁴ we look at the performance of simulations using excited state energies and transition dipoles calculated using time-dependent Hartree-Fock (TD-HF) also known as the random phase approximation (RPA), time-dependent configuration interaction with single excitations (TD-CIS), and TD-CIS with perturbative doubles correction (TD-CIS(D)).^{65,66} We also look at which basis sets can be used to reasonably describe the space in which the strong-field excitations take place (Figure 1-2).

Chapter 3⁶⁷ builds on Chapter 2 by utilizing time-dependent density functional theory (TD-DFT)^{68,69} to calculate the excited state energies and transition dipoles required for our TD-CI simulations. We examine the performance of various classes of

DFT functionals such as pure GGA functionals, meta-GGA functionals, hybrid functionals, and long-range corrected functionals. We also attempt to understand how the overall response to the laser pulse is affected by the excited state energies and transition dipoles (Figure 1-3).

Chapter 4 builds upon the work of Chapters 2 and 3, focusing on a model for ionization applied to a series of linear polyenes: ethylene, butadiene, hexatriene, and octatetraene. Modeling ionization for small molecules can be achieved by using numerical methods with absorbing potentials to produce a loss of electron density.⁷⁰⁻⁷² For larger systems, the Klamroth group has developed a heuristic ionization model⁵⁶ which utilizes TD-CIS and atom centered gaussian basis sets. In Chapter 4 we look at the different parameters which go into this heuristic model and how they affect the ionization rate of molecules in strong laser fields. We also look at which excited states contribute the most towards ionization in the hope that we can pare down the number of excited states included in the simulations. Finally we examine how well the model replicates the trends in ionization rates by comparing to ionization rates observed experimentally and calculated using other theoretical models (Figure 1-4).

Chapters 5 through 7 look at a series of studies based on collaborative work with members of the organic and inorganic divisions of chemistry at Wayne State University. By combining the efforts of experimental chemists with the methods available to computational chemists we can gain a better understanding of the chemistry of a series of novel compounds. Chapters 5⁷³ and 6 are a pair of studies in which there was a question of the underlying reasons for the preferred geometric structure of a system. In Chapter 5 we worked with the Kodanko group to understand the coordination preference for a

pentadentate chiral tripyridyldiamine ligand (Figure 1-5). When this chiral ligand complexes with a metal halide, there are five possible isomers (Figure 1-6). However, only one (isomer **C** in Figure 1-6) was observed experimentally. In this chapter we discuss the factors which contribute to the preference of isomer **C** over the other isomers. In Chapter 6 we worked with the Winter group; they were able to synthesize a paddlewheel dicopper (II) complex with the shortest Cu—Cu separation reported to date. Even though previous studies^{74,75} have declared that a Cu²⁺—Cu²⁺ bond is inaccessible, we attempt to understand the causes of the shorter separation, taking into account the effect of the ligands as well as the nature of the Cu²⁺—Cu²⁺ electronic interaction. In Chapter 7⁷⁶ we look at a system from the Verani group. They were investigating the redox properties of some materials that could be usable as molecular switches. Due to the number of unpaired electrons in the system and because of contributions of both ligand and metal centered orbitals, the nature of the oxidation state of the system can become difficult to assign. Our task was to help understand the oxidation sequence and attempt to corroborate the experimental findings (Figure 1-8).

Finally, Chapter 8 deals with the computational modeling of carbon nanotube materials. Problems in the field of materials typically deal with systems much larger than chemical systems. Periodic boundary conditions can help make some systems studied by the materials science community computationally more tractable, but not all systems are periodic. In this chapter we build a model for a system that does not have periodic symmetry, a nanotube hosting a guest molecule inside of it. Specifically we attempt to model a chemical reaction taking place inside a nanotube. Confinement within a nanotube can have a large influence on the potential energy surface of a reaction,

significantly affecting the energy profile of reactions which go through large electronic and/or conformational changes. However, the sheer number of atoms in a typical nanotube makes the entire system computationally expensive to model. In this chapter we propose and test an affordable model which can be used to optimize any molecular system of interest placed inside of a nanotube. By splitting the effects of a nanotube into electronic and mechanical contributions, we can replace a full quantum calculation on the entire system into a quantum calculation on the guest system in a polarizable environment and a molecular mechanics calculation on the confinement effect (Figure 1-9). This approach significantly improves the time it takes to fully optimize the guest system in the nanotube.

1.2 References

- (1) Baltuska, A.; Udem, T.; Uiberacker, M.; Hentschel, M.; Goulielmakis, E.; Gohle, C.; Holzwarth, R.; Yakovlev, V. S.; Scrinzi, A.; Hansch, T. W.; Krausz, F. Attosecond control of electronic processes by intense light fields, *Nature* **2003**, *421*, 611.
- (2) Brabec, T.; Krausz, F. Intense few-cycle laser fields: Frontiers of nonlinear optics, *Rev. Mod. Phys.* **2000**, *72*, 545.
- (3) Cavalieri, A. L.; Muller, N.; Uphues, T.; Yakovlev, V. S.; Baltuska, A.; Horvath, B.; Schmidt, B.; Blumel, L.; Holzwarth, R.; Hendel, S.; Drescher, M.; Kleineberg, U.; Echenique, P. M.; Kienberger, R.; Krausz, F.; Heinzmann, U. Attosecond spectroscopy in condensed matter, *Nature* **2007**, *449*, 1029.
- (4) Corkum, P. B.; Krausz, F. Attosecond science, *Nat. Phys.* **2007**, *3*, 381.
- (5) Goulielmakis, E.; Schultze, M.; Hofstetter, M.; Yakovlev, V. S.; Gagnon, J.; Uiberacker, M.; Aquila, A. L.; Gullikson, E. M.; Attwood, D. T.; Kienberger, R.; Krausz, F.; Kleineberg, U. Single-cycle nonlinear optics, *Science* **2008**, *320*, 1614.
- (6) Goulielmakis, E.; Yakovlev, V. S.; Cavalieri, A. L.; Uiberacker, M.; Pervak, V.; Apolonski, A.; Kienberger, R.; Kleineberg, U.; Krausz, F. Attosecond control and measurement: Lightwave electronics, *Science* **2007**, *317*, 769.
- (7) Ivanov, M. Y.; Spanner, M.; Smirnova, O. Anatomy of strong field ionization, *J. Mod. Opt.* **2005**, *52*, 165.
- (8) Kling, M. F.; Vrakking, M. J. J. Attosecond electron dynamics, *Annu. Rev. Phys. Chem.* **2008**, *59*, 463.

- (9) Drescher, M.; Hentschel, M.; Kienberger, R.; Tempea, G.; Spielmann, C.; Reider, G. A.; Corkum, P. B.; Krausz, F. X-ray pulses approaching the attosecond frontier, *Science* **2001**, *291*, 1923.
- (10) Krausz, F.; Ivanov, M. Attosecond physics, *Rev. Mod. Phys.* **2009**, *81*, 163.
- (11) Chelkowski, S.; Zuo, T.; Bandrauk, A. D. Ionization Rates of H-2(+) in an Intense Laser Field by Numerical-Integration of the Time-Dependent Schrodinger-Equation, *Phys. Rev. A* **1992**, *46*, R5342.
- (12) Chelkowski, S.; Zuo, T.; Atabek, O.; Bandrauk, A. D. Dissociation, Ionization, and Coulomb Explosion of H-2(+) in an Intense Laser Field by Numerical-Integration of the Time- Dependent Schrodinger-Equation, *Phys. Rev. A* **1995**, *52*, 2977.
- (13) Yu, H. T.; Zuo, T.; Bandrauk, A. D. Molecules in intense laser fields: Enhanced ionization in a one-dimensional model of H-2, *Phys. Rev. A* **1996**, *54*, 3290.
- (14) Chelkowski, S.; Foisy, C.; Bandrauk, A. D. Electron-nuclear dynamics of multiphoton H-2(+) dissociative ionization in intense laser fields, *Phys. Rev. A* **1998**, *57*, 1176.
- (15) Walsh, T. D. G.; Ilkov, F. A.; Chin, S. L.; Chateauneuf, F.; Nguyen-Dang, T. T.; Chelkowski, S.; Bandrauk, A. D.; Atabek, O. Laser-induced processes during the Coulomb explosion of H-2 in a Ti-sapphire laser pulse, *Phys. Rev. A* **1998**, *58*, 3922.
- (16) Bandrauk, A. D.; Chelkowski, S. Asymmetric electron-nuclear dynamics in two-color laser fields: Laser phase directional control of photofragments in H-2(+), *Phys. Rev. Lett.* **2000**, *84*, 3562.

- (17) Talebpour, A.; Vijayalakshmi, K.; Bandrauk, A. D.; Nguyen-Dang, T. T.; Chin, S. L. Dissociative ionization of D-2 in intense laser fields: D⁺-ion production perpendicular to the polarization of a 400-nm laser field, *Phys. Rev. A* **2000**, *62*, 42708.
- (18) Kawata, I.; Kono, H.; Fujimura, Y.; Bandrauk, A. D. Intense-laser-field-enhanced ionization of two-electron molecules: Role of ionic states as doorway states, *Phys. Rev. A* **2000**, *62*, 31401.
- (19) Bandrauk, A. D.; Chelkowski, S.; Zamojski, M. Laser phase control of electron-nuclear dynamics in dissociative ionization with intense femtosecond pulses: Exact (non-Born-Oppenheimer) numerical simulations for H-2(+), *Z. Phys. Chem.* **2000**, *214*, 1393.
- (20) Kawata, I.; Bandrauk, A. D.; Kono, H.; Fujimura, Y. Enhanced ionization of the two-electron molecule H-2 in intense laser fields: Mechanism of the creation of doorway states, *Laser Phys.* **2001**, *11*, 188.
- (21) Harumiya, K.; Kono, H.; Fujimura, Y.; Kawata, I.; Bandrauk, A. D. Intense laser-field ionization of H-2 enhanced by two-electron dynamics, *Phys. Rev. A* **2002**, *66*, 43403.
- (22) Bandrauk, A. D.; Chelkowski, S. LIED: laser induced electron diffraction by intense laser- molecule interaction - an exact non-Born-Oppenheimer simulation of the one-electron system: H-2(+), *J. Mol. Struct. THEOCHEM* **2002**, *591*, 199.
- (23) Bandrauk, A. D.; Chelkowski, S.; Kawata, I. Molecular above-threshold-ionization spectra: The effect of moving nuclei, *Phys. Rev. A* **2003**, *67*, 13407.
- (24) Bandrauk, A. D.; Lu, H. Z. Laser-induced electron recollision in H-2 and electron correlation, *Phys. Rev. A* **2005**, *72*, 23408.

- (25) Kamta, G. L.; Bandrauk, A. D. Three-dimensional time-profile analysis of high-order harmonic generation in molecules: Nuclear interferences in H-2(+), *Phys. Rev. A* **2005**, *71*, 53407.
- (26) Kamta, G. L.; Bandrauk, A. D. Three-dimensional analysis of nuclear contributions to harmonic generation in H-2(+), *Laser Phys.* **2005**, *15*, 502.
- (27) Nguyen, N. A.; Bandrauk, A. D. Electron correlation of one-dimensional H-2 in intense laser fields: Time-dependent extended Hartree-Fock and time-dependent density-functional-theory approaches, *Phys. Rev. A* **2006**, *73*, 32708.
- (28) Bandrauk, A. D.; Lu, H. Z. Electron correlation and double ionization of a 1D H-2 in an intense laser field, *J. Mod. Opt.* **2006**, *53*, 35.
- (29) Bandrauk, A. D.; Barmaki, S.; Kamta, G. L. Laser phase control of high-order harmonic generation at large internuclear distance: The H+-H-2(+) system, *Phys. Rev. Lett.* **2007**, *98*, 13001.
- (30) Usachenko, V. I.; Pyak, P. E.; Chu, S. I. High-order harmonic generation in laser-irradiated homonuclear diatomics: The velocity gauge version of the molecular strong-field approximation, *Laser Phys.* **2006**, *16*, 1326.
- (31) Guan, X. X.; Tong, X. M.; Chu, S. I. Effect of electron correlation on high-order-harmonic generation of helium atoms in intense laser fields: Time-dependent generalized pseudospectral approach in hyperspherical coordinates, *Phys. Rev. A* **2006**, *73*, 23403.
- (32) Usachenko, V. I.; Chu, S. I. Strong-field ionization of laser-irradiated light homonuclear diatomic molecules: A generalized strong-field approximation-linear combination of atomic orbitals model, *Phys. Rev. A* **2005**, *71*, 63410.

(33) Telnov, D. A.; Chu, S. I. Ab initio study of high-order harmonic generation of H-2(+) in intense laser fields: Time-dependent non-Hermitian Floquet approach, *Phys. Rev. A* **2005**, *71*, 13408.

(34) Chu, X.; Chu, S. I. Role of the electronic structure and multielectron responses in ionization mechanisms of diatomic molecules in intense short-pulse lasers: An all-electron ab initio study, *Phys. Rev. A* **2004**, *70*, 61402.

(35) Greenman, L.; Ho, P. J.; Pabst, S.; Kamarchik, E.; Mazziotti, D. A.; Santra, R. Implementation of the time-dependent configuration-interaction singles method for atomic strong-field processes, *Phys. Rev. A* **2010**, *82*.

(36) Suzuki, M.; Mukamel, S. Charge and bonding redistribution in octatetraene driven by a strong laser field: Time-dependent Hartree-Fock simulation, *J. Chem. Phys.* **2003**, *119*, 4722.

(37) Suzuki, M.; Mukamel, S. Many-body effects in molecular photoionization in intense laser fields; time-dependent Hartree-Fock simulations, *J. Chem. Phys.* **2004**, *120*, 669.

(38) Kuleff, A. I.; Breidbach, J.; Cederbaum, L. S. Multielectron wave-packet propagation: General theory and application, *J. Chem. Phys.* **2005**, *123*, 44111.

(39) Breidbach, J.; Cederbaum, L. S. Migration of holes: Formalism, mechanisms, and illustrative applications, *J. Chem. Phys.* **2003**, *118*, 3983.

(40) Breidbach, J.; Cederbaum, L. S. Migration of holes: Numerical algorithms and implementation, *J. Chem. Phys.* **2007**, *126*, 034101.

(41) Kuleff, A. I.; Cederbaum, L. S. Charge migration in different conformers of glycine: The role of nuclear geometry, *Chem. Phys.* **2007**, *338*, 320.

(42) Lünemann, S.; Kuleff, A. I.; Cederbaum, L. S. Ultrafast charge migration in 2-phenylethyl-N,N-dimethylamine, *Chem. Phys. Lett.* **2008**, *450*, 232.

(43) Hennig, H.; Breidbach, J.; Cederbaum, L. S. Electron correlation as the driving force for charge transfer: Charge migration following ionization in N-methyl acetamide, *J. Phys. Chem. A* **2005**, *109*, 409.

(44) Remacle, F.; Kienberger, R.; Krausz, F.; Levine, R. D. On the feasibility of an ultrafast purely electronic reorganization in lithium hydride, *Chem. Phys.* **2007**, *338*, 342.

(45) Remacle, F.; Levine, R. D. Charge migration and control of site selective reactivity: The role of covalent and ionic states, *J. Chem. Phys.* **1999**, *110*, 5089.

(46) Remacle, F.; Levine, R. D. The time scale for electronic reorganization upon sudden ionization of the water and water-methanol hydrogen bonded dimers and of the weakly bound NO dimer, *J. Chem. Phys.* **2006**, *125*.

(47) Remacle, F.; Levine, R. D. Probing Ultrafast Purely Electronic Charge Migration in Small Peptides, *Z. Phys. Chem.* **2009**, *221*, 647.

(48) Remacle, F.; Levine, R. D.; Ratner, M. A. Charge directed reactivity:: a simple electronic model, exhibiting site selectivity, for the dissociation of ions, *Chem. Phys. Lett.* **1998**, *285*, 25.

(49) Nest, M.; Klamroth, T.; Saalfrank, P. The multiconfiguration time-dependent Hartree-Fock method for quantum chemical calculations, *J. Chem. Phys.* **2005**, *122*, 124102.

(50) Krause, P.; Klamroth, T. Dipole switching in large molecules described by explicitly time-dependent configuration interaction, *J. Chem. Phys.* **2008**, *128*.

- (51) Krause, P.; Klamroth, T.; Saalfrank, P. Molecular response properties from explicitly time-dependent configuration interaction methods, *J. Chem. Phys.* **2007**, *127*.
- (52) Krause, P.; Klamroth, T.; Saalfrank, P. Time-dependent configuration-interaction calculations of laser-pulse-driven many-electron dynamics: Controlled dipole switching in lithium cyanide, *J. Chem. Phys.* **2005**, *123*, 74105.
- (53) Klamroth, T. Optimal control of ultrafast laser driven many-electron dynamics in a polyatomic molecule: N-methyl-6-quinolone, *J. Chem. Phys.* **2006**, *124*, 144310.
- (54) Tremblay, J. C.; Krause, P.; Klamroth, T.; Saalfrank, P. Time-dependent response of dissipative electron systems, *Phys. Rev. A* **2010**, *81*.
- (55) Tremblay, J. C.; Klamroth, T.; Saalfrank, P. Time-dependent configuration-interaction calculations of laser-driven dynamics in presence of dissipation, *J. Chem. Phys.* **2008**, *129*.
- (56) Klinkusch, S.; Saalfrank, P.; Klamroth, T. Laser-induced electron dynamics including photoionization: A heuristic model within time-dependent configuration interaction theory, *J. Chem. Phys.* **2009**, *131*.
- (57) Liang, W. K.; Isborn, C. M.; Li, X. S. Laser-Controlled Dissociation of C₂H₂²⁺ : Ehrenfest Dynamics Using Time-Dependent Density Functional Theory, *J. Phys. Chem. A* **2009**, *113*, 3463.
- (58) Liang, W.; Isborn, C. M.; Lindsay, A.; Li, X. S.; Smith, S. M.; Levis, R. J. Time-Dependent Density Functional Theory Calculations of Ehrenfest Dynamics of

Laser Controlled Dissociation of NO⁺: Pulse Length and Sequential Multiple Single-Photon Processes, *J. Phys. Chem. A* **2010**, *114*, 6201.

(59) Liang, W.; Chapman, C. T.; Ding, F.; Li, X. Modeling Ultrafast Solvated Electronic Dynamics Using Time-Dependent Density Functional Theory and Polarizable Continuum Model, *J. Phys. Chem. A* **2012**, *116*, 1884.

(60) Koch, H.; Jorgensen, P. Coupled cluster response functions, *J. Chem. Phys.* **1990**, *93*, 3333.

(61) Stanton, J. F.; Bartlett, R. J. The equation of motion coupled-cluster method: A systematic biorthogonal approach to molecular excitation energies, transition probabilities, and excited state properties, *J. Chem. Phys.* **1993**, *98*, 7029.

(62) Koch, H.; Kobayashi, R.; Demeras, A. S.; Jorgensen, P. Calculation of size-intensive transition moments from the coupled cluster singles and doubles linear response function, *J. Chem. Phys.* **1994**, *100*, 4393.

(63) Kallay, M.; Gauss, J. Calculation of excited-state properties using general coupled-cluster and configuration-interaction models, *J. Chem. Phys.* **2004**, *121*, 9257.

(64) Sonk, J. A.; Caricato, M.; Schlegel, H. B. TD-CI Simulation of the Electronic Optical Response of Molecules in Intense Fields: Comparison of RPA, CIS, CIS(D), and EOM-CCSD, *J. Phys. Chem. A* **2011**, *115*, 4678.

(65) Headgordon, M.; Maurice, D.; Oumi, M. A Perturbative Correction to Restricted Open-Shell Configuration-Interaction with Single Substitutions for Excited-States of Radicals, *Chem. Phys. Lett.* **1995**, *246*, 114.

- (66) Headgordon, M.; Rico, R. J.; Oumi, M.; Lee, T. J. A Doubles Correction to Electronic Excited-States from Configuration-Interaction in the Space of Single Substitutions, *Chem. Phys. Lett.* **1994**, *219*, 21.
- (67) Sonk, J. A.; Schlegel, H. B. TD-CI Simulation of the Electronic Optical Response of Molecules in Intense Fields II: Comparison of DFT Functionals and EOM-CCSD, *J. Phys. Chem. A* **2011**, 10.1021/jp206437s.
- (68) Dreuw, A.; Head-Gordon, M. Single-Reference ab Initio Methods for the Calculation of Excited States of Large Molecules, *Chem. Rev.* **2005**, *105*, 4009.
- (69) Marques, M. A. L.; Gross, E. K. U. Time-dependent density functional theory, *Annu. Rev. Phys. Chem.* **2004**, *55*, 427.
- (70) Riss, U. V.; Meyer, H. D. Calculation of Resonance Energies and Widths Using the Complex Absorbing Potential Method, *J. Phys. B-At. Mol. Opt. Phys.* **1993**, *26*, 4503.
- (71) Neuhauser, D.; Baer, M.; Judson, R. S.; Kouri, D. J. The Application of Time-Dependent Wavepacket Methods to Reactive Scattering, *Comput. Phys. Commun.* **1991**, *63*, 460.
- (72) Muga, J. G.; Palao, J. P.; Navarro, B.; Egusquiza, I. L. Complex absorbing potentials, *Phys. Rep.-Rev. Sec. Phys. Lett.* **2004**, *395*, 357.
- (73) Abouelatta, A. I.; Sonk, J. A.; Hammoud, M. M.; Zurcher, D. M.; McKamie, J. J.; Schlegel, H. B.; Kodanko, J. J. Synthesis, Characterization, and Theoretical Studies of Metal Complexes Derived from the Chiral Tripyridyldiamine Ligand Bn-CDPy₃, *Inorg. Chem.* **2010**, *49*, 5202.

(74) Hay, P. J.; Thibeault, J. C.; Hoffmann, R. Orbital Interactions in Metal Dimer Complexes, *J. Am. Chem. Soc.* **1975**, *97*, 4884.

(75) Clerac, R.; Cotton, F. A.; Daniels, L. M.; Gu, J. D.; Murillo, C. A.; Zhou, H. C. An infinite zigzag chain and the first linear chain of four copper atoms; Still no copper-copper bonding, *Inorg. Chem.* **2000**, *39*, 4488.

(76) Allard, M. M.; Sonk, J. A.; Heeg, M. J.; McGarvey, B. R.; Schlegel, H. B.; Verani, C. N. Bioinspired Five-Coordinate Iron(III) Complexes for Stabilization of Phenoxy Radicals, *Angew. Chem.-Int. Edit.* **2012**, *51*, 3178.

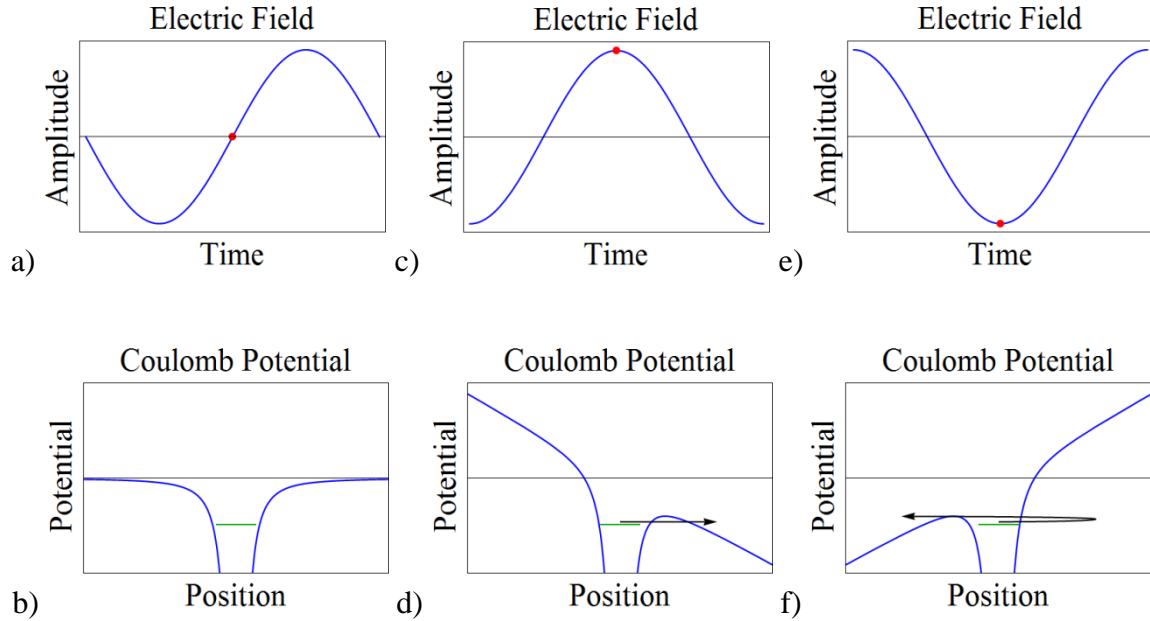


Figure 1-1. Electric component of the field of the laser pulse (top) and its effect on the coulombic potential binding an electron to a nucleus (bottom). The red dot on the electric field represents the magnitude of the electric field at a particular moment in time, the green line in the coulomb potential represents the energy level of a bound electron, and the black arrow is the motion of the electron. (a-b) Magnitude of the electric field is zero and the potential is a typical $1/r$ coulomb potential. (c-d) As the electric field nears a peak of the pulse, the coulomb potential is distorted so that the electron is either no longer bound or has a high probability of tunneling out. (e-f) Half a cycle later the electric field has changed sign and the distortion in the coulomb potential is reversed, accelerating the electron back toward the nucleus.

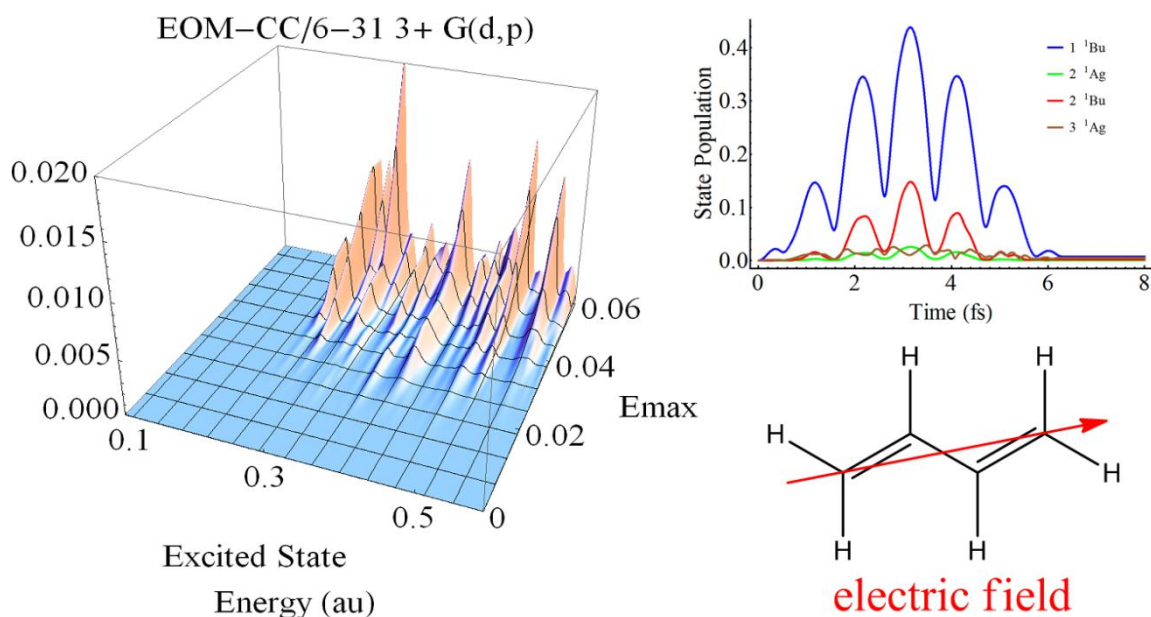


Figure 1-2. Population of the excited states of butadiene, after the pulse, as a function of field strength calculated using EOM-CC (left). Population of the first four excited states of butadiene during the laser pulse (right, top). Butadiene and the alignment of the laser pulse (right, bottom).

Image used with permission from *J. Phys. Chem. A*, **2011**, 115 (18), pp 4678–4690

Copyright 2011, American Chemical Society.

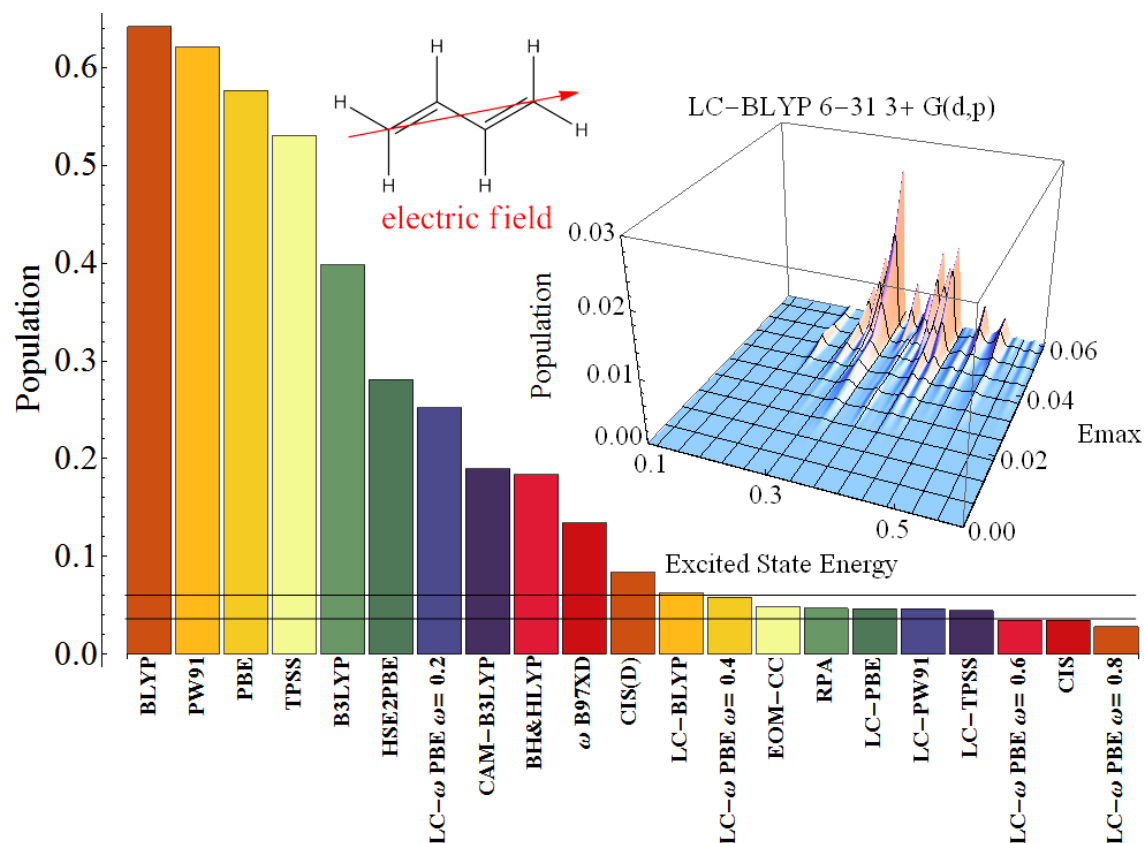


Figure 1-3. Comparison of the sum of the populations after the pulse of the excited states with energies less than 0.5 au for simulations with DFT functionals and wavefunction based methods using the 6-31 3+ G(d,p) basis and 300 excited states. The horizontal lines represent the population of EOM-CC $\pm 25\%$. Population of the excited states of butadiene, after the pulse, as a function of field strength calculated using the long-range corrected BLYP functional (inset, right).

Image used with permission from *J. Phys. Chem. A*, **2011**, 115 (42), pp 11832–11840

Copyright 2011, American Chemical Society.

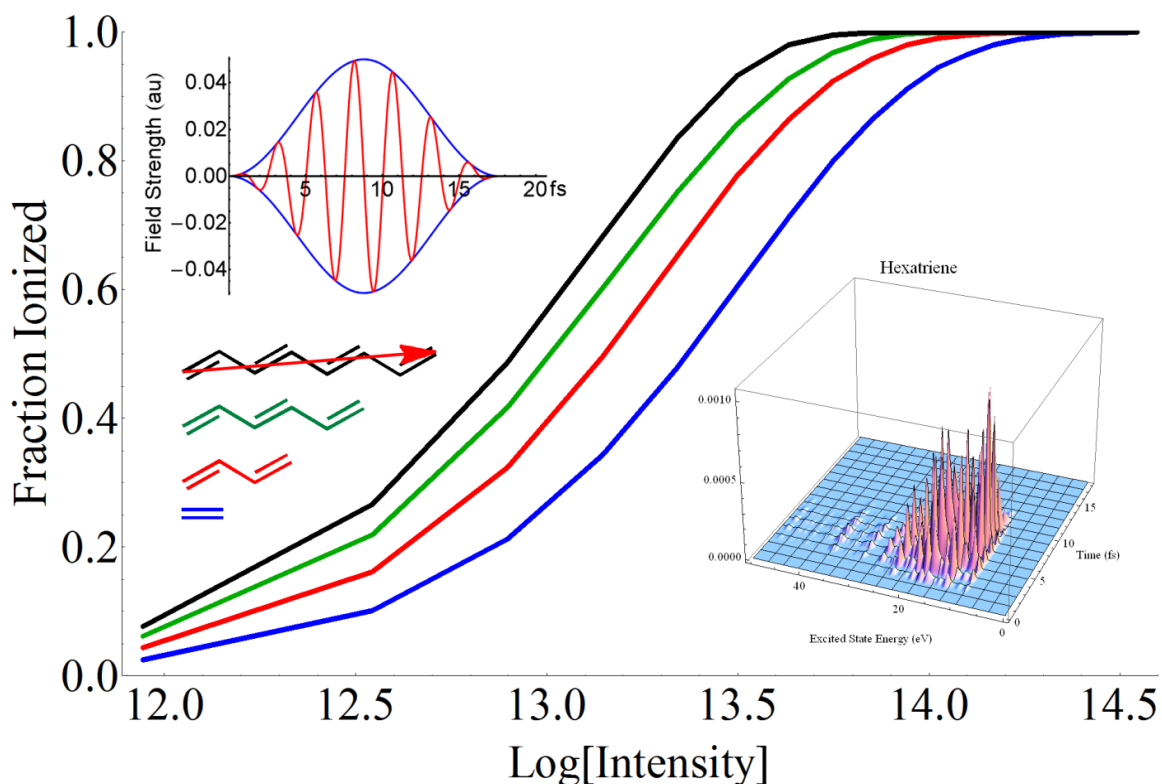


Figure 1-4. Fraction of the population ionized by the pulse as a function of the intensity (W/cm^2) for ethylene (blue), butadiene (red), hexatriene (green), octatetraene (black) calculated using the 6-31 1+ G(d,p) basis set and Klamroth's heuristic model with $d = 1$ bohr. The 7-cycle cosine pulse used in these simulations (inset, top left) and the four linear polyenes studies (inset, bottom left). The excited states which contribute the most towards ionization of hexatriene as a function of excited state energy and time step in the pulse (inset, bottom right).

Image used with permission from *J. Phys. Chem. A*, **2012**, 10.1021/jp302389a

Copyright 2012, American Chemical Society.

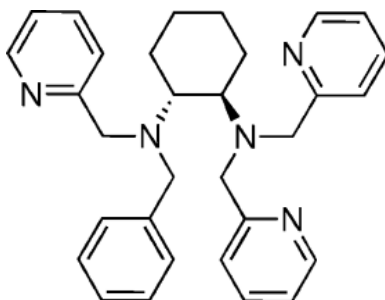


Figure 1-5. Structure of the pentadentate chiral tripyridyldiamine ligand synthesized by the Kodanko group.

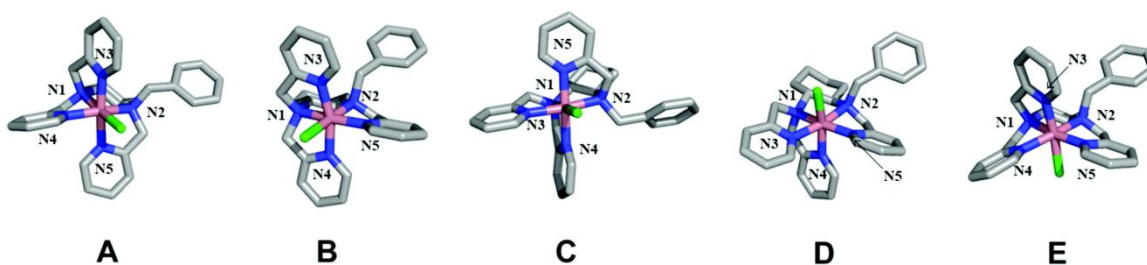


Figure 1-6. Isomers of $M(\text{Bn-CDPy}_3)\text{Cl}$ determined from calculations: A, B, and C display *mer* orientations of the pyridyl donors; D and E are *fac*.

Images used with permission from *Inorg. Chem.*, **2010**, 49 (11), pp 5202–5211

Copyright 2010, American Chemical Society.

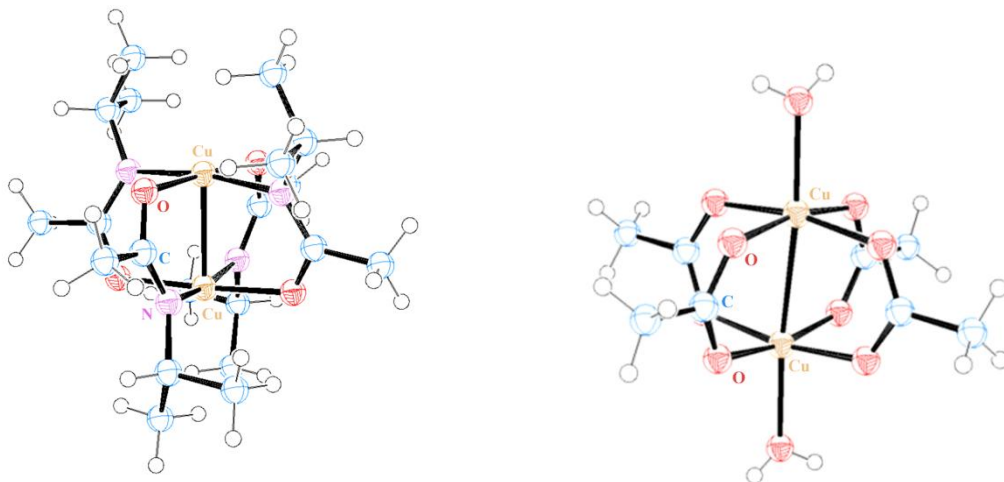


Figure 1-7. Left: X-ray crystal structure of the compound isolated by the Winter group
Right: Copper acetate compound previously found and characterized

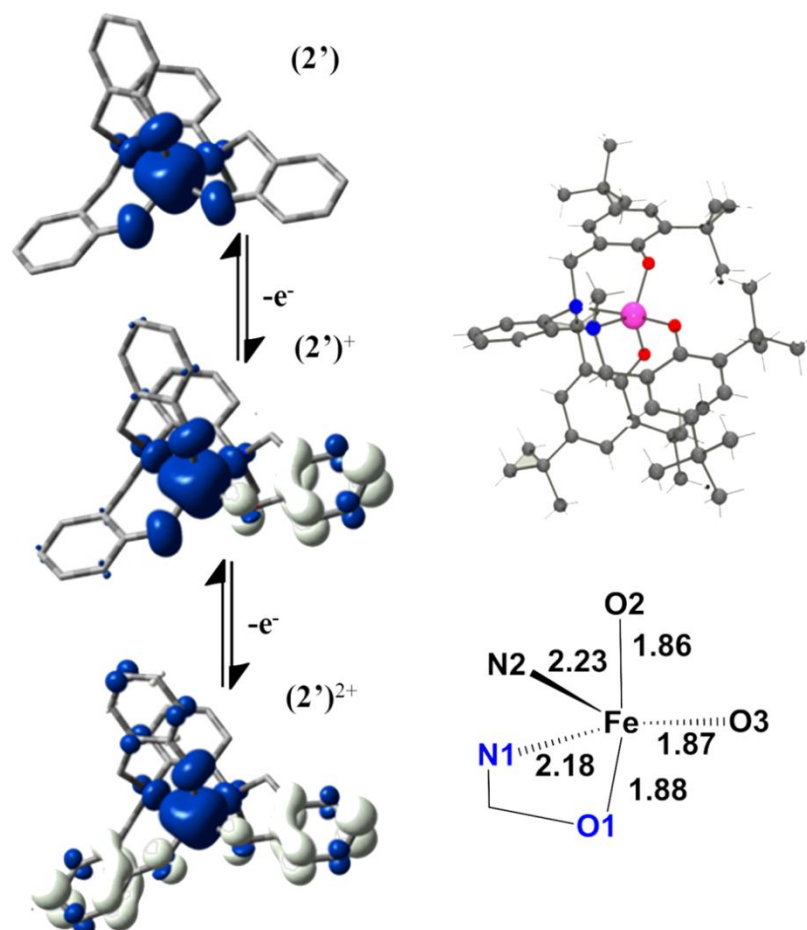


Figure 1-8 Left: Total spin density plots showing excess α and β electron spin on each of the atomic centers over the oxidation process. Right: Full and simplified representations of the Fe(II) system.

Images used with permission, from *Angew. Chem., Int. Ed.*, **2011**, 51(13), pp3178-3182

Copyright 2011, Wiley Publishing.

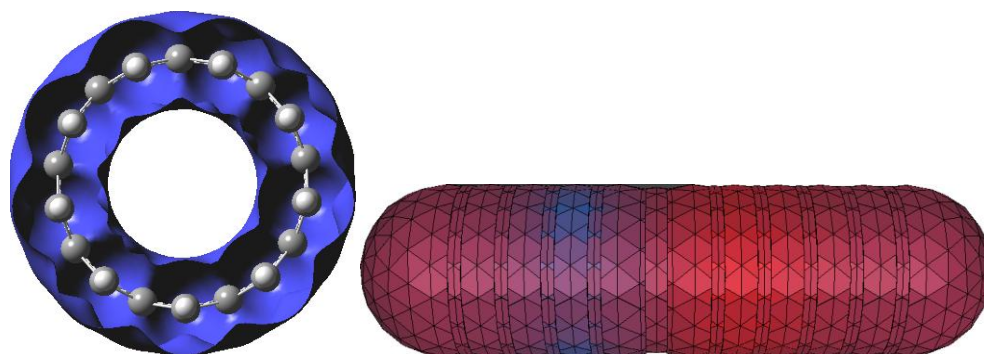


Figure 1-9 Left: Total electron density of a profile of 9,0 single walled carbon nanotube (isovalue 0.01 au) showing the interior cavity. Right: Cavity used for polarizable continuum model approximating interior nanotube cavity.

Chapter 2

TD-CI Simulation of the Electronic Optical Response of Molecules in Intense Fields: Comparison of RPA, CIS, CIS(D) and EOM-CCSD

Jason A. Sonk,¹ Marco Caricato² and H. Bernhard Schlegel^{1,*}

¹ *Department of Chemistry, Wayne State University, Detroit, Michigan 48202*

² *Gaussian, Inc., 340 Quinnipiac St. Bldg 40, Wallingford Connecticut 06492*

Reprinted with permission from *J. Phys. Chem. A*, **2011**, 115 (18), pp 4678–4690

Copyright 2011, American Chemical Society.

2.1 Introduction

When molecules are subject to short, intense femtosecond and picosecond laser pulses, a variety of strong-field effects are observed.¹⁻¹⁰ These effects include field tunneling and barrier-suppression ionization, above-threshold ionization, field-induced resonant enhancement of electronic absorption, nonadiabatic multi-electron excitation, and generation of higher-order harmonic emissions. Recent advances using higher harmonics generated by short intense pulses include imaging molecular orbitals, following chemical processes on a femtosecond time scale, and probing the detailed dynamics of ionization.^{9,11-22} Because the electric fields of intense lasers are comparable

to those sampled by valence electrons, the strong field response of a molecule cannot be treated by perturbative methods. Under these circumstances, the behavior of the electronic density interacting with intense electrical fields has to be simulated by numerical methods. For few-electron systems, accurate simulation methods are available;²³⁻⁴¹ however, these cannot be applied to larger polyatomic systems of interest in strong-field chemistry. In this chapter we examine a few of the approximate methods that can be used to simulate some aspects of these processes in molecules.

Atomic systems have been studied extensively, and accurate results are available for very simple molecules such as H_2^+ and H_2 .²³⁻⁴¹ For larger, many electron systems, some approximations are needed. Chu and co-workers⁴²⁻⁴⁷ have studied many-electron atoms and diatomics using time-dependent generalized pseudospectral methods, self-interaction corrected density functional theory, and Floquet matrix techniques. Greenman et al.⁴⁸ used TD-CIS with grid based orbitals for many electron atoms. Suzuki and Mukamel^{49,50} simulated π electron dynamics in octatetraene with a semiempirical Hamiltonian and have modeled ionization saturation intensities in a multi-electron system in a finite one-dimensional box. Cederbaum and collaborators⁵¹⁻⁵⁶ and Levine and co-workers⁵⁷⁻⁶³ used a multi-electron wavepacket dynamics approach to investigate hole migration following ionization. Klamroth, Saalfrank and co-workers⁶⁴⁻⁶⁸ have used optimal control theory and time-dependent configuration interaction with single excitations (TD-CIS) to shape short, intense pulses for state-selective excitation of N-methyl-quinoline, and employed TD-CIS(D) to simulate dipole switching in lithium cyanide. These authors have also used heuristic methods to include the effects of ionization, dissipation and dephasing.⁶⁹⁻⁷¹ Li and co-workers have combined real time

integration of time dependent density functional theory with Ehrenfest dynamics to investigate laser controlled dissociation processes.⁷²⁻⁷⁴ In previous papers we have used TD-HF (time-dependent Hartree-Fock) and TD-CIS methods to simulate the response of CO₂, polyenes, and polyacenes and their cations to short, intense laser pulses.⁷⁴⁻⁷⁹ The approximate simulations that have been carried out to date on polyatomic systems are promising, but there is a need to compare the performance of the various methods.

Practical calculations on polyatomic systems require some compromises between efficiency and accuracy. Real-time response TD-HF and TD-CIS are the least expensive methods available for larger systems but these do not include multi-electron excitations. CIS(D)^{80,81} treats the effects of higher excitations perturbatively while CISD includes double excitations explicitly. The equation-of-motion coupled cluster method (EOM-CC)⁸²⁻⁸⁵ accounts for electron correlation effects as well as higher excitations. EOM-CC is considered the method of choice for systems that are too large for extensive multi-reference configuration interaction calculations. Practical calculations are also limited in the number of basis functions and number of excited states that can be considered in the simulations. In the present chapter, we test TD-CI methods for simulating the evolution of the electron density of butadiene during a short, intense laser pulse and just prior to ionization. Modeling ionization will be covered in Chapter 4, this chapter will focus on comparing the performance of TD-CI simulations with different numbers of excited states calculated using linear response TD-HF or RPA, CIS, CIS(D) and EOM-CCSD with various basis sets.

2.2 Methods

The time dependent Schrödinger equation (TDSE) in atomic units is

$$i \frac{d\Psi(t)}{dt} = \hat{H}(t) \Psi(t) \quad (2.1)$$

The wavefunction can be expanded in terms of the ground state $|\varphi_0\rangle$ and excited states $|\varphi_i\rangle$ of the time-independent, field-free Hamiltonian.

$$\psi(t) = \sum C_i(t) |\varphi_i\rangle \quad (2.2)$$

An excited state, φ_i , can be written in terms of an excitation operator, \hat{R}_i , acting on the reference determinant φ_0 .

$$\begin{aligned} |\varphi_i\rangle &= \hat{R}_i |\varphi_0\rangle \\ \hat{R}_i &= \sum r_0 + r_i^a \hat{a}^\dagger \hat{i} + r_{ij}^{ab} \hat{a}^\dagger \hat{i} \hat{b}^\dagger \hat{j} \dots \end{aligned} \quad (2.3)$$

The excitation operator involves amplitudes, r , and creation and annihilation operators to generate single, double and higher excitations by promoting electrons from occupied orbitals ijk to unoccupied orbitals abc . For configuration interaction calculations (CIS, CISD, etc.), the amplitudes and excitation energies are obtained by diagonalizing the corresponding field-free Hamiltonian matrix of the time-independent Schrodinger equation.

$$\begin{aligned} \hat{H}_0 |\varphi_i\rangle &= \omega_i |\varphi_i\rangle \\ \langle \varphi_i | \varphi_j \rangle &= \delta_{ij} \end{aligned} \quad (2.4)$$

The excitation energies can also be obtained by linear response time-dependent Hartree-Fock theory, also known as the random phase approximation (RPA).

In the coupled cluster approach with single and double excitations (CCSD), the ground state is given by the exponential coupled cluster operator acting on the reference determinant.

$$\begin{aligned} |\varphi_0\rangle^{CCSD} &= \exp(\hat{T})|\varphi_0\rangle \\ \hat{T} &= \sum_i t_i^a \hat{a}^\dagger \hat{i} + \sum_{ij} t_{ij}^{ab} \hat{a}^\dagger \hat{i} \hat{b}^\dagger \hat{j} \end{aligned} \quad (2.5)$$

Excited states in the equation-of-motion coupled cluster method are written in terms of the excitation operator, \hat{R} , acting on the coupled cluster ground state.

$$|\varphi_i\rangle^{EOMCC} = \hat{R}_i \exp(\hat{T})|\varphi_0\rangle \quad (2.6)$$

Since the \hat{R} and \hat{T} operators commute, the amplitudes for the excitation operator can be obtained by solving for the eigenvalues of the similarity transformed field-free Hamiltonian, \bar{H}_0 .

$$\begin{aligned} \hat{H}_0 \hat{R}_i \exp(\hat{T})|\varphi_0\rangle &= \omega_i \hat{R}_i \exp(\hat{T})|\varphi_0\rangle \\ \bar{H}_0 \hat{R}_i |\varphi_0\rangle &= \omega_i \hat{R}_i |\varphi_0\rangle \\ \bar{H}_0 &= \exp(-\hat{T}) \hat{H}_0 \exp(\hat{T}) \end{aligned} \quad (2.7)$$

Because \bar{H}_0 is not Hermitian, there is also a set of left-hand eigenstates which satisfy the property of biorthogonality.

$$\begin{aligned} \langle \varphi_0 | \hat{L}_i \bar{H}_0 &= \langle \varphi_0 | \hat{L}_i \omega_i \\ \langle \varphi_0 | \hat{L}_i \bar{H}_0 \hat{R}_j |\varphi_0\rangle &= \omega_i \delta_{ij} \end{aligned} \quad (2.8)$$

Inserting Eq.(2.2) into Eq.(2.1) and multiplying from the left by $\langle \varphi_i |$, reduces the time-dependent Schrödinger equation to a set of coupled differential equations for the time-dependent coefficients,

$$i \frac{dC_i(t)}{dt} = \sum_j H_{ij}(t) C_j(t) \quad (2.9)$$

This can be integrated numerically using a unitary transform approach,

$$\mathbf{C}(t + \Delta t) = \text{Exp}[-i\mathbf{H}(t + \Delta t / 2)\Delta t] \mathbf{C}(t) \quad (2.10)$$

In the dipole approximation, the matrix elements of the field-dependent Hamiltonian in Eq.(2.9) and (2.10) can be expressed in terms of the field-free energies, ω_i , transition dipole moments, \mathbf{D}_{ij} and the electric field, $\mathbf{e}(t)$:

$$\begin{aligned} H_{ij}(t) &= \langle \varphi_i | \hat{H}(t) | \varphi_j \rangle \\ &= \langle \varphi_i | \hat{H}_0 | \varphi_j \rangle + \langle \varphi_i | \hat{\mathbf{r}} | \varphi_j \rangle \cdot \mathbf{e}(t) \\ &= \omega_i \delta_{ij} + \mathbf{D}_{ij} \cdot \mathbf{e}(t) \end{aligned} \quad (2.11)$$

For CIS(D) the same transition dipoles are used as for CIS. Because of the biorthogonality of the EOM-CC right and left eigenfunctions, the transition dipole matrix is not necessarily Hermitian. We approximate the EOM-CC transition dipole matrix by retaining only the Hermitian component $(\mathbf{D}_{ij} + \mathbf{D}_{ji}^*)/2$ and dropping the small, non-physical, non-Hermitian component.

For the full solution of the TDSE, the sum in Eq.(2.9) extends over all bound states and the continuum. For practical applications, the sum needs to be restricted to a suitable subset of states. For example, CIS includes the ground state and only the singly excited

states. CIS energies typically have errors of 1.0 eV⁸⁶ for valence excited states. Adding perturbative doubles corrections for electron correlation to the CIS excitation energies yields the CIS(D) approach. This reduces the error to ca 0.5 eV⁸⁶. The equation of motion coupled cluster method (EOM-CCSD) treats electron correlation in the ground and excited states using the coupled clusters approach. The EOM-CCSD approach gives excitation energies that are within 0.3 eV^{86,87} of the experimental results for valence excited states. Large multi-reference configuration interaction calculations would produce even more accurate excitation energies, but these are too costly for the size of molecules that we hope to study and for the number of states needed in the simulations. Within a given method (RPA, CIS, CIS(D), or EOM-CCSD), practical considerations limit the total number of states that can be used. Increasing the number of states included until no further change is seen in the simulation is one means of determining whether the number of states is adequate. Finite basis sets are usually used in molecular calculations. Since continuum functions are not included in the present calculations, the simulations cannot model ionization directly.

The present study uses a linearly polarized and spatially homogeneous external field,

$$\mathbf{e}(r, t) \approx \mathbf{E}(t) \sin(\omega t + \varphi) \quad (2.12)$$

this is a good approximation for the laser field, because typical wavelengths are much larger than molecular dimensions. The simulations in this chapter and the next use a Gaussian envelope

$$g(t) = \text{Exp}[-\alpha(t/n\tau)^2] \quad (2.13)$$

$$\begin{aligned} \mathbf{E}(t) &= \mathbf{E}_{\max} [g(t - n\tau/2) - \Delta] / [1 - \Delta] & \text{for } 0 \leq t \leq n\tau \\ \mathbf{E}(t) &= 0 & \text{for } t < 0 \text{ and } t > n\tau \end{aligned} \quad (2.14)$$

where $\tau = 2\pi/\omega$ is the period and n is the number of cycles. The offset Δ is chosen so that $\mathbf{E}(0) = 0$ and $\mathbf{E}(n\tau) = 0$. For $\omega = 0.06$ au (760 nm) and $\alpha = 16 \ln 2$, $\Delta = 1/16$, $n \approx 3$ and the FWHM ≈ 4 fs (see Figure 2-5(c) below).

The simulations covered in Chapter 4 will use a cosine envelope

$$g(t) = 1/2 + \cos[2\pi t / (n\tau)] / 2 \quad (2.15)$$

$$\begin{aligned} \mathbf{E}(t) &= \mathbf{E}_{\max} g(t - n\tau/2) & \text{for } 0 \leq t \leq nt \\ \mathbf{E}(t) &= 0 & \text{for } t < 0 \text{ and } t > nt \end{aligned} \quad (2.16)$$

where $\tau = 2\pi/\omega$ is the period and n is the number of cycles.

The RPA, CIS, CIS(D) and EOM-CCSD calculations were carried out with the development version of the Gaussian software package.⁸⁸ As in our previous studies,^{74,76} *trans* butadiene was optimized at the HF/6-31G(d,p) level of theory. Excited state calculations were carried out with 6-31G(d,p), 6-31 n+ G(d,p), 6-31(n+)G(d,p) and 6-311++G(2df,2pd) basis sets. The 6-31 n+ G(d,p) basis has one set of 5 Cartesian d functions on the carbons, one set of p functions on hydrogen and n sets of diffuse s and p functions on all carbons (n = 1, 2 and 3, with exponent of 0.04380, 0.01095, 0.0027375). The modified 6-31(n+)G(d,p) basis set is derived from the 6-31 n+ G(d,p) basis set but has diffuse s and p functions only on the end carbons. A 3 cycle Gaussian pulse with $\omega = 0.06$ au (760nm) was used in the simulations. For maximal effect the field was directed along the long axis of the molecule, specifically along the vector connecting the end carbons. Up to 500 states were included in the simulations. Mathematica⁸⁹ was used to

integrate the TD-CI equations and analyze the results. The TD-CI integrations were carried out with a step size of 0.5 au (0.012 fs). To facilitate plotting in Figures 8 – 10, the excited state populations were represented by Gaussians with an energy width of 0.01 au FWHM.

2.3 Results and Discussion

2.3.1 Orbitals and States

The ground state Hartree-Fock (HF) wavefunction of *trans* butadiene in C_{2h} symmetry consists of 13 σ orbitals (7 a_g and 6 b_u symmetry) and 2 π bonding orbitals. With the 6-31G(d,p) basis set, the HOMO-1 and HOMO (highest occupied molecular orbital) are π orbitals (π_1 and π_2 , a_u and b_g symmetry, resp.), while the LUMO (lowest unoccupied molecular orbital) and LUMO+1 are π^* orbitals (π_3 and π_4 , a_u and b_g symmetry, resp.), as shown in Figure 2-1. The states involving these four π states have large transition dipole moments that play an important role in the response of butadiene to intense laser pulses. The ground state wavefunction is 1A_g . The RPA, CIS, CIS(D) and EOM-CC levels of theory concur that the lowest singlet excited state is 1B_u and corresponds to the HOMO \rightarrow LUMO ($\pi_2 \rightarrow \pi_3$, $1b_g \rightarrow 2a_u$) excitation. Three additional low lying singlet states can be constructed from the π orbitals: the in-phase and out-of-phase linear combinations of the $\pi_2 \rightarrow \pi_4$ and $\pi_1 \rightarrow \pi_3$ excitations ($\pi_2 \rightarrow \pi_4 \pm \pi_1 \rightarrow \pi_3$) (1A_g symmetry) and $\pi_1 \rightarrow \pi_4$ (1B_u symmetry). The doubly excited configuration which excites two electrons from the HOMO to the LUMO ($2 \times \pi_2 \rightarrow \pi_3$) is also 1A_g symmetry and mixes strongly with the $\pi_2 \rightarrow \pi_4 + \pi_1 \rightarrow \pi_3$ configuration. Since EOM-CC calculations

include doubly excited configurations, this excited state is calculated to be considerably lower in energy by EOM-CC than by RPA and CIS.

As the basis set size is increased from 6-31G(d,p) to 6-31 3+ G(d,p), numerous low-lying, unoccupied, diffuse, Rydberg-like orbitals start to appear between the smaller basis set HOMO and LUMO orbitals, complicating the qualitative description of the electronic states. The energies of the first 30 excited states of 1A_g and 1B_u symmetry calculated by RPA, CIS, CIS(D) and EOM-CC with the 6-31 3+ G(d,p) basis set are compared in Figure 2-2 (because of the symmetry of the transition dipoles, states with A_u and B_g symmetry are not coupled to the A_g and B_u states by the in-plane electric field used in the simulations discussed below). Except for the lowest 1B_u state, the $\pi \rightarrow \pi^*$ states are embedded in a sea of Rydberg-like and pseudo-continuum states arising from diffuse, low-energy unoccupied orbitals. Beyond the first few states, the EOM-CC excitation energies are significantly lower than the CIS and RPA excitation energies due to the admixture of higher excitations. CIS(D) captures most of this energy lowering compared to EOM-CC, but perturbation theory can overestimate or underestimate the correction arising from double excitations. Since this becomes more problematic for higher energy states (see Figure 2-3(a)), the perturbative corrections for states above 11 eV are limited so that $0.8 E_i^{\text{CIS}} \leq E_i^{\text{CIS(D)}} \leq E_i^{\text{CIS}}$ (this affects ca 10 - 20 states out of 500 for each of the various basis set). As shown in the inset in Figure 2-3(b), adding more diffuse functions increases the number of states below the ionization threshold. In the pseudo-continuum above the IP, the excited state energies increase approximately linearly with the number of states (see Fig. 2-3(b)). The density of states, given by the

inverse of the slope of the lines, increases roughly in proportion to the number of diffuse functions added, but also depends on the location and exponents of the diffuse functions.

The vertical ionization potentials (IP) of butadiene, calculated with the unrestricted and restricted Hartree-Fock (UHF and ROHF) and coupled cluster methods using various basis sets, are listed in Table 2-1. The ROHF and UHF IPs are ca 1 and 1.4 eV lower than the experimental value, 9.072 ± 0.007 eV⁹⁰. The CCSD calculations are within 0.15 eV of the experimental value provided that diffuse functions are included in the basis set. Figure 2-2 indicates that only a few of calculated excited state of ¹A_g and ¹B_u symmetry are below the IP.

2.3.2 Transition Dipoles

The transition dipoles are summarized graphically in Figure 2-4 for states up to 15 eV. For each transition, the horizontal coordinates indicate the energies of the two states and the height of the line is given by the magnitude of the transition dipole. The ground to excited state transitions are along the two edges of the plot while the excited to excited state transitions are in the interior. The first ionization threshold is ca 9 eV, and the dense forest of lines above this energy is the result of transitions between pseudo-continuum states. The lines are peaked near the diagonal as would be expected from continuum states. The effect of basis set size is can be seen in Figure 2-4(a)-(f). The forest of lines is far too sparse with the 6-31G(d,p) basis set but much denser for the larger basis sets. The density of lines looks similar with the 6-31(1+)G(d,p), 6-31 1+ G(d,p) and 6-311++G(2df,2pd) basis sets (Fig 2-4(b), (e), (f)). The 6-31 n+ G(d,p) results (Fig. 2-4 (b), (c), (d)) become progressively denser and more strongly peaked along the diagonal,

indicating a better representation of the pseudo-continuum states. Since multiple diffuse functions (Fig. 2-4(c) and (d)) appear to be more important than higher polarization functions (Fig. 2-4(f)) for representing the states in the pseudo-continuum, the RPA, CIS, CIS(D) and EOM-CC calculations are compared using the 6-31 3+ G(d,p) basis set rather than the 6-311++G(2df,2pd) basis set. Figures 2-4(d), (g) and (h) show that the CIS, RPA and EOM-CC transition dipoles with the 6-31 3+ G(d,p) basis set are very similar on the scale of these plots. Since the CIS(D) perturbative correction are applied to the energies but not the transition dipoles, the CIS(D) figure (not shown) closely resembles the CIS results. Because the EOM-CC calculations include double excitations, some of the transition dipoles between valence states are smaller (particularly the lowest 1B_u to 1A_g $\pi \rightarrow \pi^*$ transitions). However, the transition dipoles between the pseudo-continuum states are similar in appearance to the RPA and CIS results.

2.3.3 *Simulations with Model Systems*

Since the transitions from the ground state to the 1B_u states are the most intense absorptions and these transitions involve the π orbitals, early work on polyenes in strong fields modeled the response by considering only the π orbitals.^{49,50} To help understand the response of butadiene, we first examined the behavior of some simple models of the π states. Figure 2-5 shows the results of TD-CI simulations with model two and three level systems, as well as the shape of a three cycle Gaussian pulse used in the simulations. The energies and transition dipoles for the model systems were chosen to be comparable to the lowest $\pi \rightarrow \pi^*$ excitation energies and transition dipoles of butadiene calculated with CIS/6-31G(d,p) ($\omega_0 = 0.$, $\omega_1 = 0.25$, $\omega_2 = 0.35$; $D_{01} = 2.0$, $D_{12} = 2.0$, $D_{02} = 0.0$ au). The

maximum of the gaussian pulse envelope was varied from 0 to 0.1 au (vertical axis) and the frequency of the pulse ranged from 0.01 to 0.35 au (horizontal axis). The populations for ground and excited state of the two level system are shown in Fig. 2-5(a) and (b). The prominent peak indicates that population inversion is achieved for $E_{\max} \approx 0.044$ au when the frequency is slightly higher than the one photon resonance, $\omega = 0.25$ au. This corresponds to a π pulse and the displacement to higher energy is due to Stark shifting. The other peaks are the result of higher order processes. The populations for the three level system are shown in Figures 2-5(d), (e) and (f). The behavior of the first excited state as a function of E_{\max} and ω is similar to the two level model (Fig. 2-5(e) vs. (b)). The peak in the population of the second excited state (Fig. 2-5(f)) corresponds to a two photon process (this was verified by changing the energy of the second excited state).

2.3.4 *Simulations with Butadiene*

Figure 2-6 illustrates the results of simulations for a simple model of butadiene using only the ground state and the four lowest π states computed by TD-CIS and TD-EOMCC with the 6-31G(d,p) basis set. The response of the 1A_g ground state and the lowest 1A_g excited state and the lowest two 1B_u excited states are shown; the population of the second 1A_g excited state remains less than 0.1 for the range of E_{\max} and ω examined because the transition dipoles with the other π states are small. The ground state is coupled to the lowest 1B_u state with a large transition dipole. Likewise, large transition dipoles couple this 1B_u state to the 1A_g state, and the 1A_g state to the higher 1B_u state. This can be compared to the two and three level systems shown in Figure 2-5. As expected, the response of the first excited state in butadiene is very similar to the first

excited state in the 2 and 3 level systems, dominated by the peak for the one photon process. The peak in the population of the lowest 1A_g excited state corresponds to a two photon process and the peak shown for the second 1B_u state corresponds to a three photon process (as confirmed by dependence of the peak position on the energy of the states; the one photon transition from the 1A_g ground state to the 1A_g excited state is dipole forbidden). Because of the significant contribution of two electron excitations to the 1A_g π excited state in the EOM-CC calculations, the transition dipoles coupling this state to the 1B_u states are about 40% smaller than in the CIS calculations. As a result, the response of both the 1A_g state and the second 1B_u excited state is much weaker in the TD-EOMCC simulation. The regions of decrease in the population of the ground state correspond to the peaks in the population of the excited states since the populations must sum to unity. Inspection of Figure 2-6 shows that the conditions used for subsequent simulations ($\omega = 0.06$, E_{\max} up to 0.06 au) are well away from any single or multi-photon resonances.

The populations of the four lowest π states during a three cycle Gaussian pulse are shown in Figure 2-7. In terms of both the zero-field states and the instantaneous adiabatic states (defined as the fully relaxed states in the instantaneous electric field), the populations change rapidly as the molecule is polarized by the electric field of the pulse, with the largest response coming from the lowest 1B_u state and the next largest from the lowest 1A_g excited state (which is strongly coupled to the lowest 1B_u state). The changes in the populations of the instantaneous adiabatic states are less than half the size of those seen for zero field states, but are still much larger than the final populations after the pulse. Because these fluctuations are so large, it is not readily possible to track the details

of the excitation from state to state during the pulse by using the instantaneous adiabatic states. However, the results of the interaction can still be assessed by examining the populations after the pulse.

The calculated response of butadiene to a short, intense pulse depends on the number of excited states included in the simulation as well as the theory and basis set used for the excited state calculations. An estimate of the number of excited states needed can be obtained by comparing the static polarizability computed with the sum over states formalism to the one calculated by linear response theory. Using the RPA data with the 6-31 n+ G(d,p) basis sets, approximately 120, 210, 340 and 460 states are required for n = 0 – 3, respectively, to converge the longitudinal polarizability to within 3% of the linear response value. The dependence of the simulations on the number of states is shown in Figure 2-8 for a 3 cycle Gaussian pulse with $\omega = 0.06$ au and $E_{\max} = 0.05$ au and calculated with TD-CIS/6-31 n+ G(d,p), n = 1 - 3. The top row of Fig. 2-8 shows that at the maximum of the pulse, the populations do not depend strongly on the number of states. The largest response is for 1^1B_u excited state, and the contribution is similar in magnitude for these basis sets. For the 2+ and 3+ basis sets, the 2^1B_u and 3^1B_u states are low in energy and show a significant response as well. The larger basis sets also have many more low-lying Rydberg-like and pseudo-continuum states. Even though their response is small, the sum of their contributions is significant and more states are needed in the sum over states calculation of the polarizability and in the TD-CI simulations in order to properly represent the interaction with the field. The populations after the pulse are much smaller but are more sensitive to the quality of the simulation since they depend on the cumulative response over the entire pulse. The bottom row of

Figure 2-8 shows the results after the pulse and indicates that 250, 400 and ca 500 states are needed with the 6-31 n+ G(d,p) basis sets for n= 1 - 3, respectively. This again illustrates that the small contributions from the numerous low-lying pseudo-continuum states are important for stable simulations under these conditions. Similar results were found for simulations with other levels of theory.

Figures 2-9 and 2-10 summarize the effect of basis sets and levels of theory on the response of butadiene to a 3 cycle gaussian pulse ($\omega = 0.06$ au). Populations are plotted as a function of the excited state energies and field strength up to $E_{\max} = 0.06$ au (1.26×10^{14} W cm⁻²). Figure 2-9 collects the results of TD-CIS simulations using 500 states and employing excitation energies and transition dipoles calculated with various basis sets. As expected, the populations of the excited states increase dramatically with the field strength. Above a threshold in the maximum field strength, many excited states are populated, signaling an increase in the ionization rate. Details of the populations in specific states are very sensitive to the level of theory, basis set and the number of states used in the simulation. Nevertheless, some general trends can be discerned. Without diffuse functions, the response is too weak (Fig. 2-9(a), note the 15-fold difference in the vertical scale). Adding 2 and 3 sets of diffuse functions on the end carbons (Fig. 2-9(b) and (c)) increases the response, but not as much as putting one set of diffuse functions on each carbon (Fig. 2-9(d)). With two sets of diffuse functions (Fig. 2-9(e)), significant excitation already occurs at lower field strengths. Augmenting the 6-31 2+ G(d,p) basis with a set of sp diffuse functions on the hydrogens increases the response somewhat more (not shown). The results with 3 sets of diffuse functions are very similar to 2 sets (Fig. 2-

9(f) vs (e)). Similar trends in basis set effects are found for RPA and CIS(D) simulations with 500 states.

The top row of Figure 2-10 compares TD-CI simulations with 300 states based on RPA, CIS, CIS(D) and EOM-CC calculations with the 6-31 3+ G(d,p) basis set. The RPA and CIS results are very similar, while the CIS(D) response is somewhat stronger at higher E_{\max} . The EOM-CC response is comparable to or slightly less than CIS and RPA. The results of simulations with RPA, CIS and CIS(D) using 500 states are shown in bottom row of Figure 2-10 (EOM-CC/6-31 3+ G(d,p) calculations with 500 states are not practical at this time). With the 6-31 3+ G(d,p) basis, the 500 state simulations follow the same trend as with 300 states. However, with small basis sets such as 6-31G(d,p) (not shown), the differences between the various levels of theory are more pronounced.

Because the populations of individual excited states are very sensitive to the level of theory, it is useful to compare some aggregate quantities. The depletion of the population of the ground state is equal to the sum of the excited state populations generated by the interaction with the intense pulse. Figure 2-11(a) shows the population of the ground state as a function of field strength for simulations with 300 states for various levels of theory and the 6-31 3+ G(d,p) basis set. Up to a maximum field strength of ca 0.035 au, the RPA, CIS, CIS(D) and EOM-CC ground state populations are nearly identical and show less than a 2% depletion. For E_{\max} greater than ca. 0.035 au, there is a rapid decrease in the ground state contribution as excited states become more populated. In agreement with Figure 2-10, the response of RPA, CIS and EOM-CC are similar but CIS(D) is significantly stronger. Similar trends are found for simulations with 500 states (not shown). Figure 2-11(b) compares the sum of the populations of the excited states

with energies less than 0.5 au. The results are in accord with Figure 2-10 as well as the trends the ground state populations (Fig. 2-11(a)). Interaction with the intense pulse deposits energy into the molecule by populating excited states. Figure 2-11(c) compares the sum of the excited state energies weighted by their populations for excited states with energies less than 0.5 au. Again, the values for RPA, CIS and EOM-CC are similar but CIS(D) is significantly larger. For simulations with 500 states, the amount of energy deposited in this range of states is smaller but the trends are similar.

2.4 Summary

The lowest singlet excited state of butadiene is a ${}^1B_u \pi \rightarrow \pi^*$ state and is treated fairly well by RPA, CIS, and CIS(D) when compared to EOM-CC. CIS(D) reproduces the trends in energy of the higher bound and pseudo-continuum states better than by RPA and CIS when compared to EOM-CC, but the perturbative correction for doubles can be erratic. The effect of basis set can be seen rather dramatically by looking at the dipole moments for transitions between ground and excited states and between excited states. Diffuse functions are particularly important for transitions between excited states in the pseudo-continuum, above the first ionization threshold. Higher polarization functions seem to be less important, while multiple diffuse functions should be placed on all of the heavy atoms and not just on the end carbons. Transition dipoles involving the low lying π states are smaller for EOM-CC than for CIS and RPA because the latter do not take into account the double excitation character of some of these states. Studies with 2 and 3 level model systems as well as models involving only the low lying π states of butadiene show that intense 3 cycle pulses can cause resonant 2 and 3 photon transitions. The frequency and intensity ranges for the pulse used in the simulations were chosen to avoid

these resonances. Nevertheless, above a threshold in intensity of the pulse, there is rapid population of higher states in the pseudo-continuum. The response depends on the level of theory, the basis set and the number of excited states used in the simulation. Depending on the basis set, 500 excited states or more may be needed. For the pulse parameters selected, the response is far too weak with small basis sets such as 6-31G(d,p), but consistent results are achieved with two and three sets of sp diffuse functions on each carbon. For small basis sets, the difference between levels of theory is more pronounced, but with two and three sets of diffuse functions, the CIS, RPA and EOM-CC results are similar while the CIS(D) response is too strong when compared to the more reliable EOM-CC calculations.

2.5 References

- (1) Brabec, T.; Krausz, F. Intense few-cycle laser fields: Frontiers of nonlinear optics, *Rev. Mod. Phys.* **2000**, *72*, 545.
- (2) Drescher, M.; Hentschel, M.; Kienberger, R.; Tempea, G.; Spielmann, C.; Reider, G. A.; Corkum, P. B.; Krausz, F. X-ray pulses approaching the attosecond frontier, *Science* **2001**, *291*, 1923.
- (3) Baltuska, A.; Udem, T.; Uiberacker, M.; Hentschel, M.; Goulielmakis, E.; Gohle, C.; Holzwarth, R.; Yakovlev, V. S.; Scrinzi, A.; Hansch, T. W.; Krausz, F. Attosecond control of electronic processes by intense light fields, *Nature* **2003**, *421*, 611.
- (4) Ivanov, M. Y.; Spanner, M.; Smirnova, O. Anatomy of strong field ionization, *J. Mod. Opt.* **2005**, *52*, 165.
- (5) Cavalieri, A. L.; Muller, N.; Uphues, T.; Yakovlev, V. S.; Baltuska, A.; Horvath, B.; Schmidt, B.; Blumel, L.; Holzwarth, R.; Hendel, S.; Drescher, M.; Kleineberg, U.; Echenique, P. M.; Kienberger, R.; Krausz, F.; Heinzmann, U. Attosecond spectroscopy in condensed matter, *Nature* **2007**, *449*, 1029.
- (6) Corkum, P. B.; Krausz, F. Attosecond science, *Nat. Phys.* **2007**, *3*, 381.
- (7) Goulielmakis, E.; Yakovlev, V. S.; Cavalieri, A. L.; Uiberacker, M.; Pervak, V.; Apolonski, A.; Kienberger, R.; Kleineberg, U.; Krausz, F. Attosecond control and measurement: Lightwave electronics, *Science* **2007**, *317*, 769.
- (8) Goulielmakis, E.; Schultze, M.; Hofstetter, M.; Yakovlev, V. S.; Gagnon, J.; Uiberacker, M.; Aquila, A. L.; Gullikson, E. M.; Attwood, D. T.; Kienberger, R.; Krausz, F.; Kleineberg, U. Single-cycle nonlinear optics, *Science* **2008**, *320*, 1614.

- (9) Kling, M. F.; Vrakking, M. J. J. Attosecond electron dynamics, *Annu. Rev. Phys. Chem.* **2008**, *59*, 463.
- (10) Krausz, F.; Ivanov, M. Attosecond physics, *Rev. Mod. Phys.* **2009**, *81*, 163.
- (11) Akagi, H.; Otobe, T.; Staudte, A.; Shiner, A.; Turner, F.; Dorner, R.; Villeneuve, D. M.; Corkum, P. B. Laser Tunnel Ionization from Multiple Orbitals in HCl, *Science* **2009**, *325*, 1364.
- (12) Smirnova, O.; Mairesse, Y.; Patchkovskii, S.; Dudovich, N.; Villeneuve, D.; Corkum, P.; Ivanov, M. Y. High harmonic interferometry of multi-electron dynamics in molecules, *Nature* **2009**, *460*, 972.
- (13) Wörner, H. J.; Bertrand, J. B.; Kartashov, D. V.; Corkum, P. B.; Villeneuve, D. M. Following a chemical reaction using high-harmonic interferometry, *Nature* **2010**, *466*, 604.
- (14) Sussman, B. J.; Townsend, D.; Ivanov, M. Y.; Stolow, A. Dynamic stark control of photochemical processes, *Science* **2006**, *314*, 278.
- (15) Itatani, J.; Levesque, J.; Zeidler, D.; Niikura, H.; Pepin, H.; Kieffer, J. C.; Corkum, P. B.; Villeneuve, D. M. Tomographic imaging of molecular orbitals, *Nature* **2004**, *432*, 867.
- (16) Gessner, O.; Lee, A. M. D.; Shaffer, J. P.; Reisler, H.; Levchenko, S. V.; Krylov, A. I.; Underwood, J. G.; Shi, H.; East, A. L. L.; Wardlaw, D. M.; Chrysostom, E. T.; Hayden, C. C.; Stolow, A. Femtosecond multidimensional imaging of a molecular dissociation, *Science* **2006**, *311*, 219.

(17) Haessler, S.; Caillat, J.; Boutu, W.; Giovanetti-Teixeira, C.; Ruchon, T.; Auguste, T.; Diveki, Z.; Breger, P.; Maquet, A.; Carre, B.; Taieb, R.; Salieres, P. Attosecond imaging of molecular electronic wavepackets, *Nat. Phys.* **2010**, *6*, 200.

(18) Kienberger, R.; Hentschel, M.; Uiberacker, M.; Spielmann, C.; Kitzler, M.; Scrinzi, A.; Wieland, M.; Westerwalbesloh, T.; Kleineberg, U.; Heinzmann, U.; Drescher, M.; Krausz, F. Steering attosecond electron wave packets with light, *Science* **2002**, *297*, 1144.

(19) Meckel, M.; Comtois, D.; Zeidler, D.; Staudte, A.; Pavicic, D.; Bandulet, H. C.; Pepin, H.; Kieffer, J. C.; Dorner, R.; Villeneuve, D. M.; Corkum, P. B. Laser-induced electron tunneling and diffraction, *Science* **2008**, *320*, 1478.

(20) Niikura, H.; Legare, F.; Hasbani, R.; Bandrauk, A. D.; Ivanov, M. Y.; Villeneuve, D. M.; Corkum, P. B. Sub-laser-cycle electron pulses for probing molecular dynamics, *Nature* **2002**, *417*, 917.

(21) Shafir, D.; Mairesse, Y.; Villeneuve, D. M.; Corkum, P. B.; Dudovich, N. Atomic wavefunctions probed through strong-field light-matter interaction, *Nat. Phys.* **2009**, *5*, 412.

(22) Stolow, A.; Underwood, J. G. Time-Resolved Photoelectron Spectroscopy of Nonadiabatic Dynamics in Polyatomic Molecules, *Adv. Chem. Phys.* **2008**, *139*, 497.

(23) Chelkowski, S.; Zuo, T.; Bandrauk, A. D. Ionization Rates of H-2(+) in an Intense Laser Field by Numerical-Integration of the Time-Dependent Schrodinger-Equation, *Phys. Rev. A* **1992**, *46*, R5342.

(24) Chelkowski, S.; Zuo, T.; Atabek, O.; Bandrauk, A. D. Dissociation, Ionization, and Coulomb Explosion of H-2(+) in an Intense Laser Field by Numerical-Integration of the Time- Dependent Schrodinger-Equation, *Phys. Rev. A* **1995**, *52*, 2977.

(25) Yu, H. T.; Zuo, T.; Bandrauk, A. D. Molecules in intense laser fields: Enhanced ionization in a one-dimensional model of H-2, *Phys. Rev. A* **1996**, *54*, 3290.

(26) Walsh, T. D. G.; Ilkov, F. A.; Chin, S. L.; Chateauneuf, F.; Nguyen-Dang, T. T.; Chelkowski, S.; Bandrauk, A. D.; Atabek, O. Laser-induced processes during the Coulomb explosion of H-2 in a Ti-sapphire laser pulse, *Phys. Rev. A* **1998**, *58*, 3922.

(27) Bandrauk, A. D.; Lu, H. Z. Enhanced ionization of the molecular ion H-2(+) in intense laser and static magnetic fields, *Phys. Rev. A* **2000**, *62*, 53406.

(28) Bandrauk, A. D.; Chelkowski, S.; Zamojski, M. Laser phase control of electron-nuclear dynamics in dissociative ionization with intense femtosecond pulses: Exact (non-Born-Oppenheimer) numerical simulations for H-2(+), *Z. Phys. Chem.* **2000**, *214*, 1393.

(29) Talebpour, A.; Vijayalakshmi, K.; Bandrauk, A. D.; Nguyen-Dang, T. T.; Chin, S. L. Dissociative ionization of D-2 in intense laser fields: D+-ion production perpendicular to the polarization of a 400-nm laser field, *Phys. Rev. A* **2000**, *62*, 42708.

(30) Kawata, I.; Kono, H.; Fujimura, Y.; Bandrauk, A. D. Intense-laser-field-enhanced ionization of two-electron molecules: Role of ionic states as doorway states, *Phys. Rev. A* **2000**, *62*, 31401.

(31) Bandrauk, A. D.; Chelkowski, S. Asymmetric electron-nuclear dynamics in two-color laser fields: Laser phase directional control of photofragments in H-2(+), *Phys. Rev. Lett.* **2000**, *84*, 3562.

(32) Kawata, I.; Bandrauk, A. D.; Kono, H.; Fujimura, Y. Enhanced ionization of the two-electron molecule H-2 in intense laser fields: Mechanism of the creation of doorway states, *Laser Phys.* **2001**, *11*, 188.

(33) Harumiya, K.; Kono, H.; Fujimura, Y.; Kawata, I.; Bandrauk, A. D. Intense laser-field ionization of H-2 enhanced by two-electron dynamics, *Phys. Rev. A* **2002**, *66*, 43403.

(34) Harumiya, K.; Kono, H.; Fujimura, Y.; Kawata, I.; Bandrauk, A. D. Intense laser-field ionization of H-2 enhanced by two-electron dynamics, *Phys. Rev. A* **2002**, *66*, 043403.

(35) Bandrauk, A. D.; Chelkowski, S.; Kawata, I. Molecular above-threshold-ionization spectra: The effect of moving nuclei, *Phys. Rev. A* **2003**, *67*, 13407.

(36) Kamta, G. L.; Bandrauk, A. D. Three-dimensional analysis of nuclear contributions to harmonic generation in H-2(+), *Laser Phys.* **2005**, *15*, 502.

(37) Bandrauk, A. D.; Lu, H. Z. Laser-induced electron recollision in H-2 and electron correlation, *Phys. Rev. A* **2005**, *72*, 23408.

(38) Kamta, G. L.; Bandrauk, A. D. Three-dimensional time-profile analysis of high-order harmonic generation in molecules: Nuclear interferences in H-2(+), *Phys. Rev. A* **2005**, *71*, 53407.

(39) Nguyen, N. A.; Bandrauk, A. D. Electron correlation of one-dimensional H-2 in intense laser fields: Time-dependent extended Hartree-Fock and time-dependent density-functional-theory approaches, *Phys. Rev. A* **2006**, *73*, 32708.

(40) Bandrauk, A. D.; Lu, H. Z. Electron correlation and double ionization of a 1D H-2 in an intense laser field, *J. Mod. Opt.* **2006**, *53*, 35.

(41) Bandrauk, A. D.; Barmaki, S.; Kamta, G. L. Laser phase control of high-order harmonic generation at large internuclear distance: The H⁺-H⁻²⁽⁺⁾ system, *Phys. Rev. Lett.* **2007**, *98*, 13001.

(42) Usachenko, V. I.; Pyak, P. E.; Chu, S. I. High-order harmonic generation in laser-irradiated homonuclear diatomics: The velocity gauge version of the molecular strong-field approximation, *Laser Phys.* **2006**, *16*, 1326.

(43) Guan, X. X.; Tong, X. M.; Chu, S. I. Effect of electron correlation on high-order-harmonic generation of helium atoms in intense laser fields: Time-dependent generalized pseudospectral approach in hyperspherical coordinates, *Phys. Rev. A* **2006**, *73*, 23403.

(44) Usachenko, V. I.; Chu, S. I. Strong-field ionization of laser-irradiated light homonuclear diatomic molecules: A generalized strong-field approximation-linear combination of atomic orbitals model, *Phys. Rev. A* **2005**, *71*, 63410.

(45) Telnov, D. A.; Chu, S. I. Ab initio study of high-order harmonic generation of H⁻²⁽⁺⁾ in intense laser fields: Time-dependent non-Hermitian Floquet approach, *Phys. Rev. A* **2005**, *71*, 13408.

(46) Chu, S. I.; Telnov, D. A. Beyond the Floquet theorem: generalized Floquet formalisms and quasienergy methods for atomic and molecular multiphoton processes in intense laser fields, *Phys. Rep.* **2004**, *390*, 1.

(47) Chu, X.; Chu, S. I. Role of the electronic structure and multielectron responses in ionization mechanisms of diatomic molecules in intense short-pulse lasers: An all-electron ab initio study, *Phys. Rev. A* **2004**, *70*, 61402.

(48) Greenman, L.; Ho, P. J.; Pabst, S.; Kamarchik, E.; Mazziotti, D. A.; Santra, R. Implementation of the time-dependent configuration-interaction singles method for atomic strong-field processes, *Phys. Rev. A* **2010**, *82*.

(49) Suzuki, M.; Mukamel, S. Charge and bonding redistribution in octatetraene driven by a strong laser field: Time-dependent Hartree-Fock simulation, *J. Chem. Phys.* **2003**, *119*, 4722.

(50) Suzuki, M.; Mukamel, S. Many-body effects in molecular photoionization in intense laser fields; time-dependent Hartree-Fock simulations, *J. Chem. Phys.* **2004**, *120*, 669.

(51) Kuleff, A. I.; Breidbach, J.; Cederbaum, L. S. Multielectron wave-packet propagation: General theory and application, *J. Chem. Phys.* **2005**, *123*, 44111.

(52) Breidbach, J.; Cederbaum, L. S. Migration of holes: Formalism, mechanisms, and illustrative applications Migration of holes: Numerical algorithms and implementation, *J. Chem. Phys.* **2003**, *118*, 3983.

(53) Breidbach, J.; Cederbaum, L. S. Migration of holes: Numerical algorithms and implementation, *J. Chem. Phys.* **2007**, *126*, 034101.

(54) Kuleff, A. I.; Cederbaum, L. S. Charge migration in different conformers of glycine: The role of nuclear geometry, *Chem. Phys.* **2007**, *338*, 320.

(55) Lünemann, S.; Kuleff, A. I.; Cederbaum, L. S. Ultrafast charge migration in 2-phenylethyl-N,N-dimethylamine, *Chem. Phys. Lett.* **2008**, *450*, 232.

(56) Hennig, H.; Breidbach, J.; Cederbaum, L. S. Electron correlation as the driving force for charge transfer: Charge migration following ionization in N-methyl acetamide, *J. Phys. Chem. A* **2005**, *109*, 409.

- (57) Remacle, F.; Levine, R. D. Probing Ultrafast Purely Electronic Charge Migration in Small Peptides, *Z. Phys. Chem.* **2009**, *221*, 647.
- (58) Remacle, F.; Levine, R. D. Charge migration and control of site selective reactivity: The role of covalent and ionic states, *J. Chem. Phys.* **1999**, *110*, 5089.
- (59) Remacle, F.; Levine, R. D. The time scale for electronic reorganization upon sudden ionization of the water and water-methanol hydrogen bonded dimers and of the weakly bound NO dimer, *J. Chem. Phys.* **2006**, *125*.
- (60) Remacle, F.; Levine, R. D. An electronic time scale in chemistry, *Proc. Natl. Acad. Sci. U. S. A.* **2006**, *103*, 6793.
- (61) Remacle, F.; Levine, R. D.; Ratner, M. A. Charge directed reactivity: a simple electronic model, exhibiting site selectivity, for the dissociation of ions, *Chem. Phys. Lett.* **1998**, *285*, 25.
- (62) Remacle, F.; Kienberger, R.; Krausz, F.; Levine, R. D. On the feasibility of an ultrafast purely electronic reorganization in lithium hydride, *Chem. Phys.* **2007**, *338*, 342.
- (63) Remacle, F.; Nest, M.; Levine, R. D. Laser Steered Ultrafast Quantum Dynamics of Electrons in LiH, *Phys. Rev. Lett.* **2007**, *99*, 183902.
- (64) Nest, M.; Klamroth, T.; Saalfrank, P. The multiconfiguration time-dependent Hartree-Fock method for quantum chemical calculations, *J. Chem. Phys.* **2005**, *122*, 124102.
- (65) Krause, P.; Klamroth, T. Dipole switching in large molecules described by explicitly time-dependent configuration interaction, *J. Chem. Phys.* **2008**, *128*.

- (66) Krause, P.; Klamroth, T.; Saalfrank, P. Molecular response properties from explicitly time-dependent configuration interaction methods, *J. Chem. Phys.* **2007**, *127*.
- (67) Krause, P.; Klamroth, T.; Saalfrank, P. Time-dependent configuration-interaction calculations of laser-pulse-driven many-electron dynamics: Controlled dipole switching in lithium cyanide, *J. Chem. Phys.* **2005**, *123*, 74105.
- (68) Klamroth, T. Optimal control of ultrafast laser driven many-electron dynamics in a polyatomic molecule: N-methyl-6-quinolone, *J. Chem. Phys.* **2006**, *124*, 144310.
- (69) Tremblay, J. C.; Krause, P.; Klamroth, T.; Saalfrank, P. Time-dependent response of dissipative electron systems, *Phys. Rev. A* **2010**, *81*.
- (70) Tremblay, J. C.; Klamroth, T.; Saalfrank, P. Time-dependent configuration-interaction calculations of laser-driven dynamics in presence of dissipation, *J. Chem. Phys.* **2008**, *129*.
- (71) Klinkusch, S.; Saalfrank, P.; Klamroth, T. Laser-induced electron dynamics including photoionization: A heuristic model within time-dependent configuration interaction theory, *J. Chem. Phys.* **2009**, *131*.
- (72) Liang, W. K.; Isborn, C. M.; Li, X. S. Laser-Controlled Dissociation of C₂H₂²⁺ : Ehrenfest Dynamics Using Time-Dependent Density Functional Theory, *J. Phys. Chem. A* **2009**, *113*, 3463.
- (73) Liang, W.; Isborn, C. M.; Lindsay, A.; Li, X. S.; Smith, S. M.; Levis, R. J. Time-Dependent Density Functional Theory Calculations of Ehrenfest Dynamics of

Laser Controlled Dissociation of NO⁺: Pulse Length and Sequential Multiple Single-Photon Processes, *J. Phys. Chem. A* **2010**, *114*, 6201.

(74) Smith, S. M.; Li, X. S.; Markevitch, A. N.; Romanov, D. A.; Levis, R. J.; Schlegel, H. B. Numerical simulation of nonadiabatic electron excitation in the strong field regime. 2. Linear polyene cations, *J. Phys. Chem. A* **2005**, *109*, 10527.

(75) Li, X. S.; Smith, S. M.; Markevitch, A. N.; Romanov, D. A.; Levis, R. J.; Schlegel, H. B. A time-dependent Hartree-Fock approach for studying the electronic optical response of molecules in intense fields, *Phys. Chem. Chem. Phys.* **2005**, *7*, 233.

(76) Smith, S. M.; Li, X. S.; Markevitch, A. N.; Romanov, D. A.; Levis, R. J.; Schlegel, H. B. A numerical simulation of nonadiabatic electron excitation in the strong field regime: Linear polyenes, *J. Phys. Chem. A* **2005**, *109*, 5176.

(77) Smith, S. M.; Li, X.; Markevitch, A. N.; Romanov, D. A.; Levis, R. J.; Schlegel, H. B. Numerical Simulation of Non-adiabatic Electron Excitation in the Strong Field Regime: 3. Polyacene Neutrals and Cations, *J. Phys. Chem. A* **2007**, *111*, 6920.

(78) Smith, S. M.; Romanov, D. A.; Li, X. S.; Sonk, J. A.; Schlegel, H. B.; Levis, R. J. Numerical Bound State Electron Dynamics of Carbon Dioxide in the Strong-Field Regime, *J. Phys. Chem. A* **2010**, *114*, 2576.

(79) Smith, S. M.; Romanov, D. A.; Heck, G.; Schlegel, H. B.; Levis, R. J. Observing the Transition from Stark-Shifted, Strong-Field Resonance to Nonadiabatic Excitation, *J. Phys. Chem. C* **2010**, *114*, 5645.

(80) Headgordon, M.; Maurice, D.; Oumi, M. A Perturbative Correction to Restricted Open-Shell Configuration-Interaction with Single Substitutions for Excited-States of Radicals, *Chem. Phys. Lett.* **1995**, *246*, 114.

(81) Headgordon, M.; Rico, R. J.; Oumi, M.; Lee, T. J. A Doubles Correction to Electronic Excited-States from Configuration-Interaction in the Space of Single Substitutions, *Chem. Phys. Lett.* **1994**, *219*, 21.

(82) Koch, H.; Jorgensen, P. Coupled cluster response functions, *J. Chem. Phys.* **1990**, *93*, 3333.

(83) Stanton, J. F.; Bartlett, R. J. The equation of motion coupled-cluster method: A systematic biorthogonal approach to molecular excitation energies, transition probabilities, and excited state properties, *J. Chem. Phys.* **1993**, *98*, 7029.

(84) Koch, H.; Kobayashi, R.; Demeras, A. S.; Jorgensen, P. Calculation of size-intensive transition moments from the coupled cluster singles and doubles linear response function, *J. Chem. Phys.* **1994**, *100*, 4393.

(85) Kallay, M.; Gauss, J. Calculation of excited-state properties using general coupled-cluster and configuration-interaction models, *J. Chem. Phys.* **2004**, *121*, 9257.

(86) Caricato, M.; Trucks, G. W.; Frisch, M. J.; Wiberg, K. B. Electronic Transition Energies: A Study of the Performance of a Large Range of Single Reference Density Functional and Wave Function Methods on Valence and Rydberg States Compared to Experiment, *J. Chem. Theory Comput.* **2010**, *6*, 370.

(87) Schreiber, M.; Silva-Junior, M. R.; Sauer, S. P. A.; Thiel, W. Benchmarks for electronically excited states: CASPT2, CC2, CCSD, and CC3, *J. Chem. Phys.* **2008**, *128*, 134110.

(88) Frisch, M. J.; Trucks, G. W.; Schlegel, H. B.; Scuseria, G. E.; Robb, M. A.; Cheeseman, J. R.; Montgomery, J. A.; Vreven, T.; Kudin, K. N.; Burant, J. C.; Millam, J. M.; Iyengar, S.; Tomasi, J.; Barone, V.; Mennucci, B.; Cossi, M.; Scalmani,

G.; Rega, N.; Petersson, G. A.; Nakatsuji, H.; Hada, M.; Ehara, M.; Toyota, K.; Fukuda, R.; Hasegawa, J.; Ishida, M.; Nakajima, T.; Honda, Y.; Kitao, O.; Nakai, H.; Klene, M.; Li, X.; Knox, J. E.; Hratchian, H. P.; Cross, J. B.; Bakken, V.; Adamo, C.; Jaramillo, J.; Gomperts, R.; Stratmann, R. E.; Yazyev, O.; Austin, A. J.; Cammi, R.; Pomelli, C.; Ochterski, J.; Ayala, P. Y.; Morokuma, K.; Voth, G. A.; Salvador, P.; Dannenberg, J. J.; Zakrzewski, V. G.; Dapprich, S.; Daniels, A. D.; Strain, M. C.; Farkas, Ö.; Malick, D. K.; Rabuck, A. D.; Raghavachari, K.; Foresman, J. B.; Ortiz, J. V.; Cui, Q.; Baboul, A. G.; Clifford, S.; Cioslowski, J.; Stefanov, B. B.; Liu, G.; Liashenko, A.; Piskorz, P.; Komaromi, I.; Martin, R. L.; Fox, D. J.; Keith, T.; Al-Laham, M. A.; Peng, C. Y.; Nanayakkara, A.; Challacombe, M.; Gill, P. M. W.; Johnson, B.; Chen, W.; Wong, M. W.; Gonzalez, C.; Pople, J. A. *Gaussian Development Version*; H10; Gaussian, Inc.; Pittsburgh PA; 2006.

(89) *Mathematica 7.0*; Wolfram Research, Inc.; Champaign, IL;

(90) Lias, S. G. "Ionization Energy Evaluation" in *NIST Chemistry WebBook*, *NIST Standard Reference Database Number 69*; National Institute of Standards and Technology: Gaithersburg, MD, 2010.

Table 2-1. Calculated vertical ionization potentials for butadiene^a

Basis set	Theory		
	UHF	ROHF	UCCSD
6-31G(d,p)	7.561	7.929	8.790
6-31+G(d,p)	7.696	8.060	8.935
6-31++G(d,p)	7.694	8.058	8.934
6-31 2+ G(d,p)	7.697	8.061	8.943
6-31 3+ G(d,p)	7.697	8.061	8.943
6-311++G(2df,2pd)	7.700	8.091	9.151

^a in eV, experimental value: 9.072 ± 0.007 eV⁹⁰

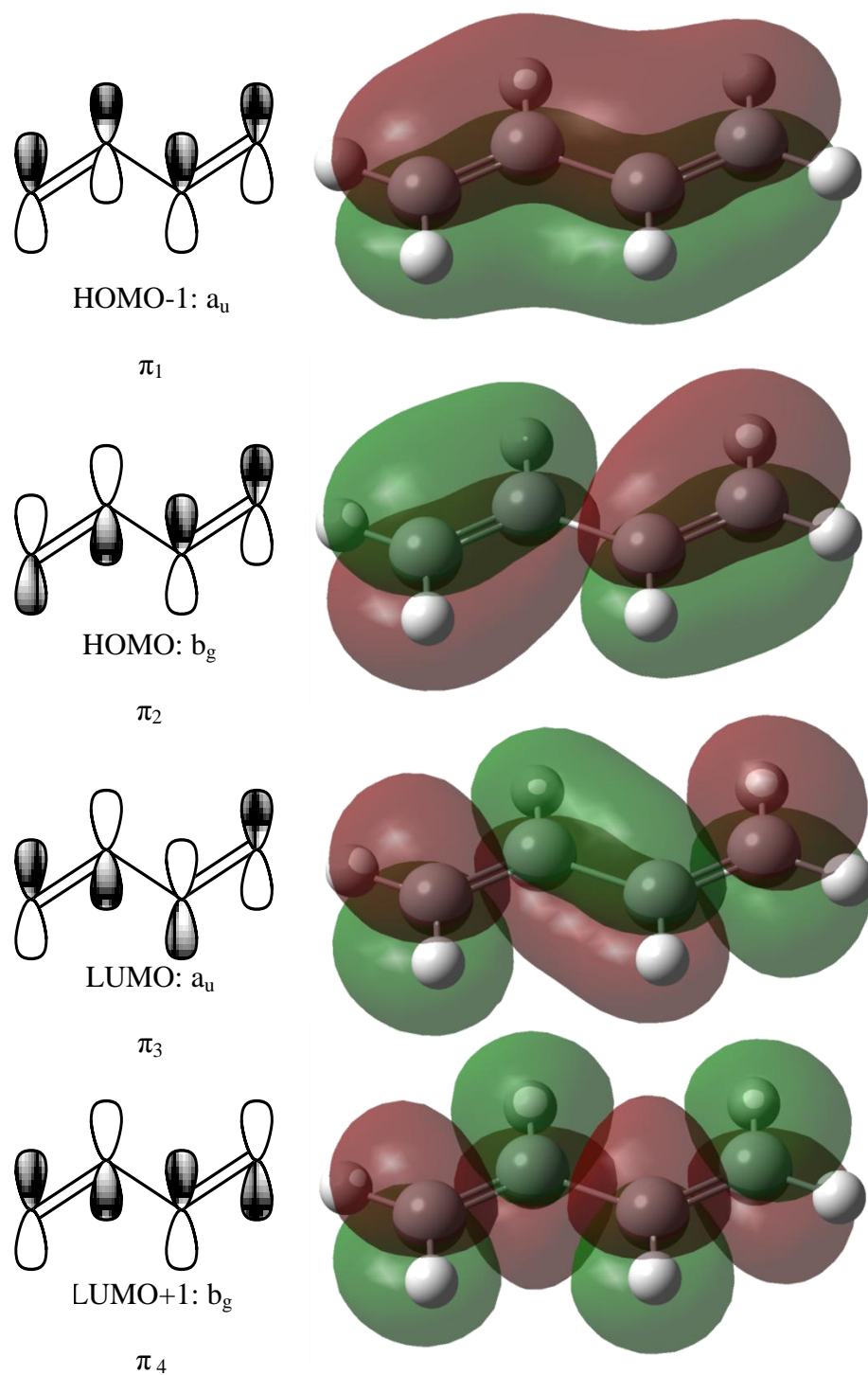


Figure 2-1. The highest occupied and lowest unoccupied π molecular orbitals of 1,3-butadiene calculated by HF/6-31G(d,p).

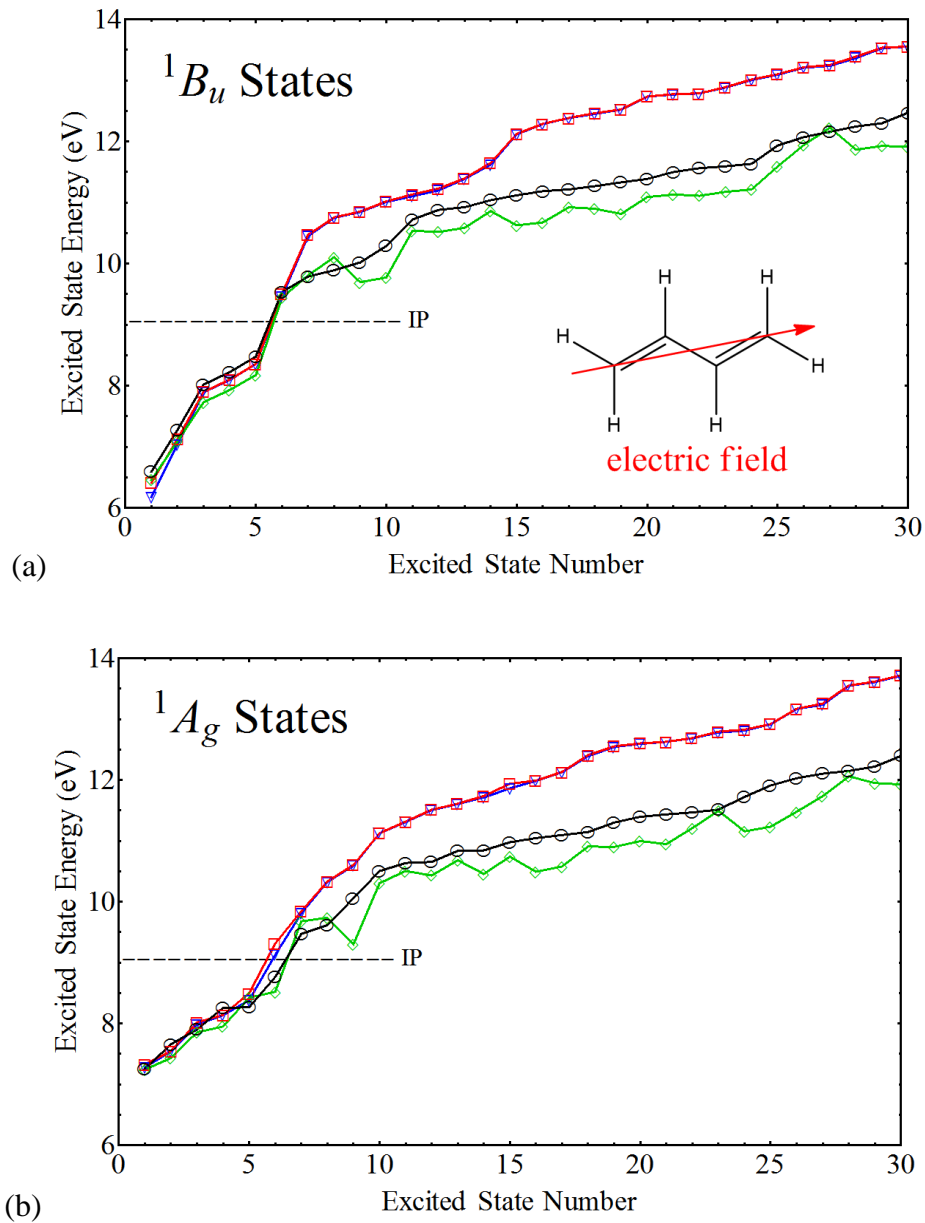


Figure 2-2. Vertical excitation energies of butadiene for the first 30 1B_u states and 1A_g states calculated with the 6-31 3+ G(d,p) basis set (RPA (blue triangles pointing down), CIS (red squares), CIS(D) (green diamonds), EOM-CC (black circles)). IP is the experimentally determined ionization potential.⁹⁰

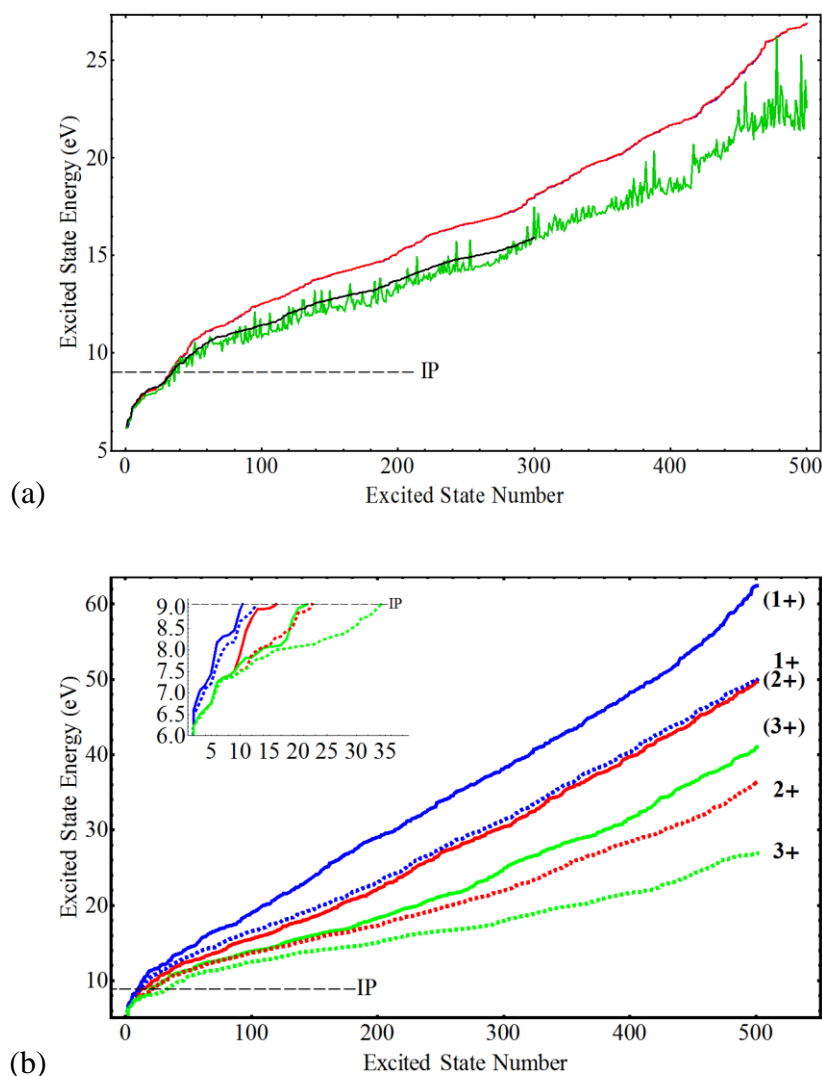


Figure 2-3. Vertical excitation energies for the first 500 states of butadiene (all symmetries) calculated with (a) the 6-31 3+ G(d,p) basis and RPA, CIS, CIS(D) and EOM-CC (blue, red, green and black, respectively), (b) CIS and the 6-31 $n+$ G(d,p) and 6-31($n+$)G(d,p) basis sets ($n=1$ blue, $n=2$ red, $n=3$ green, solid lines ($n+$), dotted lines $n+$). Inset: Number of states under the experimental ionization potential.⁹⁰

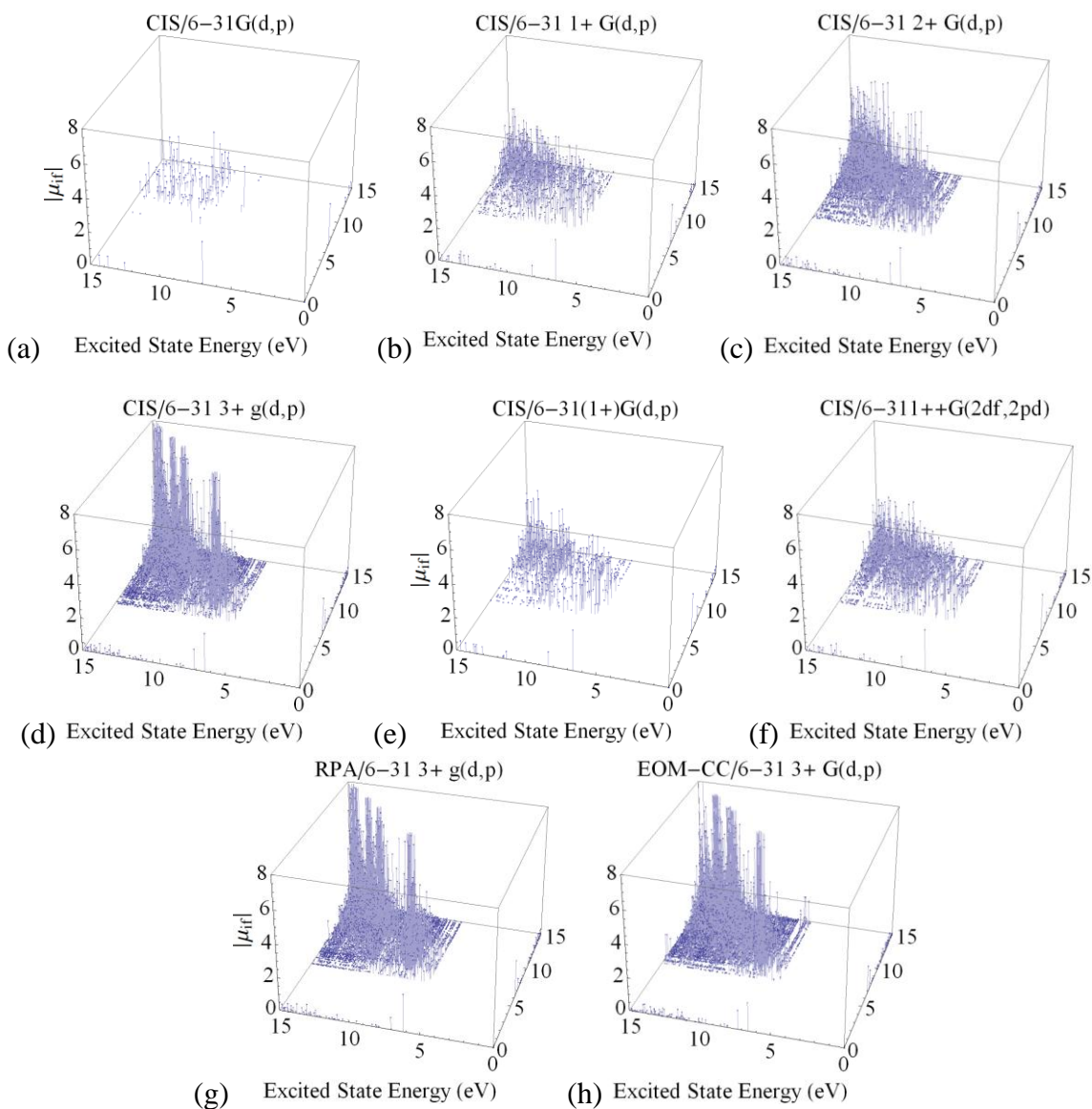


Figure 2-4. Transition dipoles for butadiene calculated with (a) CIS/6-31G(d,p), (b) CIS/6-31 1+ G(d,p), (c) CIS/6-31 2+ G(d,p), (d) CIS/6-31 3+ G(d,p), (e) CIS/6-31(1+)G(d,p), (f) CIS/6-31++G(2df,2pd), (g) RPA/6-31 3+ G(d,p), and (h) EOM-CC/6-31 3+ G(d,p).

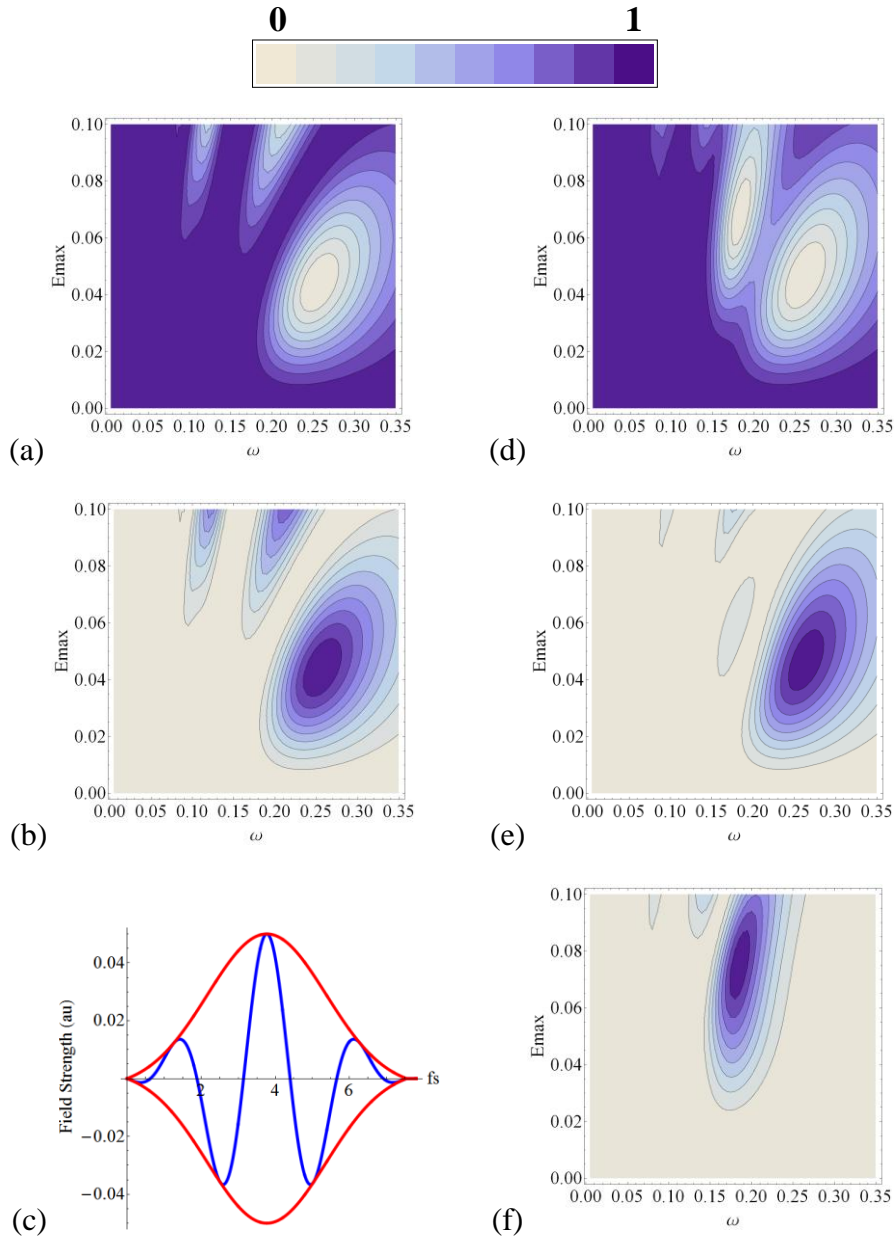


Figure 2-5. Response of model two and three level systems ($\omega_0 = 0.$, $\omega_1 = 0.25$, $\omega_2 = 0.35$; $D_{01} = 2.0$, $D_{12} = 2.0$, $D_{02} = 0.0$ au) to a 3 cycle Gaussian pulse, as a function of the pulse frequency, ω , and the maximum of the pulse envelope, E_{\max} : (a) and (b) ground and excited state populations of the two level system, (d), (e) and (f) ground and excited state populations of the three level system, (c) pulse shape.

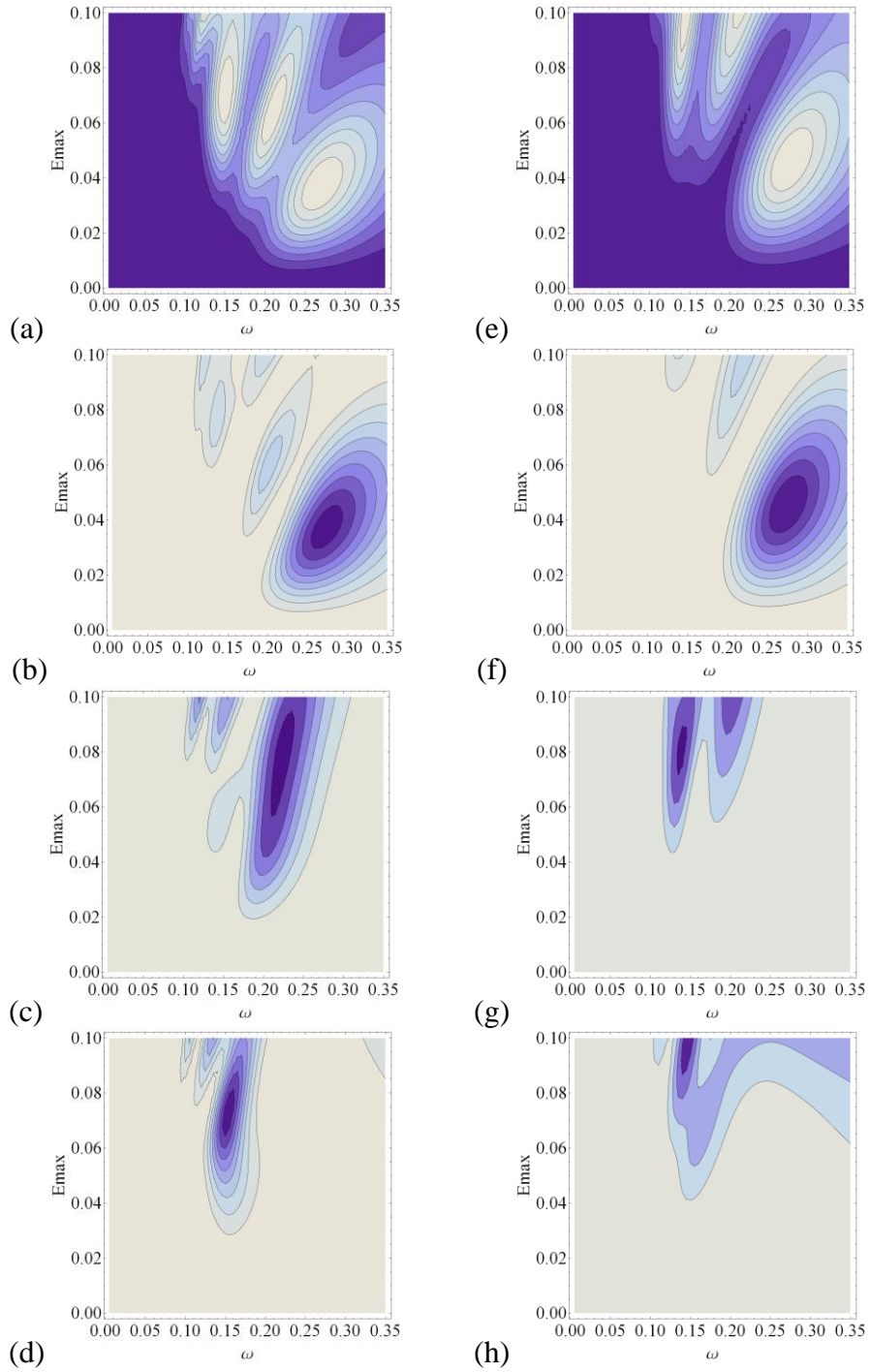


Figure 2-6. Response of the butadiene π states (1^1A_g ground state and the 1^1B_u , 2^1A_g and 2^1B_u excited states) to a 3 cycle gaussian pulse: (a)-(d) CIS/6-31G(d,p) excited state energies and transition dipoles: $\omega_0 = 0.0$, $\omega_1 = 0.256$, $\omega_2 = 0.344$, $\omega_3 = 0.369$, $\omega_4 = 0.460$; $D_{02} = D_{03} = D_{14} = D_{23} = 0.0$, $D_{01} = -2.575$, $D_{04} = 0.485$, $D_{12} = 0.430$, $D_{13} = 2.620$, $D_{24} = 0.547$, $D_{34} = 3.406$ au. (e)-(h) EOM-CC/6-31G(d,p) excited state energies and transition dipoles: $\omega_0 = 0.0$, $\omega_1 = 0.267$, $\omega_2 = 0.293$, $\omega_3 = 0.358$, $\omega_4 = 0.440$; $D_{02} = D_{03} = D_{14} = D_{23} = 0.0$, $D_{01} = -2.091$, $D_{04} = 0.555$, $D_{12} = -1.581$, $D_{13} = -0.330$, $D_{24} = -1.968$, $D_{34} = -0.114$ au.

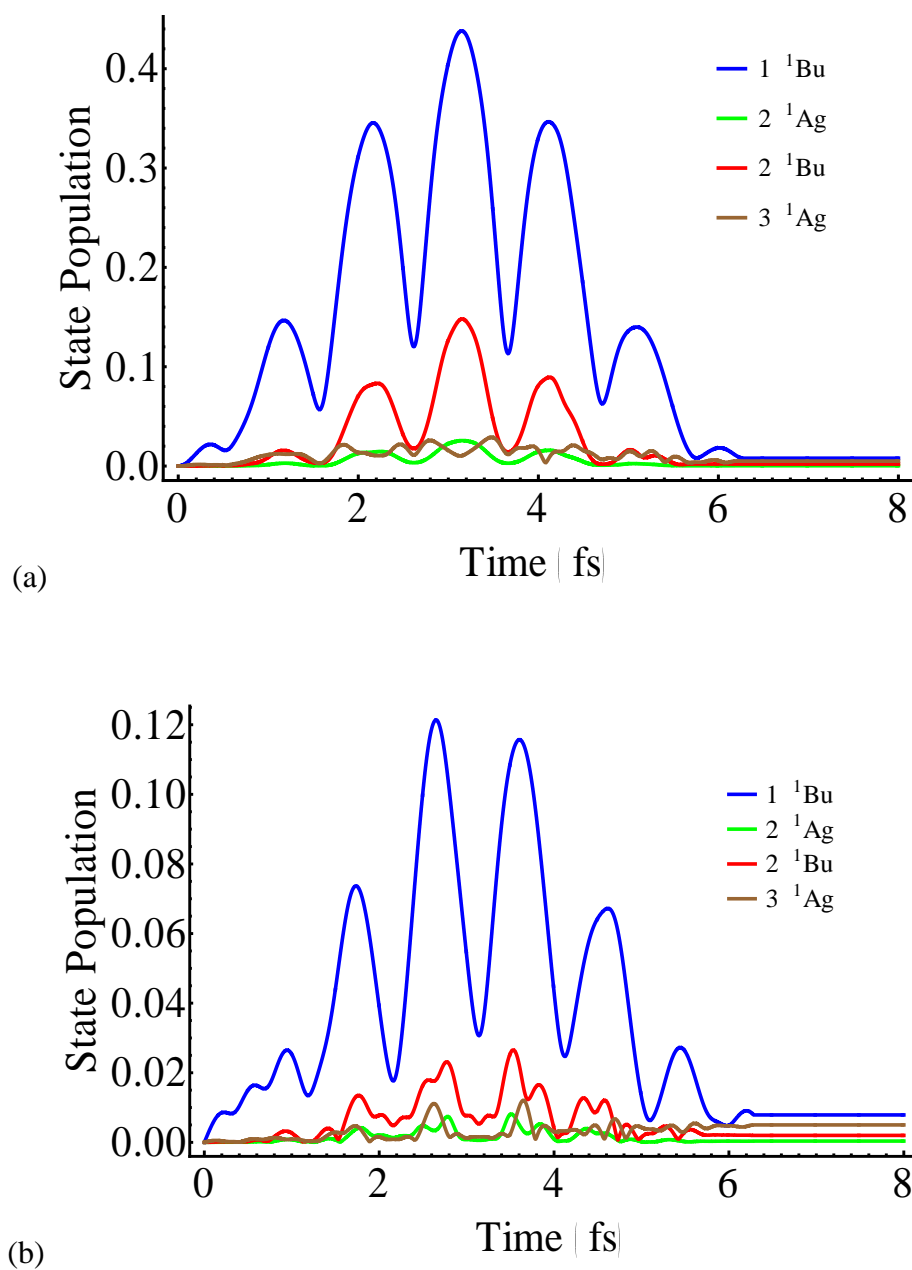


Figure 2-7. Comparison of the response of butadiene calculated with TD-CIS/6-31G(d,p) in a 3 cycle Gaussian pulse ($\omega = 0.06$ au, $E_{\max} = 0.05$ au) in terms of (a) the zero-field states and (b) the instantaneous adiabatic states.

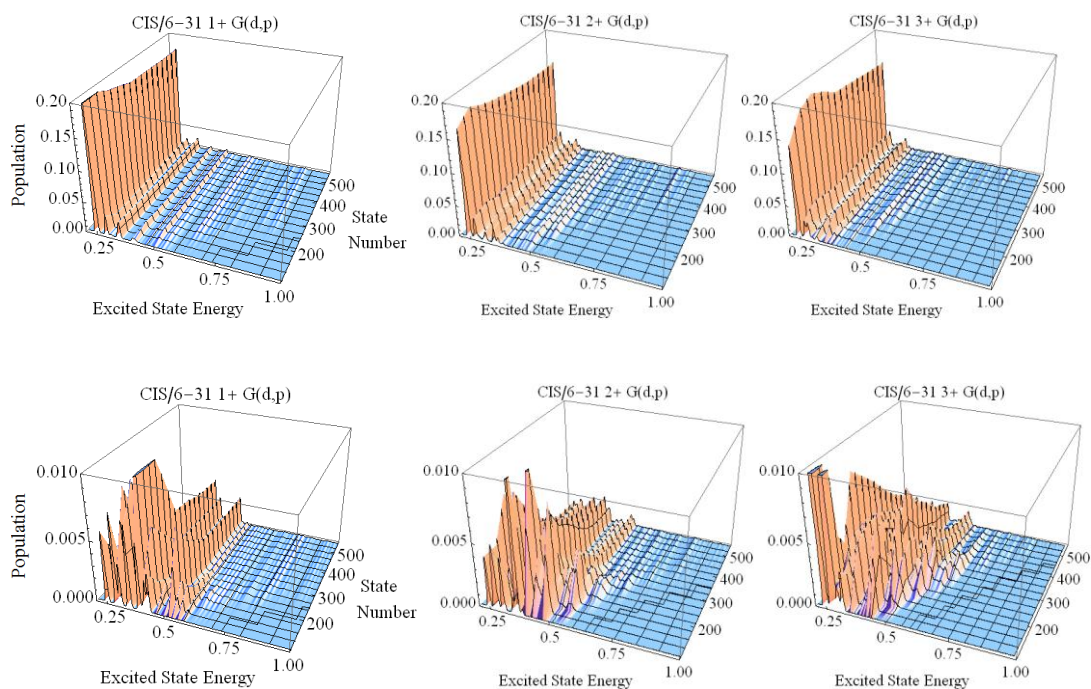


Figure 2-8. Excited state populations of butadiene as a function of number of states included in the TD-CIS simulation, at the maximum of the pulse (top row) and after the pulse (bottom row) ($\omega = 0.06$ au, $E_{\max} = 0.05$ au) with the 6-31 $n+$ G(d,p) basis sets.

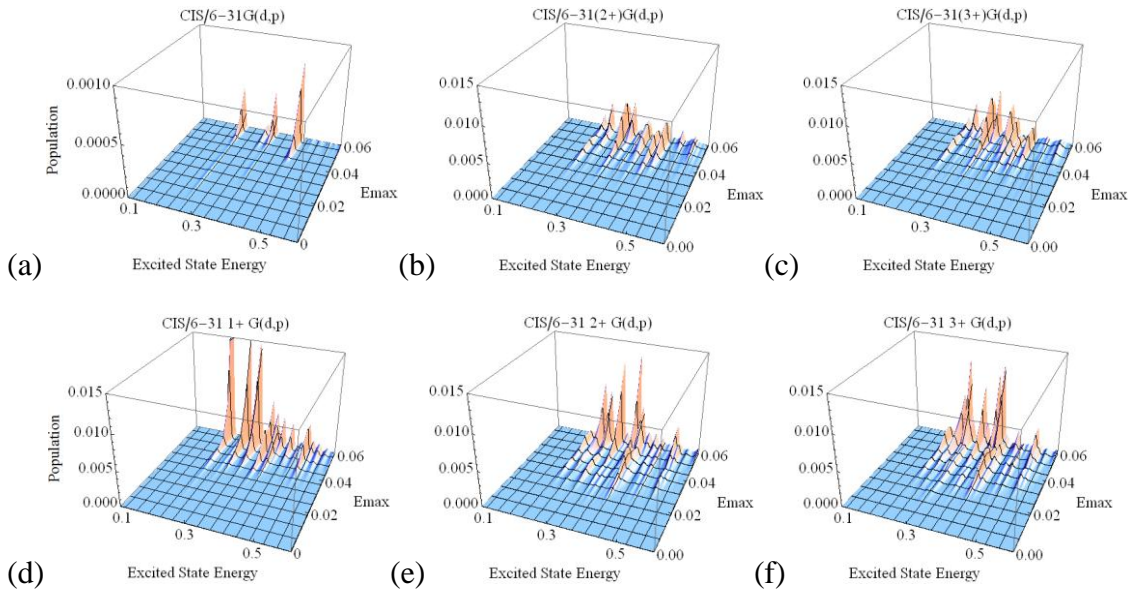


Figure 2-9. Response of butadiene subject to a 3 cycle Gaussian pulse ($\omega = 0.06$ au, $E_{\max} = 0 - 0.06$ au) calculated by TD-CIS with 500 excited states using the following basis sets (a) 6-31G(d,p), (b) 6-31(2+)G(d,p), (c) 6-31(3+)G(d,p), (d) 6-31 1+ G(d,p), (e) 6-31 2+ G(d,p) and (f) 6-31 3+ G(d,p).

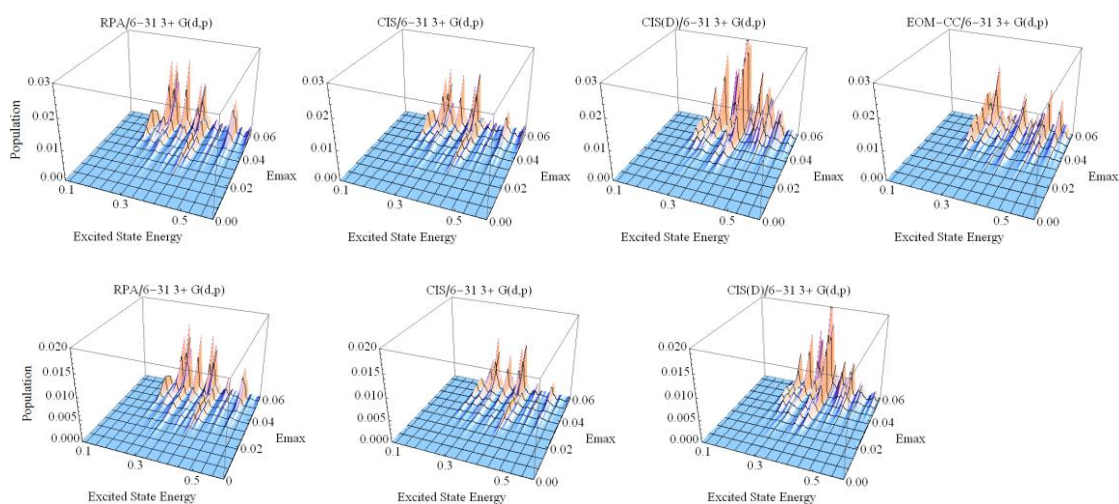


Figure 2-10. Response of butadiene subject to a 3 cycle Gaussian pulse ($\omega = 0.06$ au, $E_{\max} = 0 - 0.06$ au) calculated with the 6-31 3+ G(d,p) basis set and RPA, CIS, CIS(D) and EOM-CC using 300 states (top row) and 500 states (bottom row).

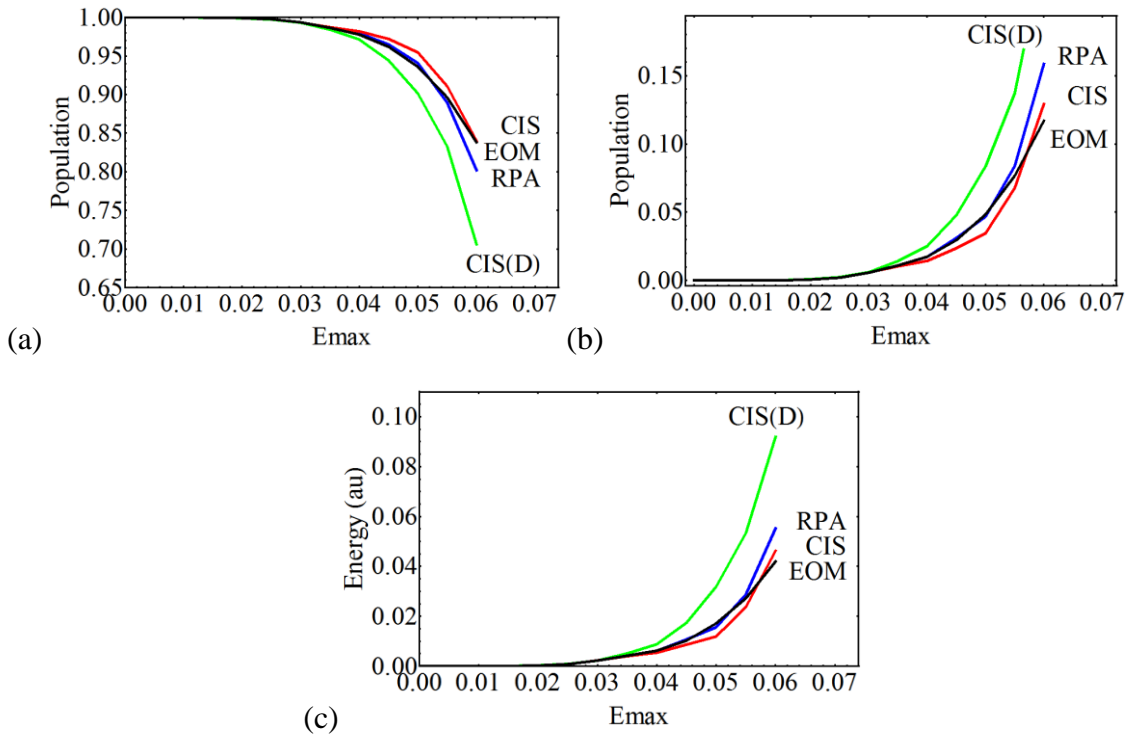


Figure 2-11. Dependence of the populations and energies on E_{\max} , the maximum field strength of the pulse: (a) ground state population, (b) sum of the populations of excited states with energies less than 0.5 au, (c) energy deposited in excited states with energies less than 0.5 au (RPA – blue, CIS – red, CIS(D) – green, EOM-CC – black).

Chapter 3

TD-CI Simulation of the Electronic Optical Response of Molecules in Intense Fields II: Comparison of DFT Functionals and EOM-CCSD

Jason A. Sonk and H. Bernhard Schlegel*

Department of Chemistry, Wayne State University, Detroit, Michigan 48202

Reprinted with permission from *J. Phys. Chem. A*, **2011**, 115 (42), pp 11832–11840

Copyright 2011, American Chemical Society.

3.1 Introduction

In the previous chapter¹, we employed the TD-CI approach to simulate the response of butadiene to an intense laser field. We were able to compare the response predicted by various levels of wavefunction based theory using the excited states and transition dipole moments calculated by those theories. We also examined the effects of basis set size and number of excited states used in the simulation. In this chapter² we explore the utility of linear-response time-dependent density functional theory for calculating the field-free excitation energies and transition dipoles needed in TD-CI simulations. The least expensive methods for calculating these field-free excitation energies and transition dipoles are configuration interaction with single excitations (CIS),

linear-response time-dependent Hartree-Fock (TD-HF, also known as the random phase approximation – RPA), and linear-response time-dependent density functional theory (TD-DFT)^{3,4}. Linear-response TD-DFT calculations do treat electron correlation, but there are many functionals to choose from. Similar to the previous chapter we again use butadiene in a short, intense laser pulse as a test case. In this chapter we will examine TD-CI simulations with excitation energies and transition dipoles calculated by a representative set of density functionals. A benefit of using TD-DFT is that excited state energies can be calculated at a fraction of the cost of more accurate EOM-CC and multireference methods. However, of the many different functionals, some may not be suitable for calculating the TD-CI simulations of molecules in strong fields.

3.2 Methods

DFT and EOM-CCSD calculations were carried out with the development version of the Gaussian software package.⁵ The functionals used in this study are listed in Table 3-1 and were chosen to sample various aspects of density functional theory. TD-DFT can have substantial errors when charge-transfer excited states are involved. The use of long-range corrected functionals is one method of treating this error. Therefore, several long-range corrected functionals were considered (LC- ω PBE, ω B97XD, CAM-B3LYP, LC-BLYP, LC-PBE, LC-PW91, LC-TPSS) in addition to a selection of standard functionals (B3LYP, BH&HLYP, HSE2PBE (HSE03), BLYP, PBE, PW91, TPSS). To assess the effects of the range parameter in the long-range corrected functionals, calculations with LC- ω PBE were carried out with $\omega=0.2, 0.4, 0.6$ and 0.8 . As in the previous chapter, *trans* butadiene optimized at the HF/6-31G(d,p) level of theory was used as the test case. Excitation energies and transition dipoles were computed with the 6-31 3+ G(d,p) basis,

which has one set of 5 Cartesian d functions on each carbon, one set of p functions on each hydrogen and 3 sets of diffuse s and p functions on each carbon, with exponents of 0.04380, 0.01095, 0.0027375. A 3 cycle Gaussian pulse with $\omega = 0.06$ au (760nm) was used in the simulations. For maximal effect the field was directed along the long axis of the molecule, specifically along the vector connecting the end carbons. As in the previous chapter, up to 500 excited states were included in the simulations. Mathematica⁶ was used to integrate the TD-CI equations and analyze the results. The TD-CI integrations were carried out with a step size of 0.5 au (0.012 fs). The same pulse parameters used in the previous chapter were used in this chapter as well (see equations 2.12—2.14)

3.3 Results and Discussion

3.3.1 *Excitation Energies and Transition Dipoles*

All of the methods agree that the lowest excited state of butadiene is 1B_u and involves a single excitation from the highest occupied orbital to the lowest unoccupied orbital. Table 3-1 shows that the standard functionals underestimate the first excitation energy while the long-range corrected functionals are in better agreement with experiment. For most of the functionals, the calculated ionization potential (IP) is within 0.2 eV of the experimental value (the exceptions are TPSS, BLYP and BH&HLYP). The standard functionals tend to be lower than the experimental IP and the long-range correct functionals are mostly higher. Thus, there is a qualitative agreement between the trends in the first excitation energy and the ionization potential, but the relation is not quantitative ($R^2=0.42$).

Figures 3-1—3-4 compare the excited state energies for the functionals listed in Table 3-1. Table 3-2 lists the average excitation energies for first 300 excited states. The results seem to be grouped within the rungs of DFT's Jacob's ladder⁷, with the generalized gradient approximation (GGA) functionals (BLYP, PBE, PW91) predicting the lowest average excitation energies. These are followed by TPSS, a meta GGA functional, while the highest average excitation energies correspond to hybrid functionals, B3LYP, HSE2PBE, and BH&HLYP. All of the standard functionals predict excited states that are on average lower in energy than EOM-CC. Figure 3-1 shows the energies of the first 500 excited states of butadiene using some of the standard functionals listed in Table 3-1 (B3LYP, PBE, HSE2PBE, PW91, TPSS). Included in this figure are the excited state energies for the first 300 states calculated by EOM-CC and the first 500 states by RPA. Compared to the EOM-CC and RPA results, the TD-DFT excitation energies with the standard functionals are lower by as much as 4 eV for the highest energy states. The largest differences are for PBE, PW91 and TPSS. Compared to EOM-CC, the best performers among the standard functionals are BH&HLYP (-2%) and HSE2PBE (8%). The other standard functionals have differences in the average excitation energy greater than 10%. Mixing in a larger amount of Hartree-Fock exchange seems to reduce the error.

Figure 3-2 explores the effect of adding Hartree-Fock (HF) exchange to the BLYP functional: BLYP (no HF exchange), B3LYP (20% HF exchange), CAM-B3LYP (between 19 and 65% HF exchange), and BH&HLYP (50% HF exchange). As the amount of Hartree-Fock exchange increases from 0% to 50% the excited state energies

approach those predicted by EOM-CC. The average error goes from -18% for BLYP to -11% B3LYP to -2% for BH&HLYP.

Most standard functionals have the wrong long-range behavior due to the self-interaction error.⁸⁻¹² As a result, the energies of Rydberg-like states are severely underestimated.¹³⁻¹⁵ Increasing the amount of Hartree-Fock exchange in a global hybrid functional improves the long-range behavior, but degrades the performance at short-range. Long-range corrected (LC) functionals address this problem is by changing from an exchange functional at short range to 100% Hartree-Fock exchange at long range. This is achieved by using a switching function to divide the Coulomb operator into short-range and long-range parts.

$$\frac{1}{r_{12}} = \frac{\text{erfc}(\omega r_{12})}{r_{12}} + \frac{\text{erf}(\omega r_{12})}{r_{12}} \quad (3.1)$$

The parameter ω controls the ratio of these components as a function of distance. Figure 3-3 shows that excitation energies computed with long-range corrected functionals are in much better agreement with EOM-CC. The ω B97XD and CAM-B3LYP functionals predict energies ~3-4% lower than EOM-CC, while the other long-range corrected functionals all predict energies slightly higher than those of EOM-CC (LC- ω PBE 3%, LC-TPSS 6%, LC-PW91 6%, LC-PBE 6% and LC-BLYP 4%).

Varying the ω -parameter changes the distance over which the switch from short range to long range behavior takes place. A relatively narrow range of ω values (from 0.2 to 0.5 bohr⁻¹) has been found by optimization of various properties for existing long-range corrected hybrid functionals.¹⁶⁻²⁹ Figure 3-4 demonstrates the effect on the

excitation energies of changing the ω parameter in the LC- ω PBE functional. When ω is too small (more DFT exchange) the excitation energies are much lower than those of EOM-CC. If ω is too large (more HF exchange) the excitation energies are significantly higher than those of EOM-CC and approach the energies predicted by RPA/TD-HF (dashed line in Figure 3-4). A value of $\omega=0.4$ is best for reproducing the EOM-CC excited state energies. This is in agreement with the optimal value of $\omega=0.4$ found for calculating enthalpies of formation, barrier heights and ionization potentials.²⁴

Correct transition dipoles should be just as important as accurate excitation energies for calculating the response to an intense laser field. A typical calculation yields several valence states below the ionization potential (IP) with more Rydberg-like states growing closer together as the energy approaches the IP. A dense collection of states above the IP forms a pseudo-continuum. There are a few key valence states with large transition dipoles, which allow for efficient excitation from the ground state to excited states and from one excited state to another. In the pseudo-continuum, the transition dipoles are largest between neighboring states that have the highest spatial overlap and therefore the largest transition dipoles. A typical plot of the transition dipoles is shown in Figure 3-5 for the B3LYP functional. The magnitudes of the transition dipoles are plotted vertically; the ground state to excited state transition dipoles are along the horizontal axes and the excited to excited state transition dipoles make up the interior of the plot. The basis set dependence of the transition dipoles calculated with the B3LYP functional is similar to those found in Chapter 2 with CIS and RPA calculations.¹ The overwhelming majority of the transition dipoles are small in magnitude (of the more than 23,000 transition dipoles with magnitudes greater than 0.001 au, more than 15,000 have

magnitudes less than 0.1 au) and only a relatively small number of transition dipoles which have large magnitudes (less than 120 with magnitudes greater than 5 au). The statistical distributions of the transition dipoles are relatively similar across all of the density functional and wavefunction methods. The average magnitudes of the transition dipoles are compared in Table 3-2.

3.3.2 TD-CI Simulations of the Response to a Short, Intense Laser Pulse

The interaction of butadiene with a three-cycle Gaussian pulse ($\omega=0.06$ au, 760 nm; eq. 2-12 and 2-13) was simulated with the TD-CI approach (eq. 2-1—2-5) using excited states calculated with various density functionals. During the interaction with the laser field, many excited states contribute to the time-dependent wavefunction. Since the pulse is not resonant with any of the excitation energies, most of the populations of the excited states return to small values after the pulse. Because the interaction with the intense pulse is non-linear, some population remains in the excited states after the field has returned to zero. These residual populations are a measure of the non-linear response of the molecule interacting with the intense laser field and of the quality of the time-dependent wavefunction during and after the interaction with the laser pulse. If the non-linear response (as measured by the residual populations) is too large or too small, then the approximate excitation energies and / or transition dipoles used in the TD-CI simulation are not suitable. Figures 3-6 and 3-7 show the residual populations of the excited states of butadiene after the pulse. The TD-CI simulations used 500 excited states and the populations after the pulse are plotted as a function of the excited state energies and field strengths up to $E_{\max} = 0.06$ au (1.26×10^{14} W/cm²). As expected, the magnitude of the excitations increases rapidly with increasing field strength. Inspection

of Figure 3-6 shows that the non-linear response computed with BLYP, PBE, and PW91 is too strong compared to EOM-CC and RPA, while their long-range corrected counterparts are in much better agreement with EOM-CC and RPA. This indicates that long-range Hartree-Fock exchange is necessary. The effect of Hartree-Fock exchange is explored further in Figure 3-7. Figures 3-7a—3-7c examine the effect of adding Hartree-Fock exchange to the BLYP functional. Mixing in HF character strongly affects the magnitude of the non-linear response. B3LYP (20% HF exchange, Fig. 3-7a) is much better than BLYP (0% HF exchange, Fig. 3-6a). BH&HLYP (50% HF exchange, Fig. 3-7b) and CAM-B3LYP (19% - 65% HF exchange, Fig. 3-7c) are a bit better than B3LYP, but the residual populations is still too large compared to EOM-CC (Fig. 3-6h). This indicates that adding a percentage of HF exchange is not enough and it is essential to switch to 100% HF exchange at long range. The performance of long-range corrected DFT calculations can be sensitive to the choice of the range parameter. Figures 3-7d—3-7g show the effect of changing the ω in the LC- ω PBE functional. Too small of a value (switching to HF exchange at a longer range) yields residual populations that are too large compared to EOM-CC. Too large of a value of ω (switching to HF exchange at a shorter range) produces results that are much smaller than the EOM-CC.

A more quantitative measure of the non-linear response can be obtained by adding up the residual populations of the excited states generated by the pulse. Figure 3-8 and Table 3-2 compare the sum of the excited state populations for states with energies less than 0.05 au, based on simulations with $E_{\max} = 0.05$ au and using 300 states. As noted previously¹, RPA and CIS are in good agreement with EOM-CC but the response of CIS(D) is a bit too strong. The non-linear response for all of the standard functionals is

far too strong. Most of the long-range corrected functionals fall within $\pm 25\%$ of the EOM-CC value. The exceptions are ω B97XD and CAM-B3LYP (too strong) and LC- ω PBE with $\omega=0.8$ (too weak).

Table 3-2 compares the sum of all excited states populations after the pulse for the various functionals, along with the average excitation energies and the average transition dipole magnitudes. The non-linear response, as measured by the sum of the excited state populations after the pulse is not correlated with the calculated ionization potential listed in Table 3-1 ($R^2 = 0.01$) and only weakly correlated with the average transition dipoles (linear fit $R^2 = 0.14$ for ground state to all excited states, $R^2 = 0.58$ for first excited states to all excited states, $R^2 = 0.42$ for all transition dipoles, see Table 3-2). The non-linear response is most strongly correlated with the first excitation energy ($R^2 = 0.85$) and the average excitation energy (Figure 3-9, $R^2 = 0.89$ for a linear fit and $R^2 = 0.98$ for a quadratic fit). In particular, if the average excitation energy is significantly below the EOM-CC value, the response is far too strong. This is the case for most of the standard functionals. The average excitation energy for long range corrected functionals is in better agreement with EOM-CC and the non-linear response is comparable to EOM-CC.

3.4 Conclusions

The TD-CI approach has been used to examine the ability of various density functionals to simulate the interaction of butadiene with a short intense laser pulse. Excitation energies calculated by TD-DFT with standard functionals are significantly lower than the EOM-CC excitation energies. Long-range corrected functionals tend to produce average excitation energies slightly higher than EOM-CC. A value of $\omega = 0.4$ in

the LC- ω PBE functional provides good agreement with EOM-CC over a wide range of excitation energies. Long-range corrected functionals also yield transition dipoles that are larger than EOM-CC on average. The non-linear response of butadiene interacting with an intense laser pulse is gauged by the residual populations of the excited states after the pulse. The non-linear response computed by TD-CI simulations based on excited states calculated with standard functionals is far too large, primarily because the excitation energies are too low. The response computed with long-range corrected functionals is comparable to that obtained with EOM-CC, RPA and CIS. This indicates that correct long-range behavior is essential for the treatment of the diffuse and highly excited states needed to describe the interaction between the electron density and a strong laser field.

3.5 References

- (1) Sonk, J. A.; Caricato, M.; Schlegel, H. B. TD-CI Simulation of the Electronic Optical Response of Molecules in Intense Fields: Comparison of RPA, CIS, CIS(D), and EOM-CCSD, *J. Phys. Chem. A* **2011**, *115*, 4678.
- (2) Sonk, J. A.; Schlegel, H. B. TD-CI Simulation of the Electronic Optical Response of Molecules in Intense Fields II: Comparison of DFT Functionals and EOM-CCSD, *J. Phys. Chem. A* **2011**, 10.1021/jp206437s.
- (3) Marques, M. A. L.; Gross, E. K. U. Time-dependent density functional theory, *Annu. Rev. Phys. Chem.* **2004**, *55*, 427.
- (4) Dreuw, A.; Head-Gordon, M. Single-Reference ab Initio Methods for the Calculation of Excited States of Large Molecules, *Chem. Rev.* **2005**, *105*, 4009.
- (5) Frisch, M. J.; Trucks, G. W.; Schlegel, H. B.; Scuseria, G. E.; Robb, M. A.; Cheeseman, J. R.; Montgomery, J. A.; Vreven, T.; Kudin, K. N.; Burant, J. C.; Millam, J. M.; Iyengar, S.; Tomasi, J.; Barone, V.; Mennucci, B.; Cossi, M.; Scalmani, G.; Rega, N.; Petersson, G. A.; Nakatsuji, H.; Hada, M.; Ehara, M.; Toyota, K.; Fukuda, R.; Hasegawa, J.; Ishida, M.; Nakajima, T.; Honda, Y.; Kitao, O.; Nakai, H.; Klene, M.; Li, X.; Knox, J. E.; Hratchian, H. P.; Cross, J. B.; Bakken, V.; Adamo, C.; Jaramillo, J.; Gomperts, R.; Stratmann, R. E.; Yazyev, O.; Austin, A. J.; Cammi, R.; Pomelli, C.; Ochterski, J.; Ayala, P. Y.; Morokuma, K.; Voth, G. A.; Salvador, P.; Dannenberg, J. J.; Zakrzewski, V. G.; Dapprich, S.; Daniels, A. D.; Strain, M. C.; Farkas, Ö.; Malick, D. K.; Rabuck, A. D.; Raghavachari, K.; Foresman, J. B.; Ortiz, J. V.; Cui, Q.; Baboul, A. G.; Clifford, S.; Cioslowski, J.; Stefanov, B. B.; Liu, G.; Liashenko, A.; Piskorz, P.; Komaromi, I.; Martin, R. L.; Fox, D. J.; Keith, T.; Al-Laham, M. A.; Peng, C. Y.; Nanayakkara, A.; Challacombe, M.; Gill, P. M. W.; Johnson, B.; Chen, W.; Wong, M.

W.; Gonzalez, C.; Pople, J. A. *Gaussian Development Version*; Revision H.10; Gaussian, Inc.; Wallingford, CT; 2010.

- (6) *Mathematica*; 8.0; Wolfram Research, Inc.; Champaign, IL; 2010.
- (7) Perdew, J. P.; Schmidt, K. *Density functional theory and its application to materials: Antwerp, Belgium, 8-10 June 2000*; American Institute of Physics: Melville, NY, 2001.
- (8) Dutoi, A. D.; Head-Gordon, M. Self-interaction error of local density functionals for alkali-halide dissociation, *Chem. Phys. Lett.* **2006**, 422, 230.
- (9) Mori-Sanchez, P.; Cohen, A. J.; Yang, W. Many-electron self-interaction error in approximate density functionals, *J. Chem. Phys.* **2006**, 125, 201102.
- (10) Ruzsinszky, A.; Perdew, J. P.; Csonka, G. I.; Vydrov, O. A.; Scuseria, G. E. Density functionals that are one- and two- are not always many-electron self-interaction-free, as shown for H_2^+ , He_2^+ , LiH^+ , and Ne_2^+ *J. Chem. Phys.* **2007**, 126, 104102.
- (11) Bally, T.; Sastry, G. N. Incorrect Dissociation Behavior of Radical Ions in Density Functional Calculations, *J. Phys. Chem. A* **1997**, 101, 7923.
- (12) Braïda, B.; Hiberty, P. C.; Savin, A. A Systematic Failing of Current Density Functionals: Overestimation of Two-Center Three-Electron Bonding Energies, *J. Phys. Chem. A* **1998**, 102, 7872.
- (13) Bauernschmitt, R.; Ahlrichs, R. Treatment of electronic excitations within the adiabatic approximation of time dependent density functional theory, *Chem. Phys. Lett.* **1996**, 256, 454.

- (14) Casida, M. E.; Jamorski, C.; Casida, K. C.; Salahub, D. R. Molecular excitation energies to high-lying bound states from time-dependent density-functional response theory: Characterization and correction of the time-dependent local density approximation ionization threshold, *J. Chem. Phys.* **1998**, *108*, 4439.
- (15) Tozer, D. J.; Handy, N. C. Improving virtual Kohn--Sham orbitals and eigenvalues: Application to excitation energies and static polarizabilities, *J. Chem. Phys.* **1998**, *109*, 10180.
- (16) Savin, A. *Recent developments and applications of modern density functional theory*; Elsevier: Amsterdam, 1996.
- (17) Gerber, I. C.; Ángyán, J. G. Hybrid functional with separated range, *Chem. Phys. Lett.* **2005**, *415*, 100.
- (18) Leininger, T.; Stoll, H.; Werner, H.-J.; Savin, A. Combining long-range configuration interaction with short-range density functionals, *Chem. Phys. Lett.* **1997**, *275*, 151.
- (19) Aron, J. C.; Paula, M.-S.; Weitao, Y. Development of exchange-correlation functionals with minimal many-electron self-interaction error, *J. Chem. Phys.* **2007**, *126*, 191109.
- (20) Chai, J. D.; Head-Gordon, M. Systematic optimization of long-range corrected hybrid density functionals, *J. Chem. Phys.* **2008**, *128*, 084106.
- (21) Hisayoshi, I.; Takao, T.; Takeshi, Y.; Kimihiko, H. A long-range correction scheme for generalized-gradient-approximation exchange functionals, *J. Chem. Phys.* **2001**, *115*, 3540.

- (22) Iann, C. G.; Janos, G. A.; Martijn, M.; Georg, K. Range separated hybrid density functional with long-range Hartree-Fock exchange applied to solids, *J. Chem. Phys.* **2007**, *127*, 054101.
- (23) Jong-Won, S.; Tsuyoshi, H.; Takao, T.; Kimihiko, H. Long-range corrected density functional calculations of chemical reactions: Redetermination of parameter, *J. Chem. Phys.* **2007**, *126*, 154105.
- (24) Vydrov, O. A.; Heyd, J.; Krukau, A. V.; Scuseria, G. E. Importance of short-range versus long-range Hartree-Fock exchange for the performance of hybrid density functionals, *J. Chem. Phys.* **2006**, *125*, 074106.
- (25) Vydrov, O. A.; Scuseria, G. E. Assessment of a long-range corrected hybrid functional, *J. Chem. Phys.* **2006**, *125*, 234109.
- (26) Yoshihiro, T.; Takao, T.; Susumu, Y.; Takeshi, Y.; Kimihiko, H. A long-range-corrected time-dependent density functional theory, *J. Chem. Phys.* **2004**, *120*, 8425.
- (27) Jacquemin, D.; Wathelet, V.; Perpète, E. A.; Adamo, C. Extensive TD-DFT Benchmark: Singlet-Excited States of Organic Molecules, *J. Chem. Theory Comput.* **2009**, *5*, 2420.
- (28) Lange, A. W.; Rohrdanz, M. A.; Herbert, J. M. Charge-transfer excited states in a pi-stacked adenine dimer, as predicted using long-range-corrected time-dependent density functional theory, *J. Phys. Chem. B* **2008**, *112*, 6304.
- (29) Ángyán, J. G.; Gerber, I. C.; Savin, A.; Toulouse, J. van der Waals forces in density functional theory: Perturbational long-range electron-interaction corrections, *Phys. Rev. A* **2005**, *72*, 012510.

- (30) Becke, A. D. Density-Functional Exchange-Energy Approximation with Correct Asymptotic-Behavior, *Phys. Rev. A* **1988**, 38, 3098.
- (31) Lee, C. T.; Yang, W. T.; Parr, R. G. Development of the Colle-Salvetti Correlation-Energy Formula into a Functional of the Electron-Density, *Phys. Rev. B* **1988**, 37, 785.
- (32) Miehlich, B.; Savin, A.; Stoll, H.; Preuss, H. Results Obtained with the Correlation-Energy Density Functionals of Becke and Lee, Yang and Parr, *Chem. Phys. Lett.* **1989**, 157, 200.
- (33) Perdew, J. P.; Burke, K.; Ernzerhof, M. Generalized gradient approximation made simple, *Phys. Rev. Lett.* **1996**, 77, 3865.
- (34) Perdew, J. P.; Burke, K.; Ernzerhof, M. Errata: Generalized Gradient Approximation Made Simple, *Phys. Rev. Lett.* **1997**, 78, 1396.
- (35) Burke, K.; Perdew, J. P.; Wang, Y. *Electronic density functional theory: recent progress and new directions*; Plenum Press, 1998.
- (36) Perdew, J. P. *Electronic structure of solids '91: proceedings of the 75. WE-Heraeus-Seminar and 21st Annual International Symposium on Electronic Structure of Solids held in Gaussig (Germany)*, ; Akademie Verlag: Berlin, 1991.
- (37) Perdew, J. P.; Burke, K.; Wang, Y. Generalized gradient approximation for the exchange-correlation hole of a many-electron system, *Phys. Rev. B* **1996**, 54, 16533.
- (38) Perdew, J. P.; Chevary, J. A.; Vosko, S. H.; Jackson, K. A.; Pederson, M. R.; Singh, D. J.; Fiolhais, C. Atoms, molecules, solids, and surfaces: Applications of the

generalized gradient approximation for exchange and correlation, *Phys. Rev. B* **1992**, *46*, 6671.

(39) Perdew, J. P.; Chevary, J. A.; Vosko, S. H.; Jackson, K. A.; Pederson, M. R.; Singh, D. J.; Fiolhais, C. Erratum: Atoms, molecules, solids, and surfaces: Applications of the generalized gradient approximation for exchange and correlation, *Phys. Rev. B* **1993**, *48*, 4978.

(40) Tao, J. M.; Perdew, J. P.; Staroverov, V. N.; Scuseria, G. E. Climbing the density functional ladder: Nonempirical meta-generalized gradient approximation designed for molecules and solids, *Phys. Rev. Lett.* **2003**, *91*, 146401.

(41) Becke, A. D. Density-functional thermochemistry. III. The role of exact exchange, *J. Chem. Phys.* **1993**, *98*, 5648.

(42) Becke, A. D. A new mixing of Hartree-Fock and local density-functional theories, *J. Chem. Phys.* **1993**, *98*, 1372.

(43) Heyd, J.; Scuseria, G. E.; Ernzerhof, M. Hybrid functionals based on a screened Coulomb potential (vol 118, pg 8207, 2003), *J. Chem. Phys.* **2006**, *124*, 219906.

(44) Paier, J.; Marsman, M.; Hummer, K.; Kresse, G.; Gerber, I. C.; Angyan, J. G. Screened hybrid density functionals applied to solids, *J. Chem. Phys.* **2006**, *125*, 249901.

(45) Tawada, Y.; Tsuneda, T.; Yanagisawa, S.; Yanai, T.; Hirao, K. A long-range-corrected time-dependent density functional theory, *J. Chem. Phys.* **2004**, *120*, 8425.

(46) Vydrov, O. A.; Scuseria, G. E.; Perdew, J. P. Tests of functionals for systems with fractional electron number, *J. Chem. Phys.* **2007**, *126*, 154109.

(47) Chai, J. D.; Head-Gordon, M. Long-range corrected hybrid density functionals with damped atom-atom dispersion corrections, *Phys. Chem. Chem. Phys.* **2008**, *10*, 6615.

(48) Yanai, T.; Tew, D. P.; Handy, N. C. A new hybrid exchange-correlation functional using the Coulomb-attenuating method (CAM-B3LYP), *Chem. Phys. Lett.* **2004**, *393*, 51.

(49) Iikura, H.; Tsuneda, T.; Yanai, T.; Hirao, K. A long-range correction scheme for generalized-gradient-approximation exchange functionals, *J. Chem. Phys.* **2001**, *115*, 3540.

(50) Saha, B.; Ehara, M.; Nakatsuji, H. Singly and doubly excited states of butadiene, acrolein, and glyoxal: Geometries and electronic spectra, *J. Chem. Phys.* **2006**, *125*, 014316.

(51) Lias, S. G. "Ionization Energy Evaluation" in *NIST Chemistry WebBook*, *NIST Standard Reference Database Number 69*; National Institute of Standards and Technology: Gaithersburg, 2010.

Table 3-1. Lowest excitation energies and vertical ionization potentials for methods used in this study.^a

Theoretical Method	Method Type	First Excited State Energy in eV	Calculated Vertical IP in eV
Time-dependent Density Functional Theory			
BLYP ³⁰⁻³²	GGA	5.428	8.766
PBE ^{33,34}	GGA	5.428	8.940
PW91 ³⁵⁻³⁹	GGA	5.529	8.976
TPSS ⁴⁰	M-GGA	5.641	8.808
B3LYP ^{31,32,41}	H-GGA 20% HF	5.730	8.933
BH&HLYP ^{5,31,32,42}	H-GGA 50% HF	5.993	8.739
HSE2PBE (HSE03) ^{43,44}	H-GGA	5.641	9.157
LC-ωPBE ^{24,25,45,46}	LC	6.241	9.088
ωB97XD ^{20,47}	LC	5.998	8.951
CAM-B3LYP ⁴⁸	LC H-GGA 19-65% HF	5.962	8.987
LC-BLYP ^{30-32,49}	LC GGA	6.233	9.097
LC-PBE ^{33,34,49}	LC GGA	6.327	9.233
LC-PW91 ^{35-39,49}	LC GGA	6.323	9.245
LC-TPSS ^{40,49}	LC M-GGA	6.334	9.195
Wave Function Based Methods			
UHF/CIS	SCF	6.415	7.697
ROHF/CIS	SCF	6.415	8.061
UCCSD	Coupled-Cluster	6.593	8.943
Experiment		6.25 ⁵⁰	9.072 \pm 0.007 ⁵¹

^aCalculated using the listed method and the 6-31 3+ G(d,p) basis set

Table 3-2. Comparison of average excitation energies, average transition dipole magnitudes, and the sum of excited state populations.^a

Theoretical Method	Average Excitation Energy in au	Average Transition Dipole Magnitude in au ^b	Population of all Excited States
Time-dependent Density Functional Theory			
BLYP	0.3695	0.4590	0.6432
PBE	0.3760	0.4398	0.5796
PW91	0.3775	0.4466	0.5278
TPSS	0.3825	0.4393	0.5381
B3LYP	0.4038	0.4699	0.4101
HSE2PBE (HSE03)	0.4196	0.4620	0.2954
BH&HLYP	0.4441	0.5053	0.1977
LC-ωPBE w= 0.2	0.4140	0.5067	0.2631
LC-ωPBE w= 0.4	0.4680	0.5368	0.0705
LC-ωPBE w= 0.6	0.4962	0.5439	0.0436
LC-ωPBE w= 0.8	0.5100	0.5416	0.0359
ωB97XD	0.4399	0.5225	0.1441
CAM-B3LYP	0.4361	0.5176	0.2027
LC-BLYP	0.4743	0.5445	0.0749
LC-PBE	0.4809	0.5417	0.0561
LC-PW91	0.4816	0.5451	0.0576
LC-TPSS	0.4826	0.5382	0.0560
Wave Function Based Methods			
EOM-CC	0.4540	0.4764	0.0640
RPA	0.4945	0.5281	0.0591
CIS	0.4950	0.5265	0.0454
CIS(D)	0.4432	0.5265	0.0986

^a Calculated using 300 states and the 6-31 3+ G(d,p) basis set with a field strength of $E_{\max} = 0.05$ au

^b for transition dipoles with a magnitude greater than 0.001 au

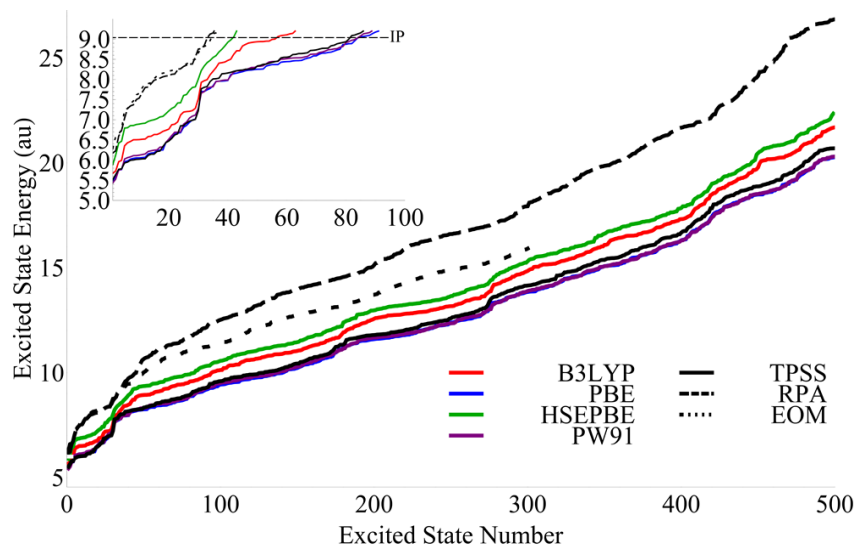


Figure 3-1. Excited state energies for the first 500 states of butadiene (all symmetries) calculated by standard density functionals: B3LYP (red), PBE (blue), HSEPB (green), PW91 (purple) using the 6-31 3+ G(d,p) basis set. For comparison EOM-CC (black, dotted) and RPA (black, dashed) energies are included.

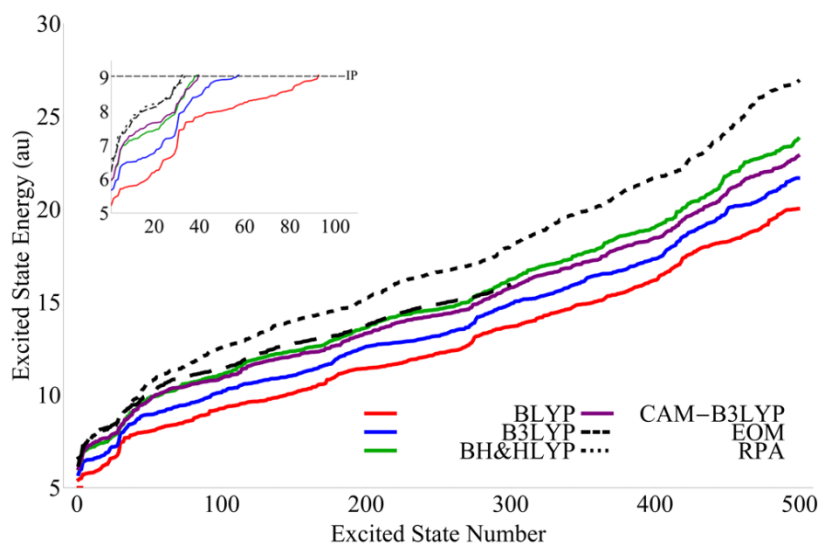


Figure 3-2. Effect of Hartree-Fock exchange for the first 500 excited states calculated using BLYP (0% HF, red), B3LYP (20% HF, blue), CAM-B3LYP (19-65% HF, purple), BH&HLYP (50% HF, green), EOM-CC (black, dashed), RPA (black, dotted). All methods used the 6-31 3+ G(d,p) basis set.

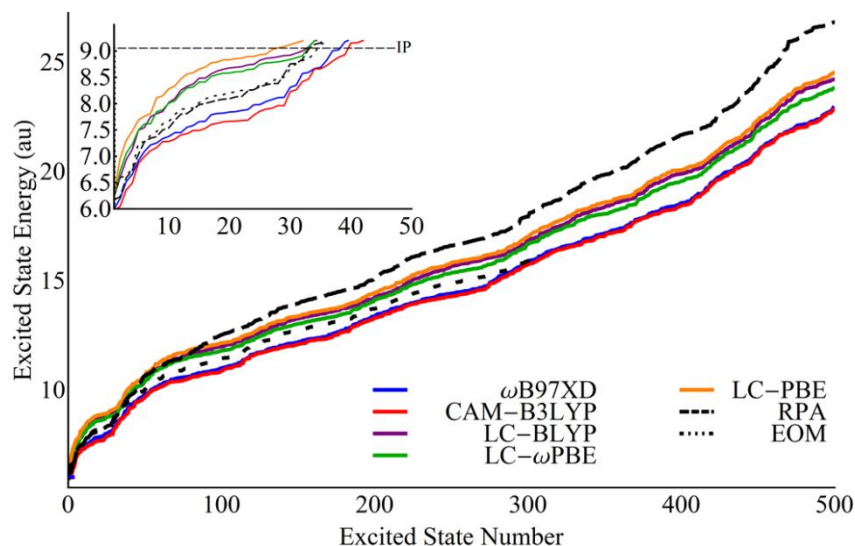


Figure 3-3. Excited state energies for the first 500 states of butadiene calculated by long-range corrected density functionals: ω B97XD (blue), CAM-B3LYP (red), LC-BLYP (purple), LC- ω PBE (green), LC-PBE (orange) using the 6-31 3+ G(d,p) basis set. For comparison EOM-CC (black, dotted) and RPA (black, dashed) energies are included.

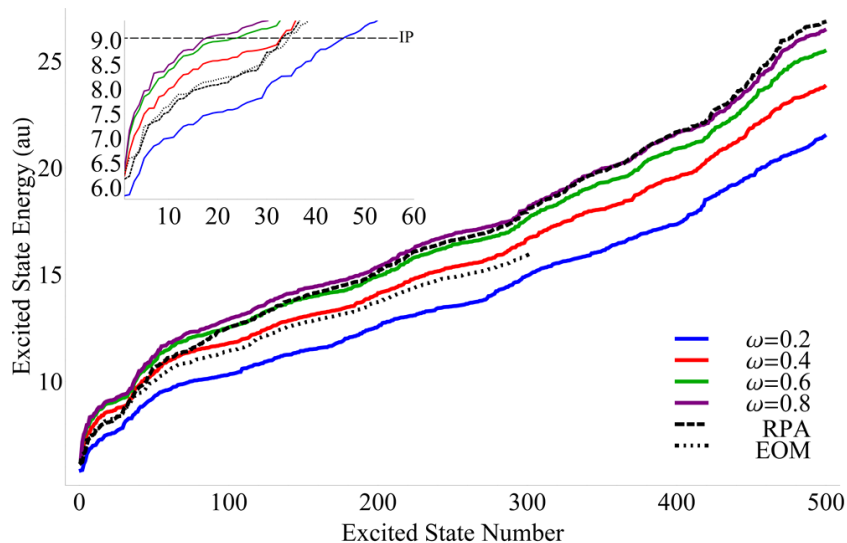


Figure 3-4. Excited state energies for the first 500 states of butadiene, calculated with LC- ω PBE/6-31 3+ G(d,p) and varying the ω -parameter: $\omega = 0.2$ (blue), $\omega = 0.4$ (default; red), $\omega = 0.6$ (green), $\omega = 0.8$ (purple), EOM-CC (black, dotted) and RPA (black, dashed) are included for comparison.

B3LYP 6-31 3+ G(d,p)

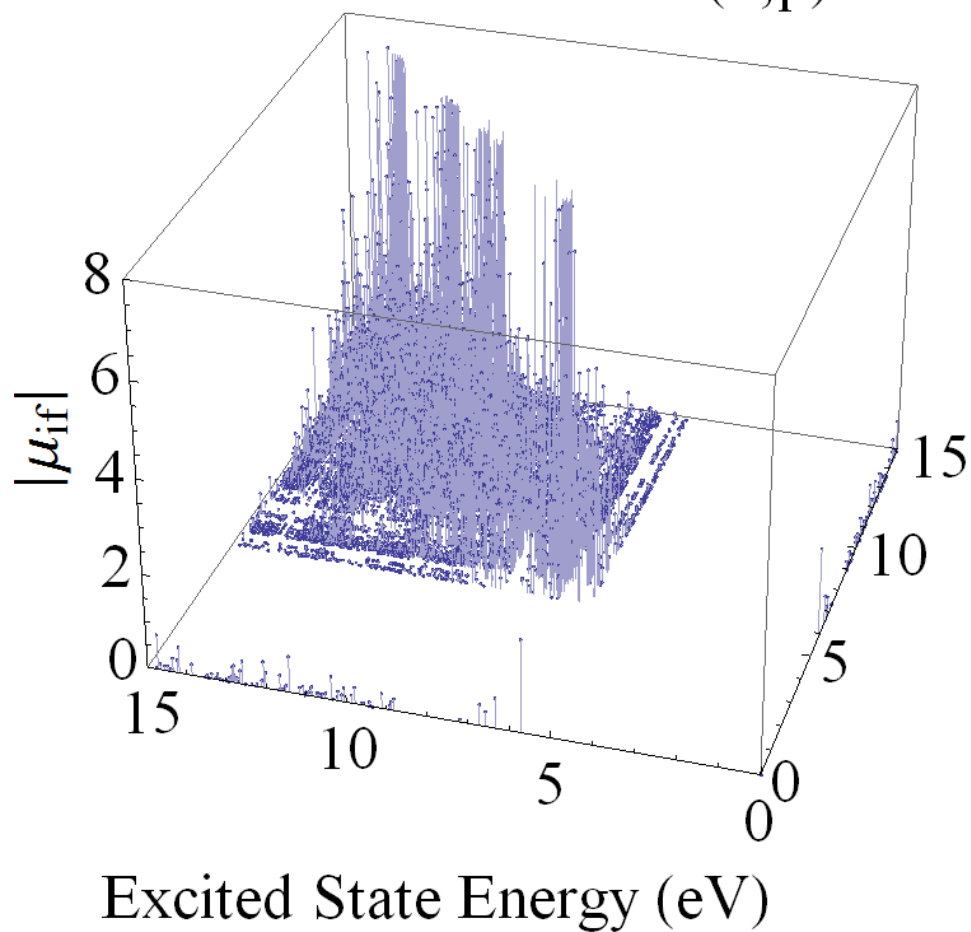


Figure 3-5. Transition dipoles for butadiene calculated with B3LYP/6-31 3+ G(d,p).

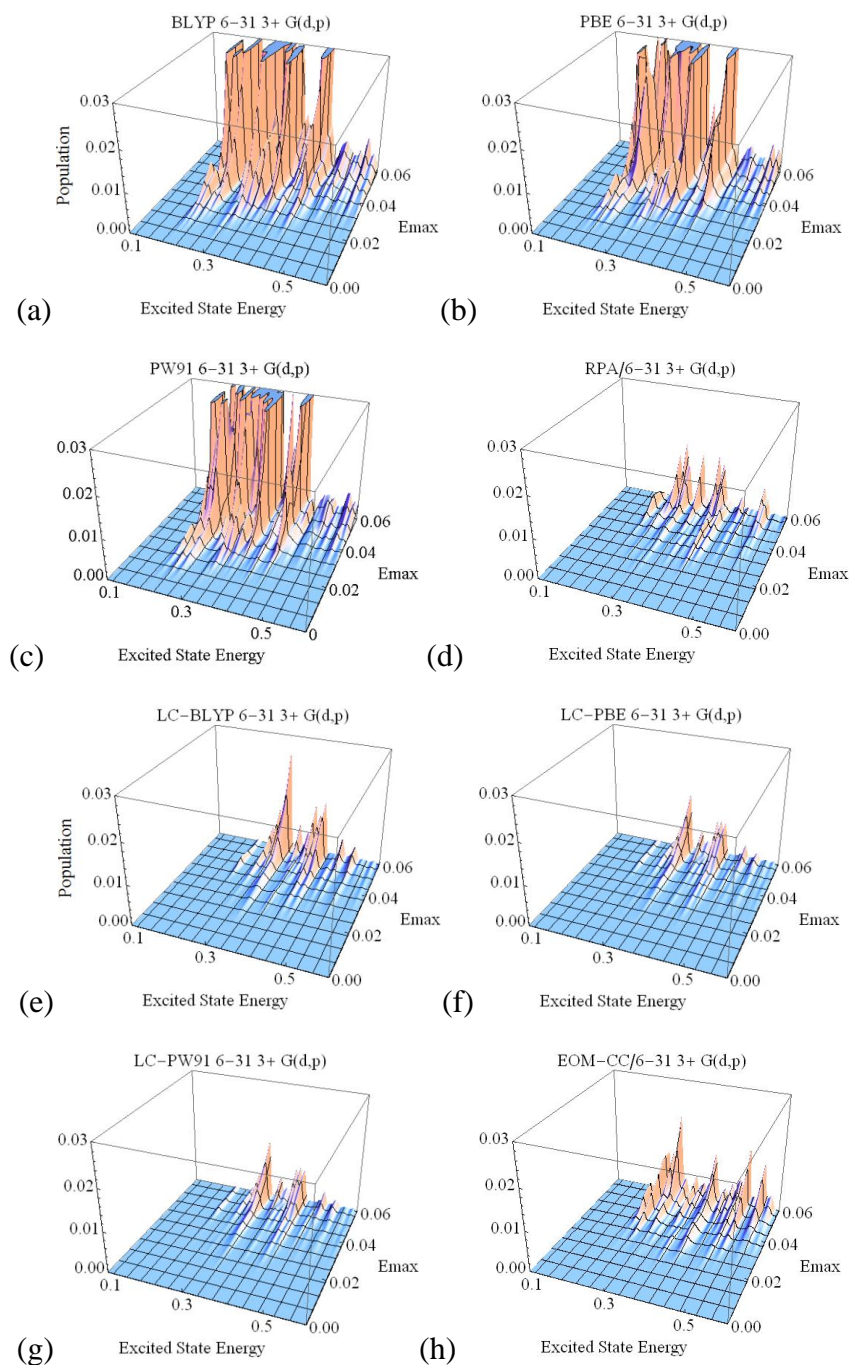


Figure 3-6. Response of butadiene subjected to a three-cycle Gaussian pulse ($\omega=0.06$ au, $E_{\max} = 0-0.06$ au) calculated with the 6-31 3+ G(d,p) basis set, using 500 states for the standard functionals (a) BLYP, (b) PBE, (c) PW91, and their long range corrected counterparts (e) LC-BLYP, (f) LC-PBE, (g) LC-PW91, (d) RPA, and (h) EOM-CC (300 states).

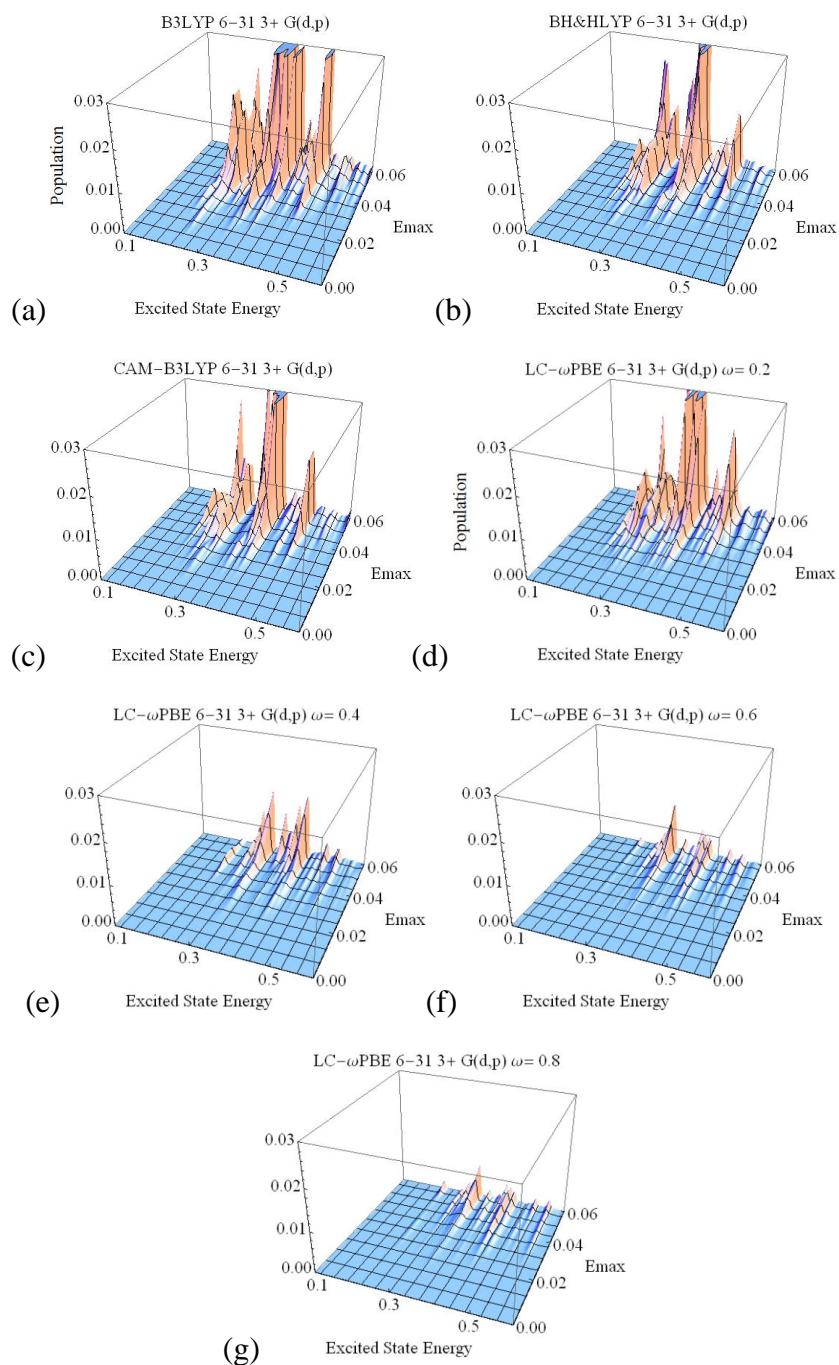


Figure 3-7. Response of butadiene subjected to a three-cycle Gaussian pulse ($\omega=0.06$ au, $E_{\max}=0-0.06$ au) calculated with the 6-31 3+ G(d,p) basis set, using 500 states for (a) B3LYP, (b) BH&HLYP, (c) CAM-B3LYP, and LC- ω PBE with (d) $\omega = 0.2$, (e) $\omega = 0.4$ (default), (f) $\omega = 0.6$, and (g) $\omega = 0.8$.

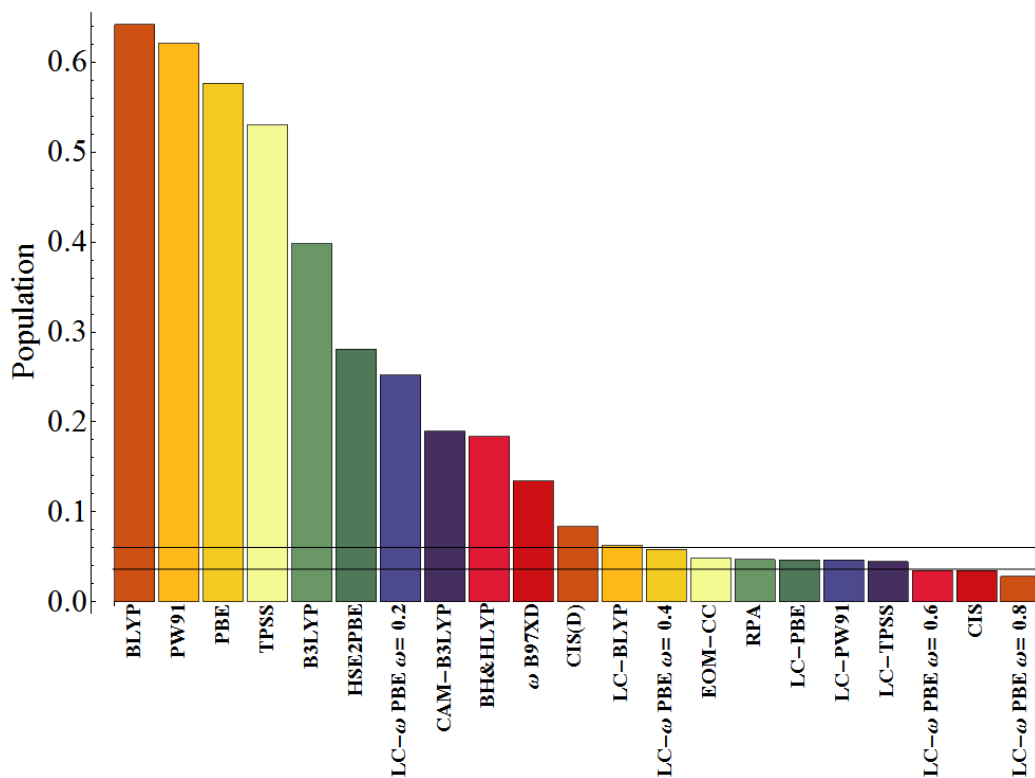


Figure 3-8. Comparison of the sum of the populations of the excited states with energies less than 0.5 au for simulations with DFT functionals and wavefunction based methods using the 6-31 3+ G(d,p) basis and 300 excited states. The horizontal lines represent the population of EOM-CC $\pm 25\%$.

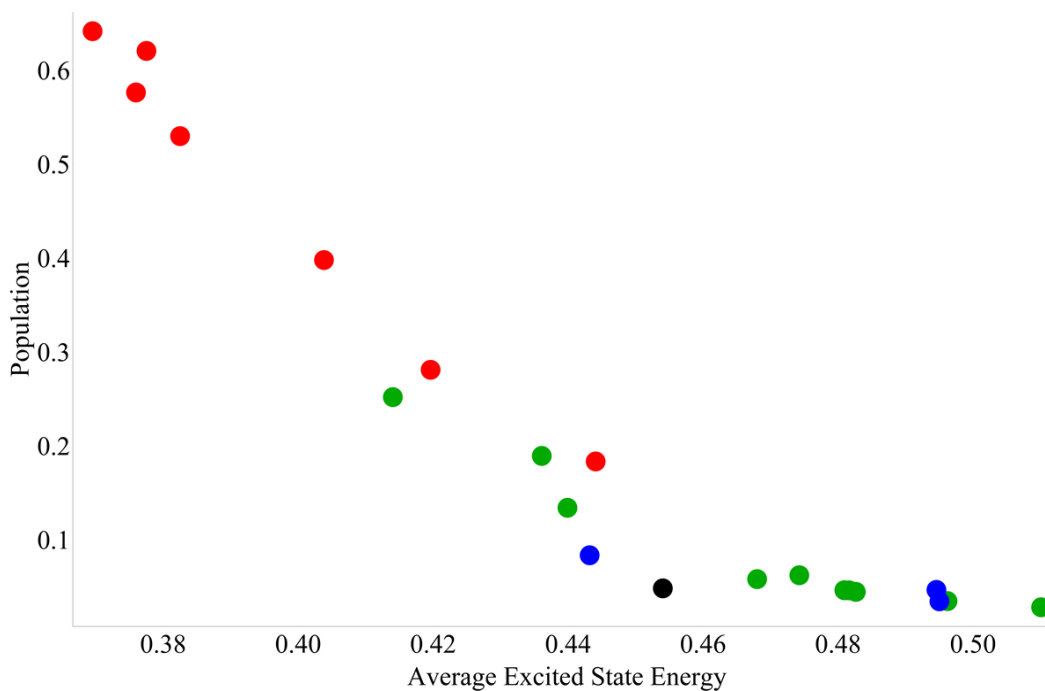


Figure 3-9. Correlation between the average excited state energy and the sum of the population of all excited states after the pulse calculated with the 6-31 3+ G(d,p) basis, $E_{\max} = 0.05$ au and 300 states for the standard DFT functionals (red), long-range corrected functionals (green), wavefunction based methods (blue) and EOM-CC (black). ($R^2=0.89$ for a linear fit and $R^2=0.98$ for a quadratic fit)

Chapter 4

TD-CI Simulation of the Strong-Field Ionization of Polyenes

Jason A. Sonk and H. Bernhard Schlegel*

Department of Chemistry, Wayne State University, Detroit, MI 48202

Reprinted with permission from *J. Phys. Chem. A*, **2012**, 10.1021/jp302389a

Copyright 2011, American Chemical Society.

4.1 Introduction

Our earlier studies¹ on linear polyenes examined the electronic excitation of conjugated molecules by short, intense laser pulses. The amount of nonadiabatic excitation was found to increase with the length of the polyene. In the previous chapters^{2,3} we looked at the number of excited states and the size of the basis set needed in TD-CIS simulations to describe the excited state populations after the laser pulse. We found that a large number of states (~300-500) and a basis set augmented with 3 sets of diffuse functions were needed to model the response to the laser pulse. These studies did not examine ionization. Earlier work from our research group has used time-dependent Hartree-Fock and TD-CIS methods to simulate the response of CO₂, polyenes, and polyacenes and their cations to short, intense laser pulses.^{1,2,4-8} Klamroth, Saalfrank and co-workers⁹⁻¹⁹ have used TD-CI to study dipole switching, pulse shaping, ionization, dephasing and dissipation. In the present work, we will use the TD-CIS approach to

simulate the ionization of a series of polyenes. For few electron systems, grid-based methods with absorbing boundary conditions can be used to calculate accurate ionization rates.²⁰⁻²² Mukamel^{23,24} and co-workers have simulated π electron dynamics in octatetraene with a semiempirical Hamiltonian and have modeled ionization saturation intensities in a multi-electron system in a finite one-dimensional box. For larger systems Klamroth and coworkers¹⁰ have developed a heuristic approach to model ionization using TD-CI and standard atom centered gaussian basis sets. For states above the ionization potential, the ionization rate is assumed to be proportional to the speed of the excited electron divided by a characteristic escape distance. This model is appropriate in the high field case where above-threshold ionization is dominant. Our goal is to see how well this model applies to the ionization rates of a series of linear polyenes and to examine the effect of the basis set size, number of states and escape distance parameter on the ionization rates.

4.2 Methods

Typical molecular electronic structure calculations use atom centered basis functions. Since continuum functions are not usually included in these calculations, the TD-CI simulations cannot model ionization directly. Klamroth and co-workers¹⁰ formulated a heuristic method to model ionization. For states above the ionization potential (IP), the energy is modified by adding an imaginary component $(i/2) \Gamma_n$ to the excited state energy, where Γ_n is the estimated ionization rate for that excited state.

$$\omega_s \rightarrow \omega_s - \frac{i}{2} \Gamma_s \quad (4.1)$$

In the following calculations the Γ_n term was added to states above the experimental IPs listed in Table 4-1. Vertical IPs calculated by UHF and Koopman's theorem are ca 1.1 and 0.2 eV lower, respectively; nevertheless the results using the UHF IPs are similar to those obtained with the experimental IPs. The ionization rate, Γ_n , for a state is obtained by summing contributions from the excited determinants that form the excited state. The ionization rate for an electron in an excited determinant is estimated from the velocity of the electron in the virtual orbital divided by an escape distance parameter, d . In turn the velocity of the electron is proportional to the square root of its orbital energy, ε_a .

$$\Gamma_s = \sum_{i,a} |a_i^a(s)|^2 \frac{\sqrt{\varepsilon_a}}{d} \quad (4.2)$$

where $|a_i^a(s)|^2$ is the probability amplitude for the determinant involving an excitation from orbital i to orbital a describing state s .

The present study uses a linearly polarized and spatially homogeneous external field similar to the ones used previously (see equation 2.12) and the cosine envelope discussed in Chapter 2 (see equation 2.25—2.16)

The CIS calculations were carried out with the development version of the Gaussian software package.²⁵ For this study ethylene, *trans* 1,3-butadiene, all *trans* 1,3,5-hexatriene, and all *trans* 1,3,5,7-octatetraene were optimized at the HF/6-31G(d,p) level of theory. Excited state calculations were carried out with the 6-31 n+ G(d,p) basis set. The 6-31 n+ G(d,p) basis has one set of five d functions on the carbons, one set of p functions on the hydrogens and n sets of diffuse s and p functions on all carbons (n = 1, 2 and 3, with exponent of 0.04380, 0.01095, 0.0027375). Some additional calculations

were carried out with the 6-311++G(2df,2pd) basis set. A 7 cycle cosine pulse with $\omega = 0.06$ au (760 nm) was used in the simulations. The length of the pulse is about 18 fs and the simulation is allowed to run for an additional 6 fs after the pulse. For maximal effect the field was directed along the long axis of the molecule, specifically along the vector connecting the end carbons. Practical considerations in the calculation of excited to excited state transition dipoles limited the simulations to ca 1000 states for butadiene and hexatriene, and 800 states for octatetraene. The total number of singly excited states and the maximum number of states used in the simulations for each molecule are listed in Table 4-1. Mathematica²⁶ was used to integrate the TD-CI equations and analyze the results. The TD-CI integrations were carried out with a step size of 0.05 au (1.2 as).

4.3 Results and Discussion

In the previous chapters² we examined various levels of theory and basis sets to help determine what one should consider when simulating the response of a molecule to an intense laser pulse. For systems which cannot directly model ionization, TD-CIS calculations of butadiene needed up to 500 excited states computed with the 6-31G(d,p) basis set with 3 additional sets of diffuse sp functions to describe the optical response to a 3 cycle, 760 nm pulse with an intensity of ca 10^{14} W cm⁻². In a similar vein, the present chapter looks at the effect of basis set size and the number of states on the ionization rate of a set of linear polyenes using Klamroth's heuristic model.

Table 4-1 lists the linear polyenes used in the present study, along with their experimentally determined ionization potentials. Also indicated in the table are the total number of singly excited states available for a given basis set and the maximum number

used in the simulations. The excited state ionization rates, Γ_n , computed with equation (4.2) and an escape distance parameter of $d = 1$ bohr are shown in Figure 4-1 for ethylene, butadiene, hexatriene and octatetraene. The general trend is Γ_n increases as the energies of the states increase, but there are large fluctuations in the value of Γ_n . The higher energy states usually involve excitation to higher energy virtual orbitals, which result in larger values of Γ_n . However, some of the higher excited states involve excitations from low lying occupied orbitals to low lying virtual orbitals, yield smaller values of Γ_n . Larger basis sets generate more states at lower energy and more low values of Γ_n . Changing the distance parameter shifts these curves up or down by the appropriate factor, but does not change the shape of the plots.

The ionization rate or lifetime of the excited states leads to a broadening of the excited state energies. The energy can be represented by a normalized Lorentzian with a width of Γ_n . Summing over all of the CIS states for a given basis set yields the density of states plots shown in Figure 4-2 for a distance parameter $d = 1$ bohr. The blue, green and red curves correspond to $n = 1, 2, 3$ for the 6-31 $n+ G(d,p)$ basis. The vertical dashed lines indicate the ionization potential and the solid vertical lines are drawn at 20 eV above the ionization potential. For higher energies, the density of states converges nicely into a broad continuum-like feature for all three basis sets for each molecule. Increasing the number of diffuse functions from $n = 1$ to $n = 3$ primarily affects the states within ca 20 eV of the ionization potential, and corresponds to an increasing number of low-lying pseudo-continuum states. For a distance parameter of $d = 10$ bohr (not shown), the widths of the states are reduced by a factor of 10 and more structure is seen in the 10 – 30

eV range. As in the $d = 1$ bohr case, the density of states at higher energies for $d = 10$. is the same for 1, 2 and 3 sets of diffuse functions.

In the heuristic model, the ionization rate depends on three factors. The probability amplitude and the molecular orbital energies are determined by the calculation, but the escape distance parameter d must be determined empirically. The ionization rate Γ_n depends inversely on d . Klamroth and co-workers found the loss of norm of their systems reached a maximum near $d = 1$. Figure 4-3 shows the loss of norm of the population as a function of d for the four linear polyenes with each of the 6-31 n+ G(d,p) basis sets using the maximum number of states listed in Table 4-1. For ethylene the peak in the loss of norm is near $d = 1$. For the longer polyenes, the peak becomes broader, extending to larger values of d , corresponding to smaller values of Γ_n .

The trends in Figure 4-3 can be understood by using perturbation theory to describe the time-dependent behavior of a simple two state problem. Let the lower state have an energy of 0, the upper state and energy of $\omega - i \Gamma/2$. If a perturbation causes the states to interact, the loss of population depends on $\text{Im}(1/(\omega - i \Gamma/2)) = (\Gamma/2) / (\omega^2 + (\Gamma/2)^2)$ as well as on the magnitude of the perturbation. The loss of population is proportional to Γ for small values of Γ , reaches maximum for $\Gamma/2 = \omega$, and goes to zero for large Γ . Thus, the maximum ionization rate for given state occurs when $\Gamma_n/2$ is equal to the excitation energy of the state. Ethylene has relatively few states that interact with the ground state under the influence of the laser field, and strong ionization occurs near $d = 1$. For longer polyenes, there are more states that interact with the ground state. Since these states are lower in energy for longer polyenes, smaller values of Γ_n and hence larger

values of d will also cause strong ionization. Because all of the polyenes ionize strongly for $d = 1$, this is the primary value used for additional analyses.

Figure 4-4 shows the 7 cycle 760 nm cosine pulse and the time evolution of the norm of the wavefunctions for ethylene, butadiene, hexatriene and octatetraene during the pulse. The norm of ethylene decreases the least, reaching ca 0.30 by the end of the pulse, while the norm for octatetraene decreases nearly to zero by after the maximum in the pulse. The instantaneous ionization rate shown in Figure 4-4(c) can be obtained from the derivative of the norm with respect to time. Alternatively, the instantaneous ionization rate can be calculated by multiplying the value of Γ_n for a state by its population and summing over all of the states. Early in the pulse, when the intensities are low, it is already apparent that the ionization rate is greatest for octatetraene and least for ethylene. Toward the end of the pulse, the ionization rate for ethylene is still significant whereas the rate for octatetraene is nearly zero. This reversal of the trend in the instantaneous rates is because the population of octatetraene is very small during the last few cycles of the pulse but the population of ethylene is still fairly large.

Inspection of the ionization rates for the individual states provides some insight into the dependence of the total ionization rate on the escape distance parameter. Instantaneous ionization rates for ethylene and hexatriene are shown in Figure 4-5 as a function of state energy and time. As expected, the populations of the excited states and hence ionization rates for these states peak when the laser field peaks and the polarization of the electronic distribution is the greatest. For each of the polyenes, the ionization is dominated by a relatively small number of excited states in the range of 0 – 20 eV above the IP. There are many more states in this range that contribute only weakly to the

ionization but are needed to treat the polarization of the electron cloud in the simulation. Even for calculations of the static polarizability in the sum-over-states formalism, states up to 20 eV above the IP are needed to get within 3% of the correct value.

The contribution of an individual state to the total ionization can be obtained by integrating its instantaneous ionization rate over the duration of the pulse. Figure 4-6 compares the results for $d = 1$ and $d = 10$ bohr for ethylene and hexatriene. For ethylene, the same states contribute to the total ionization $d = 1$ and $d = 10$ bohr. The values are smaller for the latter but the ratios are nearly the same. In the case of hexatriene, many states in the 10 – 30 eV range are involved in the ionization process for $d = 1$ bohr. For $d = 10$ bohr, the distribution is shifted toward lower energies and the contributions from these states are larger than for $d = 1$. This is in keeping with the analysis of the two state system discussed above. A larger value of d yields smaller Γ 's. Since the maximum ionization rate occurs when $\omega = \Gamma/2$, lower energy states contribute more when the Γ 's are smaller. Because hexatriene and octatetraene have more low energy states than ethylene and butadiene, ionization as a function of the escape distance d , shown in Figure 4-3, is much broader for the longer polyenes.

Figure 4-7 shows the calculated loss of norm of the TD-CIS wavefunction for each of the linear polyenes after a 7 cycle 760 nm cosine pulse with intensities up to 3.51×10^{14} W cm^{-2} (field strengths up to 0.10 au) for a distance parameter of $d = 1$ bohr. The effect of varying the number of states used in the simulation is examined in Figure 4-7(a) for butadiene with the 6-31 1+ G(d,p) basis set. Compared to the results with all 957 CIS excited states, the norm of wavefunction after the laser pulse is well represented with as few as 250 states. This corresponds to including all states that are within 20 eV of the IP.

Using only 150 states corresponds to using all the states up to ~ 19.5 eV (only 10.5 eV above the IP); doing so neglects strong contributions toward ionization from states in the in the 20-30 eV range (10-20 eV above the IP). The overall contributions from a few states in this 20-30 eV range can be quite large as can be seen in Figure 4-6. Adding more polarization functions (e.g. 6-311++G(2df,2pd) basis) has little effect on the ionization rate of butadiene (not shown). Figure 4-7(b) --- Figure 4-7(d) show the effect of diffuse functions on the loss of norm for the polyenes. With ca 1000 states, the results for butadiene and hexatriene are very similar with 1, 2 and 3 sets of diffuse functions. This indicates that ionization with Klamroth's heuristic model is not as sensitive to diffuse functions as the optical response in the absence of ionization.² For octatetraene some basis set effects can be seen. At low field strengths, the ionization rate diminishes as the number of diffuse functions is increased. However, it is not the presence of diffuse function that decreases the ionization rate, but rather the absence of higher energy states. With the 6-31 n+ G(d,p) basis, a choice of 800 states includes all excitations up to 24, 13 and 9 eV above the IP for n = 1, 2 and 3 sets of diffuse functions, respectively (compare with Figure 1(d)). Adding more diffuse functions increases the number of low energy excited states, thereby decreasing the maximum excitation energy attainable within the lowest 800 states. For the 6-31 3+ basis set, the ionization rate at small field strengths is too low because too few high energy, rapidly ionizing states are included within the set of the 800 states. Nevertheless, for $E_{\max} \geq 0.05$ au, all three basis set yield complete ionization of octatetraene by the 7 cycle 760 nm pulse.

Figure 4-8 summarizes the ionization of ethylene, butadiene, hexatriene and octatetraene as a function of the intensity for a 7 cycle 760 nm cosine pulse. At high

intensities, each of the polyenes is ionized completely by the pulse. At lower intensities, the fraction ionized is largest for octatetraene and least for ethylene, as could be anticipated qualitatively from the trend in the ionization potentials. Experimental ionization saturation intensities, I_{sat} , have been measured for a number of saturated and unsaturated hydrocarbons. Corkum and coworkers^{27,28} were able to determine $I_{\text{sat}} = 89 \times 10^{12} \text{ W cm}^{-2}$ for hexatriene and $I_{\text{sat}} = 110 \times 10^{12} \text{ W cm}^{-2}$ for ethylene. Our calculations yield strong ionizations in the right order of magnitude of intensities: 10^{12} to $10^{14} \text{ W cm}^{-2}$. However, it is not possible to compare the computed ionization rates directly with experiment. The distance parameter is empirical and has a large effect on the ionization rate. Only one orientation was used in the calculation rather than averaging over all orientations. The longer polyenes can have several conformations, but the calculations were only for the all-trans conformation. Other variables such as pulse length and shape also affect the degree of ionization.

Some of the difficulties associated with comparing the calculations and experiment can be circumvented by examining the ratios of intensities. For our 7 cycle cosine pulse, the field strengths that cause a 50% decrease in the population are 0.026 au for ethylene, 0.020 au for butadiene, 0.017 au for hexatriene and 0.015 au for octatetraene with the 6-31 1+ G(d,p) basis set and a distance parameter of $d = 1$ bohr. The ratios of intensities relative to ethylene are 0.61 for butadiene, 0.44 for hexatriene and 0.35 for octatetraene. Similar ratios are found for 75% decrease in the population and for 2 and 3 sets of diffuse functions (except for octatetraene, which would require more states for the TD-CIS simulation with 2 and 3 sets of diffuse functions, as noted above). However, the ratio for hexatriene to ethylene is significantly smaller than the ratio of 0.81 for the experimental

I_{sat} values. In the present calculations, the molecules are aligned to the laser field, possibly increasing the difference in the ionization rates.

For rare gas atoms and ions, ADK theory^{29,30} provides a good description of the dependence of the ionization rate on the ionization potential. It is known, however, that in certain cases ADK theory fails to predict correct saturation intensities for laser pulses at 800nm and shorter wavelengths because of interference effects.³¹ To circumvent these and related limitations of ADK, we compare only the ratios of the ionization rates. The ratios of ionization rates relative to ethylene computed by ADK theory are 0.59 for butadiene, 0.45 for hexatriene and 0.34 for octatetraene when integrated over the same pulse shape. The ionization rates obtained from the TD-CIS simulations compare very well with these ratios, indicating that the heuristic ionization model recovers the correct trend in dependence of the ionization rates on the ionization potentials. However, the TD-CIS simulations with the heuristic ionization model predict a much slower rise in the fraction ionized as the intensity increases. The heuristic model also leads to a much higher ionization rate at low intensities than expected from ADK. This is likely due to the fact that the heuristic approach assumes an above-threshold model for ionization whereas ADK is based on tunneling. The heuristic model for ionization in TD-CI simulations depends on only the energies of the virtual orbitals. A more sophisticated model would also take into account the shape of the orbitals and the direction of the field.

4.4 Conclusions

The heuristic approach developed by Klamroth and co-workers provides a satisfactory method for modeling the trends in ionization rates of short linear polyenes.

The ionization rate is sensitive to the escape distance parameter, and a value of $d = 1$ bohr was found suitable for ethylene, butadiene, hexatriene and octatetraene. In contrast to earlier work on modeling the optical response of polyenes to an intense pulse, ionization with Klamroth's model is less sensitive to the basis set size. The 6-31G(d,p) basis set augmented with a single set of diffuse functions on the carbon atoms yields results similar to calculations with three sets of diffuse functions. TD-CIS calculations also depend on the number of excited states used in the simulation. For the pulse parameters considered, consistent results for the ionization of linear polyenes were found using all states up to ca 20 eV above the IP. Although this method does not yield ionization rates that can be compared directly with experiment, ratios of the calculated ionization rates are in good agreement with the ratios predicted by the ADK model.

4.5 References

- (1) Smith, S. M.; Li, X. S.; Markevitch, A. N.; Romanov, D. A.; Levis, R. J.; Schlegel, H. B. A numerical simulation of nonadiabatic electron excitation in the strong field regime: Linear polyenes, *J. Phys. Chem. A* **2005**, *109*, 5176.
- (2) Sonk, J. A.; Caricato, M.; Schlegel, H. B. TD-CI Simulation of the Electronic Optical Response of Molecules in Intense Fields: Comparison of RPA, CIS, CIS(D), and EOM-CCSD, *J. Phys. Chem. A* **2011**, *115*, 4678.
- (3) Sonk, J. A.; Schlegel, H. B. TD-CI Simulation of the Electronic Optical Response of Molecules in Intense Fields II: Comparison of DFT Functionals and EOM-CCSD, *J. Phys. Chem. A* **2011**, *115*, 11832.
- (4) Li, X. S.; Smith, S. M.; Markevitch, A. N.; Romanov, D. A.; Levis, R. J.; Schlegel, H. B. A time-dependent Hartree-Fock approach for studying the electronic optical response of molecules in intense fields, *Phys. Chem. Chem. Phys.* **2005**, *7*, 233.
- (5) Smith, S. M.; Li, X. S.; Markevitch, A. N.; Romanov, D. A.; Levis, R. J.; Schlegel, H. B. Numerical simulation of nonadiabatic electron excitation in the strong field regime. 2. Linear polyene cations, *J. Phys. Chem. A* **2005**, *109*, 10527.
- (6) Smith, S. M.; Li, X. S.; Markevitch, A. N.; Romanov, D. A.; Levis, R. J.; Schlegel, H. B. Numerical simulation of nonadiabatic electron excitation in the strong-field regime. 3. Polyacene neutrals and cations, *J. Phys. Chem. A* **2007**, *111*, 6920.
- (7) Smith, S. M.; Romanov, D. A.; Heck, G.; Schlegel, H. B.; Levis, R. J. Observing the Transition from Stark-Shifted, Strong-Field Resonance to Nonadiabatic Excitation, *J. Phys. Chem. C* **2010**, *114*, 5645.

- (8) Smith, S. M.; Romanov, D. A.; Li, X. S.; Sonk, J. A.; Schlegel, H. B.; Levis, R. J. Numerical Bound State Electron Dynamics of Carbon Dioxide in the Strong-Field Regime, *J. Phys. Chem. A* **2010**, *114*, 2576.
- (9) Klamroth, T. Optimal control of ultrafast laser driven many-electron dynamics in a polyatomic molecule: N-methyl-6-quinolone, *J. Chem. Phys.* **2006**, *124*, 144310.
- (10) Klinkusch, S.; Saalfrank, P.; Klamroth, T. Laser-induced electron dynamics including photoionization: A heuristic model within time-dependent configuration interaction theory, *J. Chem. Phys.* **2009**, *131*, 114304.
- (11) Krause, P.; Klamroth, T. Dipole switching in large molecules described by explicitly time-dependent configuration interaction, *J. Chem. Phys.* **2008**, *128*, 234307.
- (12) Krause, P.; Klamroth, T.; Saalfrank, P. Time-dependent configuration-interaction calculations of laser-pulse-driven many-electron dynamics: Controlled dipole switching in lithium cyanide, *J. Chem. Phys.* **2005**, *123*, 74105.
- (13) Krause, P.; Klamroth, T.; Saalfrank, P. Molecular response properties from explicitly time-dependent configuration interaction methods, *J. Chem. Phys.* **2007**, *127*, 034107.
- (14) Nest, M.; Klamroth, T.; Saalfrank, P. The multiconfiguration time-dependent Hartree-Fock method for quantum chemical calculations, *J. Chem. Phys.* **2005**, *122*, 124102.
- (15) Tremblay, J. C.; Klamroth, T.; Saalfrank, P. Time-dependent configuration-interaction calculations of laser-driven dynamics in presence of dissipation, *J. Chem. Phys.* **2008**, *129*, 084302.

- (16) Tremblay, J. C.; Klinkusch, S.; Klamroth, T.; Saalfrank, P. Dissipative many-electron dynamics of ionizing systems, *J. Chem. Phys.* **2011**, *134*, 044311.
- (17) Tremblay, J. C.; Krause, P.; Klamroth, T.; Saalfrank, P. Time-dependent response of dissipative electron systems, *Phys. Rev. A* **2010**, *81*, 063420.
- (18) Huber, C.; Klamroth, T. Explicitly time-dependent coupled cluster singles doubles calculations of laser-driven many-electron dynamics, *J. Chem. Phys.* **2011**, *134*, 054113.
- (19) Klinkusch, S.; Klamroth, T.; Saalfrank, P. Long-range intermolecular charge transfer induced by laser pulses: an explicitly time-dependent configuration interaction approach, *Phys. Chem. Chem. Phys.* **2009**, *11*, 3875.
- (20) Riss, U. V.; Meyer, H. D. Calculation of Resonance Energies and Widths Using the Complex Absorbing Potential Method, *J. Phys. B-At. Mol. Opt. Phys.* **1993**, *26*, 4503.
- (21) Neuhauser, D.; Baer, M.; Judson, R. S.; Kouri, D. J. The Application of Time-Dependent Wavepacket Methods to Reactive Scattering, *Comput. Phys. Commun.* **1991**, *63*, 460.
- (22) Muga, J. G.; Palao, J. P.; Navarro, B.; Egusquiza, I. L. Complex absorbing potentials, *Phys. Rep.-Rev. Sec. Phys. Lett.* **2004**, *395*, 357.
- (23) Suzuki, M.; Mukamel, S. Charge and bonding redistribution in octatetraene driven by a strong laser field: Time-dependent Hartree-Fock simulation, *J. Chem. Phys.* **2003**, *119*, 4722.

- (24) Suzuki, M.; Mukamel, S. Many-body effects in molecular photoionization in intense laser fields; time-dependent Hartree-Fock simulations, *J. Chem. Phys.* **2004**, *120*, 669.
- (25) Frisch, M. J.; Trucks, G. W.; Schlegel, H. B.; Scuseria, G. E.; Robb, M. A.; Cheeseman, J. R.; Montgomery, J. A.; Vreven, T.; Kudin, K. N. *Gaussian Development Version*; et al.; Revision H.13; Gaussian, Inc.; Wallingford, CT; 2010.
- (26) Mathematica. *Mathematica*; 8.0; Wolfram Research, Inc.; Champaign, IL; 2010.
- (27) Hankin, S. M.; Villeneuve, D. M.; Corkum, P. B.; Rayner, D. M. Intense-field laser ionization rates in atoms and molecules, *Phys. Rev. A* **2001**, *64*, 013405.
- (28) Hankin, S. M.; Villeneuve, D. M.; Corkum, P. B.; Rayner, D. M. Nonlinear Ionization of Organic Molecules in High Intensity Laser Fields, *Phys. Rev. Lett.* **2000**, *84*, 5082.
- (29) Ammosov, M. V.; Delone, N. B.; Krainov, V. P. Tunnel ionization of complex atoms and of atomic ions in an alternating electromagnetic field, [*Zh. Eksp. Teor. Fiz.* **1986**, *91*, 2008], *Sov. Phys. JETP* **1986**, *64*, 1191.
- (30) Tong, X. M.; Zhao, Z. X.; Lin, C. D. Theory of molecular tunneling ionization, *Phys. Rev. A* **2002**, *66*, 033402.
- (31) Dura, J.; Gruen, A.; Bates, P. K.; Teichmann, S. M.; Ergler, T.; Senftleben, A.; Pfluger, T.; Schroter, C. D.; Moshhammer, R.; Ullrich, J.; Jaron-Becker, A.; Becker, A.; Biegert, J. Wavelength Dependence of the Suppressed Ionization of Molecules in Strong Laser Fields, *J. Phys. Chem. A* **2012**, *116*, 2662.

(32) Lias, S. G. "Ionization Energy Evaluation" in *NIST Chemistry WebBook*, *NIST Standard Reference Database Number 69*; National Institute of Standards and Technology: Gaithersburg, MD, 2010.

(33) Franklin, J. L.; Carroll, S. R. Effect of Molecular Structure on Ionic Decomposition .2. An Electron-Impact Study of 1,3- and 1,4-Cyclohexadiene and 1,3,5-Hexatriene, *J. Am. Chem. Soc.* **1969**, *91*, 6564.

(34) Jones, T. B.; Maier, J. P. Study of the Radical Cation of All Trans-1,3,5,7-Octatetraene by its Emission, $\tilde{A}^2\text{Au} \rightarrow \tilde{X}^2\text{Bg}$, and by Photoelectron-Spectroscopy, *Int. J. Mass Spectrom. Ion Process.* **1979**, *31*, 287.

Table 4-1. Linear polyenes used in the current study, their experimentally determined ionization potentials, total number of CIS excited states, and maximum number of states used in the current study.

	Experimental ionization potential (eV)	Total number of CIS states for the 6-31 n+ G(d,p) basis			Maximum number of excited states used for 6-31 n+ G(d,p)		
		n=1	n=2	n=3	n=1	n=2	n=3
ethylene	10.5138 ³²	288	336	378	288	336	378
butadiene	9.072 ³²	957	1111	1254	957	999	999
hexatriene	8.42 ³³	2016	2320	2592	999	999	999
octatetraene	7.79 ³⁴	3465	3969	4431	800	800	800

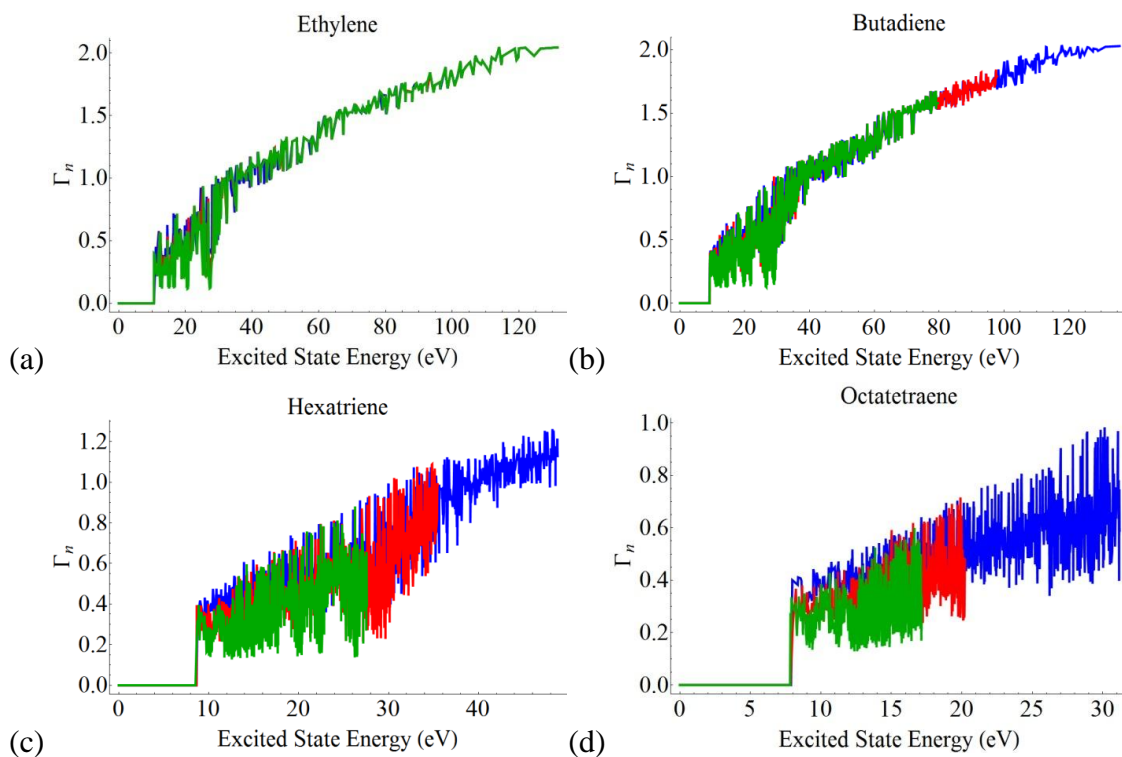


Figure 4-1. Ionization rates for the excited states of (a) ethylene, (b) butadiene, (c) hexatriene, and (d) octatetraene, using the 6-31 1+ G(d,p) (blue), 6-31 2+ G(d,p) (red), and 6-31 3+ G(d,p) (green) basis sets and a distance parameter of $d = 1$ bohr in Equation (4-2).

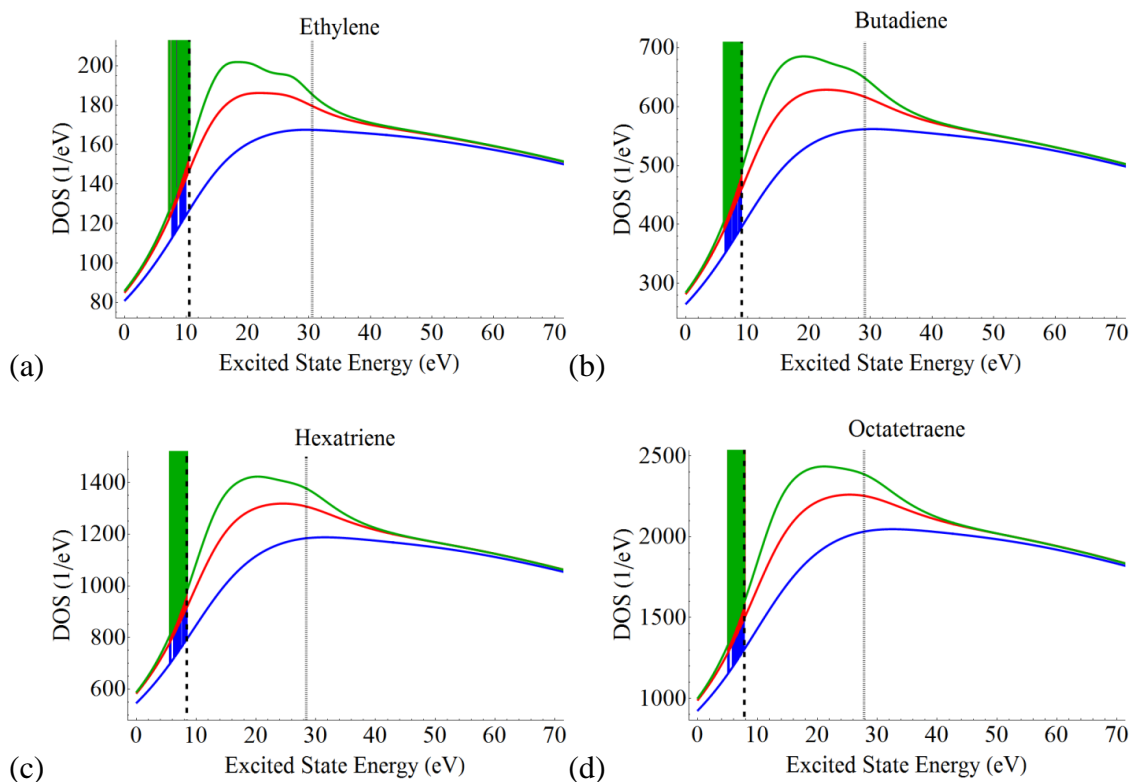


Figure 4-2. Density of states for (a) ethylene, (b) butadiene, (c) hexatriene, (d) octatetraene, found using the 6-31 1+ G(d,p) (blue), 6-31 2+ G(d,p) (red), and 6-31 3+ G(d,p) (green) basis sets, all CIS excited states, and a distance parameter $d = 1$ bohr.

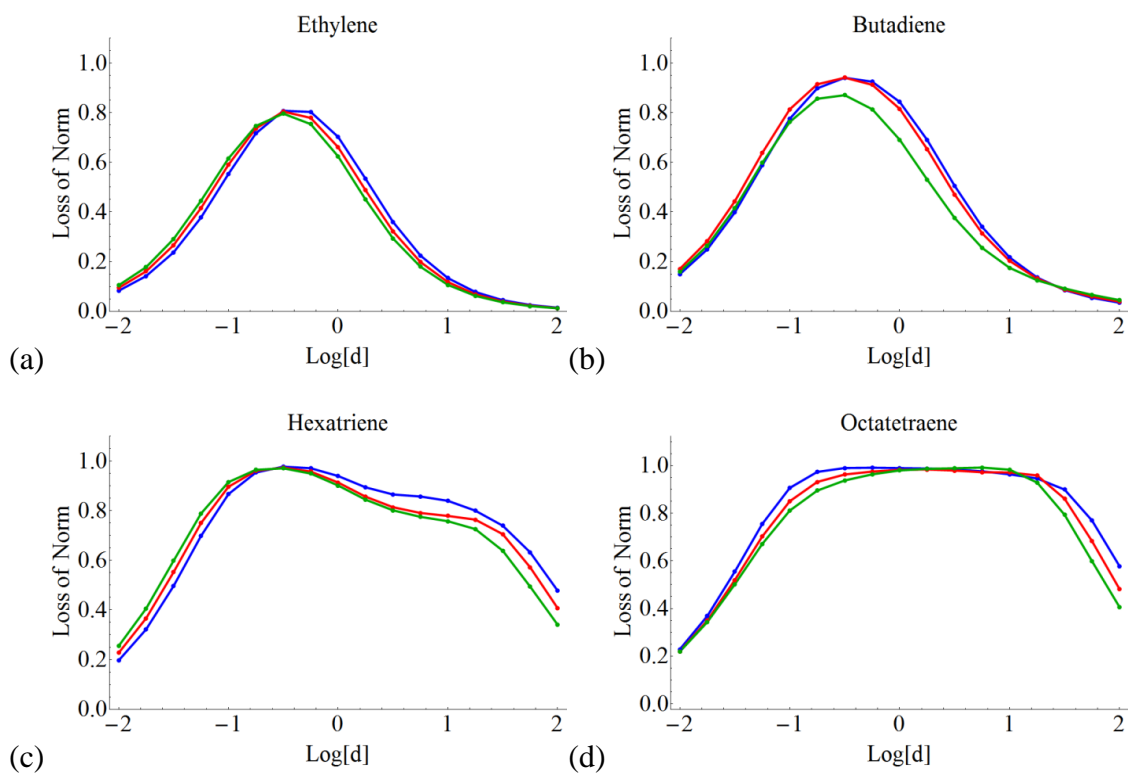


Figure 4-3. Loss of norm as a function of the distance parameter d (in bohr) for (a) ethylene, (b) butadiene, (c) hexatriene, and (d) octatetraene, using the 6-31 1+ G(d,p) (blue), 6-31 2+ G(d,p) (red), and 6-31 3+ G(d,p) (green) basis sets for $E_{\text{max}} = 0.05$ au.

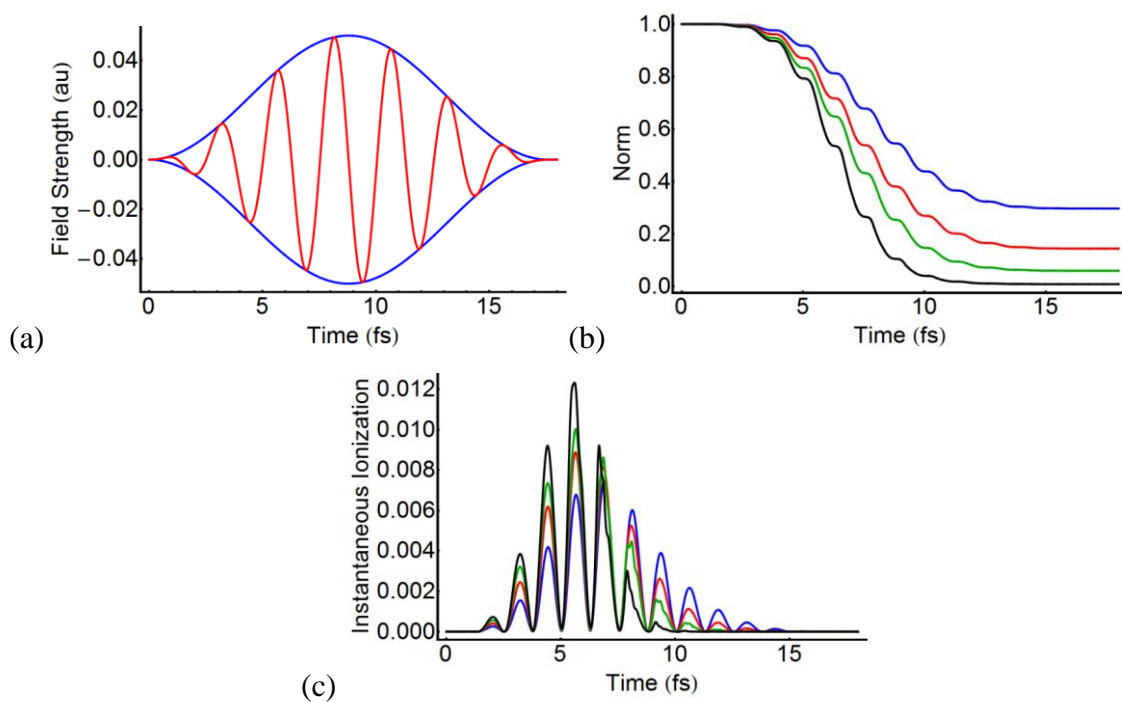


Figure 4-4. (a) Electric field for a seven cycle 760 nm cosine pulse with intensity of $0.88 \times 10^{14} \text{ W cm}^{-2}$ ($E_{\text{max}} = 0.05 \text{ au}$), (b) time evolution of the wavefunction norm during the pulse and (c) instantaneous ionization rate for ethylene (blue), butadiene (red), hexatriene (green) and octatetraene (black) with a distance parameter $d = 1 \text{ bohr}$ using the 6-31 1+ G(d,p) basis set.

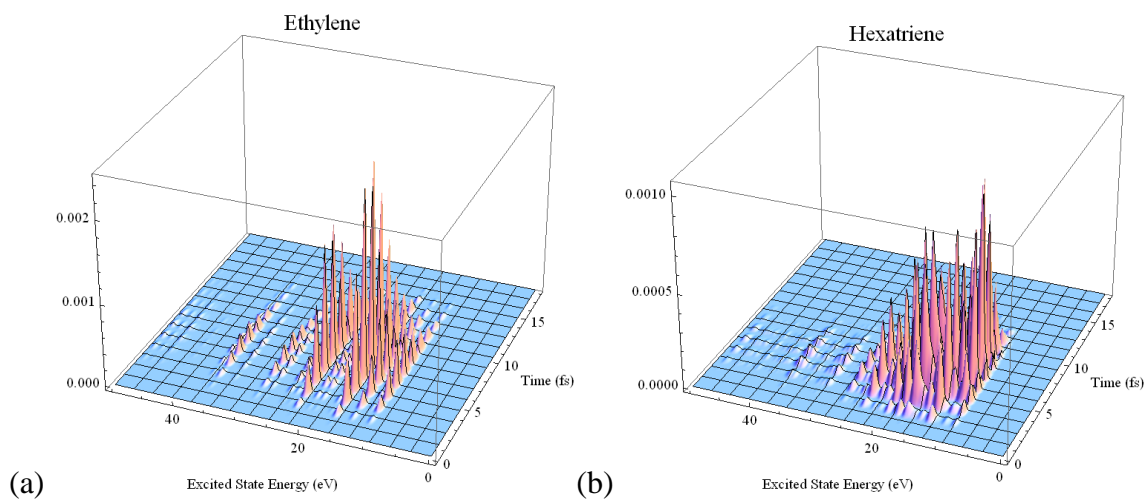


Figure 4-5. Instantaneous ionization rates as a function of state number and time for (a) ethylene and (b) hexatriene. The simulations used a 7 cycle 760 nm cosine pulse with $E_{\max} = 0.05$ atomic units, and employed a distance parameter $d = 1$ bohr, 288 excited states for ethylene and 999 excited states for hexatriene computed with the 6-31 1+ G(d,p) basis.

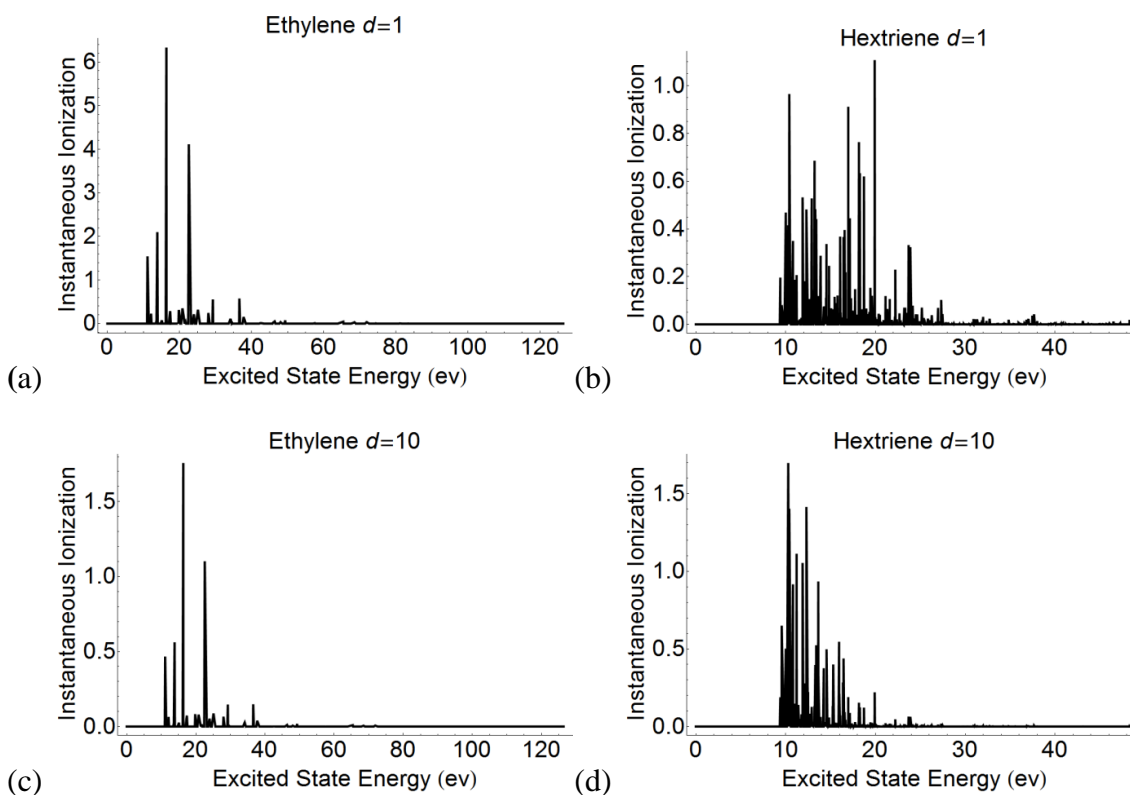


Figure 4-6. Contributions of individual states to the loss of norm for (a) ethylene with escape distance parameter $d = 1$ bohr, (b) hexatriene with $d = 1$ bohr, (c) ethylene with $d = 10$ bohr and (d) hexatriene with $d = 10$ bohr. The simulations used a 7 cycle 760 nm cosine pulse with $E_{\max} = 0.05$ atomic units, and employed 288 excited states for ethylene and 999 excited states for hexatriene computed with the 6-31 1+ G(d,p) basis.

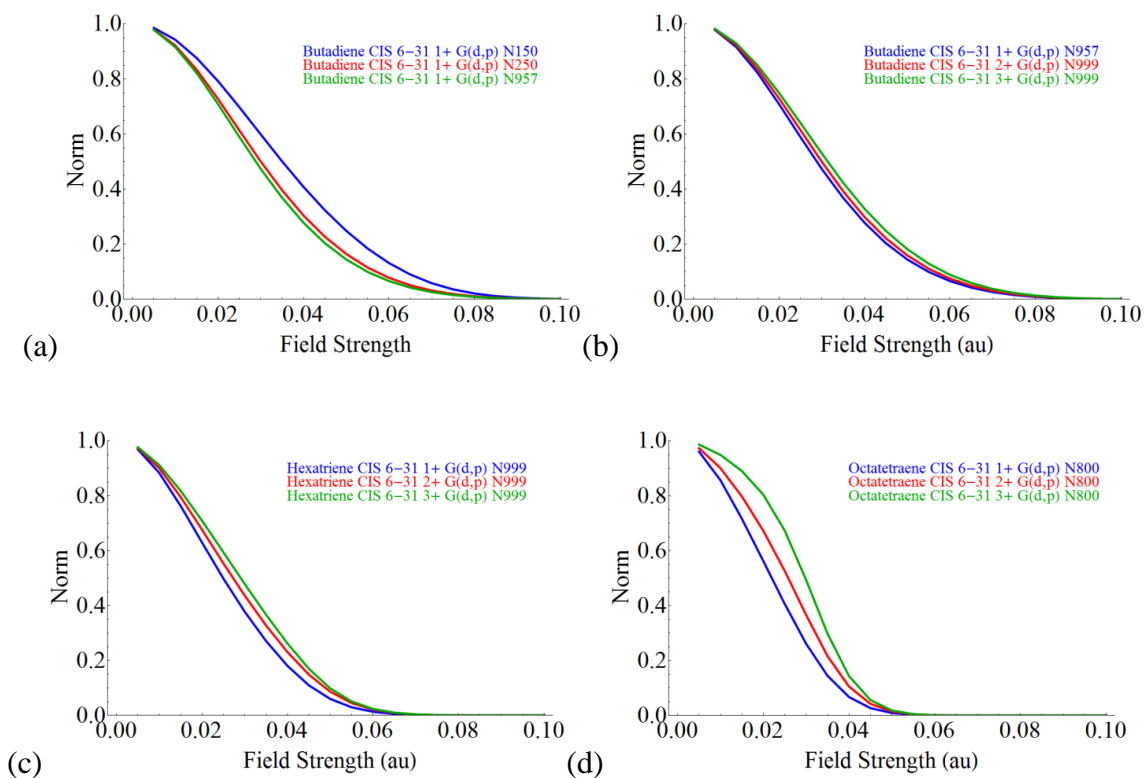


Figure 4-7. Effect of basis set size and number of states on the wavefunction norm after the pulse as a function of field strength for (a) butadiene with the 6-31 1+ G(d,p) basis set and 150 states (blue), 250 states (red), and all 957 CIS excited states (green), (b) butadiene, (c) hexatriene and (d) octatetraene with 6-31 1+ G(d,p), 6-31 2+ G(d,p) and 6-31 3+ G(d,p) basis sets (blue, red and green, respectively) with $d = 1$ bohr.

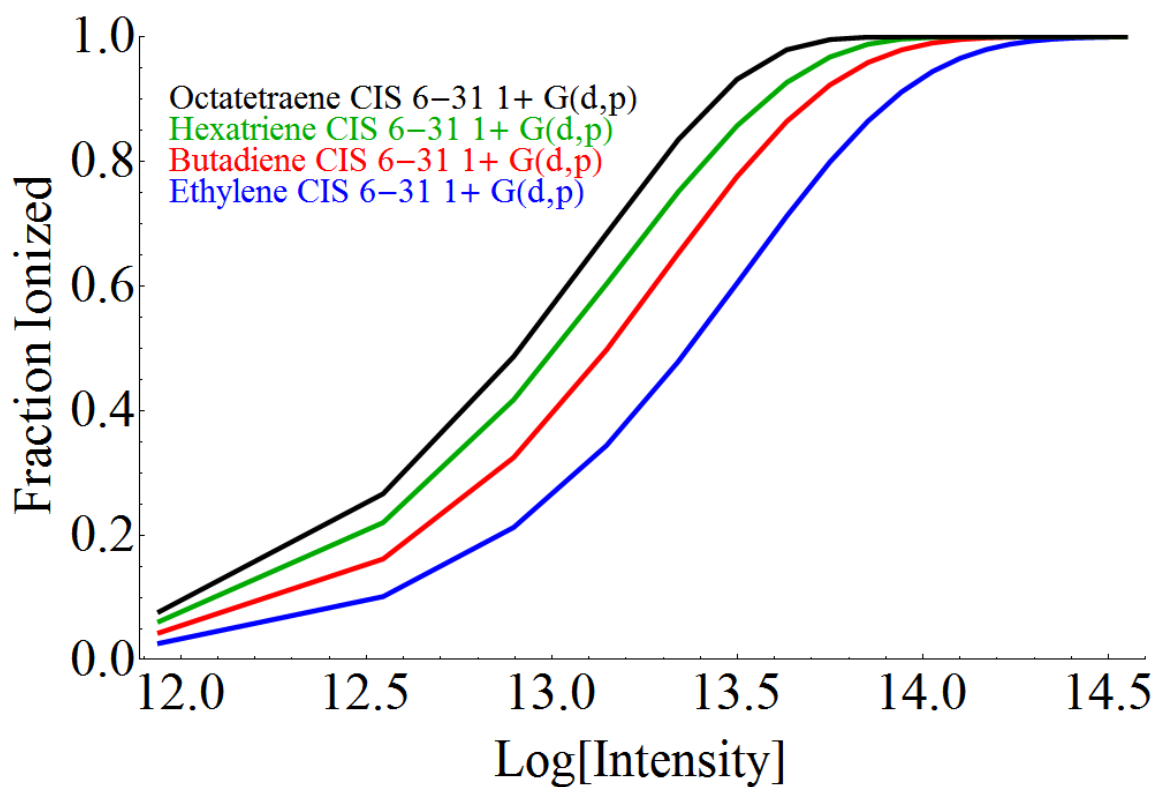


Figure 4-8. Fraction of population ionized by the pulse as a function of the intensity (W/cm^2) for ethylene (blue), butadiene (red), hexatriene (green), octatetraene (black) calculated using the 6-31 1+ G(d,p) basis set and $d = 1$ bohr.

Chapter 5

Theoretical Studies of Metal Complexes Derived from the Chiral Tripyridyldiamine Ligand Bn-CDPy3

Ahmed I. Abouelatta, Jason A. Sonk, Mirvat M. Hammoud, Danielle M. Zurcher, Joshua
J. McKamie, H. Bernhard Schlegel, and Jeremy J. Kodanko*

Department of Chemistry, Wayne State University, Detroit, Michigan 48202

With permission, adapted from:

Inorg. Chem., **2010**, 49 (11), pp 5202–5211

Copyright 2010, American Chemical Society.

5.1 Introduction

The transfer of chirality from an asymmetric ligand to a metal center has been an important and long-standing principle of coordination chemistry. Due to their ability to create an asymmetric environment around the metal center, chiral ligands have been used extensively in asymmetric synthesis and catalysis, as well as supramolecular chemistry. The ability to predict and control the coordination geometry of a ligand when bound to a metal center is certainly an important aspect of this chemistry, because the geometry can dictate the shape of the molecule and the asymmetric environment around the metal center.¹ Chirality can be introduced into a ligand by using building blocks that contain planar chiral or stereogenic centers. Of the various building blocks available, trans-1,2-diaminocyclohexane is often used as a key chiral constituent in asymmetric ligands.

Thus, this important chiral diamine can be considered a privileged scaffold for ligand design.

The coordination chemistry of nitrogen-rich pentadentate ligands has received much attention (Figure 5-1). Pentadentate ligands display the unique ability to coordinate to an octahedral metal center with five donors, while leaving the sixth position open for binding to an additional group. This special binding mode has led the way to a variety of interesting reactivities not easily accessed by other ligand types. In particular, these ligands have demonstrated the ability to stabilize high-valent metal centers^{2,3} and block bimolecular decay processes of reactive intermediates observed when using ligands of lower denticity. Also important has been their ability to participate in atom- or group-transfer reactions.⁴ Groups found in the sixth position of such complexes have included oxo,⁵⁻⁹ hydroperoxo,¹⁰⁻¹² azide,¹³ imidio,¹⁴ nitrosyl,¹⁵ nitridio,¹⁶ cyanide,¹⁷ and halogens.¹⁷ Despite such attention, the element of chirality has been noticeably absent in these ligands, with only a few examples of chiral pentadentate ligands reported that contain similar nitrogen-rich donor sets.¹⁸⁻²⁴

Considering there have been few reported examples of chiral pentadentate ligands, the Kodanko group at Wayne State University undertook studies to define new ligand sets of this type. To initiate their studies, they chose to merge the privileged scaffold *trans*-1,2-diaminocyclohexane with the general structure of the R-TPEN class of pentadentate ligands (Figure 5-1). In this process the ethyl bridge between the two basic amines of the parent Bn-TPEN was replaced with a cyclohexyl linker yielding Bn-CDPy3 (Figure 5-2). While seemingly straightforward, the new cyclohexane motif added complexity and new questions surrounding the coordination chemistry of the chiral

ligand. By differentiating the amines of the diaminocyclohexane backbone, the C_2 symmetry of the ligand is destroyed, creating a C_1 symmetric ligand in its place. This lowering of symmetry creates the opportunity for the ligand to access more coordination modes than possible for tetra- or hexadentate ligands derived from *trans*-1,2-diaminocyclohexane which carry identical donors on the two amine centers.²⁵⁻²⁸ Furthermore, the element of chirality conferred by the cyclohexane linker would create the possibility for additional stereoisomeric coordination modes, that is, modes that were equivalent or enantiomeric in the case of the R-TPEN ligands would become diastereomeric in the case of the new chiral ligand. of the Kodanko group has characterized the complex $[\text{Co}(\text{Bn-CD-Py4})\text{Cl}]\text{Cl}_2$ ²⁹ and report that a single coordination geometry is preferred from five possible modes for transition metal complexes derived from the chiral pentadentate ligand Bn-CDPy3. Our theoretical studies support experimental observations and help shed light upon the origin of coordination control.

5.2 Computational Methods

All five isomers of the cobalt-, zinc- and iron-containing structures were fully optimized using the TPSS³⁰ pure functional with an all electron cc-pVTZ³¹⁻³⁵ basis set on the ligands and the metals. Equilibrium geometries were confirmed using vibrational frequency analysis. For comparison, optimizations were also carried out with the B3LYP hybrid functional.³⁶⁻³⁸ Single point calculations were performed on the optimized structure of the ligand without the metal halide using the TPSS pure density functional with the cc-pVTZ basis set. NBO³⁹ analysis was used to look at the nature of the molecular orbitals of the calculated structures. NMR calculations were performed using the gauge-independent atomic orbital (GIAO) method⁴⁰⁻⁴³ with the TPSS functionals and

the cc-pVTZ basis set. The reference in the NMR spectrum was tetramethylsilane (TMS) calculated using the same functional and basis set. Calculations of the UV-vis spectra utilized time-dependent density functional theory (TD-DFT)⁴⁴⁻⁵⁰ with the long-range corrected LC- ω PBE⁵¹⁻⁵⁴ functional and the cc-pVTZ basis set. All calculations were performed using the development version of the Gaussian software suite.

5.3 Computational Results

As shown in Figure 5-3, five isomers can be constructed for M(Bn-CDPy3)Cl. The calculated relative energies are summarized in Table 5-1 for M = Co(III), Fe(II) and Zn(II). Results for the B3LYP calculations are comparable. For all of the complexes considered, the calculations predict isomer C to be the lowest energy, in good agreement with the X-ray crystallographic data for Co(III) and Fe(II) complexes and the NMR data for the Zn(II) complex. The metal-ligand bond lengths and angles compare very well with the available experimental structural data. For isomer C the RMSD for the heavy atoms in the crystal structure versus calculated structure is 0.182 Å for the Co(III) complex and 0.139 Å for the Fe(II) complex. The bond lengths for the d⁶ Co(III) complex are 0.2 – 0.3 Å shorter than for the Fe(II) and the Zn(II) complexes. This is in keeping with the fact that the d_{z²} and d_{x²-y²} orbitals are unoccupied in the low spin d⁶ Co(III) complex, but are singly and doubly occupied in the high spin d⁵ Fe(II) complex and the d¹⁰ Zn(II) complex. In three of the five isomers of the M(Bn-CDPy3)Cl complexes, the pyridyl donors are arranged meridionally (isomers A, B and C), and two are facial (isomers D and E). Isomer C is calculated to be the most stable. If it were not for the cyclohexane ring, isomer A would be the mirror image of isomer C and is the next most stable isomer. For each of the metals considered, isomer B is ca. 8 kcal/mol less stable

than C. In B, the two pyridyl rings are *trans* to each other and are nearly coplanar, whereas none of the pyridyl ring in isomers A and C lie in the same plane. The two facial isomers, D and E, are 10 – 16 kcal/mol less stable than C. Isomers D and E have the two pyridyl rings coplanar and *cis* to each other.

Both steric ligand distortion and ligand-metal binding energies contribute to the energy differences between the various isomers. The ligand distortion contributions are easily factored out by removing the metal chloride from the complex and computing the energy of the ligand frozen at the geometry of the complex. As shown in Table 5-1, the ligand of isomer C has the lowest distortion energy for each metal considered. Because of the shorter metal ligand bond distances, the ligand in the Co(III) complex C is 20 kcal/mol more strained than the ligand in the corresponding Fe and Zn complexes. For a given metal, the ligand of isomer A has the next lowest distortion energy, and those for the remaining isomers are 3-6 kcal/mol greater than for isomer C. The distortion energies of the ligands in the facial isomers D and E are not significantly higher than for the meridional isomers A-C.

If the difference in the strain energy is subtracted from the relative energy of the isomers, one is left with differences in the electronic contribution arising from the metal-ligand interactions. As indicated in Table 5-1, the electronic contribution for the *mer* isomers A - C is 5 – 10 kcal/mol more stabilizing than for the *fac* isomers, D and E. There is a delicate balance between the numerous factors in the electronic contribution, and it is not possible to single out one dominant term either by looking at the NBO analysis or by examining the geometric parameters. However, inspection of the structures provides evidence for the *trans* effect⁵⁵⁻⁵⁷ and for interactions of the metal-

ligand bonds with π system of the pyridyl rings. For example, metal-pyridyl bonds *trans* to an amine nitrogen in isomers A-C are always shorter than the metal-pyridyl bonds *cis* to the amine (see Table 5-2). The Fe-N and Zn-N bonds *trans* to Cl are longer than the corresponding bonds *cis* to Cl (for low spin d^6 Co(III), other factors contribute and the *trans* lengthening by Cl is not evident). Interactions of the pyridyl π orbitals with the metal-ligand anti-bonding orbitals are most clearly seen in the *fac* isomers. The M-N bonds aligned with the π orbital of the pyridyl *trans* to the Cl (e.g. R(Zn-N4) 2.215 Å and R(Zn-N2) 2.286 Å for Zn isomer E) are longer than the M-N bonds perpendicular to the π orbital (R(Zn-N5) 2.165 Å and R(Zn-N1) 2.247 Å, respectively).

Calculation of the excited states for isomer C of $[\text{Co}(\text{Bn-CDPy}_3)\text{Cl}]^{2+}$ yields a weak transition at 532 nm comparable to the weak absorption observed experimentally at 550 nm. The longest wavelength transitions calculated for the other meridional isomers are in the same region (541 and 535 nm for A and B, resp.); the transitions for the facial isomers were at shorter wavelengths (490 and 505 nm for D and E, resp.). Similar agreement is found for the iron complex: isomer C of $[\text{Fe}(\text{Bn-CDPy}_3)\text{Cl}]^{2+}$ has a transition at 389 nm compared to the observed transition at 413 nm.

The ^1H NMR spectra for $[\text{Co}(\text{Bn-CDPy}_3)\text{Cl}]^{2+}$ and $[\text{Zn}(\text{Bn-CDPy}_3)\text{Cl}]^+$ were calculated for comparison with the experimental data. As shown in Figure 5-4, there is an excellent correlation between the calculated and observed chemical shifts for the three protons at the 2-position of the pyridine rings. For each complex, two of the resonances are downfield, while the third resonance is shifted upfield by approximately 1.5 ppm. The upfield shift is due to the shielding effect of the pyridyl ring situated directly below the 2-pyridyl proton as shown in Figure 5-5. A similar effect is seen in calculations of the

iron complex, but is complicated by a very large paramagnetic contribution. Other isomers of the cobalt, zinc and iron complexes also show a large upfield shift for 2-pyridyl protons that are directly above the π system of a pyridyl ring

5.4 Discussion

The theoretical data presented here indicates that the chiral pentadentate ligand Bn-CDPy3 displays a significant thermodynamic preference for adopting the same coordination geometry in metal complexes of the general formula $[M(\text{Bn-CDPy}_3)\text{Cl}]$, regardless of the metal ion. This observation is noteworthy because five different coordination geometries are possible for the chiral ligand complexes of this formula. In the cases of the Co(III) and Fe(II) complexes, X-ray crystallographic data were used to determine the structure of the complexes. For the Zn(II) complex, 1D and 2D NMR data were consistent with the assigned structure. For the Fe(II), Co(III) and Zn(II) complexes, the calculations agreed well with the experimental data, including calculations that produced the same pattern of two downfield and one upfield resonances in the ^1H NMR spectrum for the 2-pyridyl C-H groups of the Co(III) and Zn(II) complexes.

In part, the origin of conformation control can be understood by contrasting the data for Bn-CDPy3 complexes with crystallographic data of the related complexes derived from the achiral ligand Bn-TPEN. Compounds of the general formula $[\text{Fe(II)(Bn-TPEN)X}]$ all crystallize with the same conformation (Figure 5-6, $X = \text{Cl}$), having the X group *trans* to the basic amine donor N(1), and the three pyridyl donors N(3)-N(5) adopting the *mer* geometry. In addition, two pyridine N-donors, N(3) and N(4), adopt a coplanar conformation of their rings with respect to the Fe-X bond, while the third donor ring containing N(5) is perpendicular to that axis. Therefore, the fact that

Bn-CDPy3 would prefer to adopt the same conformation upon coordination to a metal ion is not a surprise. On the basis of this analysis, three of the conformers shown in Figure 5-3 (B, D and E) can be eliminated from consideration as the most stable because they do not possess an X group *trans* to the basic amine donor N(1). Only two complexes with Bn-CDPy3, conformers A and C, adopt this preferred geometry. In the case of the Bn-TPEN complexes, the energetic difference between A and C is not an issue, because these conformers are enantiomers, therefore they are isoenergetic. However, with the chiral ligand Bn-CDPy3, A and C become diastereomeric, therefore they can exist at different relative energies. It should be noted that the same conformational preference was assumed for the cation $[\text{Fe}^{\text{IV}}(\text{O})(\text{Bn-TPEN})]^{2+}$ based on paramagnetic ^1H NMR data which indicated the same pattern of two downfield and one upfield shifts for the 2-pyridyl C-H resonances⁵ and on DFT calculations of conformational energies for different isomers.^{5,58}

What is interesting in the case of Bn-CDPy3 is what distinguishes conformations A from C. Both have same features, an X group *trans* to N(1) and a *mer* geometry of three pyridyl N-donors, with two coplanar and one perpendicular to the M-X axis. Yet, conformation C is preferred over A by greater than 2 kcal/mol in the Zn(II), Fe(II), and Co(III) complexes. Our calculations have indicated that the origins of energetic control over geometry arise from ligand strain energies in addition to the electronic preference in the interaction with the metal (see Ligand-Metal Interactions, Table 5-1). Inspection of the calculated structures indicates the ligand preference may be due to interactions between the cyclohexane ring and the groups surrounding the metal center. Namely, the calculations show 2.65 kcal/mol stabilization for the ligand in conformation C relative to

A when the metal ion is removed from the Co(III) complex. Upon inspection of the metal complexes, there are no severe steric interactions, such as eclipsing interactions, that are readily apparent which are present in A and not in C that would explain why C is preferred. However, superimposing the structures shown in Figure 5-7 gives some insight into the origin of stereocontrol. In order to visualize the overlap between the two structures in the most effective manner, the enantiomer of structure A (*ent*-A) was generated to create the same stereochemistry around the metal center, while the stereochemistry of the diaminocyclohexane unit was inverted. The metal atom, the five nitrogens and the chloride were superimposed to produce the overlapped structures. As shown in Figure 5-7, atoms surrounding the metal center exhibit good overlap, with the exception of the top pyridyl ring, which rotates slightly from structure C to *ent*-A. It is clear in C that the methylene hydrogen atom can occupy the cavity directly between two axial hydrogen atoms as shown in Figure 5-7. In *ent*-A, because the cyclohexane ring has undergone a ring flip, an axial hydrogen atom occupies this space, so in order to avoid an unfavorable non-bonding interaction, the 2-pyridyl methylene group rotates by 16° and bends by 18° relative to the Co-N-N-N plane in order to move away from the C-H group. This rotation also affects the bonding between the pyridine ring and the metal center lengthening the distance by 0.018\AA . These interactions may explain both the steric and electronic contributions to the difference in energy between structures A and C in the Co(III) complexes. Similar interactions are found in the Zn(II) and Fe(II) complexes.

5.5 Conclusions

In conclusion we have described a computational study of the chiral ligand (R,R)-Bn-CDPy3 and the characterization of zinc, iron, and cobalt complexes derived from the ligand. Experimental studies of these complexes revealed that a single coordination geometry is favored, by at least several kcal/mol, in metal complexes of Bn-CDPy3 out of five possible isomers. Theoretical data, which were in good agreement with experimental data, indicated that the preference for creating a single coordination geometry was due to both steric and electronic effects. Analysis of the calculated structures revealed some of the key interactions that enforced a strong stereoisomeric preference. Although the introduction of chirality into the pentadentate ligand certainly introduced more complexity in the coordination chemistry of the ligand relative to achiral ligands of this class, this work proves that control over geometry can be enforced and understood. A good understanding of these factors will pave the way for a selective synthesis of enantiopure complexes for applications in asymmetric catalysis.

5.6 References

- (1) Knof, U.; Von Zelewsky, A. Predetermined chirality at metal centers, **1999**, *38*, 303.
- (2) Que, L. The Road to Non-Heme Oxoferryls and Beyond, **2007**, *40*, 493.
- (3) Nam, W. High-Valent Iron(IV)-Oxo Complexes of Heme and Non-Heme Ligands in Oxygenation Reactions, **2007**, *40*, 522.
- (4) Bukowski, M. R.; Comba, P.; Lienke, A.; Limberg, C.; Lopez de Laorden, C.; Mas-Balleste, R.; Merz, M.; Que, L., Jr. Catalytic epoxidation and 1,2-dihydroxylation of olefins with bispidine-iron(II)/H₂O₂ systems, **2006**, *45*, 3446.
- (5) Klinker, E. J.; Kaizer, J.; Brennessel, W. W.; Woodrum, N. L.; Cramer, C. J.; Que, L., Jr. Structures of nonheme oxoiron(IV) complexes from X-ray crystallography, NMR spectroscopy, and DFT calculations, **2005**, *44*, 3690.
- (6) Kaizer, J.; Klinker, E. J.; Oh, N. Y.; Rohde, J.-U.; Song, W. J.; Stubna, A.; Kim, J.; Muenck, E.; Nam, W.; Que, L., Jr. Nonheme FeIVO Complexes That Can Oxidize the C-H Bonds of Cyclohexane at Room Temperature, **2004**, *126*, 472.
- (7) Bukowski, M. R.; Koehntop, K. D.; Stubna, A.; Bominaar, E. L.; Halfen, J. A.; Muenck, E.; Nam, W.; Que, L., Jr. A Thiolate-Ligated Nonheme Oxoiron(IV) Complex Relevant to Cytochrome P450, **2005**, *310*, 1000.
- (8) Sastri, C. V.; Park, M. J.; Ohta, T.; Jackson, T. A.; Stubna, A.; Seo, M. S.; Lee, J.; Kim, J.; Kitagawa, T.; Muenck, E.; Que, L., Jr.; Nam, W. Axial Ligand Substituted Nonheme FeIV:O Complexes: Observation of Near-UV LMCT Bands and Fe:O Raman Vibrations, **2005**, *127*, 12494.

- (9) Bautz, J.; Bukowski, M. R.; Kerscher, M.; Stubna, A.; Comba, P.; Lienke, A.; Munck, E.; Que, L., Jr. Formation of an aqueous oxoiron(IV) complex at pH 2-6 from a nonheme iron(II) complex H₂O₂, **2006**, *45*, 5681.
- (10) Hazell, A.; McKenzie, C. J.; Nielsen, L. P.; Schindler, S.; Weitzer, M. Mononuclear non-heme iron(III) peroxide complexes: syntheses, characterisation, mass spectrometric and kinetic studies, **2002**, 310.
- (11) Guajardo, R. J.; Tan, J. D.; Mascharak, P. K. The Secondary Amine Group of Bleomycin Is Not Involved in Intramolecular Hydrogen Bonding in "Activated Bleomycin", **1994**, *33*, 2838.
- (12) Guajardo, R. J.; Hudson, S. E.; Brown, S. J.; Mascharak, P. K. [Fe(PMA)]_n⁺ (n = 1,2): good models of iron-bleomycins and examples of mononuclear non-heme iron complexes with significant oxygen-activation capabilities, **1993**, *115*, 7971.
- (13) Berry, J. F.; Bill, E.; Bothe, E.; Weyhermueller, T.; Wieghardt, K. Octahedral Non-Heme Non-Oxo Fe(IV) Species Stabilized by a Redox-Innocent N-Methylated Cyclam-Acetate Ligand, **2005**, *127*, 11550.
- (14) Klinker, E. J.; Jackson, T. A.; Jensen, M. P.; Stubna, A.; Juhasz, G.; Bominaar, E. L.; Muenck, E.; Que, L., Jr. A tosylimido analogue of a nonheme oxoiron(IV) complex, **2006**, *45*, 7394.
- (15) Eroy-Reveles, A. A.; Leung, Y.; Beavers, C. M.; Olmstead, M. M.; Mascharak, P. K. Near-Infrared Light Activated Release of Nitric Oxide from Designed Photoactive Manganese Nitrosyls: Strategy, Design, and Potential as NO Donors, **2008**, *130*, 6650.

(16) Grapperhaus, C. A.; Mienert, B.; Bill, E.; Weyhermueller, T.; Wieghardt, K. Mononuclear (Nitrido)iron(V) and (Oxo)iron(IV) Complexes via Photolysis of [(cyclam-acetato)FeIII(N3)]⁺ and Ozonolysis of [(cyclam-acetato)FeIII(O3SCF3)]⁺ in Water/Acetone Mixtures, **2000**, *39*, 5306.

(17) Ortega-Villar, N.; Ugalde-Saldivar, V. M.; Munoz, M. C.; Ortiz-Frade, L. A.; Alvarado-Rodriguez, J. G.; Real, J. A.; Moreno-Esparza, R. Synthesis and Relative Stability of a Series of Compounds of Type [Fe(II)(bztpen)X]⁺, Where bztpen = Pentadentate Ligand, N5, and X⁻ = Monodentate Anion, **2007**, *46*, 7285.

(18) Seitz, M.; Stempfhuber, S.; Zabel, M.; Schutz, M.; Reiser, O. Helical chirality in pentacoordinate zinc complexes - Selective access to both pseudoenantiomers with one ligand configuration, **2005**, *44*, 242.

(19) Gillard, R. D.; Newman, P. D.; Vagg, R. S.; Williams, P. A. Chiral metal complexes. 43. Cobalt(III) complexes of novel asymmetric tetradentate and pentadentate aminopolypicolyl ligands, **1995**, *233*, 79.

(20) Gosiewska, S.; Lutz, M.; Spek, A. L.; Klein Gebbink, R. J. M. Mononuclear diastereopure non-heme Fe(II) complexes of pentadentate ligands with pyrrolidinyl moieties: Structural studies, and alkene and sulfide oxidation, **2007**, *360*, 405.

(21) Bernauer, K.; Pousaz, P. Stereoselectivity in reactions of metal complexes. IX. Stereoselective formation of cobalt(III) complexes with new linear pentadentate ligands, **1984**, *67*, 796.

(22) Bernauer, K.; Pousaz, P.; Porret, J.; Jeanguenat, A. Stereoselectivity in reactions of metal complexes. Part X. Kinetics and stereoselectivity of the inner-sphere

electron-transfer reaction between $[\text{Co}(\text{bamap})\text{H}_2\text{O}]^+$ [bamap = 2,6-bis(3-carboxy-1,2-dimethyl-2-azapropyl)pyridine] and optically active iron(II) complexes, **1988**, *71*, 1339.

(23) Larionov, S. V.; Myachina, L. I.; Glinskaya, L. A.; Klevtsova, R. F.; Bizyaev, S. N.; Tkachev, A. V. Synthesis and structure of the $[\text{Ni}(\text{H}_2\text{L})\text{Cl}]\text{Cl}$ complex with the chiral pentadentate nitrogen-containing ligand H₂L derived from the natural terpenoid (+)-3-carene, **2007**, *56*, 1771.

(24) Kurosaki, H.; Koike, H.; Omori, S.; Ogata, Y.; Yamaguchi, Y.; Goto, M. Synthesis, characterization, and crystal structure of the copper(II) complex of the optically active polypyridylmethylamine ligand: N,N,N'-tris(2-pyridylmethyl)-S-2-(aminomethyl)piperidine = S-P3pipda, **2004**, *7*, 1229.

(25) Costas, M.; Tipton, A. K.; Chen, K.; Jo, D.-H.; Que, L., Jr. Modeling Rieske Dioxygenases: The First Example of Iron-Catalyzed Asymmetric cis-Dihydroxylation of Olefins, **2001**, *123*, 6722.

(26) Jensen, M. P.; Costas, M.; Ho, R. Y. N.; Kaizer, J.; Payeras, A. M.; Muenck, E.; Que, L., Jr.; Rohde, J.-U.; Stubna, A. High-Valent Nonheme Iron. Two Distinct Iron(IV) Species Derived from a Common Iron(II) Precursor, **2005**, *127*, 10512.

(27) Sato, M.; Mori, Y.; Iida, T. Convenient synthesis of N,N,N',N'-tetrakis(2-pyridylmethyl)- α , ω -alkanediamines using a phase-transfer catalyst, **1992**, 539.

(28) Mori, Y.; Sato, M.; Iida, T. Synthesis and characteristics of novel transition metal complexes with high superoxide dismutase activity, **1992**, 469.

(29) Hammoud, M. M.; McKamie, J. J.; Heeg, M. J.; Kodanko, J. J. Synthesis of the chiral tripyridylamine ligand Bn-CDPy₃ and characterization of its Co(III) complex $[\text{Co}(\text{Bn-CDPy}_3)\text{Cl}]\text{Cl}_2$, **2008**, 4843.

(30) Tao, J.; Perdew, J. P.; Staroverov, V. N.; Scuseria, G. E. Climbing the Density Functional Ladder: Nonempirical Meta-Generalized Gradient Approximation Designed for Molecules and Solids, **2003**, *91*, 146401.

(31) Kendall, R. A.; Thom H. Dunning, J.; Harrison, R. J. Electron affinities of the first-row atoms revisited. Systematic basis sets and wave functions, **1992**, *96*, 6796.

(32) Peterson, K. A.; Woon, D. E.; Thom H. Dunning, J. Benchmark calculations with correlated molecular wave functions. IV. The classical barrier height of the $H+H[sub 2] \rightarrow H[sub 2]+H$ reaction, **1994**, *100*, 7410.

(33) Thom H. Dunning, J. Gaussian basis sets for use in correlated molecular calculations. I. The atoms boron through neon and hydrogen, **1989**, *90*, 1007.

(34) Woon, D. E.; Thom H. Dunning, J. Gaussian basis sets for use in correlated molecular calculations. III. The atoms aluminum through argon, **1993**, *98*, 1358.

(35) Wilson, A. K.; van Mourik, T.; Dunning, T. H. Gaussian basis sets for use in correlated molecular calculations. VI. Sextuple zeta correlation consistent basis sets for boron through neon, **1996**, *388*, 339.

(36) Becke, A. D. Density-functional thermochemistry. III. The role of exact exchange, **1993**, *98*, 5648.

(37) Lee, C.; Yang, W.; Parr, R. G. Development of the Colle-Salvetti correlation-energy formula into a functional of the electron density, **1988**, *37*, 785.

(38) Miehlich, B.; Savin, A.; Stoll, H.; Preuss, H. Results obtained with the correlation energy density functionals of becke and Lee, Yang and Parr, **1989**, *157*, 200.

- (39) Glendening, E. D.; Reed, A. E.; Carpenter, J. E.; Weinhold, F. *NBO*; Version 3.1; 1990.
- (40) McWeeny, R. Perturbation Theory for the Fock-Dirac Density Matrix, **1962**, *126*, 1028.
- (41) Ditchfield, R. Self-consistent perturbation theory of diamagnetism -- I. A gauge-invariant LCAO method for N.M.R. chemical shifts, **1974**, *27*, 789
- (42) Cheeseman, J. R.; Trucks, G. W.; Keith, T. A.; Frisch, M. J. A comparison of models for calculating nuclear magnetic resonance shielding tensors, **1996**, *104*, 5497.
- (43) Wilson, S. M.; Wiberg, K. B.; Cheeseman, J. R.; Frisch, M. J.; Vaccaro, P. H. Nonresonant Optical Activity of Isolated Organic Molecules, **2005**, *109*, 11752.
- (44) Bauernschmitt, R.; Ahlrichs, R. Treatment of electronic excitations within the adiabatic approximation of time dependent density functional theory, **1996**, *256*, 454.
- (45) Casida, M. E.; Jamorski, C.; Casida, K. C.; Salahub, D. R. Molecular excitation energies to high-lying bound states from time-dependent density-functional response theory: Characterization and correction of the time-dependent local density approximation ionization threshold, **1998**, *108*, 4439.
- (46) Stratmann, R. E.; Scuseria, G. E.; Frisch, M. J. An efficient implementation of time-dependent density-functional theory for the calculation of excitation energies of large molecules, **1998**, *109*, 8218.
- (47) Van Caillie, C.; Amos, R. D. Geometric derivatives of excitation energies using SCF and DFT, **1999**, *308*, 249.
- (48) Van Caillie, C.; Amos, R. D. Geometric derivatives of density functional theory excitation energies using gradient-corrected functionals, **2000**, *317*, 159.

(49) Furche, F.; Ahlrichs, R. Adiabatic time-dependent density functional methods for excited state properties, **2002**, *117*, 7433.

(50) Scalmani, G.; Frisch, M. J.; Mennucci, B.; Tomasi, J.; Cammi, R.; Barone, V. Geometries and properties of excited states in the gas phase and in solution: Theory and application of a time-dependent density functional theory polarizable continuum model, **2006**, *124*, 094107.

(51) Tawada, Y.; Tsuneda, T.; Yanagisawa, S.; Yanai, T.; Hirao, K. A long-range-corrected time-dependent density functional theory, **2004**, *120*, 8425.

(52) Vydrov, O. A.; Heyd, J.; Krukau, A. V.; Scuseria, G. E. Importance of short-range versus long-range Hartree-Fock exchange for the performance of hybrid density functionals, **2006**, *125*, 074106.

(53) Vydrov, O. A.; Scuseria, G. E. Assessment of a long-range corrected hybrid functional, **2006**, *125*, 234109.

(54) Vydrov, O. A.; Scuseria, G. E.; Perdew, J. P. Tests of functionals for systems with fractional electron number, **2007**, *126*, 154109.

(55) Burdett, J. K.; Albright, T. A. Trans influence and mutual influence of ligands coordinated to a central atom, **1979**, *18*, 2112.

(56) Coe, B. J.; Glenwright, S. J. Trans-effects in octahedral transition metal complexes, **2000**, *203*, 5.

(57) Anderson, K. M.; Orpen, A. G. On the relative magnitudes of cis and trans influences in metal complexes, **2001**, 2682.

(58) Wang, Y.; Wang, Y.; Han, K. Theoretical study of cyclohexane hydroxylation by three possible isomers of $[\text{FeIV}(\text{O})(\text{R-TPEN})]^{2+}$: does the pentadentate

ligand wrapping around the metal center differently lead to the different stability and reactivity?, **2009**, *14*, 533.

Table 5-1. Relative energies of the five isomers of $[\text{Co}(\text{Bn-CDPy}_3)\text{Cl}]^{2+}$, $[\text{Zn}(\text{Bn-CDPy}_3)\text{Cl}]^+$, and $[\text{Fe}(\text{Bn-CDPy}_3)\text{Cl}]^+$ in kcal/mol.

isomer	entire complex ^a	ligand only ^b	ligand-metal interaction ^c
C			
Co	0.00	0.00	0.00
Zn	0.00	0.00	0.00
Fe	0.00	0.00	0.00
A			
Co	7.12	2.65	4.47
Zn	2.49	0.86	1.63
Fe	2.79	0.96	1.83
B			
Co	7.79	3.79	4.00
Zn	7.76	3.25	4.51
Fe	8.34	3.26	5.08
D			
Co	15.73	5.70	10.04
Zn	12.44	2.73	9.71
Fe	13.12	3.29	9.83
E			
Co	13.45	3.15	10.31
Zn	12.44	2.73	9.71
Fe	12.41	2.79	9.62

^aEnergy of the $\text{M}(\text{Bn-CDPy}_3)\text{Cl}$ complex relative to isomer C.

^bSingle Point energies of the complexes with the metal chloride removed, relative to isomer C; these energies reflect the differences in the ligand distortion energies in the various isomers relative to isomer C; the ligand distortion energies for isomer C are 20.64 and 1.08 kcal/mol greater for the Co and Fe complexes than for the Zn complex.

^cEntire complex energies minus the ligand-only energies; these energies reflect the differences in the electronic interaction between the ligands and the metal chlorides

Table 5-2. Comparison of X-ray crystallographic Data and Calculated Structures for the $[\text{Co}(\text{Bn-CDPy}_3)\text{Cl}]^{2+}$, $[\text{Zn}(\text{Bn-CDPy}_3)\text{Cl}]^+$, and $[\text{Fe}(\text{Bn-CDPy}_3)\text{Cl}]^+$ Cations^a

	crystallographic data	isomer C	isomer A	isomer B	isomer D	isomer E
Co						
M—Cl	2.241(1)	2.244	2.243	2.254	2.248	2.279
M—N1	1.962(2)	1.989	1.999	1.971	1.976	1.987
M—N2	2.015(2)	2.044	2.049	2.056	2.053	2.036
M—N3	1.941(2)	1.966	1.989	1.961	1.983	1.973
M—N4	1.952(2)	1.971	1.957	1.983	1.996	2.010
M—N5	1.945(2)	1.970	2.007	1.954	1.949	1.988
Zn						
M—Cl		2.283	2.276	2.290	2.297	2.362
M—N1		2.331	2.341	2.217	2.216	2.247
M—N2		2.269	2.252	2.455	2.314	2.286
M—N3		2.175	2.228	2.227	2.242	2.268
M—N4		2.220	2.141	2.275	2.419	2.215
M—N5		2.242	2.361	2.109	2.125	2.165
Fe						
M—Cl	2.339(1)	2.269	2.267	2.270	2.282	2.340
M—N1	2.236(1)	2.307	2.319	2.245	2.246	2.257
M—N2	2.268(1)	2.308	2.298	2.435	2.311	2.304
M—N3	2.163(1)	2.144	2.213	2.218	2.260	2.240
M—N4	2.202(1)	2.184	2.124	2.233	2.316	2.213
M—N5	2.182(1)	2.222	2.284	2.104	2.145	2.187

^aBond lengths in Å and bond angles in deg; for atom numbering see Figure 5-3. For isomer C, the RMSD for the heavy atoms in the crystal structure versus calculated structure is 0.182 Å for $[\text{Co}(\text{Bn-CDPy}_3)\text{Cl}]^{2+}$ and 0.139 Å for $[\text{Fe}(\text{Bn-CDPy}_3)\text{Cl}]^+$

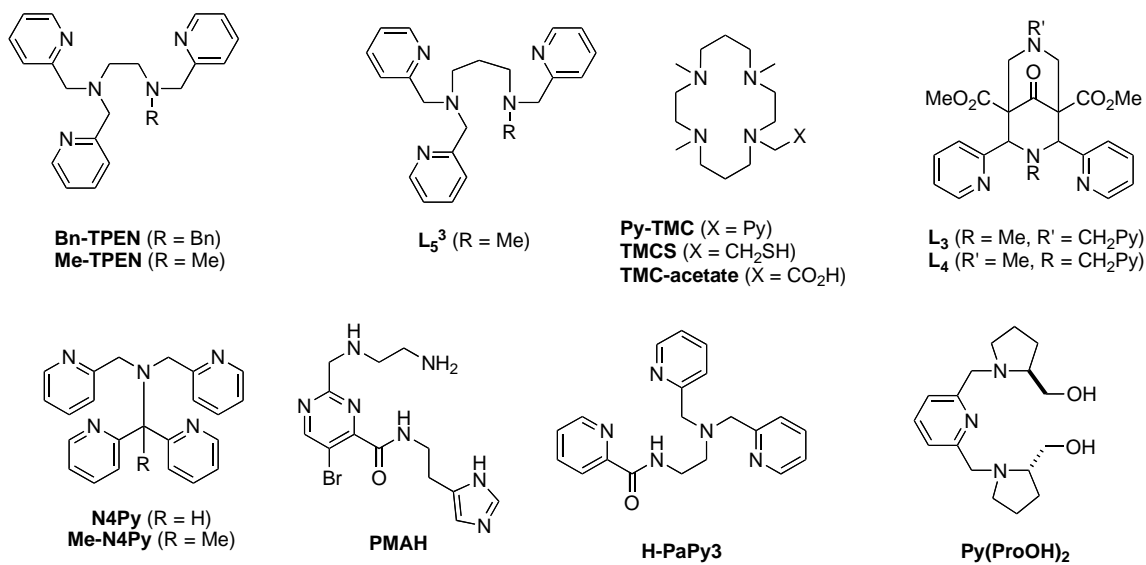


Figure 5-1. Known pentadentate ligands containing multiple N-donors and their derivatives

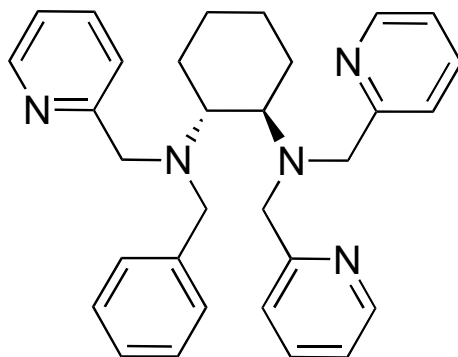


Figure 5-2. Structure of (R,R) -Bn-CDPy3 (**1**), a chiral pentadentate ligand.

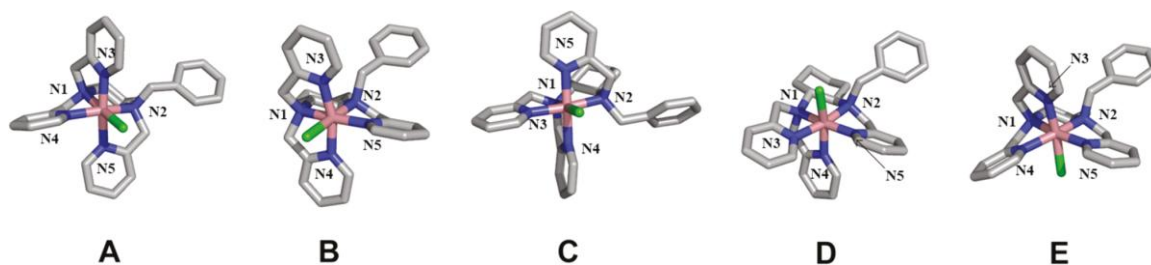


Figure 5-3. Isomers of $M(\text{Bn-CDPy}_3)\text{Cl}$ determined from calculations: A, B, and C display *mer* orientations of the pyridyl donors; D and E are *fac*.

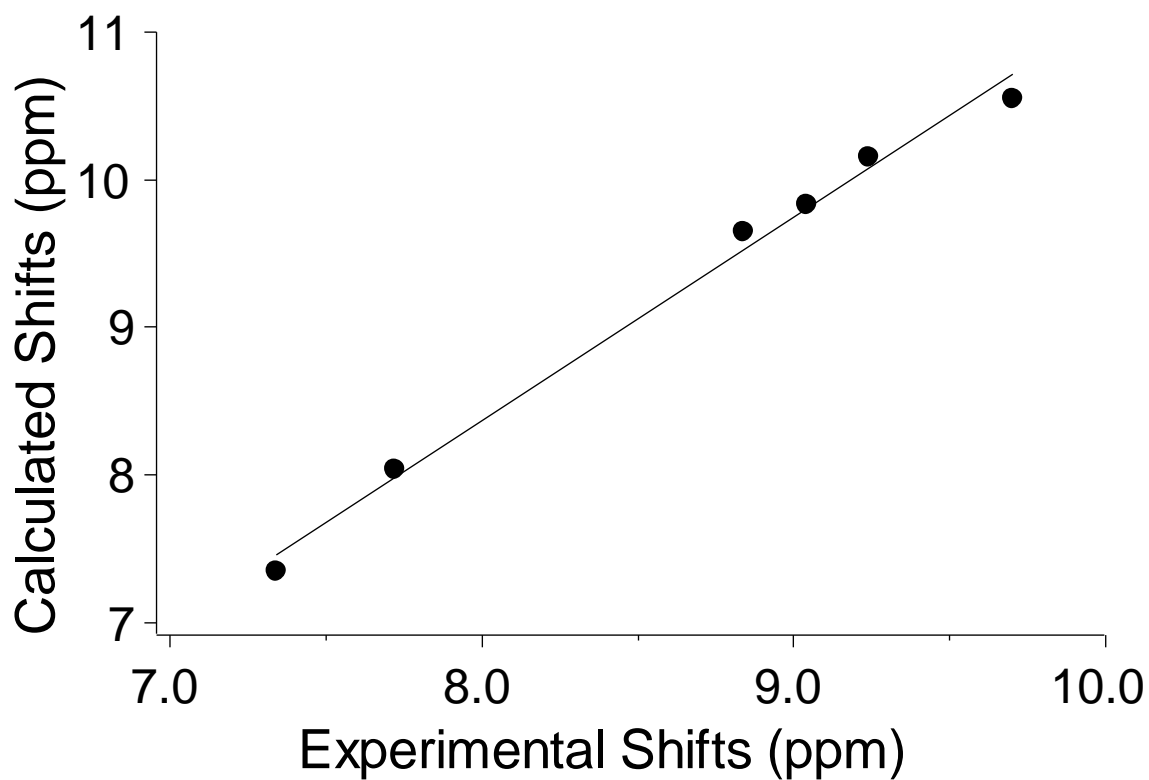


Figure 5-4. Comparison of calculated and observed chemical shifts of the three protons in the 2-position on the pyridyl rings in isomer C of $[\text{Co}(\text{Bn-CDPy}_3)\text{Cl}]^{2+}$ and $[\text{Zn}(\text{Bn-CDPy}_3)\text{Cl}]^+$ ($R^2 = 0.992$).

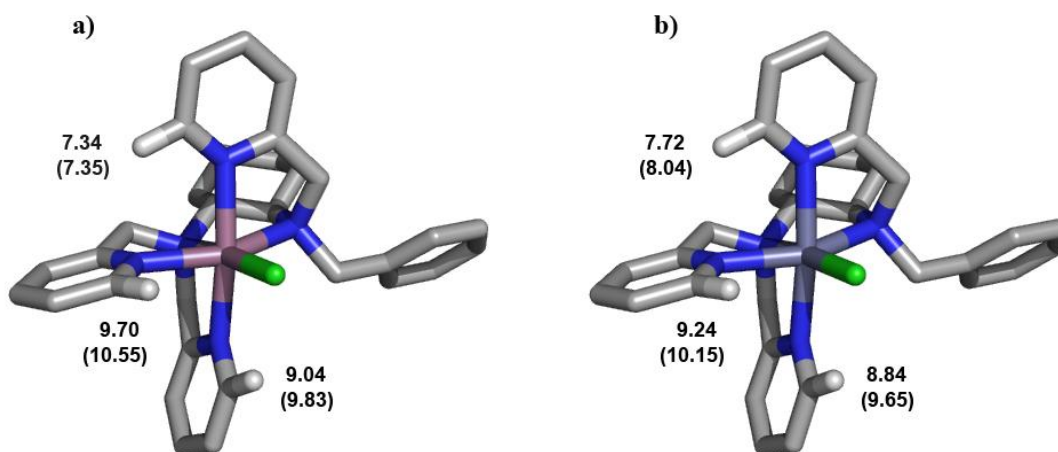


Figure 5-5. Observed vs. calculated (in parentheses) chemical shifts for the 2-pyridyl C-H protons (shown in white, other protons omitted for clarity) of (a) [Co(Bn-CDPy3)Cl]⁺ and (b) [Zn(Bn-CDPy3)Cl]⁺.

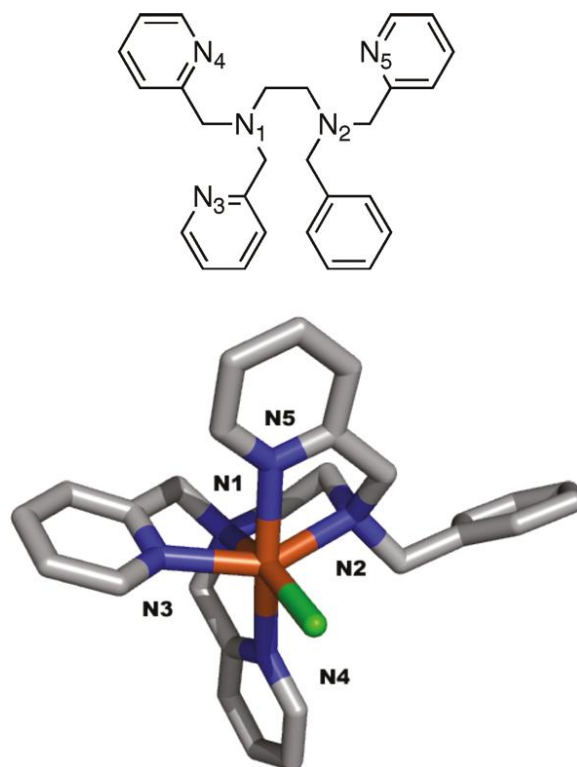


Figure 5-6. Structure of the ligand Bn-TPEN and model of the cation $[\text{Fe}(\text{Bn-TPEN})\text{Cl}]^+$ generated using X-ray crystallographic data from ref. 10. The structure of the cation is similar to $[\text{Fe}(\text{Bn-CDPy3})\text{Cl}]^+$, where the Cl group is in a *trans* configuration relative to N(1), and the three pyridyl N-donors N(3)-N(5) adopt a *mer* configuration, with two pyridine N-donors residing in a coplanar conformation with respect to the Fe-Cl bond, while the third ring is perpendicular to that axis.

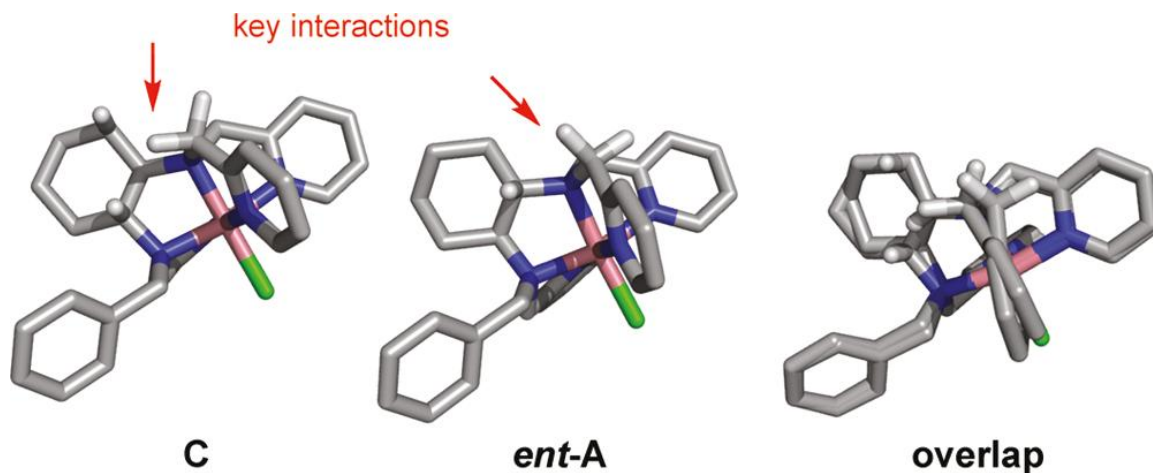


Figure 5-7. Calculated structures of the dication $[\text{Co}(\text{Bn-CDPy}_3)\text{Cl}]^{2+}$ **C**, **ent-A** (see Figure 5-3), and an overlap of the two structures that illustrates the subtle differences between the two stereoisomers. All hydrogens except those creating key interactions are omitted for clarity. In the case of **C**, a methylene hydrogen can occupy a position directly above the cyclohexane ring and between two axial hydrogen atoms, whereas with **ent-A**, the pyridyl substituent rotates to avoid an unfavorable interaction with a closer axial hydrogen atom.

Chapter 6

A Simple Model in Which Interligand Interactions Control the Cu—Cu Distance in Dinuclear Cu(II) Paddlewheel Complexes

Mahesh C. Karunaratne, Richard L. Lord, Jason A. Sonk, Mary Jane Heeg,

H. Bernhard Schlegel, and Charles H. Winter*

Department of Chemistry, Wayne State University, Detroit, Michigan 48202

6.1 Introduction

Antiferromagnetic coupling occurs when otherwise unpaired electrons align their spins in opposite directions. One of the earliest examples of antiferromagnetic coupling in a dimer compound was found in a dicopper tetraacetate bridged structure similar to the one shown to the right of Figure 6-1. When the dicopper tetraacetate structure was first discovered, the nature of the electronic structure had been the subject of considerable debate amongst chemists. The electronic structure is now very well understood¹ and the distance between the two metal centers (around 2.6 Å) is incompatible with direct bonding. The Winter group at Wayne State University has isolated an isoelectronic dicopper (II) paddlewheel complex employing amidates instead of acetates, and it exhibits a copper-copper separation of 2.4 Å, significantly shorter than has previously been reported. This could mean the presence of a copper-copper bond, which would challenge the understanding of the electronic structure of similar structures. This chapter sets out to identify the origin of this contracted Cu—Cu separation.

Dinuclear transition metal complexes of the formula M_2L_4 , where L is a monoanionic, bidentate ligand, have been studied extensively due to their short M-M distances, variable M-M bond orders, interesting paddlewheel structures, and for their spectroscopic properties.² While the presence of M—M bonds in M_2L_4 complexes is well established for many transition metals, the situation is less clear for Cu(II) complexes of the formula Cu_2L_4 . The structures of hundreds of Cu_2L_4 complexes have been determined by X-ray crystallography.³ Carboxylate-based complexes of the formula $Cu_2(O_2CR)_4L_n$ (L = neutral donor, n = 0-2) are the most numerous, and generally have Cu-Cu distances of 2.55-2.70 Å.² Many of these complexes are diamagnetic, or nearly so, which could originate through the formation of a Cu-Cu single bond between the two d^9 centers. However, an early theoretical study predicted that there is no Cu—Cu bond in $Cu_2(O_2CCH_3)_4$, and suggested that the antiferromagnetic coupling of the two d^9 metal centers arises from through-ligand coupling.¹ Several dinuclear or trinuclear Cu(II) complexes with much shorter Cu—Cu distances have been reported, and conflicting proposals have been made regarding the presence or absence of Cu-Cu bonds in these systems.^{4,5} For example, $Cu_2(PhNNNPh)_4$ has a Cu—Cu separation of 2.441(2) Å, which is the shortest such distance in any Cu_2L_4 complex reported in previous studies.⁴ The presence of a Cu—Cu bond in $Cu_2(PhNNNPh)_4$ was proposed, in view of the short Cu—Cu distance. A later theoretical study of $Cu_2(HNNNH)_4$ predicted a relatively short Cu—Cu distance of 2.484 Å, but clearly showed that no Cu—Cu bond exists.⁵ The trinuclear Cu(II) complex $[Cu_3(dpa)_4][BF_4]_2$ (dpa = di-2-pyridylamido) has very short Cu—Cu separations of 2.4029(8) and 2.4035(8) Å, whereas various solvated forms of $Cu_3(dpa)_4Cl_2$ had Cu—Cu separations of 2.471(1) to 2.493(2) Å.⁶ Magnetic studies

indicated that $[\text{Cu}_3(\text{dpa})_4][\text{BF}_4]_2$ and $\text{Cu}_3(\text{dpa})_4\text{Cl}_2$ have doublet ground states at low temperatures, but the energy difference between the doublet ground state and quartet excited state is larger for $[\text{Cu}_3(\text{dpa})_4][\text{BF}_4]_2$ than for $\text{Cu}_3(\text{dpa})_4\text{Cl}_2$. Since the through-ligand path length is nearly identical for both complexes, it was not possible to rule out a direct Cu—Cu interaction contribution to the antiferromagnetic coupling in $[\text{Cu}_3(\text{dpa})_4][\text{BF}_4]_2$.⁶

The Winter group at Wayne State University is interested in the development of new chemical precursors for the growth of transition metal thin films using atomic layer deposition (ALD).⁷ As part of these efforts, they have investigated the synthesis of copper(II) complexes containing amidate ligands. This chapter covers theoretical studies of the new Cu_2L_4 paddlewheel complex, $\text{Cu}_2(\text{MeCONiPr})_4$ (**1**), which has the shortest Cu(II)—Cu(II) distance reported to date in a Cu_2L_4 complex. The nature of the Cu—Cu interaction has been probed by our calculations, and a model is proposed to account for the variable Cu(II)—Cu(II) distances that are observed in Cu_2L_4 systems

6.2 Computational Methods

Electronic structure calculations were carried out using density functional theory (DFT)⁸ as implemented in the development version of Gaussian.⁹ Geometry optimizations were performed at the B3LYP/SDD/6-31+G(d,p)¹⁰⁻¹⁴ level of theory with no symmetry constraints. All optimized structures were confirmed to have stable wavefunctions,^{15,16} and to be local minima by analyzing the harmonic frequencies.¹⁷ Attempts were made to optimize a closed-shell singlet species that would correspond to two d^9 -Cu(II) centers formally σ -bonded, but each had a wavefunction instability indicative of antiferromagnetically (AF) coupled metals.¹⁸ Therefore, we also optimized

triplet species (one unpaired e^- at each d^9 -Cu(II) center) for comparison. The AF coupled singlets were computed to have a lower energy for all six species. Detailed energetics and structures of all species, and both corresponding orbital plots and J values for the AF coupled singlets are included in Table 6-1 and Table 6-2.

6.3 Results and Discussion

To address the issue of a Cu—Cu bond in **1**, we explored Cu_2L_4 complexes where L is bidentate formate ($\text{O-C}_\text{H}\text{-O}$), formamidate ($\text{O-C}_\text{H}\text{-NH}$), formamidinate ($\text{HN-C}_\text{H}\text{-NH}$), acetate ($\text{O-C}_\text{Me}\text{-O}$), N-methylacetamidate ($\text{O-C}_\text{Me}\text{-NMe}$), or N,N'-dimethylacetamidinate ($\text{MeN-C}_\text{Me}\text{-NMe}$). Attempts to locate a closed-shell, singlet species with σ -bonded d^9 -Cu(II) centers were unsuccessful due to wavefunction instabilities. In every case, the lowest energy singlet is instead best described as having two d^9 Cu(II) centers that are weakly antiferromagnetically coupled to each other through their $d_{x^2-y^2}$ orbitals (Cu—Cu defines the z-axis). This finding is consistent with previous calculations for $\text{Cu}_2(\text{OAc})_4$ and $\text{Cu}_2(\text{HNNNH})_4$, albeit with much longer Cu—Cu separations than **1**.^{1,5} The optimized structure for $\text{O-C}_\text{Me}\text{-NMe}$, which replaces the experimental *iPr* groups in **1** with more computationally tractable Me substituents, is slightly longer than the Cu—Cu distance in **1** (2.4148(3) versus 2.440 Å for $\text{O-C}_\text{Me}\text{-NMe}$) and matches the metal-ligand interactions well, as summarized in Table 6-3. For the methylated ligand complexes, the Cu—Cu separations decrease by 0.08 Å in going from $\text{O-C}_\text{Me}\text{-O}$ (2.504 Å) to $\text{MeN-C}_\text{Me}\text{-NMe}$ (2.416 Å) (Table 6-3, rows 2-4). The predicted Cu—Cu separation in the $\text{MeN-C}_\text{Me}\text{-NMe}$ structure is 0.024 Å shorter than the predicted value for $\text{O-C}_\text{Me}\text{-NMe}$ complex, and therefore may be an interesting target for future experimental studies. However, Cu(II) ion is reduced upon treatment with lithium amidinates to afford Cu(I) amidinate

complexes,¹⁹ and Cu(II) amidinate paddlewheel complexes may be experimentally difficult to access. We originally hypothesized that the Cu-Cu separation was regulated by different extents of charge-transfer to the Cu(II) centers. Because the electronegativity of the ligand contact atoms should matter most in this case, we tested small models where the Me groups were replaced by H atoms to ensure the trend is consistent (Table 6-3, columns 5-7). To our surprise the Cu-Cu separation ordering *reverses*, with O-C_H-O having the shortest (2.54 Å) and HN-C_H-NH having the longest (2.60 Å) Cu-Cu separation. Thus, the nature of the ligand plays a critical and non-trivial role in controlling the distance between the Cu centers.

One structural feature of the ligands stood out: the ligand twist angle as defined by the dihedral Cu-X-C-R (θ) where X is the midpoint between the two Cu centers, C is the backbone of a ligand, and R is either O or NR' (Figure 6-3). Dihedral angles of 0-16° were computed, with increases in twisting occurring when going from O → N and H → Me in the ligand. Because the metals are weakly coupled in all of these systems, it is plausible that ligand-metal and ligand-ligand interactions dictate the Cu-Cu separation. For metal-ligand interactions, the intraligand contact distances R-R (O-O, O-N and N-N) are tabulated in Table 6-3. This separation increases when replacing O with NR groups (elongation of ~0.05 Å in each series) which mirrors the Cu-Cu distance trend in the all-H models. However, the Cu-Cu distances decrease by 0.083 Å in the methylated series upon changing from O → N. Steric interactions of two types must be considered: interligand π -orbital repulsions and intraligand steric crowding between the C/N substituents. The latter are unlikely to matter in our computational models (Figure 6-4), but Me/iPr crowding in **1** may reduce the Cu-Cu distance slightly relative to O-C_{Me}-NMe

by forcing the N and O atom lone pairs that are donated to the Cu ions toward each other. A Walsh diagram for O-C_{Me}-NMe supports our hypothesis that the π -orbital repulsions control ligand twisting (Figure 6-5). The less electronegative N contact atoms have lone pairs that extend radially farther than those for O, which leads to more repulsion with nitrogen-based ligands, compared to acetate and formate. Hence, the values of θ decrease in the order RN-C_{R'}-NR > O-C_{R'}-NR > O-C_{R'}-O. Additionally, the electron-releasing nature of a Me group on the ligand central C atom increases the electron density of the N atom lone pairs and hence their size, relative to a H atom. This situation leads to more interligand π -orbital repulsions in the Me-substituted ligands, larger θ values, and shorter Cu-Cu separations, relative to the H-substituted ligands.

The intraligand contact distances R-R can be projected onto the Cu—Cu axis using θ , defining an effective intraligand contact distance that is geometrically equivalent to the two planes defined by R (Figure 6-6 inset). The distance between these planes for the O-O and N-N species correlates very well ($R^2=0.97$) with the Cu—Cu separation, as shown in Figure 6-6. Thus, a simple model to account for these data is the following: the two Cu(II) centers, being weakly coupled, are electrostatically repulsive. Metal-ligand bonding mostly overcomes this repulsion with attractive forces, and the plane defined by (i) intraligand contact distance and (ii) ligand twisting controls the Cu—Cu separation. Moreover, for the formate/acetate species where the NR groups do not sterically block solvent coordination in the axial position, an additional ligand can bind to Cu and further elongate the separation. Less quantitative agreement is seen for the two amidate species (O-C_H-NH, O-C_{Me}-NMe), because here the alternating bonding in the structure (2N and 2O per Cu) makes the definition of a plane less exact (the N and O atoms are not

coplanar), although qualitatively it agrees with our model and we have included a plot with these data in Figure 6-7.

6.4 Conclusions

We have described the properties of **1**, which contains the shortest Cu(II)—Cu(II) distance described to date in a Cu₂L₄ dinuclear complex. Theory predicts that there is no Cu—Cu bond in **1**, which suggests that the near diamagnetic character results from through-ligand coupling of the unpaired electrons. The lack of a Cu—Cu bond in **1** is consistent with previous theoretical studies of Cu₂(O₂CCH₃)₄¹ and Cu₂(HNNNH)₄,⁵ and also casts doubt upon a direct Cu—Cu interaction contribution to the antiferromagnetic coupling in [Cu₃(dpa)₄][BF₄]₂.⁶ The present results suggest that Cu₂L₄ complexes do not contain Cu—Cu bonding interactions at any distances that are likely to be accessible experimentally with O- and N-based bidentate ligands. To account for the short Cu-Cu separation in **1**, we have proposed a model in which interligand O/O, O/N, or N/N lone pair repulsions cause the bidentate ligands to twist slightly relative to the Cu—Cu vector. This twist angle θ becomes larger as the number of N atoms in the ligand increases, due to the lower electronegativity of N compared to O and concomitant larger size of the N atom lone pairs. Larger values of θ lead to shorter Cu-Cu distances by compressing the Cu—Cu vector. Steric crowding between H and Me groups on the ligand C and N atoms were not significant in our theoretical models, but the Cu-Cu distance in **1** is 0.025 Å shorter than the O-C_{Me}-NMe model. Hence, steric congestion between larger alkyl groups may also contribute to shortening of the Cu—Cu distances in Cu₂L₄ complexes by compressing the O/N or N/N lone pair separations. Finally, our proposed model may be

useful in understanding metal-metal distance trends in dinuclear and oligonuclear complexes with bridging ligands where there is little or no metal-metal bonding.

6.5 References

- (1) Hay, P. J.; Thibeault, J. C.; Hoffmann, R. Orbital Interactions in Metal Dimer Complexes, *J. Am. Chem. Soc.* **1975**, *97*, 4884.
- (2) Cotton, F. A.; Murillo, C. A.; Walton, R. A. *Multiple Bonds Between Metal Atoms*; Springer Science and Business Media, Incorporated, 2005.
- (3) Melnik, M.; Kabesova, M.; Koman, M.; Macaskova, L.; Garaj, J.; Holloway, C. E.; Valent, A. Copper(II) coordination compounds: Classification and analysis of crystallographic and structural data - III. Dimeric compounds, *J. Coord. Chem.* **1998**, *45*, 147.
- (4) Corbett, M.; Hoskins, B. F.; McLeod, N. J.; Oday, B. P. Binuclear Metal(II) Complexes of 1,3-Diphenyltriazene - Crystal and Molecular-Structures of Nickel(II), Palladium(II) and Copper(II) Derivatives, *Aust. J. Chem.* **1975**, *28*, 2377.
- (5) Clerac, R.; Cotton, F. A.; Daniels, L. M.; Gu, J. D.; Murillo, C. A.; Zhou, H. C. An infinite zigzag chain and the first linear chain of four copper atoms; Still no copper-copper bonding, *Inorg. Chem.* **2000**, *39*, 4488.
- (6) Berry, J. F.; Cotton, F. A.; Lei, P.; Murillo, C. A. Further structural and magnetic studies of tricopper dipyridylamido complexes, *Inorg. Chem.* **2003**, *42*, 377.
- (7) Knisley, T. J.; Ariyasena, T. C.; Sajavaara, T.; Saly, M. J.; Winter, C. H. Low Temperature Growth of High Purity, Low Resistivity Copper Films by Atomic Layer Deposition, *Chem. Mat.* **2011**, *23*, 4417.
- (8) Parr, R. G.; Yang, W. *Density-Functional Theory of Atoms and Molecules*; Oxford University Press, 1994.
- (9) Frisch, M. J.; Trucks, G. W.; Schlegel, H. B.; Scuseria, G. E.; Robb, M. A.; Cheeseman, J. R.; Montgomery, J. A.; Vreven, T.; Kudin, K. N.; Burant, J. C.; Millam, J. M.; Iyengar, S.; Tomasi, J.; Barone, V.; Mennucci, B.; Cossi, M.; Scalmani, G.; Rega, N.; Petersson, G. A.; Nakatsuji, H.; Hada, M.; Ehara, M.; Toyota, K.; Fukuda, R.; Hasegawa, J.; Ishida, M.;

Nakajima, T.; Honda, Y.; Kitao, O.; Nakai, H.; Klene, M.; Li, X.; Knox, J. E.; Hratchian, H. P.; Cross, J. B.; Bakken, V.; Adamo, C.; Jaramillo, J.; Gomperts, R.; Stratmann, R. E.; Yazyev, O.; Austin, A. J.; Cammi, R.; Pomelli, C.; Ochterski, J.; Ayala, P. Y.; Morokuma, K.; Voth, G. A.; Salvador, P.; Dannenberg, J. J.; Zakrzewski, V. G.; Dapprich, S.; Daniels, A. D.; Strain, M. C.; Farkas, Ö.; Malick, D. K.; Rabuck, A. D.; Raghavachari, K.; Foresman, J. B.; Ortiz, J. V.; Cui, Q.; Baboul, A. G.; Clifford, S.; Cioslowski, J.; Stefanov, B. B.; Liu, G.; Liashenko, A.; Piskorz, P.; Komaromi, I.; Martin, R. L.; Fox, D. J.; Keith, T.; Al-Laham, M. A.; Peng, C. Y.; Nanayakkara, A.; Challacombe, M.; Gill, P. M. W.; Johnson, B.; Chen, W.; Wong, M. W.; Gonzalez, C.; Pople, J. A. *Gaussian Development Version; Revision H.10*; Gaussian, Inc.; Wallingford, CT; 2010.

(10) Vosko, S. H.; Wilk, L.; Nusair, M. Accurate spin-dependent electron liquid correlation energies for local spin density calculations: a critical analysis, *Can. J. Phys.* **1980**, *58*, 1200.

(11) Lee, C. T.; Yang, W. T.; Parr, R. G. Development of the Colle-Salvetti correlation-energy formula into a functional of the electron density, *Phys. Rev. B* **1988**, *37*, 785.

(12) Becke, A. D. Density-functional thermochemistry. III. The role of exact exchange *J. Chem. Phys.* **1993**, *98*, 5648.

(13) Stephens, P. J.; Devlin, F. J.; Chabalowski, C. F.; Frisch, M. J. Ab Initio Calculation of Vibrational Absorption and Circular Dichroism Spectra Using Density Functional Force Fields, *J. Phys. Chem.* **1994**, *98*, 11623.

(14) Andrae, D.; Häußermann, U.; Dolg, M.; Stoll, H.; Preuß, H. Energy-adjusted *ab initio* pseudopotentials for the second and third row transition elements: Molecular test for M₂ (M=Ag, Au) and MH (M=Ru, Os), *Theor. Chem. Acc.* **1991**, *78*, 247.

(15) Schlegel, H. B.; McDouall, J. J. *Computational Advances in Organic Chemistry: Molecular Structure and Reactivity*; Kluwer Academic Publishers, 1991.

- (16) Bauernschmitt, R.; Ahlrichs, R. Stability analysis for solutions of the closed shell Kohn-Sham equation, *J. Chem. Phys.* **1996**, *104*, 9047.
- (17) Schlegel, H. B. Optimization of equilibrium geometries and transition structures, *J. Comput. Chem.* **1982**, *3*, 214.
- (18) Neese, F. Definition of corresponding orbitals and the diradical character in broken symmetry DFT calculations on spin coupled systems, *J. Phys. Chem. Solids* **2004**, *65*, 781.
- (19) Lim, B. S.; Rahtu, A.; Park, J. S.; Gordon, R. G. Synthesis and characterization of volatile, thermally stable, reactive transition metal amidinates, *Inorg. Chem.* **2003**, *42*, 7951.

Table 6-1. Detailed energetics (in hartree) for all of the species.*J* values listed in cm^{-1} .

Species	E(SCF) Triplet / E_h	E(SCF) Singlet / E_h	<i>J</i> / cm^{-1}
O-CH-O	-1151.517715	-1151.519805	-459
O-CH-NH	-1072.008924	-1072.011421	-548
HN-CH-NH	-992.471406	-992.473716	-507
O-CMe-O	-1308.832720	-1308.833793	-236
O-CMe-NMe	-1386.526398	-1386.527724	-291
MeN-CMe-NMe	-1464.183293	-1464.184542	-274

Table 6-2. Isocontour plots (0.05 au) of the corresponding orbitals for the AF coupled singlets. In all cases the alpha and beta orbitals are localized to one side of the molecule, and correspond to a Cu-centered radical consistent with the oxidation assignment Cu^{II} .

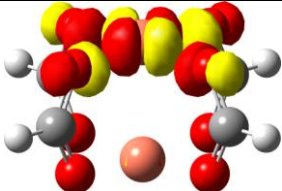
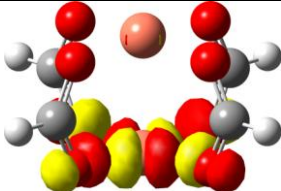
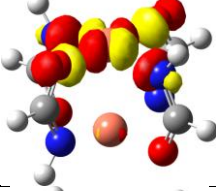
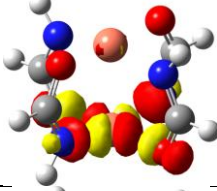
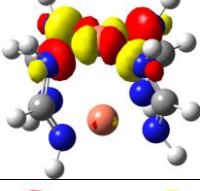
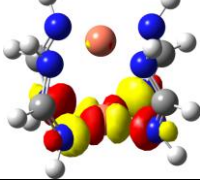
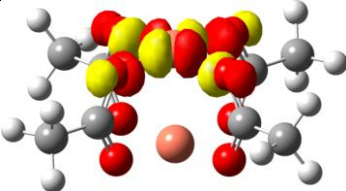
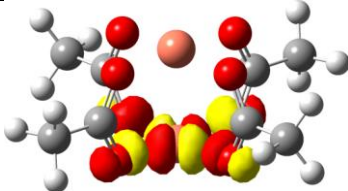
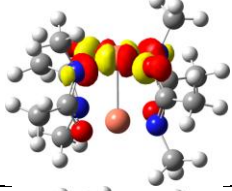
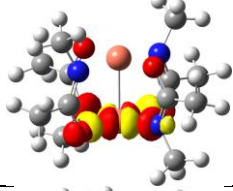
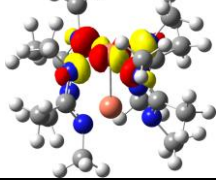
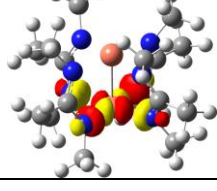
Species	α Corresponding Orbital	β Corresponding Orbital	$S_{\alpha\beta}$
O-CH-O			0.17
O-CH-NH			0.21
HN-CH-NH			0.19
O-CMe-O			0.13
O-CMe-NMe			0.15
MeN-CMe-NMe			0.16

Table 6-3. Geometric data for crystal structure and optimized geometries with bond lengths in Å and bond angles in degrees.

	Cu—Cu	R—R	θ
O-C_{Me}-NⁱPr (1)^a	2.4148(3)	2.274	7.4/7.1
O-C_{Me}-O	2.504	2.262	0.0
O-C_{Me}-NMe	2.440	2.290	4.1
MeN-C_{Me}-NMe	2.416	2.309	15.8
O-C_H-O	2.536	2.273	0.0
O-C_H-NH	2.547	2.306	0.0
HN-C_H-NH	2.595	2.330	10.8

^aExperimental values from X-ray structure data.

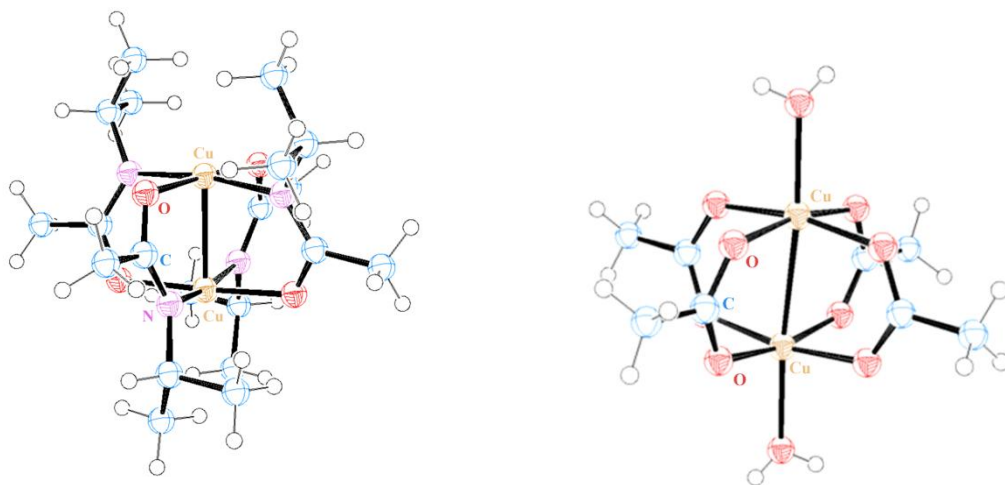


Figure 6-1. Left: X-ray crystal structure of the compound isolated by the Winter group.
Right: Copper acetate compound previously found and characterized

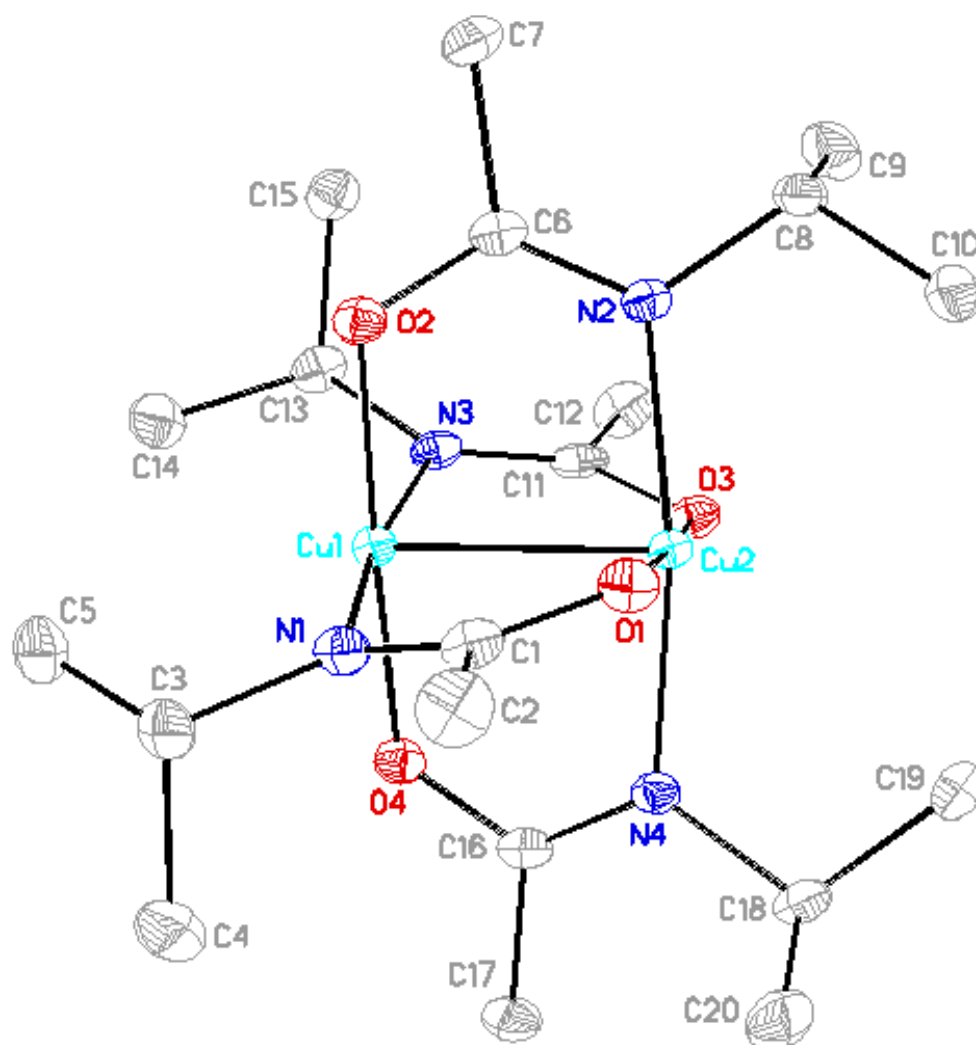


Figure 6-2. Perspective view of **1** with selected bond lengths (Å) and angles (°): Cu1-N1 1.996(2), Cu1-N3 1.987(1), Cu2-N2 1.999(2), Cu2-N4 1.997(2), Cu1-O2 1.955(1), Cu1-O4 1.955(1), Cu2-O1 1.963(1), Cu2-O3 1.958(1), Cu1-Cu2 2.4148(3), N1-Cu1-N3 171.21(6), N1-Cu1-O2 89.37(6), N1-Cu1-O4 90.21(6), N3-Cu1-O2 89.28(6), N3-Cu1-O4 90.66(6), O2-Cu1-O4 176.86(5), N2-Cu2-N4 171.15(6), N2-Cu2-O1 89.75(6), N2-Cu2-O3 89.90(6), N4-Cu2-O1 90.66(6), N4-Cu2-O3 89.18(6), O1-Cu2-O3 176.77(6).

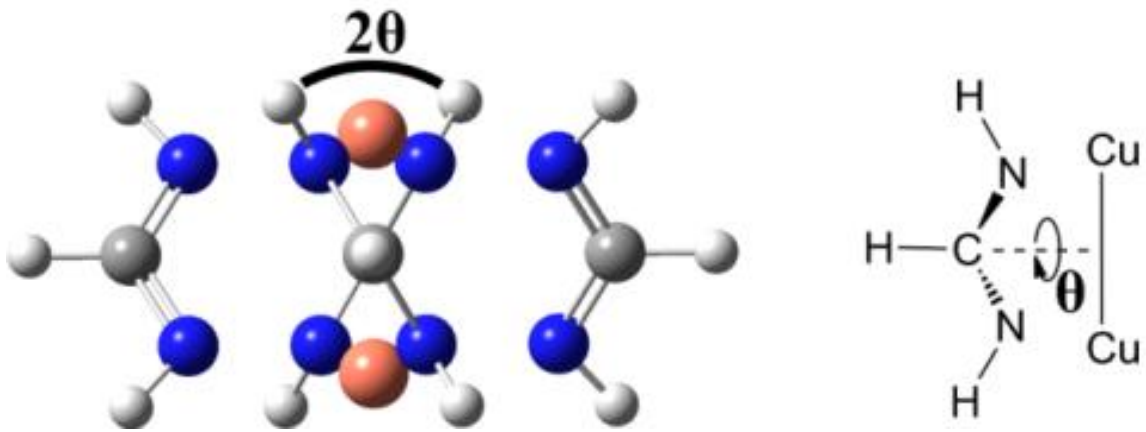


Figure 6-3. Definition of the Twist Angle θ

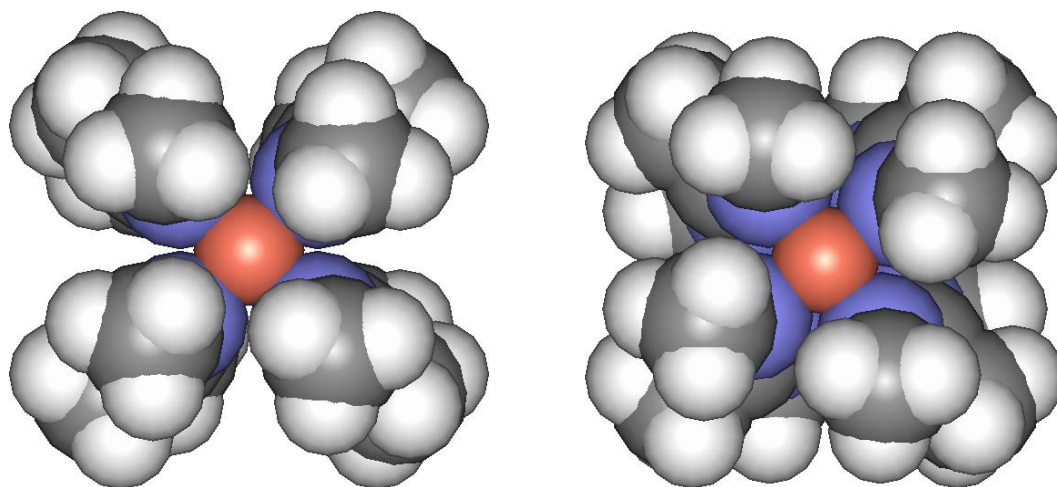


Figure 6-4. CPK model looking down the Cu–Cu axis of the MeN–C_{Me}–NMe model before and after ligand tilting. The shortest H···H distance between neighboring methyl groups is 2.66 and 2.98 Å, respectively.

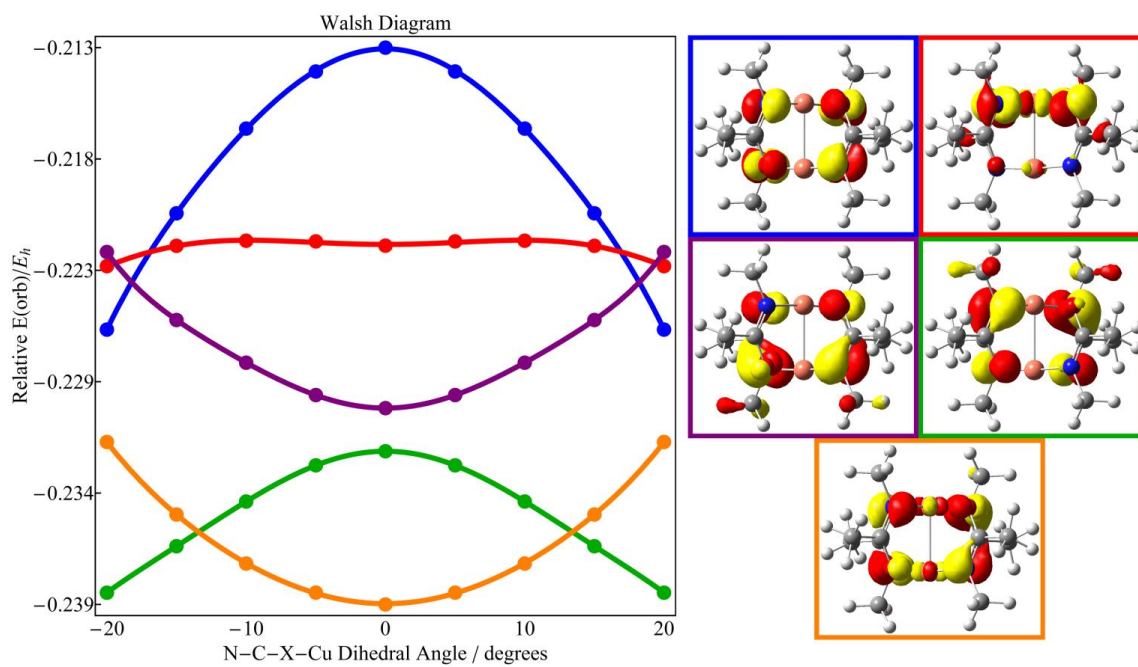


Figure 6-5. Walsh diagram for the O-C_{Me}-NMe model. The orbital which is most sensitive to the angular tilt is the antisymmetric combination of the ligand π -orbitals.

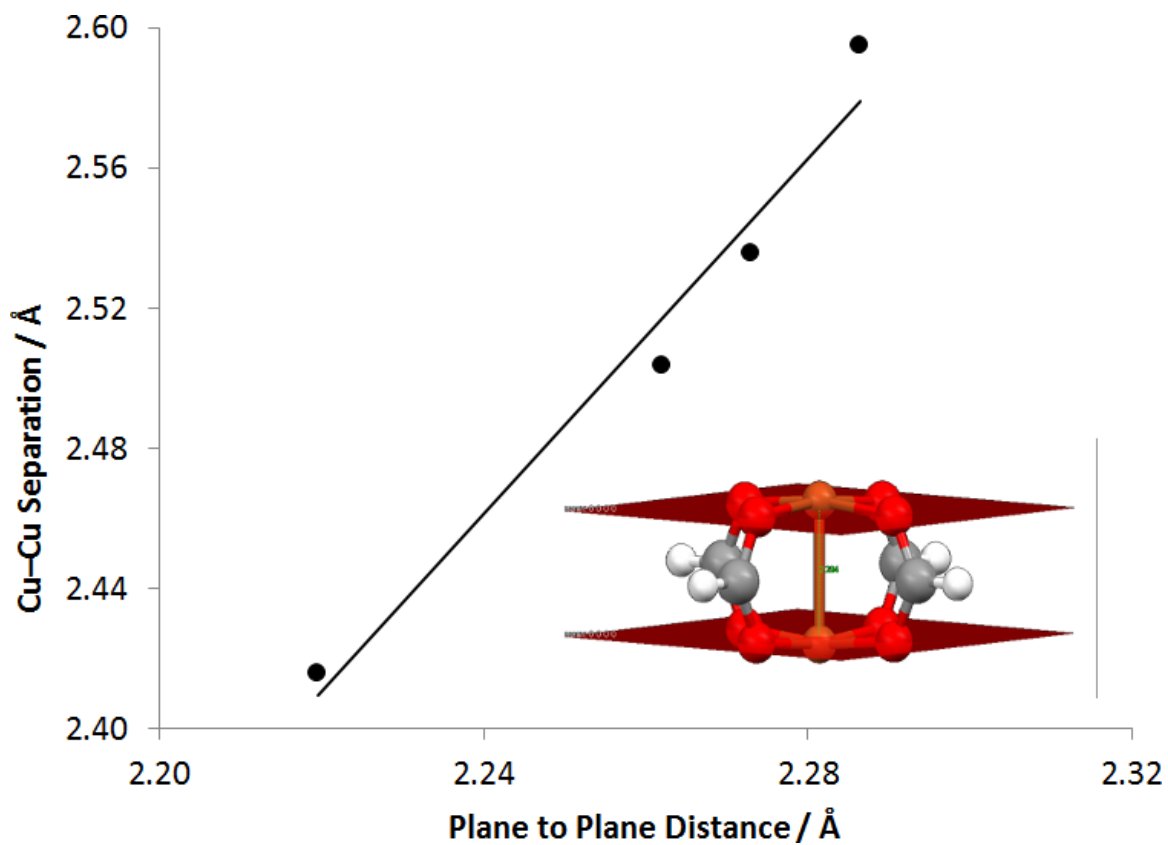


Figure 6-6. Correlation between plane-to-plane and Cu-Cu separation. Linear regression analysis: $y = 2.54x - 3.23$; $R^2 = 0.97$.

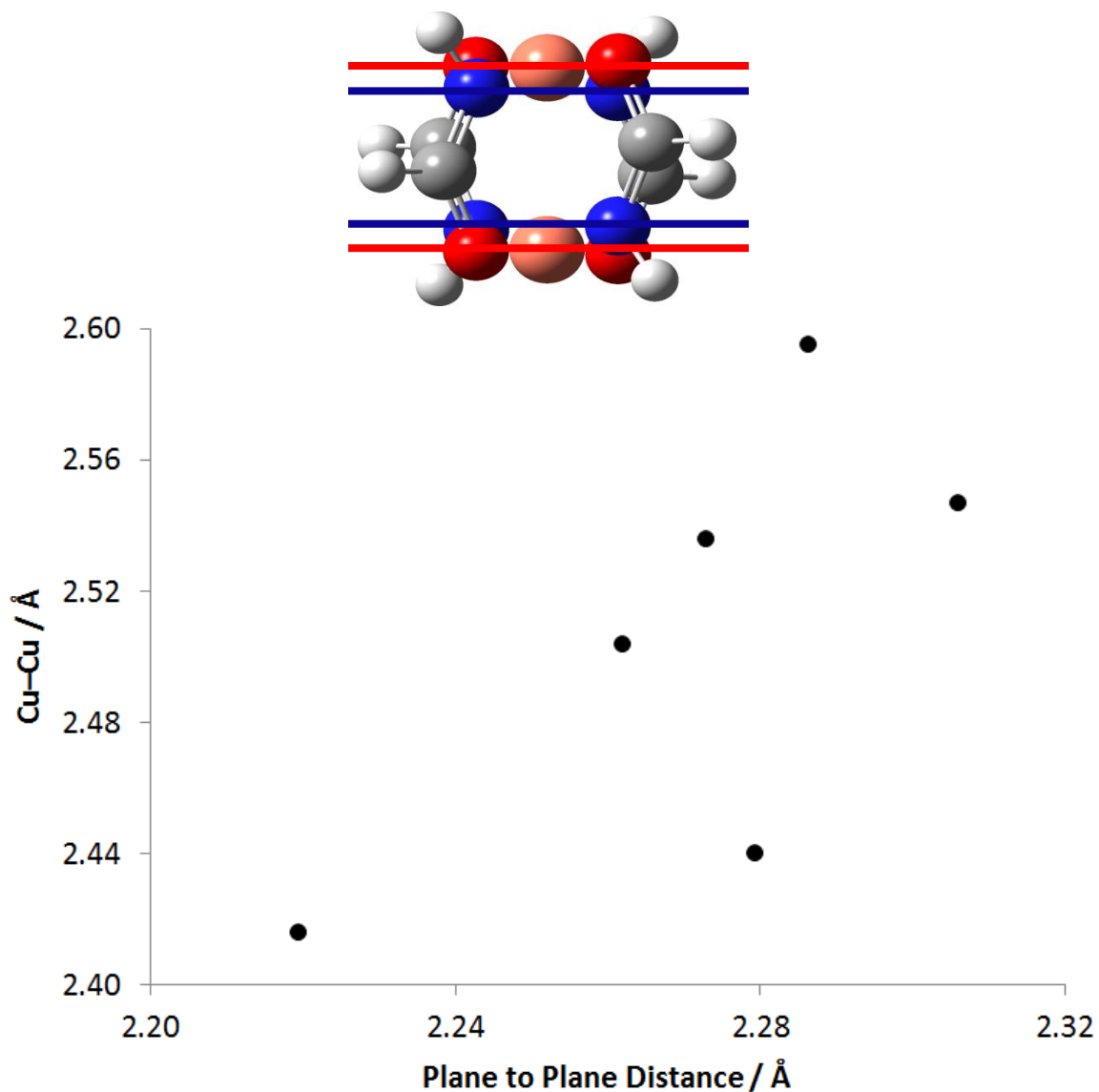


Figure 6-7. Linear regression plot including the amidate complexes. Because the interligand contact plane is not as clearly defined (top), the simple $r \cdot \cos(\theta)$ argument overestimates the Cu–Cu separation. Linear regression plot: $y = 1.63x - 1.20$; $R^2 = 0.49$.

Chapter 7

Bioinspired Five-Coordinate Iron(III) Complexes for Stabilization of Phenoxy Radicals

Marco M. Allard, Jason A. Sonk, Mary Jane Heeg, Bruce R. McGarvey,

H. Bernhard Schlegel, and Cláudio N Verani*

Department of Chemistry, Wayne State University, Detroit, Michigan 48202

With permission, adapted from:

Angew. Chem., Int. Ed., **2011**, 51(13), pp3178-3182

Copyright 2011, Wiley Publishing.

7.1 Introduction

The Verani group at Wayne State University is interested in integrating biomimetic principles into molecular materials that have customized and controllable properties.^{1,2} The notion of stimulus-triggered molecular switching between two or more ground states of comparable energy³⁻⁹ is particularly relevant because such switching leads to detectable electronic and structural changes. Coordination complexes that merge transition-metal ions with ligands that stabilize organic radicals are among the most promising candidates for redox-responsive switching processes. The Verani group is investigating bioinspired designs that incorporate the basic geometries that are present in redox-versatile enzymes, such as tyrosine hydroxylase¹⁰ and intradiol dioxygenase,¹¹⁻¹³ in

which five-coordinate iron(III) centers support radical-based mechanisms for generating l-3,4-dihydroxyphenylalanine (l-DOPA) and cleaving catechol-type rings, respectively. The Verani group has reported the behavior of high-spin iron(III) complexes that are confined to low-symmetry, pentadentate N_2O_3 environments.¹⁴⁻¹⁶ In these complexes, the assignment of oxidation states^{17,18} becomes challenging because of the contributions of ligand- and metal-centered orbitals to the same redox process, and the presence of five unpaired electrons. Nonetheless, they have shown that high oxidation states are unavailable to the metal ion, and that the ligand supports up to three consecutive oxidations, which leads to antiferromagnetic interactions. Our group has helped further the understanding of the sequence in which the phenolate oxidations occur by modifying the broken symmetry approach to enable better approximate molecular orbital assignments.

In spin-unrestricted systems the alpha and beta orbitals are not required to have similar spatial orbitals. Under spin restricted molecular orbital theory, systems with unpaired electrons tend to fill half filled orbitals last and, conversely, those half filled orbitals would be the first to be oxidized. In this case spin restricted MO theory would lead us to construct MOs where the unpaired electrons are found on the metal centers of the complexes synthesized by the Verani group. These metal orbitals would then contain the electrons mostly likely to be oxidized as opposed to the observed ligand electrons being oxidized first. Because the alpha and beta orbitals are not required to have the same spatial distribution in spin-unrestricted calculations it can be difficult to determine the nature of the orbitals describing the unpaired electrons. In MO theory the wavefunction is invariant to transformation among the occupied alpha orbitals and among

the occupied beta orbitals. This allows us to transform the orbitals to maximize their spatial overlap. The resultant orbitals are then sorted in terms of the optimal overlap between the alpha and beta orbitals, giving us the corresponding or biorthogonal orbitals. Because of the rotation of the orbitals, the Fock matrix is no longer diagonal and energetic information is lost. However the biorthogonal orbitals can be used to transform the Fock matrix in order to obtain some energetic information of the corresponding orbitals. A spin restricted orbital energy diagram can then be constructed by averaging the alpha and beta biorthogonal orbital energies. By constructing a corresponding molecular orbital diagram with orbital energetic information, a better description of redox properties of molecule with high degrees of electronic spin can be obtained.

7.2 Methods

The five-coordinate species $[\text{Fe}^{\text{III}}\text{L}^1]$ (**1**) and $[\text{Fe}^{\text{III}}\text{L}^2]$ (**2**), in which a low-symmetry ligand field is purposefully enforced around the $3d^5$ metal ion by the N_2O_3 ligands, synthesized by the Verani group is shown in Figure 7-1a. Ligands $[\text{L}^1]^{3-}$ and $[\text{L}^2]^{3-}$ both contain N_2O_3 environments with three phenolate moieties, denoted A, A', and B; phenolates A and A' share the same amine group and are chemically equivalent, whereas phenolate B is attached to either an azomethine group in L^1 or to a methylamine group in L^2 . Both species have four accessible ground states: $[\text{Fe}^{\text{III}}\text{L}]^0/[\text{Fe}^{\text{II}}\text{L}]^-$, $[\text{Fe}^{\text{III}}\text{L}]^+$, $[\text{Fe}^{\text{III}}\text{L}]^{2+}$, and $[\text{Fe}^{\text{III}}\text{L}]^{3+}$. In this chapter we set out to determine the sequence in which each of the phenolate rings is oxidized in the presence of the azomethine and the methylamine groups and the nature of the orbitals from which the electrons are lost, with the intent to contribute to the fundamental understanding of the redox and electronic behavior of high-spin $3d^5$ ions in five-coordinate ligand fields, and provide significant

insight into bioinspired redox cycling. To make the system computationally tractable, model systems were formed by removing the *tert*-butyl groups from the phenolate rings, yielding **1'** and **2'** in Figure 7-1b

Spin unrestricted density functional theory (DFT) calculations were carried out on **1'** and **2'** with the B3LYP¹⁹⁻²² functional and the 6-31G(d)²³⁻³² basis set in the development version of Gaussian³³. Solvation in dichloromethane was modeled with the integral equation formalism polarizable continuum model (IEF-PCM)³⁴⁻³⁶. Geometries were fully optimized without symmetry constraints, and stationary points were verified via frequency analysis. Molecular orbital analysis was facilitated by using the biorthogonal or corresponding orbital approach³⁷; energies for these orbitals were obtained by a unitary transform of the unrestricted Fock matrices into the biorthogonal basis. The averages of the energies of the alpha and beta biorthogonalized orbitals were used to approximate the energies of the restricted MO energies and these energies were used to build a classical restricted MO ladder diagram.

7.3 Results and Discussion

Electronic structure calculations were carried out on the models **1'** and **2'** and the products of the sequential oxidations $\mathbf{1}' \rightarrow \mathbf{1}'^+ \rightarrow \mathbf{1}'^{2+}$ and $\mathbf{2}' \rightarrow \mathbf{2}'^+ \rightarrow \mathbf{2}'^{2+}$ were investigated. Based on available experimental evidence,^{14,15,38-40} an antiferromagnetic coupling between the iron(III) center and the phenoxyl radicals was assumed. Figure 7-2 shows the structural changes and spin density plots for the two species (**1'** and **2'**) and their first and second oxidized states, only minor distortions are observed upon oxidation for each of the two species. The amount of spin density and the charges that are related to each phenolate/phenoxyl ring can be quantified by adding the contributions of the ring atoms

together (Table 7-1). The phenolate rings for **1'** and **2'** exhibit Mulliken spin densities of 0.17–0.24 and charges of -0.3–0.4. In contrast the monocation **1'⁺** has an excess of β density. This excess is consistent with a phenoxyl radical on ring A' that has a calculated spin density of -0.88 and charge of 0.20. Indeed, in the equivalent structure the Fe—OA' bond is lengthened by approximately 0.11 Å and the C=O bond is shortened by 0.06 Å. These values suggest that the ring becomes quinoid-like in nature and less effective as an electron donor. As a consequence, the Fe—O bonds to both of the remaining phenolate rings A and B shorten. Species **1'²⁺** behaves in a similar manner and a second phenolate to phenoxyl conversion takes place on ring A. The relative absence of geometric rearrangements fosters the overall redox bistability that is required for fast redox cycling between these species. Species **2'⁺** behaves differently to species **1'⁺** upon oxidation. The first oxidation leads to the formation of a phenoxyl radical on ring B. This is in clear opposition to the oxidation of ring A' in **1'**. The phenolate of ring B is associated with the methyl-substituted nitrogen atom and has Mulliken spin density and charge of -0.92 and 0.13, respectively. The Fe—O bond is elongated by 0.13 Å and the C=O bond is shortened to 1.28 Å. These changes are in excellent agreement with the values observed for the quinoid-like structure of **1'⁺**. The values that were calculated for **2'²⁺** also agree with the general trends that were discussed above for **1'²⁺**. It seems apparent that the nature of the nitrogen atoms (as a tertiary amine or an azomethine) leads to subtle but significant changes in the phenolate rings. The more π -acidic imino group stabilizes the phenolate-based HOMO that becomes less oxidizable than the equivalent aminophenolates. This change drives the electrochemical specificity of **1** and **2**. To our knowledge, this effect has not been reported for iron phenolate complexes before.

The analysis of MOs in high-spin species with $S=5/2$ that are antiferromagnetically coupled to $S=1/2$ organic radicals is far from trivial. In this study it was achieved by furthering the approach of corresponding biorthogonal orbitals that was used by Neese to analyze magnetic coupling in coordination complexes,³⁷ in which the energies of the corresponding α and β orbitals are averaged to construct a classical MO ladder diagram. This unitary transform of the unrestricted Fock matrices into the biorthogonal basis allows a qualitative energy ladder to be built for each of the compounds (Table 7-2). An increase in the charge for both complexes leads to a typical decrease in the relative energies of all of the frontier orbitals. This change indicates an increase in the ionization potential of the complexes that is related to a larger positive charge. Figures 7-3 and 7-4 depict the MO diagrams constructed with arbitrarily assigned d orbitals of the relevant singly and doubly occupied MOs (black and blue respectively) and spin coupled pairs (red). For **1'** we have determined $d_{x^2-y^2} > d_z^2 > d_{yz} > d_{xz} > d_{xy}$ and for **2'** we have determined as $d_{xz} > d_{xy} > d_{x^2-y^2} > d_{yz} > d_z^2$. The first doubly occupied MO relates to the electrochemical processes that correspond to the oxidation of the phenolate to phenoxyl radical, and accurately portrays the primary locus of the radical in **2'**. Similarly, for **2'+** the first doubly occupied MO relates to the second oxidative process. Interestingly, the presence of the azomethine group in complex **1'** leads to a shorter Fe—N1 bond and a longer Fe—O1 bond. This geometry affects the iron-based, singly occupied MO that coincides with the N1—Fe—O1 plane, and has an increased energy because of a π -antibonding interaction. The series **1'**→**1'+**→**1'2+** has comparable oxidation behavior, however, the elongation of the Fe—O1 bond results in a reduction in the energy of the remaining four 3d orbitals. These calculations required the use of the

IEF-PCM solvation model for the first doubly occupied MOs. Without solvation, the resulting radicals become delocalized over the three phenolate groups and lack physical meaning. As recently observed by Klüfers and co-workers⁴¹ in square planar high-spin Fe^{2+} species, it seems that five-coordination and low local symmetries around the metal ion support the formation of unique, highly nondegenerate MOs that are considerably distinct from an idealized $t_{2g}^*e_g^*$ octahedral scheme. These MOs rearrange in terms of energy upon ligand oxidation, which lowers the HOMOs, stabilizes the radicals, and allows redox cycling.

7.4 Conclusions

In conclusion, two iron(III) complexes that incorporate the basic geometrical principles that are found in enzymes that form and cycle radicals were synthesized. Both species were formed with pentadentate N_2O_3 ligands that confer a low symmetry on the metal ion. To understand the results of experimental studies of the electronic and redox properties of five coordination, these complexes were examined by theoretical methods. Subtle structural changes in the ligand, such as the introduction of a methyl group to the bridging nitrogen atom or the presence of an azomethine group, are sufficient to change the oxidation sequence of the phenolate groups. Computational calculations corroborated the experimental findings and allowed individual redox loci to be assigned for each of these compounds and the corresponding oxidized species. These results allow us to move one step further towards the development of redox-active molecular materials.

7.5 References

- (1) Kahn, O. Chemistry and physics of supramolecular magnetic materials, *Accounts Chem. Res.* **2000**, *33*, 647.
- (2) Sato, O.; Tao, J.; Zhang, Y. Z. Control of magnetic properties through external stimuli, *Angew. Chem.-Int. Edit.* **2007**, *46*, 2152.
- (3) Kahn, O.; Martinez, C. J. Spin-transition polymers: From molecular materials toward memory devices, *Science* **1998**, *279*, 44.
- (4) Fabbrizzi, L.; Licchelli, M.; Pallavicini, P. Transition metals as switches, *Accounts Chem. Res.* **1999**, *32*, 846.
- (5) Park, J.; Pasupathy, A. N.; Goldsmith, J. I.; Chang, C.; Yaish, Y.; Petta, J. R.; Rinkoski, M.; Sethna, J. P.; Abruna, H. D.; McEuen, P. L.; Ralph, D. C. Coulomb blockade and the Kondo effect in single-atom transistors, *Nature* **2002**, *417*, 722.
- (6) Dei, A.; Gatteschi, D.; Sangregorio, C.; Sorace, L. Quinonoid metal complexes: Toward molecular switches, *Accounts Chem. Res.* **2004**, *37*, 827.
- (7) Wassel, R. A.; Gorman, C. B. Establishing the molecular basis for molecular electronics, *Angew. Chem.-Int. Edit.* **2004**, *43*, 5120.
- (8) Flores-Torres, S.; Hutchison, G. R.; Soltzberg, L. J.; Abruna, H. D. Ruthenium molecular wires with conjugated bridging ligands: Onset of band formation in linear inorganic conjugated oligomers, *J. Am. Chem. Soc.* **2006**, *128*, 1513.
- (9) Kay, E. R.; Leigh, D. A.; Zerbetto, F. Synthetic molecular motors and mechanical machines, *Angew. Chem.-Int. Edit.* **2007**, *46*, 72.

- (10) Ramsey, A. J.; Hillas, P. J.; Fitzpatrick, P. F. Characterization of the active site iron in tyrosine hydroxylase - Redox states of the iron, *J. Biol. Chem.* **1996**, *271*, 24395.
- (11) Ferraroni, M.; Seifert, J.; Travkin, V. M.; Thiel, M.; Kaschabek, S.; Scozzafava, A.; Golovleva, L.; Schlomann, M.; Briganti, F. Crystal structure of the hydroxyquinol 1,2-dioxygenase from *Nocardioides simplex* 3E, a key enzyme involved in polychlorinated aromatics biodegradation, *J. Biol. Chem.* **2005**, *280*, 21144.
- (12) Borowski, T.; Siegbahn, P. E. M. Mechanism for catechol ring cleavage by non-heme iron intradiol dioxygenases: A hybrid DFT study, *J. Am. Chem. Soc.* **2006**, *128*, 12941.
- (13) Pau, M. Y. M.; Davis, M. I.; Orville, A. M.; Lipscomb, J. D.; Solomon, E. I. Spectroscopic and electronic structure study of the enzyme-substrate complex of intradiol dioxygenases: Substrate activation by a high-spin ferric non-heme iron site, *J. Am. Chem. Soc.* **2007**, *129*, 1944.
- (14) Lanznaster, M.; Hratchian, H. P.; Heeg, M. J.; Hryhorczuk, L. M.; McGarvey, B. R.; Schlegel, H. B.; Verani, C. N. Structural and electronic behavior of unprecedented five-coordinate iron(III) and gallium(III) complexes with a new phenol-rich electroactive ligand, *Inorg. Chem.* **2006**, *45*, 955.
- (15) Lanznaster, M.; Heeg, M. J.; Yee, G. T.; McGarvey, B. R.; Verani, C. N. Design of molecular scaffolds based on unusual geometries for magnetic modulation of spin-diverse complexes with selective redox response, *Inorg. Chem.* **2007**, *46*, 72.

- (16) Lesh, F. D.; Shanmugam, R.; Allard, M. M.; Lanznaster, M.; Heeg, M. J.; Rodgers, M. T.; Shearer, J. M.; Verani, C. N. A Modular Approach to Redox-Active Multimetallic Hydrophobes of Discoid Topology, *Inorg. Chem.* **2010**, *49*, 7226.
- (17) Chaudhuri, P.; Verani, C. N.; Bill, E.; Bothe, E.; Weyhermuller, T.; Wieghardt, K. Electronic structure of bis(o-iminobenzosemiquinonato)metal complexes (Cu, Ni, Pd). The art of establishing physical oxidation states in transition-metal complexes containing radical ligands, *J. Am. Chem. Soc.* **2001**, *123*, 2213.
- (18) Chirik, P. J.; Wieghardt, K. Radical Ligands Confer Nobility on Base-Metal Catalysts, *Science* **2010**, *327*, 794.
- (19) Vosko, S. H.; Wilk, L.; Nusair, M. Accurate spin-dependent electron liquid correlation energies for local spin density calculations: a critical analysis, **1980**, *58*, 1200.
- (20) Lee, C.; Yang, W.; Parr, R. G. Development of the Colle-Salvetti correlation-energy formula into a functional of the electron density, **1988**, *37*, 785.
- (21) Becke, A. D. Density-functional thermochemistry. III. The role of exact exchange, **1993**, *98*, 5648.
- (22) Stephens, P. J.; Devlin, F. J.; Chabalowski, C. F.; Frisch, M. J. Ab Initio Calculation of Vibrational Absorption and Circular Dichroism Spectra Using Density Functional Force Fields, *J. Phys. Chem.* **1994**, *98*, 11623.
- (23) Binning Jr., R. C.; Curtiss, L. A. Compact contracted basis-sets for 3rd-row atoms - GA-KR, **1990**, *11*, 1206.

- (24) Blaudeau, J.-P.; McGrath, M. P.; Curtiss, L. A.; Radom, L. Extension of Gaussian-2 (G2) theory to molecules containing third-row atoms K and Ca, **1997**, *107*, 5016.
- (25) Ditchfield, R.; Hehre, W. J.; Pople, J. A. Self-Consistent Molecular Orbital Methods. 9. Extended Gaussian-type basis for molecular-orbital studies of organic molecules, **1971**, *54*, 724.
- (26) Francl, M. M.; Pietro, W. J.; Hehre, W. J.; Binkley, J. S.; DeFrees, D. J.; Pople, J. A.; Gordon, M. S. Self-Consistent Molecular Orbital Methods. 23. A polarization-type basis set for 2nd-row elements, **1982**, *77*, 3654.
- (27) Gordon, M. S. The isomers of silacyclopropane, **1980**, *76*, 163.
- (28) Hariharan, P. C.; Pople, J. A. Influence of polarization functions on molecular-orbital hydrogenation energies, *Theoretica Chimica Acta* **1973**, *28*, 213.
- (29) Hariharan, P. C.; Pople, J. A. Accuracy of AH equilibrium geometries by single determinant molecular-orbital theory, **1974**, *27*, 209.
- (30) Hehre, W. J.; Ditchfield, R.; Pople, J. A. Self-Consistent Molecular Orbital Methods. 12. Further extensions of Gaussian-type basis sets for use in molecular-orbital studies of organic-molecules, **1972**, *56*, 2257.
- (31) Rassolov, V. A.; Pople, J. A.; Ratner, M. A.; Windus, T. L. 6-31G* basis set for atoms K through Zn, *Journal of Chemical Physics* **1998**, *109*, 1223.
- (32) Rassolov, V. A.; Ratner, M. A.; Pople, J. A.; Redfern, P. C.; Curtiss, L. A. 6-31G* Basis Set for Third-Row Atoms, **2001**, *22*, 976.
- (33) Frisch, M. J.; Trucks, G. W.; Schlegel, H. B.; Scuseria, G. E.; Robb, M. A.; Cheeseman, J. R.; Scalmani, G.; Barone, V.; Mennucci, B.; Petersson, G. A.;

Nakatsuji, H.; Caricato, M.; Li, X.; Hratchian, H. P.; Izmaylov, A. F.; Bloino, J.; Zheng, G.; Sonnenberg, J. L.; Hada, M.; Ehara, M.; Toyota, K.; Fukuda, R.; Hasegawa, J.; Ishida, M.; Nakajima, T.; Honda, Y.; Kitao, O.; Nakai, H.; Vreven, T.; Montgomery, J. A., Jr.; Peralta, J. E.; Ogliaro, F.; Bearpark, M.; Heyd, J. J.; Brothers, E.; Kudin, K. N.; Staroverov, V.; Kobayashi, R.; Normand, J.; Raghavachari, K.; Rendell, A.; Burant, J. C.; Iyengar, S. S.; Tomasi, J.; Cossi, M.; Rega, N.; Millam, J. M.; Klene, M.; Knox, J. E.; Cross, J. B.; Bakken, V.; Adamo, C.; Jaramillo, J.; Gomperts, R.; Stratmann, R. E.; Yazyev, O.; Austin, A. J.; Cammi, R.; Pomelli, C.; Ochterski, J. W.; Martin, R. L.; Morokuma, K.; Zakrzewski, V. G.; Voth, G. A.; Salvador, P.; Dannenberg, J. J.; Dapprich, S.; Parandekar, P. V.; Mayhall, N. J.; Daniels, A. D.; Farkas, O.; Foresman, J. B.; Ortiz, J. V.; Cioslowski, J.; Fox, D. J. *Gaussian DV*; Revision H.04; Gaussian, Inc.; Wallingford, CT; 2009.

(34) Miertus, S.; Scrocco, E.; Tomasi, J. Electrostatic Interaction of a Solute with a Continuum - A Direct Utilization of *ab initio* Molecular Potentials for the Prevision of Solvent Effects¹, *Chem. Phys.* **1981**, *55*, 117.

(35) Miertus, S.; Tomasi, J. Approximate Evaluations of the Electrostatic Free-Energy and Internal Energy Changes in Solution Processes, *Chem. Phys.* **1982**, *65*, 239.

(36) Tomasi, J.; Mennucci, B.; Cammi, R. Quantum Mechanical Continuum Solvation Models, **2005**, *105*, 2999.

(37) Neese, F. Definition of corresponding orbitals and the diradical character in broken symmetry DFT calculations on spin coupled systems, *J. Phys. Chem. Solids* **2004**, *65*, 781.

(38) Imbert, C.; Hratchian, H. P.; Lanznaster, M.; Heeg, M. J.; Hryhorczuk, L. M.; McGarvey, B. R.; Schlegel, H. B.; Verani, C. N. Influence of ligand rigidity and ring substitution on the structural and electronic behavior of trivalent iron and gallium complexes with asymmetric tridentate ligands, *Inorg. Chem.* **2005**, *44*, 7414.

(39) Kurahashi, T.; Kobayashi, Y.; Nagatomo, S.; Tosha, T.; Kitagawa, T.; Fujii, H. Oxidizing intermediates from the sterically hindered iron salen complexes related to the oxygen activation by nonheme iron enzymes, *Inorg. Chem.* **2005**, *44*, 8156.

(40) Kurahashi, T.; Fujii, H. One-Electron Oxidation of Electronically Diverse Manganese(III) and Nickel(II) Salen Complexes: Transition from Localized to Delocalized Mixed-Valence Ligand Radicals, *J. Am. Chem. Soc.* **2011**, *133*, 8307.

(41) Wurzenberger, X.; Piotrowski, H.; Klufers, P. A Stable Molecular Entity Derived from Rare Iron(II) Minerals: The Square-Planar High-Spin-d(6) (FeO₄)-O-II Chromophore, *Angew. Chem.-Int. Edit.* **2011**, *50*, 4974.

Table 7-1. Mulliken charge and spin density analysis and selected bond length(Å) for $1'$, $1'^+$, $1'^{2+}$, $2'$, $2'^+$, and $2'^{2+}$.^a

	Mulliken Spin Density	Mulliken Charge	Fe—O	C(ring)—O
$1'$ S = 5/2				
Fe ³⁺	4.19	1.34		
Ring A	0.24	-0.42	1.86	1.34
Ring A'	0.23	-0.43	1.87	1.34
Ring B (C=N)	0.17	-0.30	1.93	1.31
$1'^+$ S = 4/2				
Fe ³⁺	4.17	1.39		
Ring A	0.28	-0.30	1.83	1.34
Ring A' (R [↑])	-0.88	0.20	1.98	1.28
Ring B	0.23	-0.40	1.88	1.31
$1'^{2+}$ S = 3/2				
Fe ³⁺	4.18	1.34		
Ring A (R [↑])	-0.87	0.33	1.93	1.28
Ring A' (R [↑])	-0.90	0.29	1.97	1.28
Ring B	0.34	-0.44	1.85	1.32
$2'$ S = 5/2				
Fe ³⁺	4.18	1.30		
Ring A	0.21	-0.35	1.88	1.34
Ring A'	0.22	-0.35	1.88	1.33
Ring B	0.22	0.23	1.88	1.33
$2'^+$ S = 4/2				
Fe ³⁺	4.16	1.34		
Ring A	0.28	-0.25	1.84	1.35
Ring A'	0.27	-0.20	1.85	1.34
Ring B (R [↑])	-0.92	0.13	2.01	1.28
$2'^{2+}$ S = 3/2				
Fe ³⁺	4.12	1.39		
Ring A	0.45	-0.19	1.83	1.34
Ring A' (R [↑])	-0.90	0.27	1.96	1.28
Ring B (R [↑])	-0.91	0.27	1.97	1.28

^aB3LYP/6-31G(d) with IEF-PCM solvation in dichloromethane. R[↑] denotes the phenoxy

location.

Table 7-2. Orbital energies for $1'$, $1'^+$, $1'^{2+}$, $2'$, $2'^+$, and $2'^{2+}$

(1)						(2)					
BiOrMo	A Canon MO	Eh	B Canon MO	Eh	Average Eh	BiOrMo	A Canon MO	Eh	B Canon MO	Eh	Average Eh
115	115	-0.361985	112	-0.328798	-0.345392	120	131	-0.363956	120	-0.347505	-0.355731
116	124	-0.355003	119	-0.305424	-0.330214	121	119	-0.361523	123	-0.321651	-0.341587
117	119	-0.354026	117	-0.302250	-0.328138	122	120	-0.359352	122	-0.304651	-0.332002
118	123	-0.351931	118	-0.299807	-0.325869	123	130	-0.355598	125	-0.291441	-0.323520
119	122	-0.346057	120	-0.297330	-0.321694	124	125	-0.340386	124	-0.269052	-0.304719
120	118	-0.342512	110	-0.296975	-0.319744	125	122	-0.332993	126	-0.266893	-0.299943
121	120	-0.341101	121	-0.262099	-0.301600	126	127	-0.331007	116	-0.261245	-0.296126
122	112	-0.340364	122	-0.101038	-0.220701	127	128	-0.329134	127	-0.091850	-0.210492
123	117	-0.336177	123	-0.093223	-0.214700	128	129	-0.329032	128	-0.089249	-0.209141
124	121	-0.311628	124	-0.078285	-0.194957	129	126	-0.317921	129	-0.080357	-0.199139
125	126	-0.309587	125	-0.075300	-0.192444	130	124	-0.312026	130	-0.070063	-0.191045
126	110	-0.303672	126	-0.067039	-0.185356	131	116	-0.284433	131	-0.044029	-0.154231
127	127	-0.079252	127	-0.049200	-0.064226	132	132	-0.027013	132	-0.026641	-0.026827
128	128	-0.022610	128	-0.021335	-0.021973	133	133	-0.024961	133	-0.023509	-0.024235
129	129	-0.009603	129	-0.008129	-0.008866	134	134	-0.007136	134	-0.006209	-0.006673
130	130	-0.002916	130	-0.001574	-0.002245	135	135	-0.002254	135	-0.001015	-0.001635

(1) ⁺						(2) ⁺					
BiOrMo	A Canon MO	Eh	B Canon MO	Eh	Average Eh	BiOrMo	A Canon MO	Eh	B Canon MO	Eh	Average Eh
115	122	-0.400228	114	-0.372173	-0.386201	120	126	-0.376948	119	-0.333221	-0.355085
116	114	-0.398525	117	-0.330978	-0.364752	121	125	-0.370315	124	-0.313847	-0.342081
117	117	-0.382091	116	-0.329233	-0.355662	122	117	-0.369253	123	-0.298250	-0.333752
118	116	-0.377402	111	-0.327203	-0.352303	123	119	-0.367629	122	-0.293774	-0.330702
119	120	-0.370876	119	-0.312812	-0.341844	124	130	-0.365504	126	-0.279141	-0.322323
120	123	-0.369845	118	-0.279552	-0.324899	125	123	-0.353530	113	-0.270767	-0.312149
121	121	-0.360749	121	-0.279215	-0.319982	126	129	-0.348746	114	-0.265278	-0.307012
122	125	-0.339655	122	-0.133590	-0.236623	127	122	-0.347619	127	-0.128850	-0.238235
123	111	-0.333678	123	-0.127028	-0.230353	128	124	-0.305245	128	-0.124835	-0.215040
124	118	-0.322779	124	-0.120944	-0.221862	129	113	-0.272760	129	-0.116559	-0.194660
125	119	-0.304803	125	-0.102284	-0.203544	130	114	-0.266849	130	-0.105561	-0.186205
126	126	-0.194384	126	-0.090508	-0.142446	131	131	-0.192415	131	-0.082726	-0.137571
127	127	-0.097696	127	-0.079026	-0.088361	132	132	-0.045314	132	-0.057078	-0.051196
128	128	-0.047338	128	-0.057878	-0.052608	133	133	-0.042942	133	-0.052587	-0.047765
129	129	-0.038998	129	-0.052511	-0.045755	134	134	-0.041645	134	-0.042465	-0.042055
130	130	-0.029478	130	-0.038597	-0.034038	135	135	-0.028714	135	-0.041256	-0.034985

(1) ²⁺						(2) ²⁺					
BiOrMo	A Canon MO	Eh	B Canon MO	Eh	Average Eh	BiOrMo	A Canon MO	Eh	B Canon MO	Eh	Average Eh
115	122	-0.429042	114	-0.364519	-0.396781	120	109	-0.418631	117	-0.374372	-0.396502
116	114	-0.418137	109	-0.357374	-0.387756	121	125	-0.395445	121	-0.330264	-0.362855
117	123	-0.410307	117	-0.336690	-0.373499	122	128	-0.392114	122	-0.329442	-0.360778
118	119	-0.388260	116	-0.335383	-0.361822	123	123	-0.387055	125	-0.298722	-0.342889
119	118	-0.387244	120	-0.302484	-0.344864	124	124	-0.383791	126	-0.293871	-0.338831
120	124	-0.374263	115	-0.297722	-0.335993	125	129	-0.377330	118	-0.287098	-0.332214
121	109	-0.370951	121	-0.297077	-0.334014	126	120	-0.343383	120	-0.276987	-0.310185
122	115	-0.345244	122	-0.174768	-0.260006	127	121	-0.322441	127	-0.164806	-0.243624
123	117	-0.327388	123	-0.162480	-0.244934	128	122	-0.321111	128	-0.156419	-0.238765
124	116	-0.326899	124	-0.160302	-0.243601	129	118	-0.290063	129	-0.150539	-0.220301
125	125	-0.217064	125	-0.148075	-0.182570	130	130	-0.211756	130	-0.132451	-0.172104
126	126	-0.211742	126	-0.114653	-0.163198	131	131	-0.208373	131	-0.109983	-0.159178
127	127	-0.119031	127	-0.107915	-0.113473	132	132	-0.063813	132	-0.073783	-0.068798
128	128	-0.069296	128	-0.079857	-0.074577	133	133	-0.059076	133	-0.070847	-0.064962
129	129	-0.059254	129	-0.075269	-0.067262	134	134	-0.056179	134	-0.069597	-0.062888
130	130	-0.055771	130	-0.072923	-0.064347	135	135	-0.054771	135	-0.068368	-0.061570

^aB3LYP/6-31G(d) with IEF-PCM solvation in Dichloromethane.

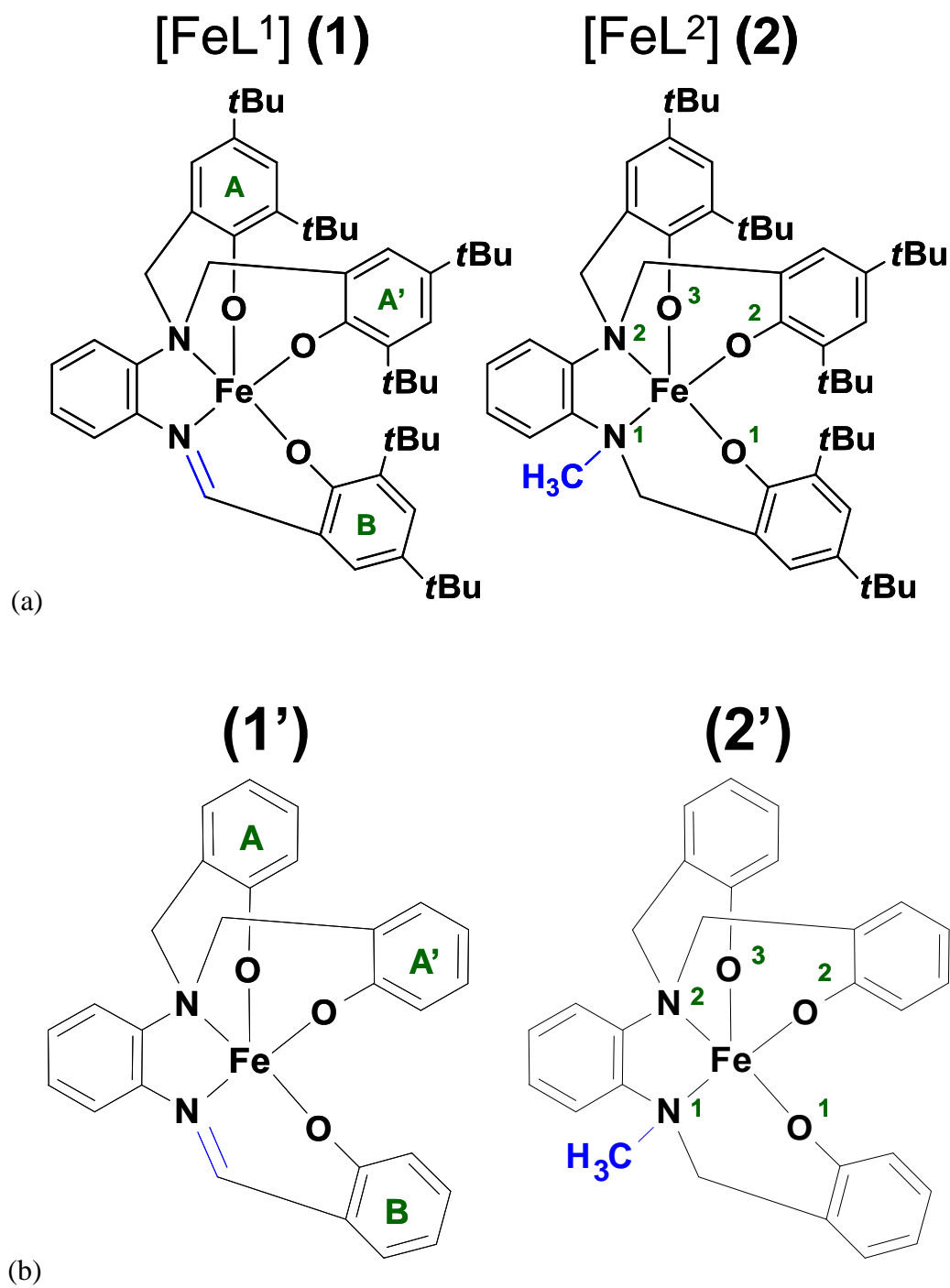


Figure 7-1. Experimental structures of **1** and **2** (top) and computational models for **1'** and **2'** (bottom)

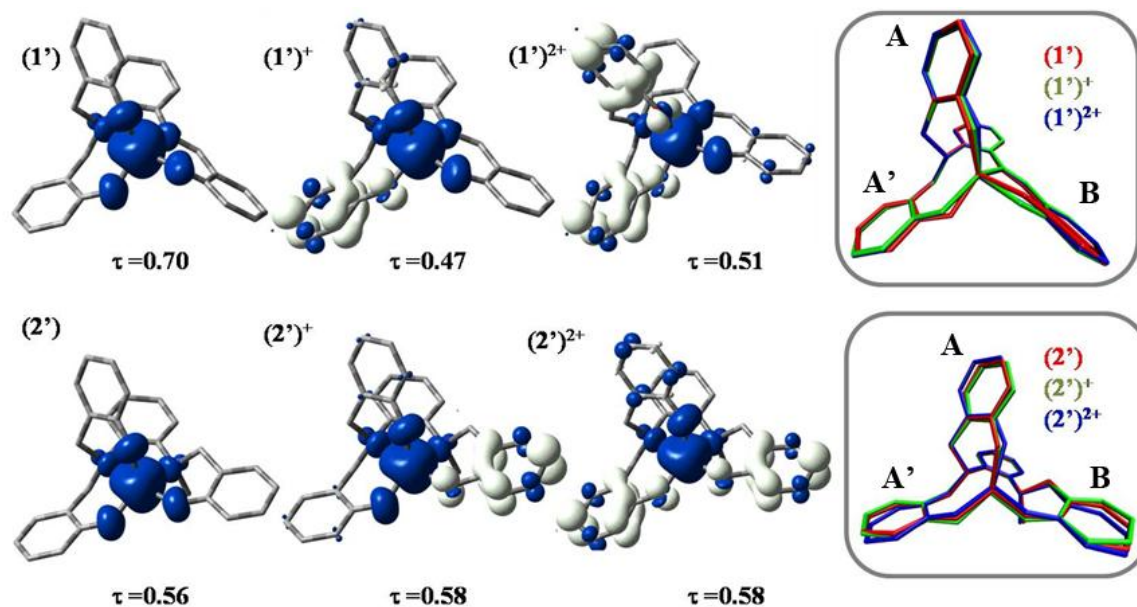


Figure 7-2. Spin density plots for the oxidation series of **1'** (top, left) and **2'** (bottom, left). The white and blue areas of electron density correspond to excess α and β electron spin density, respectively. Superimposition of the optimized geometries of the sequential oxidation of **1'** (top, right) and **2'** (bottom, right).

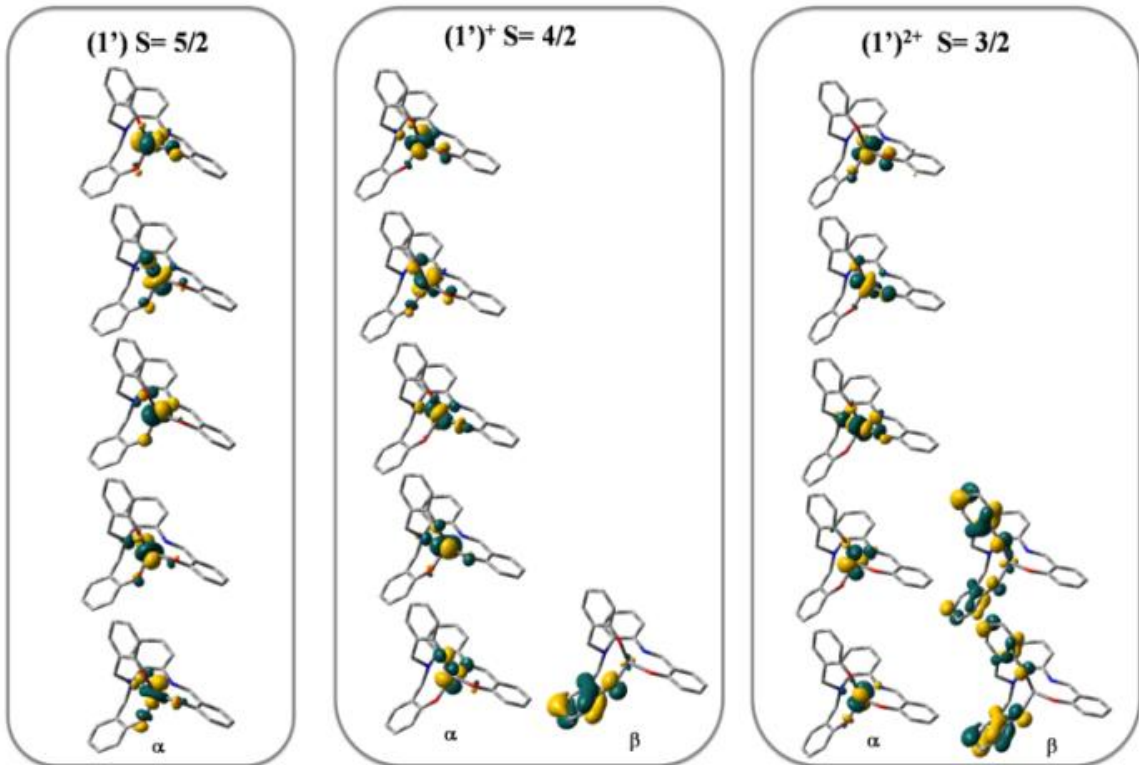
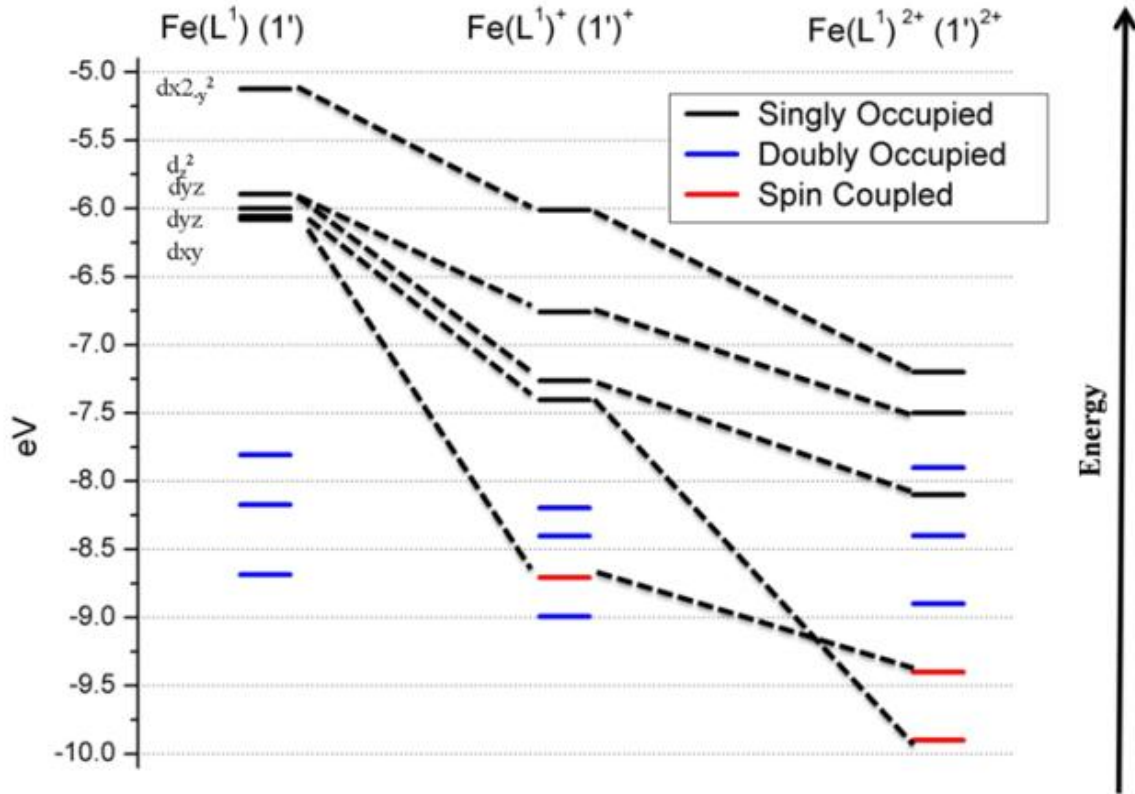


Figure 7-3. Average orbital energy ladder (top) and selected frontier orbitals (bottom, α -SOMOs and spin coupled Pairs with Hydrogen atoms omitted for clarity) for $\mathbf{1'}$, $\mathbf{1'^+}$, and $\mathbf{1'^{2+}}$. (B3LYP/6-31G(d) IEF-PCM dichloromethane).

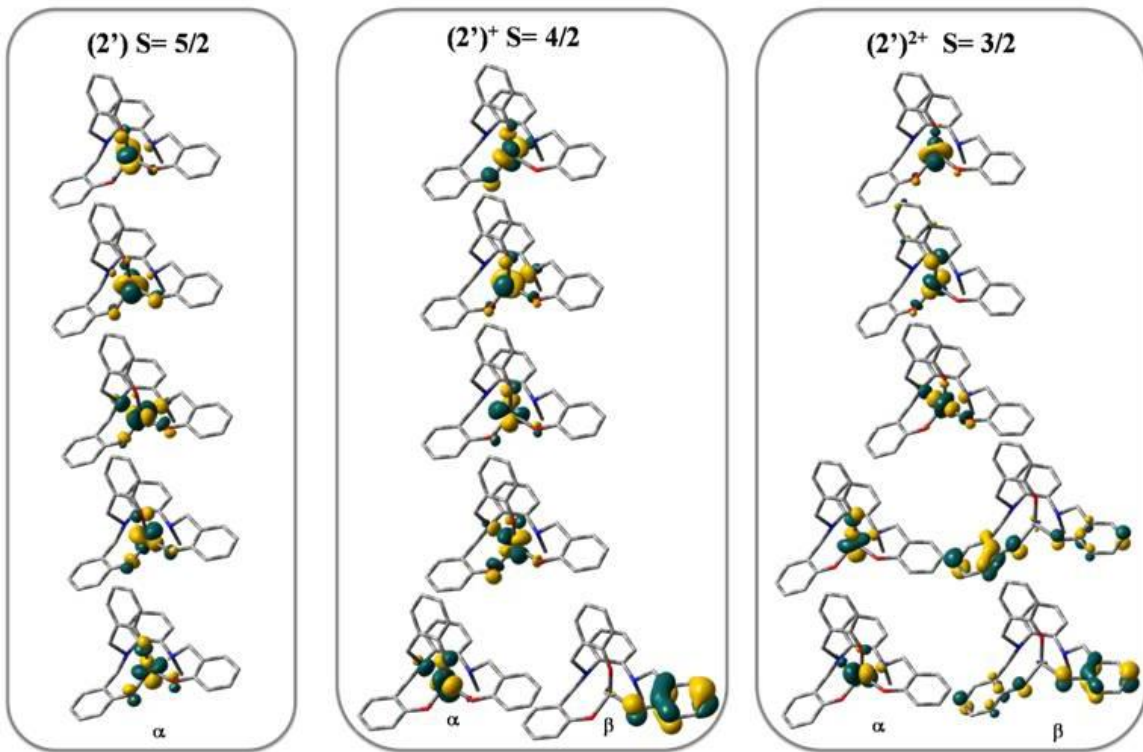
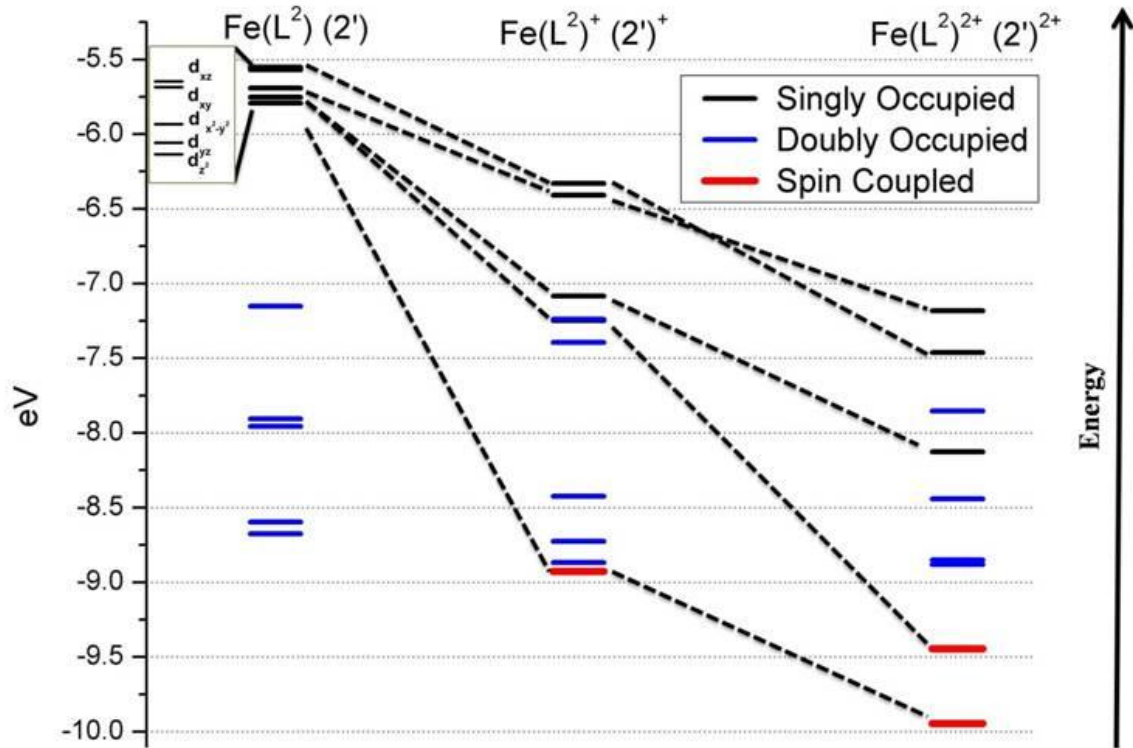


Figure 7-4. Average orbital energy ladder (top) and selected frontier orbitals (bottom, α -SOMOs and spin coupled Pairs with Hydrogen atoms omitted for clarity) for $\mathbf{2'}$, $\mathbf{2'^+}$, and $\mathbf{2'^{2+}}$. (B3LYP/6-31G(d) IEF-PCM dichloromethane).

Chapter 8

Modeling Reactions inside Single Walled Carbon Nanotubes

Jason A. Sonk, Evelyn M. Goldfield, and H. Bernhard Schlegel*

Department of Chemistry, Wayne State University, Detroit, Michigan 48202

Manuscript in Preparation

8.1 Introduction

Since their discovery, carbon nanotubes have been examined for use in a wide variety of applications in chemistry, physics, and medicine.¹⁻¹⁵ Of the many applications, their use as a host environment has been studied with great interest¹⁶⁻²⁶ and they are known to be able to host a variety of guest molecules within them. The interior of a nanotube offers a unique environment for chemical reactions. The small interior diameter provides mechanical confinement and the highly polarizable walls of the nanotube act like a high dielectric solvent. The physical confinement of reactants within single walled carbon nanotubes (SWCNTs) can affect both reaction rates and reaction equilibria in a variety of ways including selective adsorption of reactants, products and transition states, as well as induce steric effects and geometric constraints. In addition to the physical confinement, the electronic environment of SWCNTs can influence the electronic structure of species inside of them. Studies have shown that a system confined

to a SWCNT can be thought of as being in a solid solvent.²⁷⁻³¹ The level of control provided by computational modeling of nanotubes has the potential to provide a wealth of insight into predicting novel interactions and reactions taking place inside and around a nanotube environment which would allow researchers to be able to predict the behavior of reagents in nanotube environments without first having to synthesize and prepare their host-guest system of interest. However, even in a small nanotube segment, ~1.1 nm in length and ~0.7 nm in diameter, there are approximately 110 heavy atoms which is a challenge for quantum chemical calculations. Experimentally observed nanotubes can vary in length and diameter by up to several orders of magnitude, increasing the number of heavy atoms dramatically. Unfortunately, since the computational time needed to simulate structures scales approximately as the number of atoms to the fourth power¹⁹, running calculations on various nanotubes of interest can be prohibitive. As a first approach one may turn to molecular mechanics and semiempirical methods which, while computationally efficient, miss out on significant electronic interactions between nanotubes and reagents. In this chapter we develop an inexpensive, chemically accurate modeling method that facilitates the analysis of chemical reactions in and around single walled carbon nanotubes (SWCNT). The role of the SWCNT can be partitioned into an electronic interaction coupled with a geometric confinement so it should be possible to scale down the complexity of the overall system considerably. Geometric confinement can be handled very well by molecular mechanics methods. On the other hand, the electronic interactions are more difficult and more expensive to model well. In this chapter we focus on developing an inexpensive model for the electronic interactions between a SWCNT and a guest molecular system within the nanotube. The validity of

this SWCNT model will be tested by comparing the potential energy surfaces of several systems of interest calculated using the CNT models and the full SWCNT system. Doing so will allow us to determine the limitations of the model and the shortcomings of any approximations made in parameterizing the proposed model. With this knowledge in hand the SWCNT models can then be used to predict reactions of various substituents inside nanotubes.

8.2 Methods

To make optimization of a species inside of a nanotube more affordable we propose a model which partitions the effects of a nanotube on a guest species into two parts: (a) the electrostatic interactions are handled using a solvation model and (b) the physical confinement is handled using molecular mechanics. Solvation models come in two varieties: explicit solvation models which include individual solvent molecules in the calculation and implicit solvation models which account for the interactions between solvent and solute molecules by using a polarizable medium to represent the solvent. The behavior of this polarizable medium mimics the alignment of dipoles and the consequent electrostatic induction interactions between solvent and solute molecules. The resulting electric field is known as a reaction field. The highly polarizable nature of the π -electrons in a SWCNT allow the electronic environment of the nanotube to behave much in the same way that a solvent would around a solute molecule creating a similar reaction field. There are several computational models available to simulate the interaction between a solute and solvent. For this study we utilized the integral equation formulation of the polarizable continuum model (IEF-PCM)^{32,33} to represent the electronic interaction between the nanotube and the molecule of interest inside the nanotube. The IEF-PCM

method models a solvent through the use of the dielectric constant for the solvent. The dielectric constant for a nanotube can be obtained from the Clausius-Mossotti equation³⁴⁻

36

$$\varepsilon = 1 + \rho\alpha \left(1 - \frac{1}{3}\rho\alpha \right)^{-1} + \frac{1}{3}\rho^2\alpha^2 \quad (8.1)$$

The Clausius-Mossotti relation combines the number density of atoms (ρ) and the polarizability (α) to obtain an effective dielectric constant. A 13.53 Å long 9,0 nanotube (C₁₀₈H₁₈) was optimized using the B3PW91³⁷⁻⁴³ density functional with a 3-21G basis set. The calculated isotropic polarizability for this SWCNT is 219.41 Å³ and yields an effective dielectric constant of 2.41. This is close to the dielectric constant of benzene (2.247) but far from the dielectric constant of water (78.36).

To test the model for the electronic interaction between a SWCNT and a guest, we need a system that shows a large difference between the gas phase and solution. One such system is the hydrogen bonded complex between ammonia and hydrogen chloride. In the gas phase, the most stable form is H₃N-HCl but in a high dielectric solvent the most stable form is H₃NH⁺-Cl⁻. The reaction profile for the migration of the central proton from the chloride to the ammonia was obtained by elongating the H-Cl distance and optimizing all of the remaining coordinates in the gas phase. The effect of solvation is compared to implicit solvation using various solvents at the CCSD/6-311++G(d,p) level of theory. The effects of the nanotube on the H₃N—HCl system were explored using molecular mechanics, semi-empirical, and single point DFT calculations. The DFT calculations used the B3PW91 functional with the 3-21G basis set for the nanotube and

the 6-311++G(d,p) basis set for $\text{H}_3\text{N}-\text{HCl}$. This chapter only considers the effect of confinement by the nanotube and neglects any changes to the nanotube geometry and any possibility of bonding between the guest molecule and the walls of the nanotube.

8.3 Results and Discussion

The system to be studied in this chapter is the hydrogen bonded $\text{NH}_3-\text{H}'-\text{Cl}$ system shown in Figure 8-1. For a comparison for when the system is placed inside the nanotube we begin by examining the energy profile for the transfer of a proton (H') in the hydrogen bonded $\text{NH}_3-\text{H}'-\text{Cl}$ system. Figure 8-2 shows relative energies for the relaxed potential energy scan of the $\text{H}'-\text{Cl}$ distance as H' is transferred away from the chloride towards the ammonia calculated at the CCSD/6-311++G(d,p) level of theory in the gas phase, and in benzene and water solutions each of which use a PCM for the solvation model. Table 8-1 lists how the $\text{N}-\text{H}'$ distance and the $\text{H}-\text{N}-\text{H}'$ angle change as the $\text{H}'-\text{Cl}$ distance is lengthened. The energetics in the gas phase indicate that the system has a minimum energy around an HCl separation of 1.30 \AA , with a corresponding $\text{R}(\text{N}-\text{H}')=1.90 \text{ \AA}$, which is close to 1.28 \AA found for the HCl distance in isolated gas phase HCl . In the gas phase the $\text{NH}_3-\text{H}'-\text{Cl}$ system is best described as two neutral species NH_3 and HCl separated by a hydrogen bond of 1.90 \AA . In benzene there are two distinct minima, one near the gas phase energy minimum and another shallow minimum around $\text{R}(\text{H}'-\text{Cl})=1.72 \text{ \AA}$ (30% longer than the gas phase minimum) and $\text{R}(\text{N}-\text{H}')=1.15 \text{ \AA}$. In water the energy minimum shifted to longer HCl bond distances approaching 2 \AA with a corresponding $\text{R}(\text{N}-\text{H}')=1.05 \text{ \AA}$. At these distances the system has transferred the proton from HCl to the ammonia and is best described as the ammonium chloride salt.

The first approach one might take to modeling reactions inside of carbon nanotubes might be to use a QM/MM approach, with high level quantum mechanics for the guest system inside the nanotube and a lower level of theory for the nanotube itself. Figure 8-3 shows a few QM/MM calculations on the $\text{NH}_3\text{—H—Cl}$ system using the ONIOM approach. The hydrogen bonded guest system was calculated using B3PW91/6-311++G(d,p) while the nanotube was represented by molecular mechanics, and two semi-empirical approaches. Geometries were obtained by placing the optimized geometries of the gas phase reaction path for the guest system calculated at CCSD/6-311++G(d,p) inside the nanotube resulting in C_{3v} symmetry for the entire system. To obtain reference energies for the guest system inside the 9,0 nanotube, single point energies were obtained by calculations using B3PW91/6-311++G(d,p) for the guest and B3PW91/3-21G for the tube. Using molecular mechanics on the nanotube ignores any electronic interaction between the tube and the system inside. As a result QM/MM calculations recreate the gas-phase-like energies for the reaction profile. The next step might be to utilize a semi-empirical method for the nanotube. While this does improve the energetics of the system inside the nanotube compared to molecular mechanics, the energetics are not in agreement with the energies found using B3PW91 for the entire system.

The small section of the relatively narrow 9,0 nanotube used in this chapter contains 108 heavy atoms and as such any fully quantum mechanical optimizations on the nanotube and any guest molecules inside of them can become quite costly. Previous work^{27,28} has shown that by removing the nanotube entirely and approximating the contribution the tube makes towards confinement of a guest species using a polarizable continuum model to be quite accurate at reproducing the energetics of S_N2 type reactions

taking place inside of the nanotube. In these studies the polarizability for a 9,0 nanotube was calculated and the Clausius-Mossotti relation (equation (8.1)) was used to obtain an effective dielectric constant of 2.41. Figure 8-4 shows the effect of immersion of the $\text{NH}_3\text{—H—Cl}$ system into solvents of varying dielectric strength employing the same gas phase reaction path optimized at CCSD/6-311++G(d,p) used in the previous figure. Going from the gas phase (black curve, $\epsilon = 1$) to a benzene (red curve, $\epsilon = 2.27$) solution lowers the energy of the ionic species by approximately 15 kcal/mol, doubling the dielectric constant from benzene to chloroform (blue curve, $\epsilon = 4.71$), only stabilizes the ionic species another 7 kcal/mol. The final 16 fold increase in the dielectric constant in going from chloroform to water (green curve, $\epsilon = 78.36$) only stabilizes the ionic system another 7 kcal/mol. In addition, the gas phase reaction profile predicts the dimer of the neutral guests as the favored geometry with an H—Cl separation of about 1.3 Å. Going from the gas phase to benzene solvent shifts this preference to the ionic dimer system with an H—Cl distance closer to 1.7 Å. Changing to chloroform and water further increases the H—Cl separation to 1.8 Å and 1.9 Å, respectively. From this it can be concluded that an ionic solute in a PCM is more sensitive to the initial increase of the dielectric constant than further increases of the dielectric constant. The same gas phase optimized geometries were placed into a 9,0 SWCNT resulting in C_{3v} symmetry. Full quantum calculations using the B3PW91 density functional with the 3-21G basis set on the nanotube and the 6-311++G(d,p) basis set on the guest system (dashed purple) yields energies similar to the results from the PCM calculation using the benzene dielectric constant.

For polarizable continuum models of solvation, the stabilization energy depends on the cavity size as well as the dielectric constant. Figure 8-5 shows the relative energies of chloride ion in a PCM solvent as a function of dielectric constant and cavity scaling factor. The greatest amount of stabilization afforded by the PCM occurs within the first 10 units of increasing dielectric constant. This is in agreement with the conclusions from Figure 8-4. This stabilization decreases rapidly as the size of the cavity increases, going from 40 kcal/mol stabilization for a cavity with a scaling factor of 1 to only approximately 5 kcal/mol stabilization for a cavity 4 times the normal size. With this in mind, the very good agreement between the energies predicted by the single point energies of the $\text{NH}_3\text{—H—Cl}$ system in the tube (dashed line in Figure 8-4) and the energies obtained using the dielectric constant of benzene in a PCM calculation (red line in Figure 8-4) indicates that using benzene as the PCM solvent is acceptable, and it may not be necessary to reoptimize the dielectric constant for a particular tube used in a simulation..

As demonstrated in Figure 8-5, for a given dielectric constant the electronic energy of a species in solution depends strongly on the cavity size. Standard PCM calculations build a solvent cavity by finding the union of scaled van der Waals spheres placed on the heavy atoms of the solute. This yields an appropriate solute shaped cavity. However, for a guest system inside a nanotube, the shape of the cavity should depend on the nanotube and not on the shape of the guest molecule. To approximate the interior of a nanotube we can build a cavity with a series of overlapping spheres aligned along the nanotube axis (Figure 8-6b). The spheres are kept close enough so that the overlap of the

spheres creates a smooth cavity which closely approximates the nanotube interior. We refer to this cavity as the sausage PCM cavity.

Figure 8-7 shows the change in the potential energy curve along the reaction path for the transfer of a proton in the hydrogen bonded $\text{NH}_3\text{—H—Cl}$ system as the sausage PCM cavity size is varied. The radius of a m,n nanotube can be calculated from the indices using the equation

$$r = \frac{2.46\text{\AA}}{2\pi} \sqrt{m^2 + mn + n^2} \quad (8.2)$$

Table 8-2 lists the calculated radii for a 9,0 and an 8,0 nanotube along with the approximate radii for the cavity inside of a nanotube, found by subtracting the typical van der Waals radius of a carbon atom from the nanotube radius. The radius of a 9,0 SWCNT is 3.52 Å while the radius of the cavity is 2.02 Å. Comparing these values to the potential energy curves in Figure 8-7 demonstrate that for a solvent radius of 3.52 Å there is little energy stabilization compared to the gas phase energies. This value falls between 3.65 Å and 2.72 Å, both of which behave very much like the gas phase reaction path by favoring the neutral $\text{NH}_3\text{—HCl}$ system geometry. In fact a large change in the solvated energies is not seen until the cavity radius has been decreased to smaller than 2.15 Å suggesting that the cavity radius and not the nanotube radius listed in Table 8-2, is the most appropriate one for approximating the nanotube cavity size in sausage PCM calculations.

Figure 8-8 shows energies from the geometries optimized in the sausage PCM solvent cavity for a 9,0 CNT (blue, dashed) and an 8,0 CNT (red, dashed) and the same

geometries placed inside each of the nanotubes (solid curves). From this figure it can be seen that the sausage PCM cavity used in conjunction with the benzene solvent parameters reliably reproduces the full QM relative energies for the 9,0 SWCNT over the entire reaction coordinate, while the energies start to differ at longer distances in the 8,0 SWCNT. The ionic character of the system at these distances leads to changes in the size of the electron density and in the small 8,0 SWCNT this may lead to these energy differences.

The next step is to add in the effect of confinement of guest species within the walls of a nanotube. To achieve this we can add in the nanotube around our sausage PCM using molecular mechanics. Figure 8-9 shows the energies for the $\text{NH}_3\text{—H—Cl}$ system in the gas phase, and in three 9,0 nanotube models using the same geometries as in Figure 8-8. The three models are the full quantum nanotube (green), only the sausage PCM representing the nanotube (blue), and the sausage PCM with a molecular mechanics nanotube surrounding the nanotube (red). Compared to the sausage PCM cavity, the addition of the molecular mechanics nanotube slightly destabilizes the energies of the ionic system compared to the PCM. The energy difference may be due to using the benzene dielectric value of 2.27 instead of the effective dielectric constant for the nanotube of 2.41. This model can be described as an ONIOM calculation where the nanotube is represented at a low level using molecular mechanics, and the guest system is represented at a high level using a B3PW91/6-311++G(d,p) calculation in a PCM cavity. We refer to this approach as the ONIOM and sausage model and it should be efficient for the optimization of reaction profiles of guest species inside nanotubes.

8.4 Conclusions

We have described the construction of an affordable nanotube model useful for full optimizations of guest molecules placed inside the nanotube environment. Taking advantage of the polarizable continuum model, which is used to model solute molecules in a solvent environment, allows us to circumvent costly parameterization of the model. Instead of optimizing a nanotube to find the polarizability and thus an effective dielectric constant for the tube, we can use benzene as the solvent in the PCM calculation along with a cavity radius which approximates the size of the interior cavity of the nanotube. Calculations with this model reproduce energies and internal coordinates of full quantum chemical calculations of the system inside the nanotube. Optimizations using this ONIOM and sausage model show promise for optimizations of systems inside of a nanotube however more work is needed to replicate the fully quantum mechanically optimized geometries.

8.5 References

- (1) Deheer, W. A.; Chatelain, A.; Ugarte, D. A Carbon Nanotube Field-Emission Electron Source, *Science* **1995**, *270*, 1179.
- (2) Che, G. L.; Lakshmi, B. B.; Fisher, E. R.; Martin, C. R. Carbon nanotubule membranes for electrochemical energy storage and production, *Nature* **1998**, *393*, 346.
- (3) Tans, S. J.; Verschueren, A. R. M.; Dekker, C. Room-temperature transistor based on a single carbon nanotube, *Nature* **1998**, *393*, 49.
- (4) Schlapbach, L.; Züttel, A. Hydrogen-storage materials for mobile applications, *Nature* **2001**, *414*, 353.
- (5) Baughman, R. H.; Zakhidov, A. A.; de Heer, W. A. Carbon nanotubes - the route toward applications, *Science* **2002**, *297*, 787.
- (6) Niyogi, S.; Hamon, M. A.; Hu, H.; Zhao, B.; Bhowmik, P.; Sen, R.; Itkis, M. E.; Haddon, R. C. Chemistry of single-walled carbon nanotubes, *Accounts Chem. Res.* **2002**, *35*, 1105.
- (7) Sun, Y. P.; Fu, K. F.; Lin, Y.; Huang, W. J. Functionalized carbon nanotubes: Properties and applications, *Accounts Chem. Res.* **2002**, *35*, 1096.
- (8) Xia, Y. N.; Yang, P. D.; Sun, Y. G.; Wu, Y. Y.; Mayers, B.; Gates, B.; Yin, Y. D.; Kim, F.; Yan, Y. Q. One-dimensional nanostructures: Synthesis, characterization, and applications, *Adv. Mater.* **2003**, *15*, 353.
- (9) Charlier, J. C.; Blase, X.; Roche, S. Electronic and transport properties of nanotubes, *Rev. Mod. Phys.* **2007**, *79*, 677.

- (10) Singh, R.; Pantarotto, D.; Lacerda, L.; Pastorin, G.; Klumpp, C.; Prato, M.; Bianco, A.; Kostarelos, K. Tissue biodistribution and blood clearance rates of intravenously administered carbon nanotube radiotracers, *Proc. Natl. Acad. Sci. U. S. A.* **2006**, *103*, 3357.
- (11) Shannon, M. A.; Bohn, P. W.; Elimelech, M.; Georgiadis, J. G.; Marinas, B. J.; Mayes, A. M. Science and technology for water purification in the coming decades, *Nature* **2008**, *452*, 301.
- (12) Stankovich, S.; Dikin, D. A.; Dommett, G. H. B.; Kohlhaas, K. M.; Zimney, E. J.; Stach, E. A.; Piner, R. D.; Nguyen, S. T.; Ruoff, R. S. Graphene-based composite materials, *Nature* **2006**, *442*, 282.
- (13) Yang, W. R.; Ratinac, K. R.; Ringer, S. P.; Thordarson, P.; Gooding, J. J.; Braet, F. Carbon Nanomaterials in Biosensors: Should You Use Nanotubes or Graphene?, *Angew. Chem.-Int. Edit.* **2010**, *49*, 2114.
- (14) He, S. J.; Song, B.; Li, D.; Zhu, C. F.; Qi, W. P.; Wen, Y. Q.; Wang, L. H.; Song, S. P.; Fang, H. P.; Fan, C. H. A Graphene Nanoprobe for Rapid, Sensitive, and Multicolor Fluorescent DNA Analysis, *Adv. Funct. Mater.* **2010**, *20*, 453.
- (15) Liu, C.; Li, F.; Ma, L. P.; Cheng, H. M. Advanced Materials for Energy Storage, *Adv. Mater.* **2010**, *22*, E28.
- (16) Saito, Y.; Yoshikawa, T.; Okuda, M.; Fujimoto, N.; Sumiyama, K.; Suzuki, K.; Kasuya, A.; Nishina, Y. Carbon Nanocapsules Encaging Metals and Carbides, *J. Phys. Chem. Solids* **1993**, *54*, 1849.
- (17) Saito, Y. Nanoparticles and Filled Nanocapsules, *Carbon* **1995**, *33*, 979.

- (18) Smith, B. W.; Monthioux, M.; Luzzi, D. E. Encapsulated C-60 in carbon nanotubes, *Nature* **1998**, *396*, 323.
- (19) Okada, S.; Saito, S.; Oshiyama, A. Energetics and electronic structures of encapsulated C-60 in a carbon nanotube, *Phys. Rev. Lett.* **2001**, *86*, 3835.
- (20) Monthioux, M. Filling single-wall carbon nanotubes, *Carbon* **2002**, *40*, 1809.
- (21) Takenobu, T.; Takano, T.; Shiraishi, M.; Murakami, Y.; Ata, M.; Kataura, H.; Achiba, Y.; Iwasa, Y. Stable and controlled amphoteric doping by encapsulation of organic molecules inside carbon nanotubes, *Nat. Mater.* **2003**, *2*, 683.
- (22) Khlobystov, A. N.; Britz, D. A.; Briggs, G. A. D. Molecules in carbon nanotubes, *Accounts Chem. Res.* **2005**, *38*, 901.
- (23) Wang, L. X.; Zou, H. T.; Yi, C. H.; Xu, J.; Xu, W. L. Finite-Length Effect of Carbon Nanotubes on the Encapsulation and Decomposition of Nitromethane: ONIOM Calculation, *Curr. Nanosci.* **2011**, *7*, 1054.
- (24) Castillo, A.; Lee, L.; Greer, A. Encapsulation and convex-face thiozonolysis of triatomic sulfur (S₃) with carbon nanotubes, *J. Phys. Org. Chem.* **2012**, *25*, 42.
- (25) Debbichi, L.; Dappe, Y. J.; Alouani, M. Effect of van der Waals interaction on energetics and transport properties of a single anthracene molecule adsorbed or confined inside a carbon nanotube, *Phys. Rev. B* **2012**, *85*, 045437.
- (26) Zoberbier, T.; Chamberlain, T. W.; Biskupek, J.; Kuganathan, N.; Eyhusen, S.; Bichoutskaia, E.; Kaiser, U.; Khlobystov, A. N. Interactions and reactions of

transition metal clusters with the interior of single-walled carbon nanotubes imaged at the atomic scale, *J. Am. Chem. Soc.* **2012**, *134*, 3073.

(27) Halls, M. D.; Raghavachari, K. Carbon nanotube inner phase chemistry: The Cl- exchange S(N)2 reaction, *Nano Lett.* **2005**, *5*, 1861.

(28) Halls, M. D.; Schlegel, H. B. Chemistry inside carbon nanotubes: The Menshutkin S(N)2 reaction, *J. Phys. Chem. B* **2002**, *106*, 1921.

(29) Wang, W. Z.; Wang, D. L.; Zhang, Y.; Ji, B. M.; Tian, A. M. Hydrogen bond and halogen bond inside the carbon nanotube, *J. Chem. Phys.* **2011**, *134*.

(30) Xiao, B.; Zhao, J. Z.; Ding, Y. H.; Sun, C. C. Theoretical study of the P-Ylide reaction in the carbon nanotube, *Sci. China Ser. B-Chem.* **2009**, *52*, 1969.

(31) Westphal, E.; Pliego, J. R. Ab initio, density functional theory, and continuum solvation model prediction of the product ratio in the S(N)2 reaction of NO₂- with CH₃CH₂Cl and CH₃CH₂Br in DMSO solution, *J. Phys. Chem. A* **2007**, *111*, 10068.

(32) Miertus, S.; Scrocco, E.; Tomasi, J. Electrostatic Interaction of a Solute with a Continuum - A Direct Utilization of Ab Initio Molecular Potentials for the Prediction of Solvent Effects, *Chem. Phys.* **1981**, *55*, 117.

(33) Tomasi, J.; Mennucci, B.; Cammi, R. Quantum mechanical continuum solvation models, *Chem. Rev.* **2005**, *105*, 2999.

(34) Kuz'min, V. L.; Romanov, V. P.; Zubkov, L. A. Propagation and scattering of light in fluctuating media, *Phys. Rep.* **1994**, *248*, 71.

(35) Morice, O.; Castin, Y.; Dalibard, J. Refractive-Index of a Dilute Bose-Gas, *Phys. Rev. A* **1995**, *51*, 3896.

(36) Born, M.; Wolf, E.; Bhatia, A. B. *Principles of Optics: Electromagnetic Theory of Propagation, Interference and Diffraction of Light*; Cambridge University Press, 1999.

(37) Becke, A. D. Density-functional thermochemistry. III. The role of exact exchange, *J. Chem. Phys.* **1993**, *98*, 5648.

(38) Perdew, J. P. *Electronic structure of solids '91: proceedings of the 75. WE-Heraeus-Seminar and 21st Annual International Symposium on Electronic Structure of Solids held in Gaussig (Germany)*, ; Akademie Verlag: Berlin, 1991.

(39) Perdew, J. P.; Chevary, J. A.; Vosko, S. H.; Jackson, K. A.; Pederson, M. R.; Singh, D. J.; Fiolhais, C. Atoms, molecules, solids, and surfaces: Applications of the generalized gradient approximation for exchange and correlation, *Phys. Rev. B* **1992**, *46*, 6671.

(40) Perdew, J. P.; Chevary, J. A.; Vosko, S. H.; Jackson, K. A.; Pederson, M. R.; Singh, D. J.; Fiolhais, C. Erratum: Atoms, molecules, solids, and surfaces: Applications of the generalized gradient approximation for exchange and correlation, *Phys. Rev. B* **1993**, *48*, 4978.

(41) Perdew, J. P.; Burke, K.; Ernzerhof, M. Generalized gradient approximation made simple, *Phys. Rev. Lett.* **1996**, *77*, 3865.

(42) Perdew, J. P.; Burke, K.; Wang, Y. Generalized gradient approximation for the exchange-correlation hole of a many-electron system, *Phys. Rev. B* **1996**, *54*, 16533.

(43) Perdew, J. P.; Burke, K.; Wang, Y. Erratum: Generalized gradient approximation for the exchange-correlation hole of a many-electron system, *Phys. Rev. B* **1998**, *57*, 14999.

Table 8-1. Relaxed scan of the H'—Cl bond distance calculated at CCSD/6-311++G(d,p) in the gas phase and using PCM with benzene and water as solvents.

H'—Cl	Gas Phase		PCM Benzene		PCM Water	
	H'—N (Å)	H—N—H' (°)	H'—N (Å)	H—N—H' (°)	H'—N (Å)	H—N—H' (°)
1.20	2.07	112.47	2.02	112.66	1.96	112.92
1.30	1.90	112.25	1.82	112.41	1.73	112.58
1.40	1.67	111.79	1.55	111.80	1.44	111.62
1.50	1.42	111.00	1.33	111.02	1.26	111.21
1.60	1.26	110.30	1.21	110.49	1.17	110.81
1.70	1.18	109.84	1.15	110.12	1.12	110.50
1.80	1.13	109.51	1.11	109.89	1.09	110.30
1.90	1.10	109.27	1.08	109.68	1.07	110.16
2.00	1.08	109.09	1.07	109.54	1.05	109.93

Table 8-2. Radius of Nanotubes used

Nanotube	Radius of Nanotube	Radius of Cavity ($R_{\text{nanotube}} - R_C$)
9,0 SWCNT	3.52 Å	2.02 Å
8,0 SWCNT	3.13 Å	1.63 Å

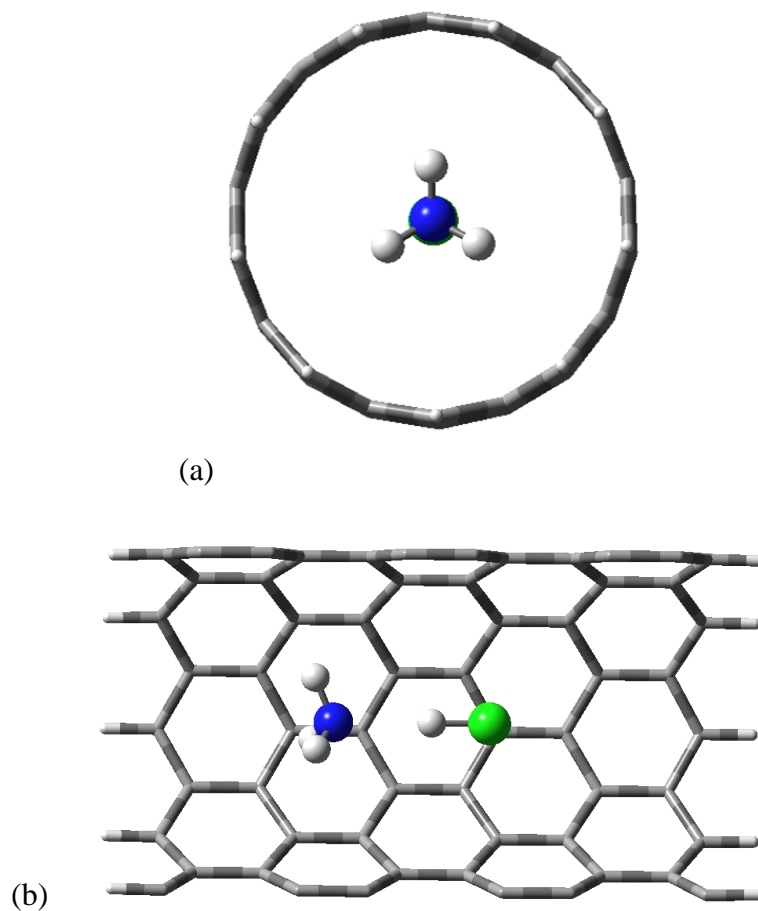


Figure 8-1. The $H_3N-H-Cl$ guest system inside a 9,0 single walled nanotube (a) axial view and (b) side view of the nanotube and guest system, exhibiting C_{3v} symmetry.

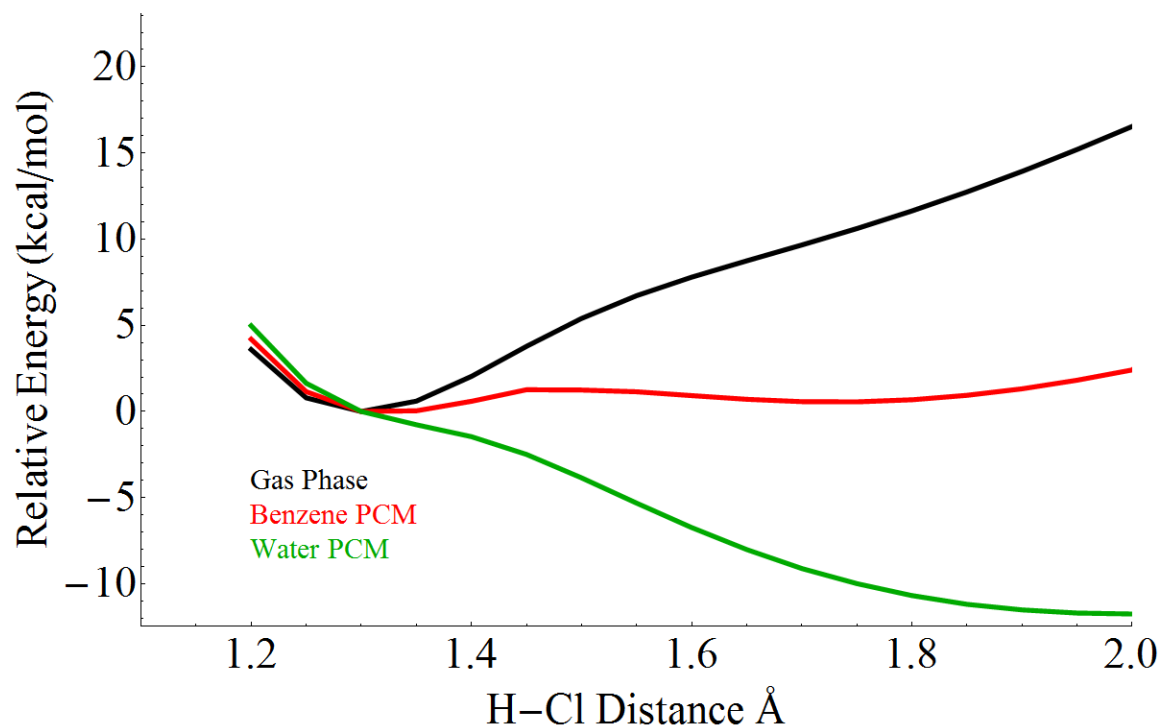


Figure 8-2. Relaxed scan of the H—Cl distance for the NH₃—H—Cl hydrogen bonded system. Calculated using CCSD/6-311++G(d,p) in the gas phase (black), in a benzene solution using PCM (red), and in water solution using PCM (green). The zero of energy has been set to the geometry corresponding to the gas phase minimum energy structure.

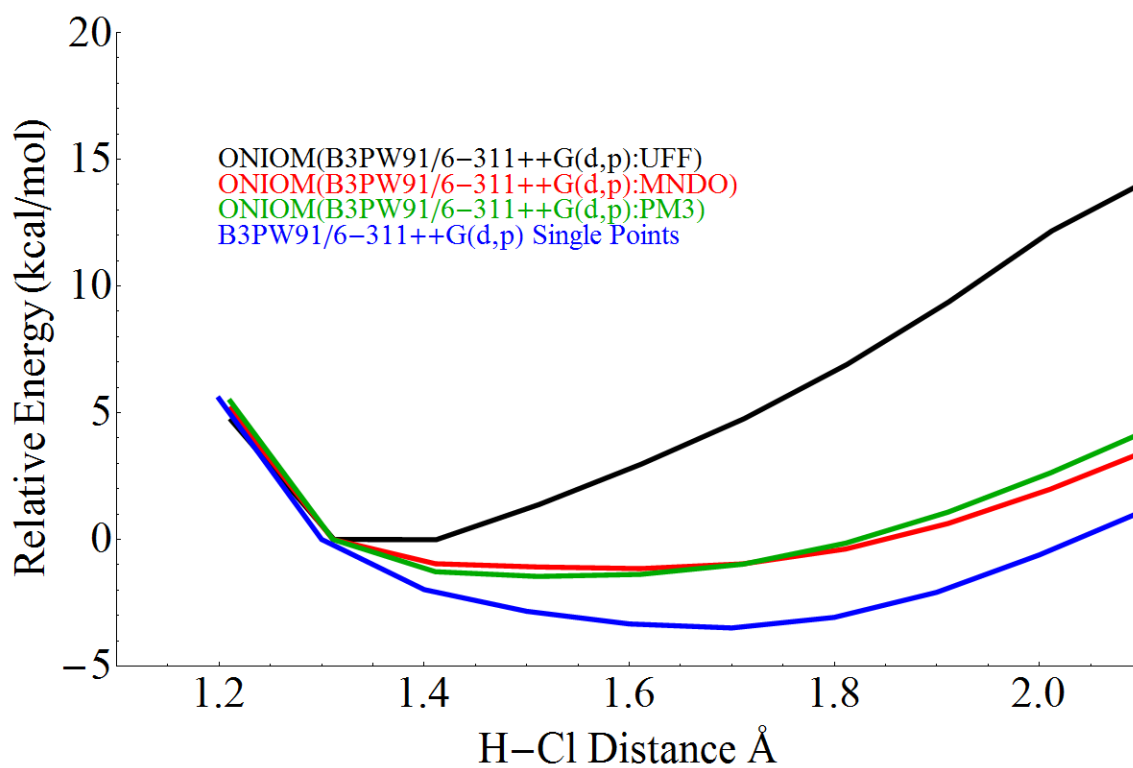


Figure 8-3. Relaxed scan along the transfer of H⁺ from HCl to NH₃ calculated using (black) ONIOM(B3PW91/6-311++G(d,p):UFF), (red) ONIOM(B3PW91/6-311++G(d,p):MNDO), (green) ONIOM(B3PW91/6-311++G(d,p):PM3), compared against (blue) single point energies of the PCM optimized aqueous solution geometries centered in a 9,0 nanotube with C_{3v} symmetry.

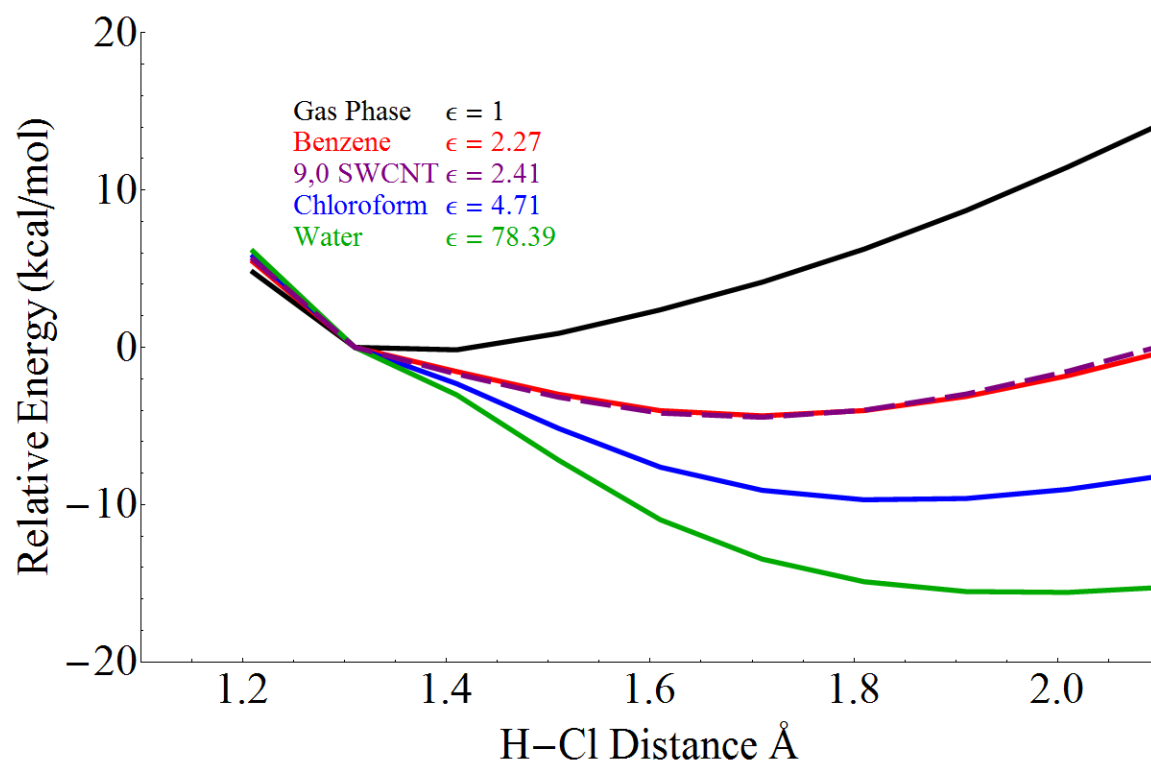


Figure 8-4. Series of single point calculations based on the geometries taken from a relaxed scan of the H—Cl distance for the $\text{NH}_3\text{—H—Cl}$ guest system in the gas phase calculated using CCSD/6-311++G(d,p). Single point energies calculated using B3PW91/6-311++G(d,p) in the gas phase (green), benzene PCM (blue), chloroform PCM (black), water (red), in a 9,0 SWCNT (dashed purple).

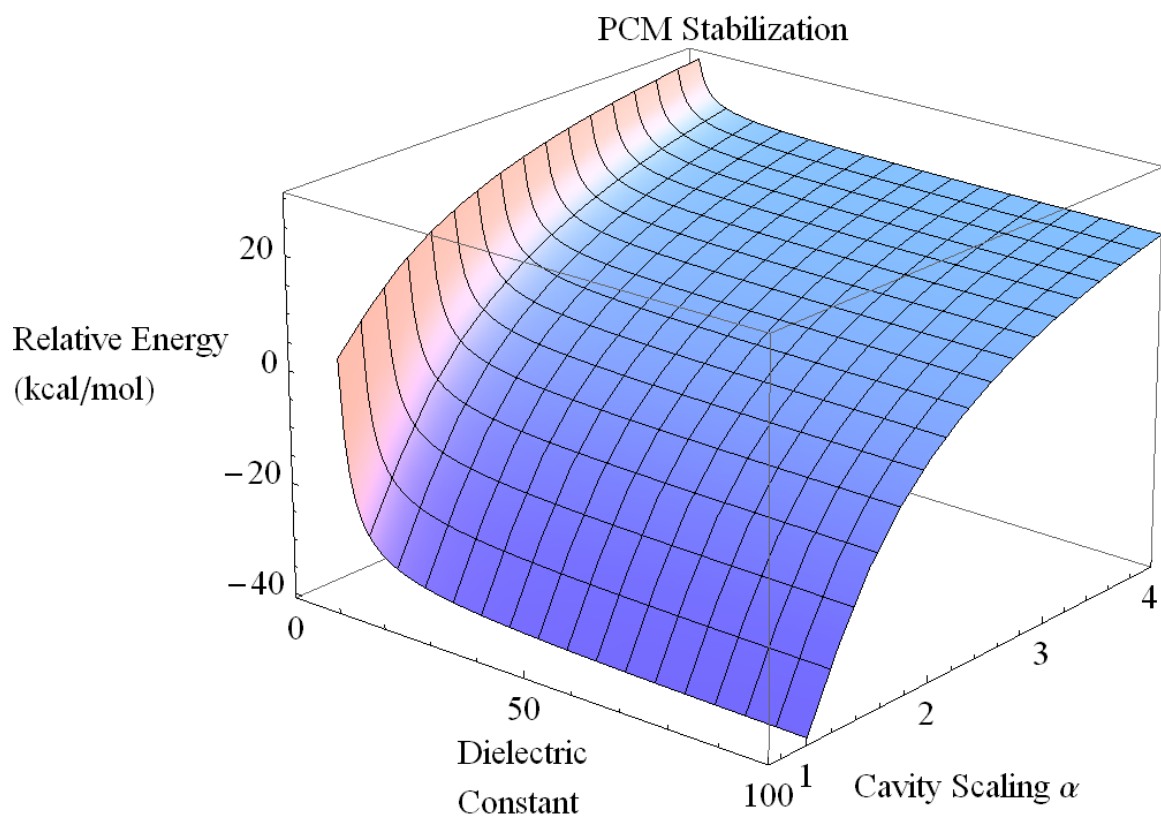


Figure 8-5. Effect of PCM solvation on chloride ion as a function of dielectric constant and cavity scaling parameter. Calculated using HF/cc-pVDZ.

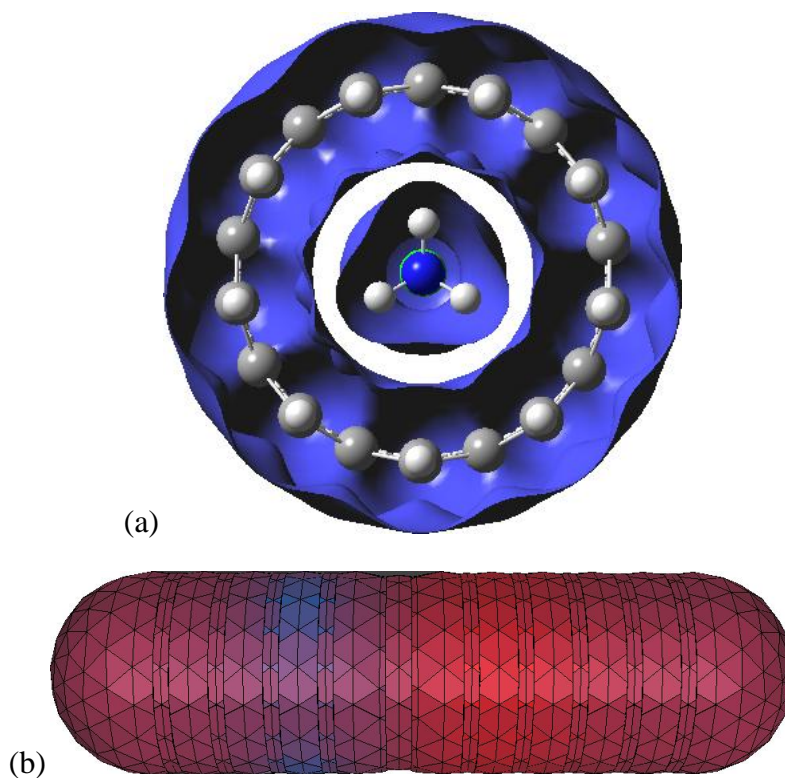


Figure 8-6. (a) Electron isodensity (Isovalue = 0.01 au) surface of the 9,0 nanotube and guest system. (b) Sausage PCM cavity constructed to approximate the interior surface of the nanotube. 12 PCM cavity spheres are centered along the axis of the nanotube every angstrom starting at the tube opening.

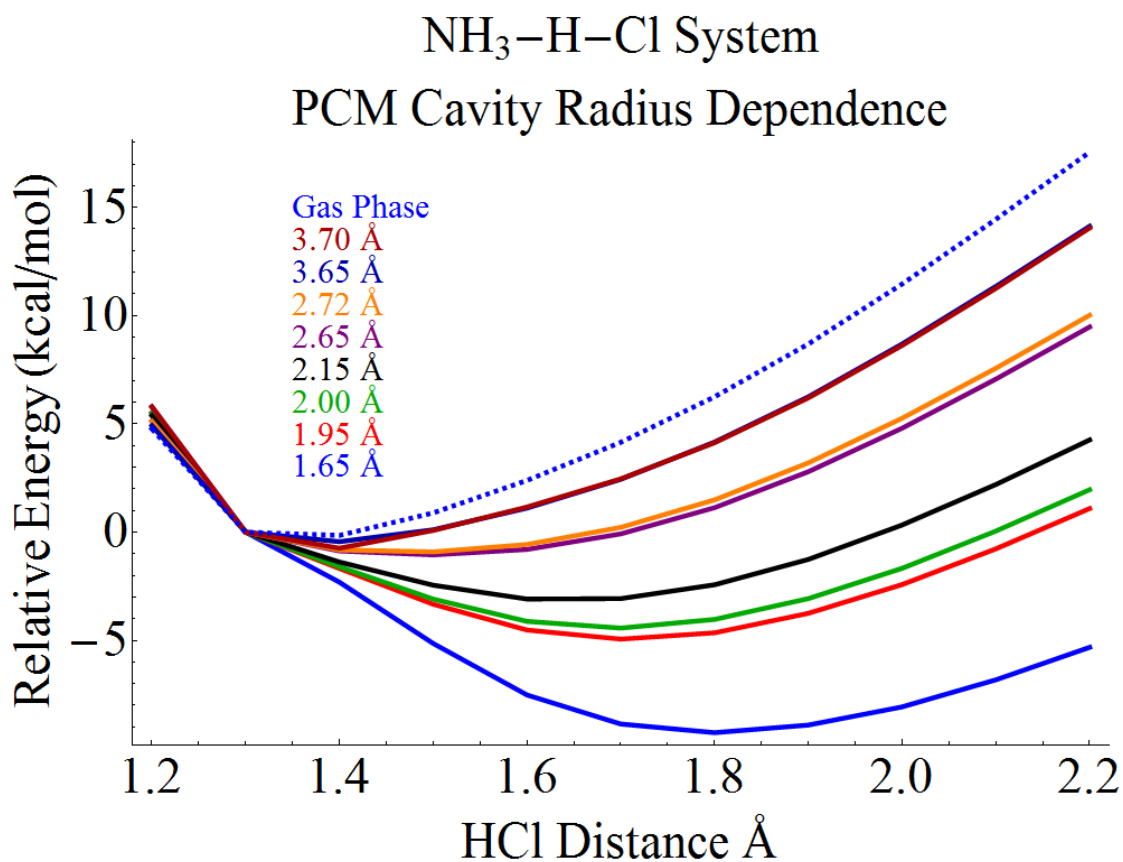


Figure 8-7. Effect of PCM sausage cavity radius on energies along the reaction coordinate of the transfer of a proton in the hydrogen bonded NH₃–H–Cl system. Calculations were performed using the dielectric of benzene, and the gas phase CCSD/6-311++G(d,p) optimized geometries; energies are calculated using the B3PW91/6-311++G(d,p) level of theory.

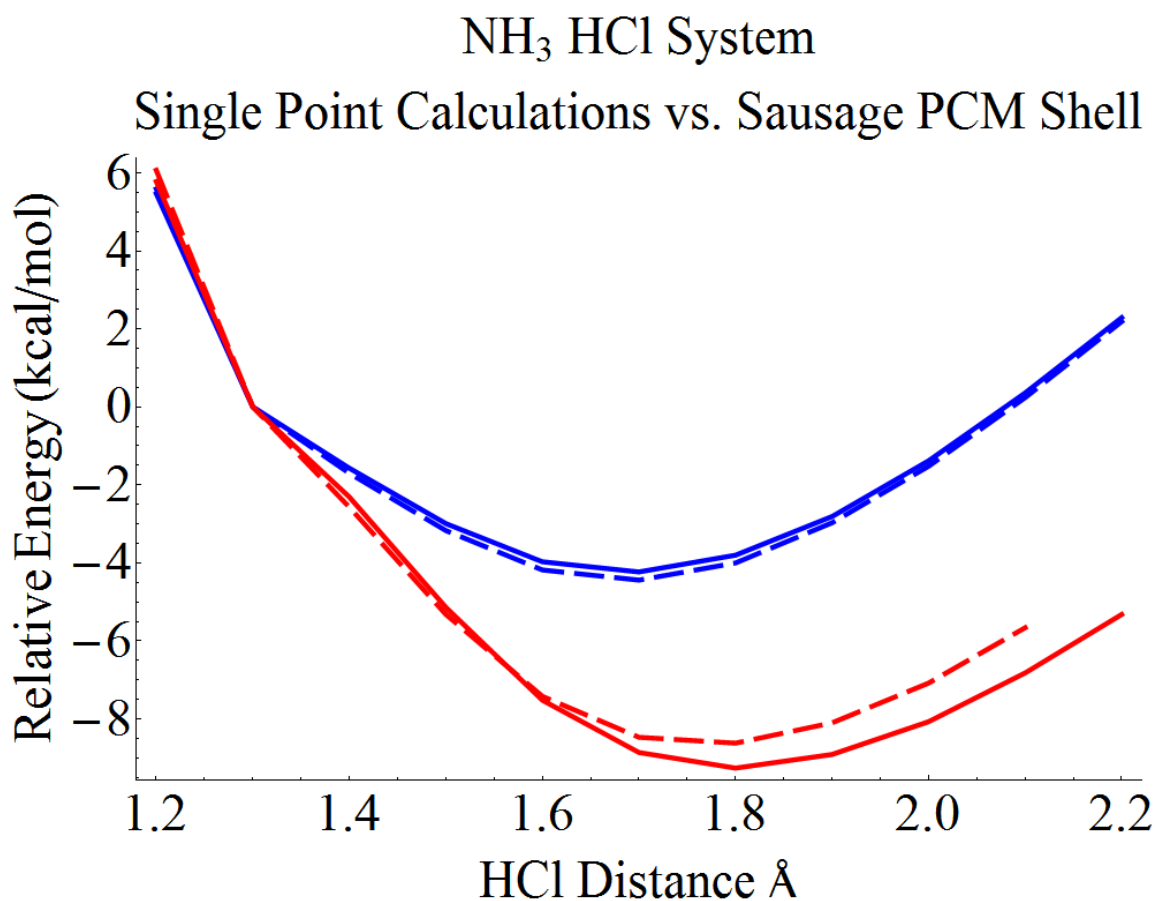


Figure 8-8. Relative energies along the reaction coordinate of the transfer of a proton in the hydrogen bonded NH₃—H—Cl system in a 9,0 nanotube (blue) and an 8,0 nanotube (red). Comparison between the relaxed scan calculated at B3PW91/6-311++G(d,p) using the sausage PCM model (dashed) and single point calculations of the optimized geometries from sausage PCM calculations (solid).

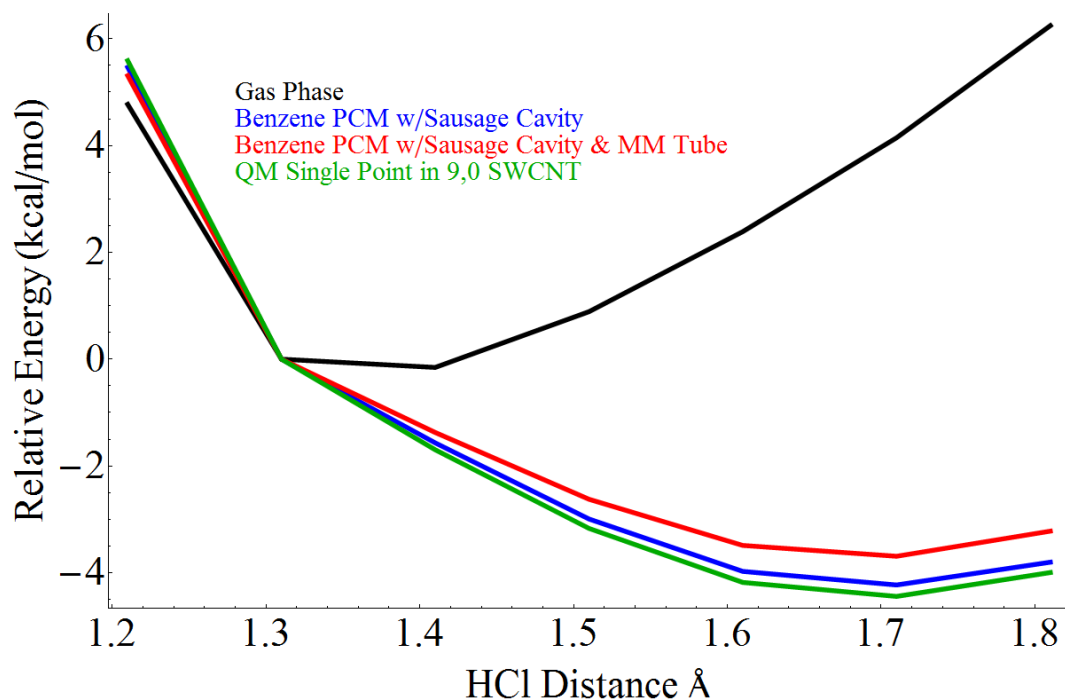


Figure 8-9. Energies along the reaction coordinate of the transfer of a proton in the hydrogen bonded $\text{NH}_3\text{—H—Cl}$ system, using fixed geometries optimized from previous sausage PCM calculations. In the gas phase (black), in a 9,0 nanotube (green), in the sausage PCM for a 9,0 nanotube (blue), and in the 9,0 SWCNT sausage PCM with a molecular mechanics tube around the PCM (red).

Chapter 9

Conclusions

9.1 Chapter 2: TD-CI Simulations of Strong-Field Chemistry

In Chapter 2 we initially set out to model the electron dynamics of butadiene after exposure to an intense laser pulse while neglecting any loss of electron density due to ionization. Without experimental data as a reference, we compared the ground and excited state populations of butadiene calculated via TD-HF, TD-CIS, and TD-CIS(D) to a more accurate simulation using the ground and excited state populations calculated by EOM-CC. The excited state energies found by all the methods are in agreement with each other up to the IP of butadiene, after which the methods start to differ. CIS(D) continues to be in agreement with EOM-CC, while TD-CIS and TD-HF predict energies higher than those of EOM-CC and CIS(D). Even then the energies predicted by CIS(D) tend to oscillate about the EOM-CC values because of the perturbative nature of the doubles correction in the CIS(D) method. We found that to reasonably represent the final populations of the excited states after the pulse a basis set augmented with up to 3 sets of diffuse functions on the heavy atoms was required. The amount of population transferred into the excited states increases by an order of magnitude by adding a single set of diffuse functions. The additional diffuse functions help fill out the states in the pseudo-continuum. Adding higher angular momentum functions had little effect on the excited state populations. To achieve convergence on the populations of the excited states after the pulse more than 450 excited states are needed. At low field strengths all the methods

agree on the amount of population transferred out of the ground states. It is not until the field strength reaches 0.04 au that the populations start to differ. Despite lacking electron correlation, TD-HF and TD-CIS faithfully reproduce the population lost by the ground state as that predicted by EOM-CC. CIS(D) on the other hand predicts that the ground state is depleted more than the other methods predict.

9.2 Chapter 3: TD-DFT Simulations of Strong Field Chemistry

In this chapter, we compared the performance of TD-CI simulations with excited states calculated by TD-DFT to simulations with RPA, CIS, CIS(D) and EOM-CCSD excited states. The TD-DFT calculations used functionals of the GGA, meta-GGA, hybrid and long-range corrected variety. In contrast to the TD-CIS and TD-HF methods used in the previous chapter, the functionals in the TD-DFT calculations include electron correlation but there are many functionals to choose from. We again use butadiene as our test molecule with the same pulse as the previous chapter. Our goals, Similar to the previous chapter, our goal was to identify functionals which reproduce the molecular response to the laser pulse as obtained with EOM-CC. In addition we set out to better understand the contributions that the excited state energies and transition dipoles made to the excited state populations.

We observed that the excitation energies calculated by standard GGA and meta-GGA functionals are significantly lower than the EOM-CC excitation energies. Mixing in different amounts of Hartree-Fock exchange, either through the use of hybrid functionals or long-range corrected functionals causes the excitation energies to approach those computed by EOM-CC. Varying the parameter which controls the distance over which the long-range correction takes place greatly influences the excited state energies.

A value of $\omega = 0.4$ in the LC- ω PBE functional provides good agreement with EOM-CC over a wide range of excitation energies. Lower values of ω yield excited state energies lower than EOM-CC and higher values of ω yield excited state energies approaching the Hartree-Fock excited state energies. The magnitudes of the transition dipoles for all the DFT and wavefunction based methods used in the previous chapter were largely in agreement with each other. The standard and hybrid functionals yield transition dipole magnitudes slightly lower than those found by EOM-CC while the long-range corrected functionals and the wave function based methods predict transition dipole magnitudes slightly larger than EOM-CC. Similar to the previous chapter the amount of population transferred into the excited states is the metric with which we gauged the relative performance of each of the methods. The amount of population in the excited states obtained with standard functionals is far too large. Hybrid functionals have the next lowest amount of population transferred into the excited states, but it is not until the long-range corrections are included in the functionals that the response is within 25% of the EOM-CC calculations. The response computed with long-range corrected functionals is comparable to that obtained with EOM-CC, RPA and CIS. This indicates that correct long-range behavior is essential for the treatment of the diffuse and highly excited states needed to describe the interaction between the electron density and a strong laser field. The population of the excited states was compared to the averages of the excited state energies and transition dipole magnitudes. Strong correlation was found between the excited state energies and the population, however little correlation was found between the population and transition dipole magnitudes. No correlation was found between the excited state populations and calculated ionization potentials using each of the methods.

9.3 Chapter 4: Strong-Field Ionization of Linear Polyenes

The previous two chapters focused on modeling the electron dynamics of butadiene after interacting with an intense laser field but did not treat ionization. One method for modeling ionization is through the use of absorbing boundary potentials. A complex potential in a system's Hamiltonian does not conserve the norm of the wavefunction and can mimic the loss of electron density. The difficulty comes in constructing a suitable absorbing potential. If the complex potential is too steep the simulations yield more reflection than absorption. If the complex potential is too close to the molecule, the absorption is too strong even in weak fields. If the potential conforms to the shape of an arbitrary molecule, integrals involving the absorbing potential are difficult to calculate. To circumvent these problems Klamroth and co-workers developed a heuristic model based on the premise that the higher the energy of the excited electron, the faster it would escape from the molecule. An imaginary term representing the ionization rate is added to the energies of excited states above the ionization potential. This term depends on the CI coefficients which describe the state, the energies of the destination orbitals which contribute to the excited state and an escape distance parameter. In this chapter we compared the strong-field ionization of the linear polyenes: ethylene, butadiene, hexatriene, and octatetraene. The loss of norm after the laser pulse was found to be sensitive to the escape distance parameter and a value of $d = 1$ bohr was found to be suitable for all of the polyenes. The longer polyenes however can support a larger range of the distance parameter since they have more lower energy states which contribute to ionization. In contrast to the non-ionizing models discussed in Chapters 2 and 3, modeling ionization with Klamroth's model is less sensitive to the basis set size.

The 6-31G(d,p) basis set augmented with a single set of diffuse functions on the carbon atoms yields results similar to calculations with larger basis sets. It was also found that the states which contribute the most towards ionization are within the 20 eV of the ionization potential for each of the polyenes. This confirms that only a subset of the excited states is needed to converge the loss of norm after the pulse. Experimental ionization saturation values are available for hexatriene and ethylene. While the heuristic ionization model yields ionization saturation values in the right order of magnitude, we cannot compare our results directly with experiment. However, ratios of the calculated ionization rates are in good agreement with the ratios predicted by the ADK ionization model.

9.4 Chapters 2-4 Summary & Future Directions

In the chapters just described, we were able to determine which basis sets and the number of excited state which are best suited to give reasonable descriptions of the electron dynamics in polyenes after interaction with an intense laser field. Extra diffuse functions, which allow electrons to be further away from the molecule, have more of a profound effect on the population of excited states opposed to the addition of polarization functions. The high number of excited states helps to fully describe the polarization of a molecule, but transitions from low energy states to high energy states are key to describing the overall response. However, transitions between the highest energy excited states can be ignored and the predicted response is comparable to the response if those transitions were included. This indicates that these transitions may be able to be replaced with just the polarizability contributed by those states for use in simulations, thereby greatly decreasing the cost of the simulation. The TD-HF, TD-CIS methods and long-

range corrected density functionals reproduce excited states, transition dipoles and populations of excited states in good agreement with those predicted by EOM-CC, but at a much lower cost. By using the heuristic model mentioned in Chapter 4 to simulate ionization we find that the basis sets with extra diffuse functions no longer predict significantly different excited state populations after the pulse. This work can be extended to more accurate models of the ionization by explicitly using an absorbing boundary potential. Ultimately, modeling ionization with an absorbing potential should require less parameterization, be sensitive to the direction of the laser field, and take into account the shape of the orbitals from which the ionized electron is leaving.

9.5 Chapters 5-7:

Applications of Electronic Structure Theory to Problems in Inorganic Chemistry

The compounds our experimental collaborators have been able to develop have the potential to be employed in a variety of applications. The Co(III), Zn(II) and Fe(II) complexes isolated by the Kodanko group can lead to the development of reagents useful in asymmetric synthesis and catalysis. Our theoretical work on their systems have provided insight as to why the isolated isomer is the only one observed experimentally, and have given a degree of assurance that the isolated isomer is the isomer that will be predominantly present in future work with those compounds. This will help assuage any concerns of any unpredicted product and will help assist in the design of more applications of these species.

The dicopper Cu(II) complex synthesized by the Winter group was initially part of an effort to design new precursors for growth of films using atomic layer deposition. From their work they found a shorter Cu—Cu separation than has been previously been

observed. Our calculations have provided evidence for the factors controlling the metal separation. With this in mind it may be possible to predict how to obtain even smaller Cu—Cu separation distances, however the ligands proposed in our theoretical studies are known to reduce the Cu(II) ion and therefore this complex may be experimentally inaccessible. Nevertheless, with the insight gained from our computational study, other ligands can be designed to alter the Cu—Cu distance. These results should be applicable to other paddlewheel complexes as well.

The Verani group has been working on a series of complexes for use in the development of molecular switches. In order to be efficient switches the complexes must not only be stable over long term redox cycling, but also the redox properties of the complex of interest must be customizable and behave predictably. To obtain the level of control necessary to develop applicable molecular switches, one must have a fundamental understanding of the redox properties and oxidation states of the species involved in the processes. The theoretical support we have provided for the Verani group has corroborated their experimental findings of a series of Fe(III) based complexes. By modifying the corresponding orbital method to obtain energetic data, a quantitative description can be obtained for the character of orbitals involved in the redox process. Future work will expand upon this work by exploring other complexes with different metal centers.

9.8 Chapter 8: Applications of Electronic Structure Theory to Material Systems

The aim of this chapter is to construct an inexpensive model to allow optimizations of a guest molecular system within a nanotube. To achieve this, the

interactions nanotube are split into two components, a geometric component which contributes to the physical confinement of the guest inside of the tube, and an electronic component which affects the electronic structure of the guest. The electronic component is represented by a polarizable continuum model (PCM), while the geometric component is represented by a molecular mechanics (MM) description of the nanotube-guest interaction. This greatly reduces the cost of modeling guest systems inside nanotubes. The reaction profile for a simple system in this model was shown to agree with single point calculations of the whole system. With this model in place, larger, chemically more complex systems can be studied. The nanotube used in testing this model was by 1-2 orders of magnitude smaller than the nanotubes used experimentally. This model can be used to model reactions on such larger systems and provide a theoretical framework to study reactions taking place in these larger nanotubes.

ABSTRACT**APPLICATIONS OF ELECTRONIC STRUCTURE THEORY TO PROBLEMS
IN STRONG-FIELD CHEMISTRY, INORGANIC, AND NANOMATERIAL
SYSTEMS**

by

JASON ANTHONY SONK

August 2012

Advisor: Dr. H. Bernhard Schlegel**Major:** Chemistry (Physical)**Degree:** Doctor of Philosophy

This dissertation covers research performed on applications of electronic structure theory to various fields of chemistry and is divided into eight chapters. Chapter 2 covers modeling electron dynamics of butadiene interacting with a short, intense, non-resonant laser pulse in the absence of ionization. The effects of basis set size and number of excited states included in TD-CI simulations using wavefunction based methods is examined. Chapter 3 expands on this work by examining the response using excitation energies calculated by time-dependent density functional theory. Several DFT functionals are tested including: standard, hybrid, and long-range corrected functionals. The degree to which excited state energies and transition dipoles contribute to the final populations of the excited states is also examined. Chapter 4 investigates the strong-field ionization of a series of linear polyenes of increasing length using a heuristic ionization model. Also tested is the ionization dependence on parameters of the ionization model, basis set size, and number of states included in the simulation.

Chapter 5 describes a study on a chiral pentadentate ligand synthesized by the Kodanko group and the geometrical preference for a single isomer out of five possible isomers. Electronic structure theory indicates that the favored geometry is due to the chiral ligand, which prefers to be in a single conformation in metal complexes due to steric interactions. Chapter 6 covers a paddlewheel dinuclear Cu(II) complex synthesized by the Winter group. This complex has the shortest Cu—Cu separation reported to date and electronic structure theory is used to explore the cause of this small separation. A simple model is proposed where the metal separation is governed by twisting of the ligand due to interligand π orbital interactions. Chapter 7 describes work done in collaboration with the Verani group, exploring the redox properties of some five-coordinate Fe(III) complexes. Chapter 8 sets out to develop an inexpensive model that can be used to optimize guest systems inside single walled nanotubes. The model takes advantage of the highly polarizable nature of nanotubes and is calibrated using a simple hydrogen bonded system. Benchmarks are made to test the reliability of the model.

AUTOBIOGRAPHICAL STATEMENT

JASON ANTHONY SONK

EDUCATION

Wayne State University, Doctor of Philosophy in Chemistry, May 2012.

Thesis Topic: "Applications of Electronic Structure Theory to Problems in Strong-Field Chemistry, Inorganic Chemistry and Materials Systems".

University of Texas at San Antonio, Bachelor of Science in Chemistry, December 2002.

Undergraduate research topic: "Complexes of Pd(en)Cl₂ with 1,5-naphthyridine: Possible host-guest chemistry".

SELECTED PUBLICATIONS

Sonk, J. A.; Schlegel, H. B.; Strong Field Ionization of Linear Polyenes, Accepted: *J.Phys.Chem.A*, (10.1021/jp302389a)

Karunaratne, M.; Lord, R.L.; **Sonk, J. A.**; Heeg, M.J.; Schlegel, H.B.; Winter, C.H.; A Simple Model in Which Interligand Interaction Controls the Cu—Cu Distance in Dinuclear Cu(II) Paddlewheel Complexes, (*In Preparation*)

Allard, M. M.; **Sonk, J. A.**; Heeg, M. J.; McGarvey, B. R.; Schlegel, H. B.; Verani, C. N.; Bioinspired Five-Coordinate Iron(III) Complexes for Stabilization of Phenoxy Radicals. *Angew. Chem. Int. Ed.*, **2011**, (10.1002/anie.201103233)

Sonk, J. A.; Schlegel, H. B.; TD-CI Simulation of the Electronic Optical Response of Molecules in Intense Fields II: Comparison of DFT Functionals and EOM-CCSD. *J. Phys. Chem. A* **2011**, *115*, 11832–11840 (10.1021/jp206437s)

Sonk, J. A.; Caricato, M.; Schlegel, H. B.; TD-CI Simulation of the Electronic Optical Response of Molecules in Intense Fields: Comparison of RPA, CIS, CIS(D) and EOM-CCSD. *J. Phys. Chem. A* **2011**, *115*, 4678-4690 (10.1021/jp107384p)

Abouelatta, A. I.; **Sonk, J. A.**; Hammoud, M. M.; Zurcher, D. M.; McKamie, J. J.; Schlegel, H. B.; Kodanko, J. J.; Synthesis, Characterization and Theoretical Studies of the Metal Complexes Derived from the Chiral Tripyridyldiamine Ligand Bn-CDPy3. *Inorg. Chem.* **2010**, *49*, 5202-5211. (10.1021/ic100322p)